



UNIVERSIDADE FEDERAL DO CEARÁ
CENTRO DE TECNOLOGIA
DEPARTAMENTO DE ENGENHARIA METALÚRGICA E DE MATERIAIS
PROGRAMA DE PÓS-GRADUAÇÃO EM ENGENHARIA E CIÊNCIAS DE
MATERIAS

PABLO BRUNO PAIVA LEÃO

**MICROSCALE ANALYSES OF SAE1075 STEEL UNDER DIFFERENT STAGES OF
LAB-SIMULATED PROCESS ROUTES BASED ON WIRE MANUFACTURING FOR
TENSILE ARMOR APPLICATION IN FLEXIBLE PIPES.**

FORTALEZA

2023

PABLO BRUNO PAIVA LEÃO

**MICROSCALE ANALYSES OF SAE1075 STEEL UNDER DIFFERENT STAGES OF
LAB-SIMULATED PROCESS ROUTES BASED ON WIRE MANUFACTURING FOR
TENSILE ARMOR APPLICATION IN FLEXIBLE PIPES.**

Thesis presented to the doctorate programs in Materials Science and Engineering of the Universidade Federal do Ceará, as a requisite to obtain a doctor degree in Materials Science and Engineering.

Advisor: Prof. Dr. Hamiton Ferreira Gomes de Abreu.

Co-advisor: Prof. Dr. Antonio José Ramirez.

FORTALEZA

2023

Dados Internacionais de Catalogação na Publicação
Universidade Federal do Ceará
Sistema de Bibliotecas

Gerada automaticamente pelo módulo Catalog, mediante os dados fornecidos pelo(a) autor(a)

L477m Leão, Pablo Bruno Paiva.

Microscale analyses of SAE1075 steel under different stages of lab-simulated process routes based on wire manufacturing for tensile armor application in flexible pipes. / Pablo Bruno Paiva Leão. – 2023.
147 f. : il. color.

Tese (doutorado) – Universidade Federal do Ceará, Centro de Tecnologia, Programa de Pós-Graduação em Engenharia e Ciência de Materiais, Fortaleza, 2023.

Orientação: Prof. Dr. Hamilton Ferreira Gomes de Abreu .

Coorientação: Prof. Dr. Antonio José Ramirez Londono.

1. Aço perlitico. 2. Riser. 3. EBSD. 4. MEV. 5. In-situ. I. Título.

CDD 620.11

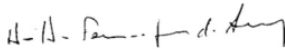
PABLO BRUNO PAIVA LEÃO

**MICROSCALE ANALYSES OF SAE1075 STEEL UNDER DIFFERENT STAGES OF
LAB-SIMULATED PROCESS ROUTES BASED ON WIRE MANUFACTURING FOR
TENSILE ARMOR APPLICATION IN FLEXIBLE PIPES.**


Thesis presented to the doctorate programs in
Materials Science and Engineering of the
Universidade Federal do Ceará, as a requisite to
obtain a Doctor degree in Materials Science and
Engineering.

Approved on: 14/12/2023.


PANEL MEMBERS



HAMILTON FERREIRA GOMES DE ABREU
UFC - Orientador

Documento assinado digitalmente
 **MAURO ANDRES CERRA FLOREZ**
Data: 23/12/2023 21:06:24-0300
Verifique em <https://validar.iti.gov.br>


MAURO ANDRES CERRA FLOREZ
UFC - Examinador Interno

Documento assinado digitalmente
 **WALNEY SILVA ARAUJO**
Data: 26/12/2023 09:28:45-0300
Verifique em <https://validar.iti.gov.br>


WALNEY SILVA ARAUJO
UFC - Examinador Interno



ANTONIO JOSE RAMIREZ LONDONO
- Examinador Externo à Instituição

Documento assinado digitalmente
 **JOSE ADAILSON DE SOUZA**
Data: 26/12/2023 09:35:49-0300
Verifique em <https://validar.iti.gov.br>

JOSÉ ADAILSON DE SOUZA
CENPES - Examinador Externo à Instituição

Documento assinado digitalmente
 **SERGIO SOUTO MAIOR TAVARES**
Data: 25/12/2023 21:51:39-0300
Verifique em <https://validar.iti.gov.br>

SÉRGIO SOUTO MAIOR TAVARES
UFF - Examinador Externo à Instituição

To God.

To my parents, Antonio and Ana.

ACKNOWLEDGEMENTS

This thesis would not have been able to be developed without the extreme help and support of several individuals: family, friends, coworkers from SENAI, and employers from the Federal University of Ceará and the Ohio State University.

I would like to express my deepest, kind, honest, and special thanks to Professors Dr. Hamilton Ferreira Gomes de Abreu, Dr. Atonio José Ramirez, and Dr. João Rodrigues de Barros Neto, for all their support, continuous guidance, advice, acceptance, leadership, encouragement, and assistance during the progress of this research. Without one of them, this research would not have been successful.

I am also grateful for all the Lacam members, Professor Dr. Samuel Filgueiras Rodrigues, Professor Dr. Francisco José dos Santos Oliveira, Dr. Jorge Luiz Cardoso, Dr. Luis Flavio Gaspar Herculano, Dr. Marcos Natan da Silva Lima, MSc. Rodrigo de Carvalho Paes Loureiro, and MSc. Francisco Felipe de Moraes Fideles, for their help in the experiments, partnership, thoughtful ideas, technical discussion, and support.

I would like to express my deep sense of gratitude to my colleagues at The Ohio State University, Dr. Shutong Zhang, Dr. Andres Acuna, MSc. Ana Luísa Terasawa da Rosa, and MSc. Henry Leon, for all the support and shared experiences.

I want to thank all the employers from Laboratório de Caracterização de Materiais – LACAM, SENAI Maracanaú, Laboratório de Pesquisa e Tecnologia em Soldagem – LPTS, Central Analítica of UFC, Center for Electron Microscopy and Analysis – CEMAS, and the Manufacturing and Materials Joining Innovation Center – Ma²JIC.

I want to thank the Coordenação de Aperfeiçoamento de Pessoal de Nível Superior – CAPES, Brazilian agencies, for all the financial support received during my doctorate studies.

I am especially grateful to my lovely girlfriend, Hana Livia Frota Coelho; my parents, Antonio Barroso Leão and Ana Maria Paiva; my brother, Thales Breno Paiva Leão and my second family, Adriano Coelho, Teina Coelho, Arthur Coelho, Raul Coelho, and Ysa Coelho, for all the great moments, daily encouragement, happiness, true love, support, and personal development.

“Sonhos determinam o que você quer. Ação
determina o que você conquista.”

Aldo Novak

RESUMO

As camadas de armadura de tração em risers flexíveis são geralmente feitas de fios de aço perlítico com formato retangular e produzidos em uma sequência de fabricação da seguinte forma: laminação a quente → tratamento de patenteamento (PT) → conformação a frio → enrolamento do fio em espiras → alívio de tensões → processo de reenrolamento do arame → conformação helicoidal do fio ao redor da tubulação. Considerando rota de fabricação acima, o comportamento microestrutural e cristalográfico do aço perlítico em cada uma dessas etapas do processo e em etapas combinadas não são relatados simultaneamente na literatura. Nesse sentido, esta pesquisa estudou extensivamente um aço comercial SAE1075 por meio de análises em microescala (principalmente imagem por elétrons secundários e difração de elétrons retroespalhados) ao longo da rota de processos, mencionados anteriormente, e em escala laboratorial simulando a rota real de fabricação dos fios da armadura de tração. Com base nisso, as operações de laminação e tratamentos térmicos foram inicialmente simuladas em laboratório e em quatro rotas de processo com diferentes configurações de 45% de laminação a quente, PT e 65% de laminação a frio. Ainda neste cenário, as amostras laminadas a frio produzidas pelas quatro rotas distintas foram submetidas a dois tratamentos de alívio de tensões (400 e 700 °C por 60 s) e seguidos pela simulação do processo de reenrolamento de fios, por meio de análises alternadas de dobramento comum por três pontos. Essas duas temperaturas de alívio de tensões, a 400 (SR400) e 700 (SR700) °C, resultaram, respectivamente, em microestruturas perlíticas lamelares e parcialmente esferoidizadas. Além disso, uma investigação mais precisa das condições de perlita lamelar e parcialmente esferoidizada sob dobramento cíclico de três pontos foi realizada por meio de visualizações de elétrons secundários *in situ* em um microscópio eletrônico de varredura (SEM). Considerando o processo final de torção helicoidal do fio retangular em torno da tubulação, uma máquina de torneamento com um guia de eixo cilíndrico foi utilizada para reproduzir o processo real de torção helicoidal. Foram usados dois ângulos de enrolamento (20 e 60° em relação ao eixo longitudinal do eixo cilíndrico) em amostra com formato de tiras longas e estreitas de aço perlítico lamelar e parcialmente esferoidizado, após terem sido dobradas ciclicamente. Neste procedimento experimental, o comportamento da deformação das amostras SR400 e SR700 foi brevemente avaliado em relação aos principais componentes de tensão gerados durante uma torção helicoidal (cisalhamento, dobramento transversal e dobramento normal). Também, o efeito da tensão de cisalhamento no comportamento de deformação da microestrutura do aço perlítico, geralmente realizado através de experimentos comuns de torção com uma visualização microestrutural

difícil, foi investigado por meio de teste de tração-cisalhamento in situ em um SEM. Além disso, a correlação de imagens digitais foi empregada nas visualizações in situ por elétrons secundários realizadas neste trabalho. Os resultados indicaram uma rota de fabricação prejudicial para a microestrutura perlítica resultante. Nesse caso, uma condição de aço perlítico com a orientação de microtextura $\{111\} \langle 112 \rangle$ de laminação a frio mais alta seguida pelo tratamento de alívio de tensões a 700 °C por 60 segundos (SR700) foi a única condição propensa à suscetibilidade de trincas durante os experimentos de dobramento comum. Especificamente, a condição SR700 apresentou um fenômeno de amolecimento e uma falha mais precoce durante os testes de dobramento in situ por três pontos em comparação com a condição SR400. Por fim, esta microestrutura parcialmente esferoidizada foi mais suscetível ao componente de dobramento normal durante a operação de torção helicoidal, o que resulta em maior heterogeneidade de deformação na seção transversal do arame retangular, principalmente para um ângulo de enrolamento helicoidal pequeno.

Palavras-chave: Aço perlítico; Riser; EBSD; MEV; In-situ; Laminação; Tratamento de patenteamento; Dobramento; Cisalhamento; Torção helicoidal.

ABSTRACT

Tensile armor layers in flexible risers are usually made of rectangular pearlitic steel wires and produced in a manufacturing sequence as follows: hot-rolling → patenting treatment (PT) → cold forming → wire coiling → stress relief → re-winding wire process → helical wire shaping around the pipeline. Concerning this manufacturing route, the microstructural and crystallographic behavior of pearlitic steel in each process step and combined are not reported simultaneously in the literature. This research extensively studied a commercial SAE1075 pearlitic steel via microscale analyses (mainly secondary electron imaging and electron backscattered diffraction) throughout a lab-scaled set of processes that simulate the actual manufacturing route for tensile armor wire production. Based on this, the rolling operations and heat thermal treatments were initially lab-simulated in four process routes with different setups of 45% hot-rolling, PT, and 65% cold-rolling. Still, in this scenario, the cold-rolled specimens produced through the four distinct routes underwent two stress relief treatments (at 400 and 700 ° C for 60 s). They succeeded by simulating the re-winding wire process via four alternated regular three-point bending procedures. These two stress relief temperatures, at 400 (SR400) and 700 (SR700) ° C, resulted in lamellar and partially spheroidized pearlitic microstructures. In addition, a more accurate investigation of the lamellar and partially spheroidized pearlitic conditions under cyclic three-point bending was performed via in-situ secondary electron imaging in a scanning electron microscope (SEM). Regarding the helical wire shaping around the pipeline, a lather machine with a cylindrical shaft guide was used to reproduce the actual helical torsion process with two wound angles (20 and 60° about the longitudinal axis of the cylindrical shaft) in long and narrow strips of the lamellar and partially spheroidized pearlitic steel conditions after being cyclic three-point bent. In this experimental procedure, the deformation behavior of the SR400 and SR700 cyclic bent specimens was briefly evaluated concerning the main stress components under the helical torsion state (shear, transverse bending, and normal bending). Also, the effect of the shear stress on the deformation behavior of pearlitic steel microstructure, usually carried out by hard microstructural visualization of regular torsion experiments, was investigated via in-situ tensile-shear test in SEM. Furthermore, digital imaging correlation was employed in this work's in-situ secondary electron visualizations. The results indicated a harmful manufacturing route for the resultant pearlitic microstructure. In this case, a pearlitic steel condition with the highest cold rolled $\{111\} \langle 112 \rangle$ microtexture orientation followed by stress relief at 700 ° C for 60 seconds

(SR700) was the only condition prone to crack susceptibility during the regular bending experiments. In detail, the SR700 displayed a softening phenomenon and an earlier failure during the in-situ three-point bending test compared to the SR400 specimen. Finally, this partially spheroidized microstructure was more susceptible to the normal bending component during the helical torsion operation, which results in more heterogeneity of strain throughout the cross-section of the rectangular specimen, mainly under a small helical wound angle.

Keywords: Pearlitic steel; Riser; EBSD; SEM; In-situ; Rolling; Patenting treatment; Bending; Shear; Helical torsion.

LIST OF FIGURES

Figura 1	– Illustration of a hybrid riser.....	15
Figura 2	– The layers in flexible risers.....	16
Figura 3	– Schemes of the subdivision structures in a pearlite microstructure. T_{θ} means cementite thickness.....	16
Figura 4	– Schematic illustration of the (a) re-winding wire into the bobbins process and (b) tensile armor machine.....	17
Figura 5	– Stereographic projection of the $\{100\}$ pole in a cubic crystal. (a) Crystal inside the reference sphere. (b) Projection of the $\{100\}$ pole onto the RD-TD plan. (c) $\{100\}$ pole figure of a cubic crystal and the position indication of the (100) pole via the β and α angles.....	19
Figura 6	– (a) A complete 001 inverse pole figure. (b) A unit stereographic triangle indicated by the letter A in the complete inverse pole figure.....	20
Figura 7	– Definition of the Euler angles ($\varphi_1, \Phi, \varphi_2$) according to the Bunge notation.....	20
Figura 8	– (a) Representation of crystals before the rotation, and (b) after the rotation via the Euler angles ($\varphi_1, \Phi, \varphi_2$)	21
Figura 9	– ODF section at $\varphi_2=45^\circ$ with the location of its texture components. The fiber α , fiber γ , and fiber θ represent the $\langle 110 \rangle$ family's directions parallel to the rolling direction (RD), $\langle 111 \rangle$ family's directions parallel to the normal direction (ND), and $\langle 001 \rangle$ family's directions parallel to the normal direction (ND), respectively.....	21
Figura 10	– Scheme of the four laboratory processing routes performed in the present work. (a) Overall flowchart representation of the process routes. (b) Illustrative diagram of the individual steps performed in the hot rolling (≈ 45) process. (c) Isothermal transformation diagram with representative details of the patenting treatments carried out in this study. The numbers in millimeters (mm) contained in Figures 1 (a) and 1 (b) represent the samples' thicknesses	30

- Figura 11 – Color-coded inverse pole figure (IPF) map, grain boundary distribution map, and orientation distribution function (ODF) at $\phi_2 = 45^\circ$, respectively, for the samples: (a)(b)(c) S1, (d)(e)(f) R2S1, (g)(h)(i) R3S1, (j)(k)(l) R4S1 and (m)(n)(o) R4S2. The black arrows in the color-coded IPF and grain boundary distribution maps of the R4S1 sample point out a shear band..... 34
- Figura 12 – Pearlitic block size average of the hot-rolled (S1) and the patenting treated (R2S1, R3S1, and R4S2) samples, and (b) distribution of grain boundary type per area regarding the samples S1, R2S1, R3S1, R4S1, and R4S2..... 36
- Figura 13 – Color-coded inverse pole figure (IPF) map, Scanning electron microscope (SEM) Secondary electrons (SE) image of the IPF map area and SEM SE image in higher magnification, respectively, of (a)(b)(c) sample S1, (d)(e)(f) sample R2S1, (g)(h)(i) sample R3S1, (j)(k)(l) sample R4S1 (the red arrows indicate a shear band) and (m)(n)(o) sample R4S2..... 37
- Figura 14 – Values of interlamellar spacing, microhardness, and colony size for the S1, R2S1, R3S1, and R4S2 processed conditions..... 38
- Figura 15 – SEM SE image of GB- α (indicated by the big white arrows) and pearlite distribution in the matrix of the (a) sample S1, (b) sample R2S1 (the smaller white arrows indicate Widmanstatten ferrite), (c) sample R3S2, and (d) sample R4S2..... 39
- Figura 16 – SEM SE image, color-coded IPF map and ODF at $\phi_2 = 45^\circ$, respectively for each cold-rolled samples: (a)(b)(c) R1S1, (d)(e)(f) R2S2, (g)(h)(i) R3S2 and (j)(k)(l) R4S3. In the SE images, small white arrows indicate bent and broken cementite lamellae caused by shear bands, while big white arrows point out bent and broken cementite lamellae due to their hard initial orientation with the rolling direction..... 41
- Figura 17 – (a) Pearlitic block size before 65% cold-rolling reduction against its $\{111\}\langle 112 \rangle$ microtexture component intensity after 65% cold-rolling reduction for the R1S1, R2S2, R3S2, and R4S3 samples (the red dashed circle and the special case reference meaning a different cold-rolling process in the R4S3 condition) and (b) Values of microhardness, interlamellar spacing, and

	their variation concerning one condition before in the process route of the R1S1, R2S2, R3S2, and R4S3 cold-rolled samples.....	43
Figura 18	– SEM SE image of the 65% cold-rolled pearlitic steel (R3S2) after stress relief treatment at (a) 400 °C during 60 seconds (R3400) and (b) 700 °C during 60 seconds (R3700) (The red arrows point out disconnected and elongated cementite, the yellow arrows indicate partially spheroidized cementite, and the orange arrows indicate the completely spheroidized cementite)	44
Figura 19	– SEM SE images indicate cementite spheroidization in the shear bands (pointing out by white arrows) and in the irregular bent cementite zone (pointing out by an orange arrow) after stress relief treatment at 700 °C for 60 seconds (R3700 condition)	45
Figura 20	– Color-coded IPF map, grain boundary distribution map, distribution of grain boundary type per area, ODF at $\phi_2 = 45^\circ$ and Taylor factor map, respectively, of the (a)(c)(e)(f)(h) sample R3400 and (b)(d)(e)(g)(i) sample R3700. The dashed white circle indicates a region with recrystallized small grains	47
Figura 21	– Crack from the R3700crack sample condition in the tensile region of the fourth bending experiment and below the left side of the superior pin. (a) SEM SE image of the entire crack. (b) SEM SE image of a region with crack deviation and microcracks. (c) Color-coded IPF map of the region containing the crack deviation and one microcrack. The dashed white circles indicate small grains deformed in a direction almost parallel to the main crack and shear bands. (d) ODF at $\phi_2 = 45^\circ$ calculated from the IPF map in Figure 102 (c). (e) SEM SE image of a smooth crack deviation. (f) SEM SE image of the region close to the crack tip. (g) SEM SE image from a crack’s tip region showing the bending of a lamellar pearlite.....	49
Figura 22	– Tip of a crack in the R3700crack sample condition, located below the left side of the superior pin in the tensile region after four alternating bending experiments. (a) SEM SE image. (b) Color-coded IPF map. The dashed white circles indicate regions of small grains deformed in a direction close to the crack propagation and shear bands. (c) Grain boundary distribution map. (d) Taylor factor map. The white arrow indicates a non-recrystallized and non-rotated grain with local shear strains.....	51

Figura 23	– Crack from the R3700crack sample condition in the tensile region of the fourth bending experiment and below the right side of the superior pin. (a) SEM SE image of the entire crack. (b) SEM SE image of the crack tip. (c) Color-coded IPF map of the crack tip. The dashed white circles indicate regions of small grains deformed in a direction close to the crack propagation. (d) Microcracks from an adjacent region around the main crack.....	52
Figura 24	– Flowchart sketch of the lab-simulated processing route performed in the present study. The numbers in millimeters (mm) represent the sample’s thickness	58
Figura 25	– Details of the scanning transmission electron microscopy (STEM) implemented in this work. (a) Schematic position of the thin foils extracted from the surfaces of the SR400 and SR700 samples via focused ion beam (FIB) microscopy. (b) Superior view of the transparent foil after its thickness reduction by FIB technique (c) Lateral view of the transparent foil after its thickness reduction by FIB technique (d) FIB thin foil set up for STEM imaging, and (e) for transmission backscattered electron diffraction (<i>t</i> -EBSD) analysis.....	60
Figura 26	– Details of the in-situ and interrupted three-point bending (TPB) experiments carried out in this work. (a) Kammrath-Weiss tensile-compression stage coupled with an adapter MZ.V32 for the TPB tests. (b) Schematic sketch of the areas (red squares) where the high magnification secondary images were acquired during the in situ TBP performance. (c) Illustrative scheme of the region (red squares) where the electron backscattered diffraction analyses were performed during the interrupted TPB operation.....	61
Figura 27	– Initial microstructural characteristics of the SR400 and SR700 conditions. Start secondary electron (SE) micrographs obtained via scanning electron microscopy, bright field images acquired via scanning transmission electron microscopy technique, and grain boundary distribution (GBD) maps collected via electron backscattered diffraction analysis, respectively, of (a) (c) (e) SR400 and (b) (d) (f) SR700 specimens. (g) The total length of the grain boundary types measured from the GBD maps of SR400 and SR700	

	conditions. The yellow and orange arrows in the SE micrographs indicate shear bands and disrupted cementite zones, respectively.....	65
Figura 28	– Engineering stress-Engineering strain curves obtained from tensile tests of SR400 and SR700 conditions. The black arrow indicates a discontinuous yielding behavior for the SR700 specimen under tensile deformation.....	67
Figura 29	– Scanning transmission electron backscattered diffraction (<i>t</i> -EBSD) of SR400. (a) Scanning transmission electron microscopy bright field image of SR400 specimen. (b) Phases map of one region where the <i>t</i> -EBSD was performed in SR400. (c) Image quality map from the same <i>t</i> -EBSD area shown in Figure 6(b). (d) (100), (110), and (111) pole figures of ferrite obtained from five <i>t</i> -EBSD maps in SR400. (e) (100), (110) and (111) pole figures of cementite obtained from five <i>t</i> -EBSD maps in SR400 (f) Overlapped (100), (110) and (111) pole figures from ferrite and cementite from the SR400's <i>t</i> -EBSD maps..	69
Figura 30	– Scanning transmission electron backscattered diffraction (<i>t</i> -EBSD) of SR700. (a) Scanning transmission electron microscopy bright field image of SR700 specimen. (b) Phases map of one region where the <i>t</i> -EBSD was performed in SR700. (c) Image quality map from the same <i>t</i> -EBSD area shown in Figure 6(b). (d) (100), (110), and (111) pole figures of ferrite obtained from five <i>t</i> -EBSD maps in SR700. (e) (100), (110) and (111) pole figures of cementite obtained from five <i>t</i> -EBSD maps in SR700 (f) Overlapped (100), (110) and (111) pole figures of ferrite and cementite from the SR700's <i>t</i> -EBSD maps.....	70
Figura 31	– Elongation-load hysteresis curves obtained during the cyclic in-situ three-point bending (TPB) test for (a) SR400 and (b) SR700 pearlitic steel conditions. Total elongation-load plotted from Elongation-load hysteresis data obtained during the in-situ cyclic TPB experiment for (c) SR400 and (d) SR700 specimens. In Figure 8 (a) and 8 (b), ϵ_{rpe} means reverse plastic elongation.....	72
Figura 32	– Macro scanning electron microscope (SEM) images around the moment the crack achieved the lateral surface (RD - ND) of the SR400 specimen during the fourth successive in-situ three-point bending test: (a) Just before the crack arrived on the lateral surface (RD - ND), (b) At the moment the crack arrives	

on the lateral surface (RD - ND), (c) Just after the crack arrived on the lateral surface (RD - ND), (d)(e) Different instants of the crack propagation throughout the specimen's thickness (about the ND direction), (f) At the moment the crack stopped to propagate throughout the specimen's thickness (about the ND direction) in higher magnification, and (g) Final lateral crack in a lower magnification..... 75

Figura 33 – Macro scanning electron microscope (SEM) images at the moment the crack achieved the lateral surface (RD - ND) of the SR700 specimen during the fourth successive in-situ three-point bending test: (a) Just before the crack arrived on the lateral surface (RD - ND), (b) At the moment the crack arrives on the lateral surface (RD - ND), (c) Just after the crack arrived on the lateral surface (RD - ND), (d)(e) Different instants of the crack propagation throughout the specimen's thickness (about the ND direction), and (f) Final lateral crack..... 77

Figura 34 – High magnification SEM images of SR400 specimen during cyclic in-situ TPB experiment, in the unbent condition (B0) and at the maximum loading pin displacement (2.5 mm) during B1, B2 and B3, respectively, for the two constant evaluated specimen's regions: 10 nm below the (a)(c)(e)(g) top and 10 nm above the (b)(d)(f)(h) bottom. (i) (j) Eulerian strain maps, e_{yy} , obtained via digital image correlation (DIC) from the area marked by orange dashed rectangles in Figure 34(g) and Figure 34(h) during the first three subsequent bending procedures..... 79

Figura 35 – High magnification SEM images of SR700 specimen during cyclic in-situ TPB experiment, in the unbent condition (B0) and at the maximum loading pin displacement (2.5 mm) during B1, B2 and B3, respectively, for the two constant evaluated specimen's regions: 10 nm below the (a)(c)(e)(g) top and 10 nm above the (b)(d)(f)(h) bottom. (i) (j) Eulerian strain maps, e_{yy} , obtained via digital image correlation (DIC) from the area marked by orange dashed rectangles in Figure 35(g) and Figure 35(h) during the first three subsequent bending procedures..... 80

Figura 36 – Color-coded inverse pole figure (IPF) map and image quality (IQ) map, respectively, in the interrupted TPB condition of: (a)(b) unbent condition (B0).

(e)(f) After B1, (i)(j) After B2, (m)(n) After B3, and (q)(r) During B4 for SR400 specimen, and (c)(d) unbent condition (B0), (g)(h) After B1, (k)(l) After B2, (o)(p) After B3, and (s)(t) During B4 for SR700 specimen. The big black and the small white arrows in Figure 36(a) indicate the mostly violet big pearlitic block with many small bad indexed regions and shear bands, respectively. The small black arrows in Figure 36(g) indicate zones with many small ferritic grains. The yellow dashed rectangles in Figure 36(b) and Figure 36(d) show the reference areas for both evaluated specimens, where the image quality intensities were acquired for all TBP steps. The small yellow arrows in Figure 36(i), Figure 36(j), Figure 36(k), and Figure 36(l) indicate the matched regions between the IPF and IQ maps..... 83

Figura 37 – Average image quality (IQ) intensity vs. bending condition during the interrupted three-point bending operation for SR400 and SR700. The IQ intensities were obtained from the image quality maps in Figure 36 on the delimited areas indicated by yellow dashed rectangles in Figure 36 (b) and Figure 36 (d)..... 85

Figura 38 – Scanning electron microscope (SEM) fractographic observation of the SR400 specimen after the cyclic in-situ three-point bending test. (a) Overview of the SR400 bending fracture on the RD-TD surface. (b) Fracture region in the edge of the SR400 specimen. (c) Fracture surface of the crack in the lateral section (RD-ND). (d)(e)(f) Fracture surface, in different magnifications, of the crack in the RD-TD area..... 89

Figura 39 – Scanning electron microscope (SEM) fractographic observation of the SR700 specimen after the cyclic in-situ three-point bending test. (a) Overview of the SR700 bending fracture on the RD-TD surface. (b) Fracture region in the edge of the SR700 specimen. (c) Fracture surface of the crack in the lateral section (RD-ND). (d)(e)(f) Fracture surface, in different magnifications, of the crack in the RD-TD area..... 90

Figura 40 – A tensile armor machine during the manufacturing process of the riser 94

Figura 41 – Stress components in tensile armor. Where σ_{12} is a shear stress component, σ^n is a normal bending stress component, σ^c is a frictional stress caused between adjacent layers, and σ^t is a transverse bending stress component..... 95

Figura 42	– Flowchart sketch of the lab-simulated processes employed in pearlitic steel in this study. The numbers in millimeters (mm) mean the samples' thickness.....	96
Figura 43	– Schematic view of the helical torsion performed in a lather machine under a wound angle of (a) 20° and (b) 60°.....	97
Figura 44	– Secondary electron images on the longitudinal section of the following samples' conditions: (a) SH40, (b) SH42, (c) SH46, (d) SH70, (e) SH72, and (f) SH76.....	100
Figura 45	– Inverse figure pole maps on the longitudinal section of the following samples' conditions: (a) SH40, (b) SH42, (c) SH46, (d) SH70, (e) SH72, and (f) SH76.....	101
Figura 46	– Microhardness maps on the cross-section of the stress-relieved specimens at 400°C for 60 seconds followed by helical torsion under a wound angle of (a) 0° (SH40), (b) 20° (SH42), and (c) 60° (SH46)	102
Figura 47	– Microhardness maps on the cross-section of the stress-relieved specimens at 700°C for 60 seconds followed by helical torsion under a wound angle of (a) 0° (SH70), (b) 20° (SH72), and (c) 60° (SH76)	103
Figura 48	– Microhardness average from the microhardness maps in Figure 46 and Figure 47.....	103
Figura 49	– Schematic proceedings employed in this work to produce the start investigated pearlitic steel conditions (UC and DR). (a) Diagram with representative details of the thermal treatment with slow cooling performed in the UC specimen (b) Illustrative flowchart of the laboratory processing route undergone by the DR specimen. The numbers in millimeters (mm) contained in Figure 49 (b) represent the samples' thickness.....	109
Figura 50	– Details of the In-situ shear experiment implemented in this work. (a) Sketch of the tensile-shear specimen geometry with its dimensions in millimeters. (b) Machined tensile-shear specimen. (c) Central region of the tensile-shear specimen. (d) Kammrath-Weiss tensile stage. (e) The tensile stage set up in the SEM chamber.....	110

Figura 51	– Initial metallurgical characteristics of both pearlitic steel conditions (UC and DR) used in the in-situ tensile-shear experiment. Start SEM microstructures of the (a) UC and (b) DR samples. Color-coded inverse pole figure (IPF) map, kernel average misorientation (KAM) map, and grain boundary distribution map, respectively, for the (c)(d)(e) UC and (f)(g)(h) DR conditions. (i) Distribution of the pearlitic morphological angles about the tensile axis, (j) distribution of KAM values, and (k) distribution of grain boundary type per area for UC and RD.....	112
Figura 52	– Elongation-load curves obtained during the in-situ tensile-shear test for UC and DR pearlitic steel conditions. The points marked with x represent the stages where the captured SEM images were selected for demonstrating the progress of the tensile-shear experiment.....	115
Figura 53	– Macro SEM images of the UC specimen’s deformation during the in-situ tensile-shear test following, as a reference, the x-marks in its elongation-load curve (see Figure 52): (a) 1CU, (b) 2CU, (d) 3CU, (e) 4CU, (g) just before 5CU in a lower magnification, (h) just before 5CU in the regular magnification, (i) 5CU, (j) after 5CU in a lower magnification. (c) Illustrative diagram reference of the stress components and geometrical analysis position during the in-situ tensile-shear test. (f) Eulerian u -displacement map obtained via digital image correlation (DIC) from the 1CU up to the 4CU stage. The red dashed rectangles represent the region where the images in high magnification of Figure 55 were taken.....	117
Figura 54	– Macro SEM images of the DR specimen’s deformation during the in-situ tensile-shear test following, as a reference, the x-marks in its elongation-load curve (see Figure 52): (a) 1DR, (b) 2DR, (d) 3DR, (e) 4DR, (g) 5DR, and (h) after 5DR. (c) Illustrative diagram reference of the stress components and geometrical analysis position during the in-situ tensile-shear test. (f) Eulerian u -displacement map obtained via digital image correlation (DIC) from the 1DR up to the 4DR stage. The red dashed rectangles represent the region where the images in high magnification of Figure 56 were taken.....	118
Figura 55	– High magnification SEM images of the UC specimen’s deformation during the in-situ tensile-shear test following, as a reference, the x-marks in its	

- elongation-load curve (see Figure 52): (a) (b) 1UC, (d) (e) 2UC, (g) (h) 3UC, and (j) (k) 4UC. (c) Illustrative diagram reference of the stress components and geometrical analysis position during the in-situ tensile-shear test. (f) (i) (l) Eulerian shear strain maps, e_{xy} , obtained via digital image correlation (DIC), in the respective stages 2CU, 3CU, and 4CU of the UC's elongation-load curve in Figure 52..... 119
- Figura 56 – High magnification SEM images of the DR specimen's deformation during the in-situ tensile-shear test following, as a reference, the x-marks in its elongation-load curve (see Figure 52): (a) (b) 1DR, (d) (e) 2DR, (g) (h) 3DR, and (j) (k) 4DR. (c) Illustrative diagram reference of the stress components and geometrical analysis position during the in-situ tensile-shear test. (f) (i) (l) Eulerian shear strain maps, e_{xy} , obtained via digital image correlation (DIC), in the respective stages 2DR, 3DR, and 4DR of the DR's elongation-load curve in Figure 52..... 121
- Figura 57 – (a) Elongation-load curve of, (b) color-coded IPF map before, (c) backscattered electron (BSE) image on the same area of the color-coded IPF map before, (d) color-coded IPF map after, (e) BSE image on the area indicated by a yellow dashed rectangle in the IPF map after, (f) SE image on the same area of the IPF map after, (g) orientation distribution function (ODF) at $\phi_2 = 45^\circ$ calculated with monoclinic symmetry from the IPF map before, and (h) ODF at $\phi_2 = 45^\circ$ calculated with monoclinic symmetry from the IPF map after the interrupted DR's tensile-shear experiment. (i) Intensity of the γ (ND//<111>) fiber in the ODFs shown in Figure 57 (g) and (h)..... 123
- Figura 58 – SE image of decohesion in the cementite/ferrite interface after the interrupted tensile-shear test in pearlites with their lamellar morphological angles of (a) $\approx 20.7^\circ$ (b) $\approx 12.3^\circ$ about the tensile axis..... 126
- Figura 59 – SEM fractographic observation of the UC specimen after the in-situ tensile-shear test. (a) Overview of UC's shear fracture surface. (b) The central region of the UC's rupture surface. (c) Shear fracture with dimples (region I). (d)(e)(f)(g) Shear fracture with a flat surface (Region II) 127
- Figura 60 – Ciclo da informação SEM fractographic observation of the RD specimen after the in-situ tensile-shear test. (a) Overview of RD's shear fracture surface. (b)

Shear fracture with a flat surface (Region II). (c) (d)(e)(f)(g) Shear fracture with dimples (region I) 128

Figura 61 – Color-coded IPF maps on large areas of the non-deformed UC specimen containing their biggest pearlitic block size with the maximum length of (a) 168.8 μm , and (b) 167.6 μm 130

LIST OF TABLES

Tabela 1	– Chemical composition of the as-received pearlitic steel (wt%)	30
Tabela 2	– Summary of the main microtexture components found in the ODFs shown in Figure 2 for the five samples before 65% cold-rolling reduction	35
Tabela 3	– Summary of the samples' conditions investigated in this work with their respective abbreviated names.....	97
Tabela 4	– Summary of the initial microstructure characteristics of the UC and DR pearlitic steel conditions.....	114
Tabela 5	– Structural properties and microhardness average of the UC and DR conditions.....	115

LIST OF ABBREVIATIONS

PT	Patenting Treatment
SR400	Stress Relieved at 400 °C
SR700	Stress Relieved at 700 °C
SEM	Scanning Electron Microscope
EBSD	Electron Backscatter Diffraction
ODF	Orientation Distribution Function
ND	Normal Direction
TD	Transversal Direction
RD	Rolling Direction
IS	Interlamellar Spacing
PAGS	Prior Austenite Grain Size
HRP	Hot-Rolling Process
BCC	Body-Centered Cubic
DIC	Digital Image Correlation
SE	Secondary Electron
ATs	Austenitization Temperatures
R2S1	Route 2 - Sample 1
R3S1	Route 3 - Sample 1
R4S2	Route 4 - Sample 2
R1S1	Route 1 - Sample 1
R2S2	Route 2 – Sample 2
R3S2	Route 3 – Sample 2
R4S1	Route 4 - Sample 1
R4S3	Route 4 – Sample 3
IPF	Inverse Pole Figure
mrd	Multiple Random Densities
PBS	Pearlitic Block Size
LABs	Low Angle Boundaries
GNDs	Geometrically Necessary Dislocations
GB- α	Grain Boundary of Ferrite
RWWB	Re-Winding Wire into the Bobbins

OR	Orientation Relationship
TPB	Three-Point Bending
STEM	Scanning Transmission Electron Microscopy
t-EBSD	Transmission Electron Backscatter Diffraction
FEG	Field Emission Gun
FIB	Focused Ion Beam
WD	Working Distance
IQ	Image Quality
TSL	Tensile Armor Layer
TS	Tensile-Shear

LIST OF SYMBOLS

Fe	Iron
C	Carbon
°C	Degrees celsius
s	Seconds
H ₂ S	Hydrogen sulphide
Fe ₃ C	Cementite
CO ₂	Carbon dioxide
α	Ferrite
θ	Cementite
γ	Austenite
mm	Milimeters
wt%	Percentage by weight
μm	Micrometers
ΔT	Variation of temperature
m	Strain-rate sensitivity
HV	Vickers hardness
N	Newtons
e_{rpe}	Reverse plastic elongation
e_{yy}	Eulerian y-normal strain
e_{xy}	Eulerian shear strain
φ_1	Euler Angle phi one.
Φ	Euler angle phi.
φ_2	Euler angle phi two.

TABLE OF CONTENTS

1	INTRODUCTION.....	14
1.1	Riser, tensile armor layer, and pearlitic steel	14
1.2	Crystallographic microanalysis and types of texture visualization	18
1.3	Motivation for the thesis	21
1.4	Objectives of the thesis	23
1.4.1	<i>General objective.....</i>	23
1.4.2	<i>Specific objectives.....</i>	23
1.5	Thesis organization.....	24
2	RESULTS: MICROSTRUCTURE, MICROTEXTURE, AND CRACK SUSCEPTIBILITY IN PEARLITIC STEEL DURING LAB-SIMULATED PROCESSES AIMING TENSILE ARMOR APPLICATION IN FLEXIBLE PIPELINES.....	26
2.1	Review	26
2.2	Methodology.....	29
2.2.1	<i>Samples processing.....</i>	29
2.2.2	<i>Samples Characterization.....</i>	31
2.3	Results and discussion.....	32
2.3.1	<i>Samples before 65% cold-rolling reduction.....</i>	32
2.3.2	<i>65% cold-rolled samples.....</i>	39
2.3.3	<i>Stress-relieved samples after 65% cold-rolling reduction in route 3.....</i>	43
2.3.4	<i>Mechanism of crack nucleation and propagation during bending test.....</i>	48
3	RESULTS: IN-SITU AND INTERRUPTED CYCLIC THREE-POINT BENDING TESTS IN SEM OF TWO PEARLITIC STEEL MICROSTRUCTURES: LAMELLAR AND PARTIALLY SPHEROIDIZED.....	54
3.1	Review	54
3.2	Methodology.....	57
3.2.1	<i>Specimens processing.....</i>	57
3.2.2	<i>Tensile test, scanning transmission electron microscopy (STEM) image, and transmission electron backscatter diffraction (t-EBSD) analysis.....</i>	59
3.2.3	<i>In-situ and interrupted three-point bending experiment.....</i>	60
3.3	Results and discussion.....	63

3.3.1	<i>The characteristics of the starting pearlitic steel before the in-situ bending experiment.....</i>	63
3.3.2	<i>In-situ three-point bending (TPB) experiments and digital image correlation (DIC).....</i>	71
3.3.3	<i>Electron backscattered (EBSD) in interrupted three-point bending (TPB) experiments.....</i>	82
3.3.4	<i>Fractured surfaces after the in-situ three-point bending (TPB) experiments....</i>	88
4	RESULTS: INFLUENCE OF HELICAL TORSION ON THE DEFORMATION BEHAVIOR OF TWO PEARLITIC STEEL MICROSTRUCTURES: LAMELLAR AND PARTIALLY SPHEROIDIZED.....	93
4.1	Review	93
4.2	Methodology.....	95
4.2.1	<i>Samples' lab-processing.....</i>	95
4.2.2	<i>Samples' characterization.....</i>	97
4.3	Results and discussion.....	98
5	RESULTS: IN-SITU TENSILE-SHEAR TEST IN SEM AND DIC ANALYSIS OF TWO PEARLITIC STEEL MICROSTRUCTURES: UNDERFORMED-COARSE AND DEFORMED-REFINED.....	105
5.1	Review	105
5.2	Methodology.....	107
5.2.1	<i>Samples processing.....</i>	107
5.2.2	<i>In-situ tensile-shear (TS) experiment and digital image correlation (DIC).....</i>	108
5.2.3	<i>Interrupted tensile-shear (TS) experiment in the RD specimen.....</i>	110
5.3	Results and discussion.....	111
5.3.1	<i>Initial microstructural characteristics of pearlitic steel before the tensile-shear (TS) experiment.....</i>	111
5.3.2	<i>In-situ tensile-shear (TS) experiments and digital image correlation (DIC).....</i>	114
5.3.3	<i>Interrupted shear-tensile (TS) experiment of DR specimen</i>	122
5.3.4	<i>Fracture surfaces.....</i>	125
6	CONCLUSIONS AND RECOMMENDATIONS FOR FURTHER WORKS.....	131
6.1	Conclusions.....	131

6.1.1	<i>Microstructure, microtexture, and crack susceptibility in pearlitic steel during lab-simulated processes aiming tensile armor application in flexible pipelines.....</i>	131
6.1.2	<i>In-situ and interrupted cyclic three-point bending tests in SEM of two pearlitic steel microstructures: lamellar and partially spheroidized.....</i>	132
6.1.3	<i>Influence of helical torsion on the deformation behavior of two pearlitic steel microstructures: Lamellar and partially spheroidized</i>	133
6.1.4	<i>In-situ tensile-shear test in SEM and DIC analysis of two pearlitic steel microstructures: undeformedcoarse and deformed-refined.....</i>	133
6.2	Recommendation for future works.....	134
	REFERENCES.....	136

1 INTRODUCTION

This chapter briefly describes the manufacture and application of pearlitic steel wires for tensile armor in flexible risers in the oil and gas sector. In addition, this section includes the basic concepts of texture visualization, details of the thesis organization, and the objectives of the thesis.

1.1 Riser, tensile armor layer, and pearlitic steel

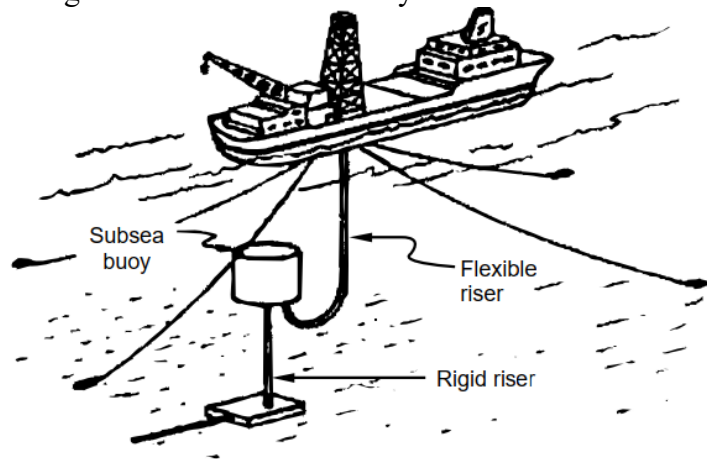
The transfer of crude oil from the sea bed to the offshore structures on the ocean top surface is a paramount and fundamental process for the oil and gas industry, mainly regarding deep-depth wells (above 1.5 km). This procedure occurs under hostile operational conditions like a dynamic ocean environment and high service pressures/temperatures. These features challenge the technological projects of the structures employed in this activity. In this context, oil pipelines are special devices for the oil and gas sector due to their excellent efficiency in fluid transportation. The first oil pipelines implemented in offshore operation dates from 1897 in the United States of America (LEFFLER *et al.*, 2003; FERNANDO *et al.*, 2017).

In Brazil, Petrobras started its first ocean oil exploration in 1968. This mark resulted in new opportunities for fossil fuel extraction in Brazil's deep and ultradeep sea zones (HILL *et al.*, 2006). In 2018, Brazil's marine reservoir corresponded to around 95.7% of the national crude oil production. By this same period, the pre-salt, an ultra-deepwater exploration that may achieve up to 7 km in water depth, represented 55.2% of the general Brazilian production, which means 521.5 million barrels of crude oil (AGENCIA NACIONAL DE PETRÓLEO, 2019). In this case, the pre-salt fields provided a tremendous productive efficiency compared to the regular wells. For instance, in 1968 (pos-salt), the crude oil production was 500 thousand barrels per day, while in 2018 (pre-salt), this number increased three times (1.5 million barrels per day) by exploring only 0.54% of the wells' number used during the post-salt period (PETROBRAS, 2021). In the present year (2023), Petrobras achieved a total of 2.06 million oil barrels per day due to pre-salt wells (COM, 2023). Moreover, the pre-salt exploration demands long-service life equipment because of severe operational environmental conditions. Given this, the pipes entitled risers were developed and designed to be widely employed in this specific oil and gas application.

In particular, risers are pipeline systems that connect the static structures on the marine bottom to the floating vessels on the ocean surface. They can be coupled to subsea buoys and are classified into two types: rigid and flexible. In addition, there is the hybrid risers, which

means a combination of rigid and flexible riser structures, as illustrated in Figure 1 (BAI *et al.*, 2012).

Figure 1 – Illustration of a hybrid riser.



Source: American petroleum institute, (2007).

The unbonded flexible risers are complex structures comprising combined concentric metal and polymer layers (see Figure 2). This tubular arrangement can resist torsion, tensile, bending, and external/internal pressures in shallow or ultradeep waters. In addition, the flexible riser's layers can slip over each other when this system undergoes external or internal loadings. Each of these covers has a specific function during the riser performance. For instance, the carcass prevents the pipe from collapsing due to hydrostatic pressure or the buildup of gases inside the riser structure.

Regarding the pressure armor layer, this cover's role is to support the inner polymer barrier and the core system to resist pressure loadings in the radial direction. Another layer called tensile armor also promotes axial rigidity while minimally compromising the riser's flexibility. Furthermore, the tensile armor layer still supports all the riser weights and transfers the load to the vessel structure, making this cover paramount for risers' application. In detail, the tensile armor is constituted of many flat wires made of carbon steel (usually pearlitic steel) (BAI *et al.*, 2012; DE SOUSA *et al.*, 2014; TAGLIARI *et al.*, 2019; MARINHO *et al.*, 2006; DENNIS, 2018).

Given this, pearlitic steels present a great combination of torsion toughness and tensile strength due to their microstructural arrangement of hard Fe_3C – cementite (orthorhombic) and soft α -ferrite (body-centered cubic) forming the pearlite microconstituent. As a result, pearlitic steels are widely required for wire-related applications such as tensile armor. Pearlite is usually

applied in a lamellar morphology, as illustrated in Figure 3, but spheroidized pearlite is needed for applications requiring more ductility. The general substructures of pearlite microstructure are schematic shown in Figure 3. The austenitic grain is the biggest substructure in the pearlitic microstructure, which refers to the prior austenitic grain formed during the austenitization heat treatment process (above temperatures around 723 °C). At room temperature, the pearlite consists of ferrite and cementite. Therefore, the region delimited by the prior austenitic boundaries comprises some pearlitic blocks defined by the same ferritic crystallographic orientation. More specifically, a pearlitic block area can have many pearlitic colonies determined by the cementite lamellae's geometrical directions. Finally, the interlamellar spacing (distance between two following cementite lamellae) is a fundamental parameter for controlling strength in pearlitic steel (LI *et al.*, 2011; YOKOYAMA *et al.*, 2002; TAKAHASHI *et al.*, 1978a; FIGUEIREDO; LANGDON, 2021).

Figure 2 – The layers in flexible risers.

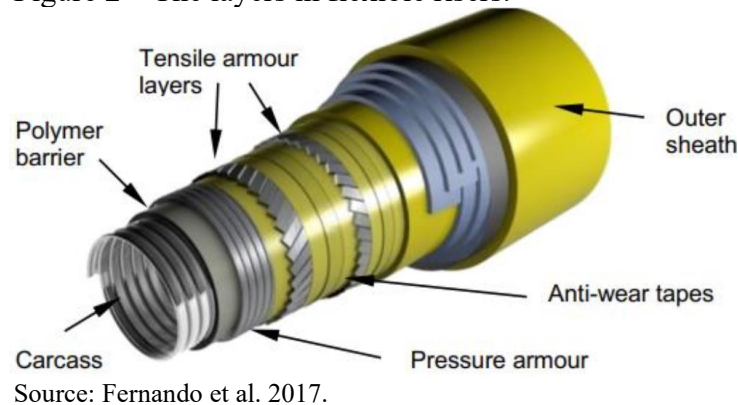
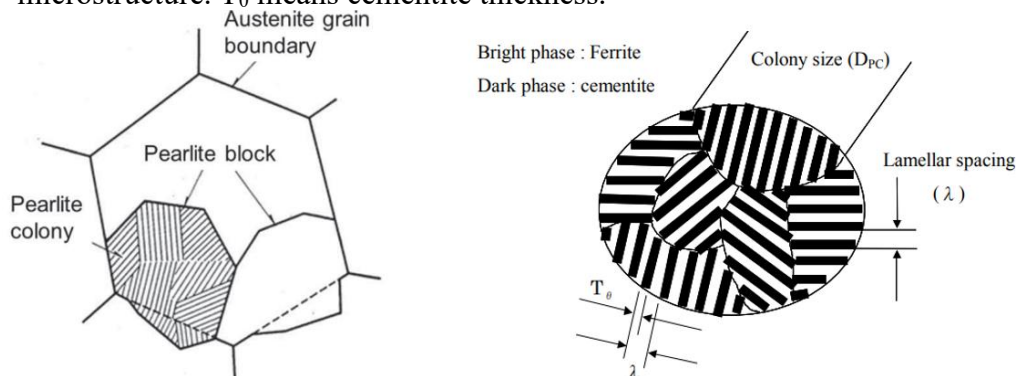


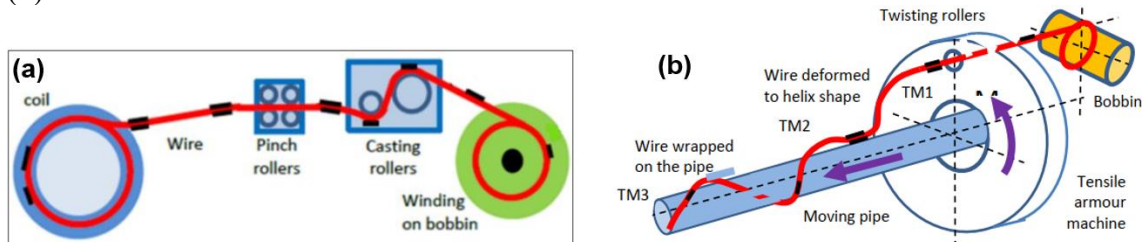
Figure 3 – Schemes of the subdivision structures in a pearlite microstructure. T_{θ} means cementite thickness.



Furthermore, the tensile armor wires are produced via hot rolling followed by cold

rolling processes to achieve a final rectangular wire shape. Moreover, patenting thermal treatment is usually introduced after the hot rolling or during the steps of the cold rolling reduction for interlamellar spacing refinement. Then, the cold rolled wires are wound in coils and can be batch stress-relieved. After that, the wire still undergoes two more severe plastic deformation processes. In the first process, the coil is unwound, passed through an arrangement of pinch and casting rollers to ensure the wire defects tolerance, and finally, it is re-wound for bobbins. In the second plastic deformation procedure, the wire is twisted to the final helix shape on the pipe. In particular, during the final helical shaping operation, the tensile armor machine can wind the wires in a range of angles between 20 and 60 degrees about the pipe's longitudinal axis. These processes are shown in Figure 4 and may introduce a new residual stress state in the material. Moreover, a regular riser has two tensile armor layers and two more can be installed when significant axial loadings are expected, such as deepwater performance (FERNANDO *et al.*, 2017; BAI *et al.*, 2012; AMERICAN PETROLEUM INSTITUTE, 2007; LU *et al.*, 2006; CLARKE *et al.*, 2011; BAI *et al.*, 2014; KOENIG, 1998).

Figure 4 – Schematic illustration of the (a) re-winding wire into the bobbins process and (b) tensile armor machine.



Source: Fernando *et al.* (2017).

Concerning the tensile armor under the riser's operation, although the flat pearlitic steel wires have high ultimate tensile strength, they may experience service failure. The mode failure of tensile armors will depend on the load state that they will experience. For example, radial buckling, also known as bird caging, is caused when the wires are subjected to large compressive loads. Moreover, external aspects like wind, waves, and currents introduce a constant motion in the riser floating systems, and sometimes, it can generate torsion loads in the set of wires structure; consequently, as the tensile armor wires are in a helical pattern, tensile or compression stresses can be established, possibly leading to the rupture of one or several wires. In addition, the flat pearlitic steel wires are designed to work with loadings well above the average service charge; however, some factors, such as corrosion, may decrease the steel resistance, reducing service life. In this case, two polymer sheaths, called the outer sheath and

internal polymer barrier, ensure corrosion protection, as shown in Figure 2. The external and the inner polymer protective layers act by avoiding contact between steel/seawater (Carbon dioxide) and steel/service fluid products (hydrogen sulfide and Carbon dioxide), respectively. Unfortunately, the pressure of some service fluid products, such as hydrogen sulfide (H_2S), can achieve a high value, which enables its diffusion through the internal polymer barrier.

Furthermore, carbon dioxide (CO_2) may be injected into the reservoir to enhance oil and gas recovery. Besides that, degradation or damage of the outer sheath may allow seawater to enter the annulus region (the region between both polymer protection layers). So, high-strength steel wires are prone to embrittlement caused by CO_2 and H_2S (BAI *et al.*, 2012; LAST *et al.*, 2002; SIMONSEN, 2014; ATIA; MOHAMMEDI, 2018).

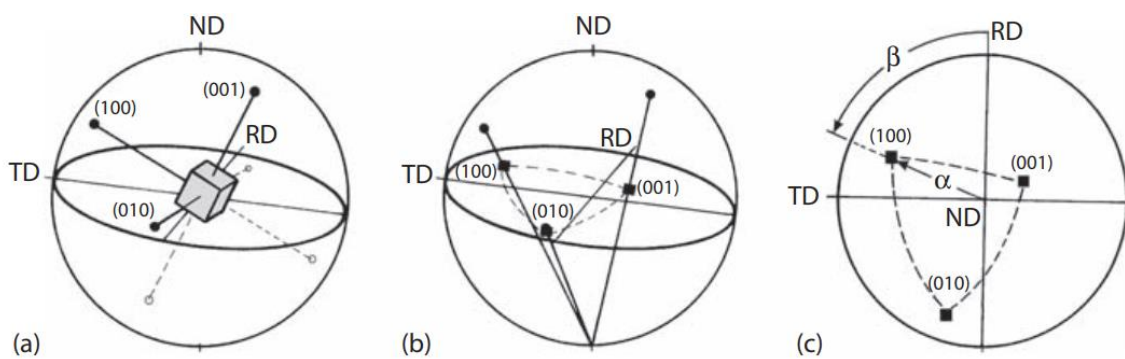
1.2 Crystallographic microanalysis and types of texture visualization

Polycrystalline materials are constituted by many crystals delimited by zones known as grain boundaries. Based on this, an isolated crystal (grain) has its crystallographic orientation relative to the sample's axis. This grain orientation can differ or be identical to the other grains. When most of the grains have a preferential crystallographic orientation, the material presents a texture. Otherwise, the material is randomly orientated. In this context, the information assessment of crystallographic orientation from a few or even only one crystal (a grain in steel) is regularly defined as microtexture analysis. Moreover, the Electron Backscatter Diffraction (EBSD) technique is the regular tool for acquiring diffraction patterns (Kikuchi patterns) from a set of grains on a metallic specimen (HUMPHREYS, 2004).

Generally, the conventional texture or microtexture representation methods are pole figure, inverse pole figure, and orientation distribution function (ODF). The pole figure represents a two-dimensional stereographic projection of intersection points in a reference sphere achieved by normal vectors to a specific plan (hkl) in a crystal set in the origin coordinate of the reference sphere. For instance, Figure 5a illustrates points in a reference unit sphere intersected by normal vectors to a cubic crystal's $\{100\}$ plans (pole). In this case, the unit sphere has the macroscopic coordinate system of the specimen (ND: normal direction, TD: transversal direction, and RD: rolling direction). Next, the intersection points (pole) in the three-dimensional sphere are projected in the 2D plan (RD-TD) in the sphere center that represents the pole figure (see Figure 5b and 5c). More specifically, the β and α symbols in Figure 5c are angles that determine the position of a given pole. Given this, β and α represent the

azimuth of the pole (where $= 0^\circ$ is in the normal direction axis of the reference sphere) and the pole rotation around the polar axis, respectively. Finally, when the material has a preferential orientation, the poles of different grains start to be clustered together in the stereographic projection. In this context, the density of the discrete points clustered is usually represented by contour lines (SUWAS; RAY, 2014; ENGLER; RANGLE, 2009).

Figure 5 – Stereographic projection of the $\{100\}$ pole in a cubic crystal. (a) Crystal inside the reference sphere. (b) Projection of the $\{100\}$ pole onto the RD-TD plan. (c) $\{100\}$ pole figure of a cubic crystal and the position indication of the (100) pole via the β and α angles.



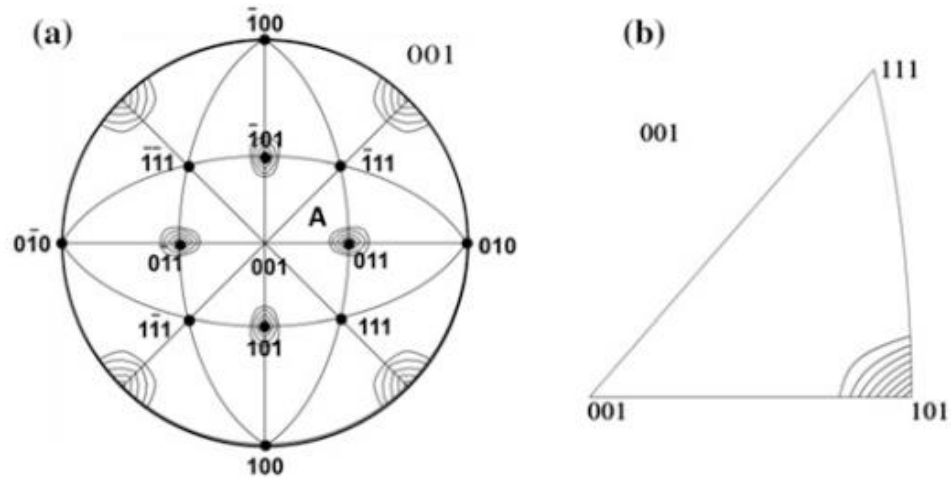
Source: Engler and Rangle, (2009).

On the other hand, the inverse pole figure corresponds to the opposite representation of the regular pole figure. This means that the sample directions are projected into the crystal frame. Another point is that the projection plan of a crystal in the inverse pole figure is standardized due to its geometric symmetry. For instance, the cubic crystal symmetry can provide 24 similar unit triangles, as presented in Figure 6a. Consequently, the inverse figure pole is usually expressed by only a unit stereographic triangle (see Figure 6b). Figure 6 presents a complete inverse figure pole and a unit stereographic triangle in detail by considering the wire axis 001 (sample's direction). In this regard, the complete 001 inverse figure pole and the unit of a 001 stereographic triangle show that many grains have their $\langle 101 \rangle$ axes nearly aligned toward the wire axis (SUWAS; RAY, 2014).

In contrast, the pole figures are considered to have a poor resolution of orientation distribution, although they are a valuable representation of texture. This feature results from the two-dimensional stereographic projection of a three-dimensional crystal orientation. The orientation distribution function (ODF) can mitigate this lack of information. The ODF identifies a specimen's probability density of components $(hkl)[uvw]$. In this case, the crystal orientation is determined by the Euler angles $(\varphi_1, \Phi, \varphi_2)$, which is obtained by three consecutive

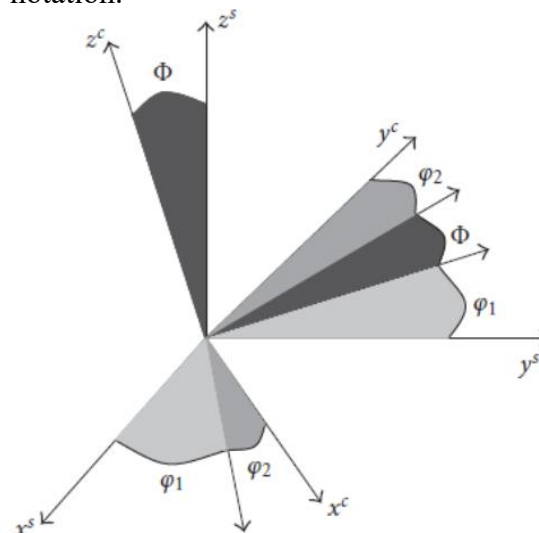
rotations (see Figure 7) applied in the crystal's perpendicular axes [100], [010], and [001] for matching them (x^c , y^c , and z^c) with the sample's coordinates: TD, ND, and RD (x^s , y^s , and z^s). Figure 8 presents a schematic illustration of the crystals before and after the rotations following the Euler angles (φ_1 , Φ , φ_2) (SUWAS; RAY, 2014).

Figure 6 – (a) A complete 001 inverse pole figure. (b) A unit stereographic triangle indicated by the letter A in the complete inverse pole figure.



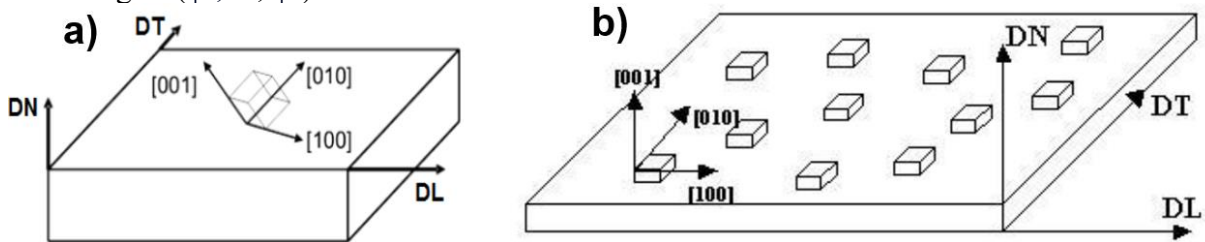
Source: Suwas and Ray, (2014).

Figure 7 – Definition of the Euler angles (φ_1 , Φ , φ_2) according to the Bunge notation.



Source: KESTENS and JACOBS, 2008.

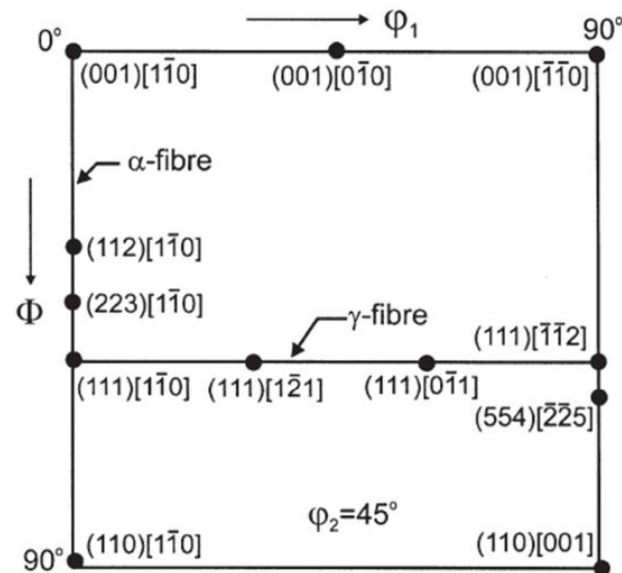
Figure 8 – (a) Representation of crystals before the rotation, and (b) after the rotation via the Euler angles ($\varphi_1, \Phi, \varphi_2$)



Source: Stojakovic, (2008) and Abreu, (1998).

Also, the ODF generates the orientation distribution in the three-dimensional orientation space (Euler space). In this context, the angles of the Euler space follow the symmetric geometry of the crystal. For instance, $\varphi_1, \Phi,$ and φ_2 vary from 0 to 90° in a crystal cubic symmetry. However, the ODFs are split into sections that, for steels usually is considered the $\varphi_2=45^\circ$ where there are many texture components of interest, as shown in Figure 9.

Figure 9 – ODF section at $\varphi_2=45^\circ$ with the location of its texture components. The fiber α , fiber γ , and fiber θ represent the $\langle 110 \rangle$ family's directions parallel to the rolling direction (RD), $\langle 111 \rangle$ family's directions parallel to the normal direction (ND), and $\langle 001 \rangle$ family's directions parallel to the normal direction (ND), respectively.



Source: Humphreys, (2004).

1.3 Motivation for the thesis

Unbonded flexible risers are essential for crude oil and CO₂ gas transportation throughout shallow or ultradeep seawater portions between the seabed production system and the surface production platforms. The risers' tensile armor layers ensure flexibility and allow them to resist most tensile, torsional, and bending loads. Moreover, the risers are mainly structurally supported by their tensile armor layers that are comprised of many rectangular carbon steel wires. However, the flat carbon steel wires (mostly pearlitic steel) are susceptible to failure due to the combined effect of the high service stresses and aggressive environmental conditions (Stress Corrosion Cracking).

Consequently, the rupture of the flat pearlitic wires from the tensile armor layers can result in the catastrophic riser's collapse. This event can create large economic losses and environmental impacts:

- Collision and damage of the collapsed riser to the anchoring system, neighboring risers, and other subsea facilities;
- Work fluids leakage;
- Maintenance costs;
- Production suspension.

Thunder (2023) reported that some risers, used to inject CO₂ gas back into the reservoir, failed a few years ago. These risers were designed to last at least twenty-five years, but they failed prematurely (in three years) due to the induction of stress corrosion (THUNDER, 2023). Therefore, it is fundamental to evaluate the resistance of pearlitic steel against stress corrosion cracking. However, before the final application, the flat wires pass through a complex set of manufacturing processes (hot rolling → patenting treatment → cold forming → stress relief heat treatment → re-winding wire into bobbins → helical wire shaping around the pipeline structure). In this context, it is evident that the first essential step is to understand the influence of the manufacturing process parameters on the metallurgical features of pearlitic steel. Then, in the second plan, investigate the possible manufactured pearlitic steel conditions under stress corrosion cracking.

In particular, the microstructure morphology of pearlitic steels will depend on the manufacturing process that can result in the most common pearlitic morphology in current use: lamellar or spheroidized (NING *et al.*, 2014; HU *et al.*, 2013; GUO *et al.*, 2015; ZHOU *et al.*, 2019; ZHOU *et al.*, 2018; DURGAPRASAD *et al.*, 2018; TANAKA *et al.*, 2018; LI *et al.*, 2015). Additionally, it is vital to evaluate the crystallographic characteristics of the steel's grains

to understand the material's crack susceptibility. For instance, in a ferritic/pearlitic steel, Arafin and Szpunar (2009) revealed that the grain boundaries are prone to cracking when they have the {100} grain orientation with $\langle 100 \rangle$ rotation axis. In addition, Szpunar et al. (2015a) and Szpunar et al. (1998) described that high-angle boundaries with high stored energy are susceptible to crack propagation. In contrast, low-angle boundaries and coincidence site lattices don't.

Finally, through an innovative approach based on microtexture, grain boundary character distribution, microstructure, and in-situ scanning electron microscopy (SEM) experiments, this thesis aims to investigate the influence of the tensile armor manufacturing processes via lab-simulated routes on the metallurgical features of SAE1075 pearlitic steel specimens, followed by their mechanic and deformation behaviors assessment under bending, shear, and helical torsion conditions. These results were accomplished by considering the features of the processes' parameters of tensile armor production found in the literature to manufacture the pearlitic steel specimens (rollings, patent treatment, stress relief treatments, bending, and torsion processes). If this role is better understood, it will increase the opportunity to improve the pearlitic steel wire resistance and, consequently, increase the safety and reliability of the risers.

1.4 Objectives of the thesis

1.4.1 General objective

The general goal of this thesis is to investigate the effect of key parameters of the manufacturing route processes for producing tensile armor wires (that englobes hot-rolling, patenting treatment, cold rolling, and stress relief treatment) on the microscale metallurgical features (microstructure, microtexture, and microhardness) of commercial SAE1075 pearlitic steel at laboratory scale and their resultant impact on the pearlitic steel performance under three-point bending, tensile shear, and helical torsion conditions.

1.4.2 Specific objectives

- To evaluate the metallurgical microscale behavior (microstructural details, microtexture, and microhardness) of commercial SAE1075 pearlitic steel during the first steps of the lab-simulated manufacture route (hot rolling, patenting treatment, cold forming, and stress relief heat treatment).
- To evaluate the deformation behaviors, mechanical performance, and possible failure modes of commercial SAE1075 pearlitic steel under a cyclic in-situ three-point bending

experiment (simulating the re-winding wire into bobbins process) regarding two stress-relieved circumstances (400 and 700 °C for 60 s) and constant route parameters of hot rolling, cold rolling, and patenting treatment.

- To investigate the deformation behaviors, mechanical performance, and possible failure modes of undeformed-coarse and deformed-refined pearlitic microstructures under an in-situ tensile-shear experiment.
- To determine a potentially harmful condition (crack susceptibility or unsuitable mechanical performance) of commercial SAE1075 pearlitic steel.
- To raise an initial understanding of the deformation behaviors of rectangular flat wires of commercial SAE1075 pearlitic steel under two helical torsion conditions (wound angle of 20 and 60°) regarding two stress-relieved circumstances (400 and 700 °C for 60 s) and constant route parameters of hot rolling, cold rolling, patenting treatment, and bending deformations.

1.5 Thesis organization

This thesis was organized into six chapters based accordingly on the aforementioned objectives aimed to be achieved. Therefore, the content of this thesis is structured as follows:

The present chapter (**Chapter 1**) provides a summary background of the subject under study.

In **Chapter 2**, the influence of the key parameters and process sequence for the production of tensile armor wires (hot rolling → patenting treatment → cold forming → stress relief heat treatment), variation in a laboratory scale has been extensively investigated on the evolution of microstructure, microtexture, and crack susceptibility in commercial pearlitic steel.

Then, in **Chapter 3**, to simulate the re-winding wire into bobbins operation, the cyclic bending performance of the resultant lamellar and partially spheroidized pearlitic steel conditions, produced via lab-simulated manufacturing routes for tensile armor wires, were investigated via in situ and interrupted scanning electron microscopy employment.

Concerning the difficulties in analyzing the pearlitic microstructure deformation during regular or helical torsion experiments, **Chapter 4** focuses on evaluating the deformation behavior of undeformed-coarse and deformed-refined pearlitic steel microstructures under the in situ tensile-shear test in a scanning electron microscope.

Chapter 5 focuses on a brief investigation of the influence of the two helical torsion conditions on the deformation behavior of rectangular wires with lamellar and partially

spheroidized pearlitic microstructures.

Finally, **Chapter 6** supplies a list of the thesis conclusions and recommendations for further work.

2 RESULTS: MICROSTRUCTURE, MICROTEXTURE, AND CRACK SUSCEPTIBILITY IN PEARLITIC STEEL DURING LAB-SIMULATED PROCESSES AIMING TENSILE ARMOR APPLICATION IN FLEXIBLE PIPELINES

2.1 Review

The microstructure of fully pearlitic steels is generally composed of a lamellar arrangement of alternating soft ferrite (α) and hard cementite (θ) plates. According to Takahashi et al. (1978a), the structure of lamellar pearlite can be defined in two hierarchical categories: pearlite colony and pearlite block (or nodule). Specifically, the pearlite colony is defined by the region that comprises the same direction of cementite lamellae, whereas zones with the identical crystallographic orientation of ferrite refer to a pearlite block that is developed from the prior austenite (γ) grain boundary. In this concern, the control of the Interlamellar Spacing (IS) of pearlite and the Prior Austenite Grain Size (PAGS) may result in an excellent combination of high strength and satisfactory ductility in pearlitic steel (TALEFF *et al.*, 2002). This mechanical relationship ascribes pearlitic steels to be required for many wire-related applications, such as suspension bridge cables, tire wires, piano wires, and even in the oil and gas sector as tensile armors in flexible pipelines (BARIK *et al.*, 2021; TAGLIARI *et al.*, 2019).

Regarding tensile armor employment, flat pearlitic steel wires are twisted around the pipe in a helical shape forming a strong layer. This set of wires promotes axial rigidity while minimally compromising the pipeline flexibility, supporting all the pipeline weight and transferring the load to the vessel structure (TALEFF *et al.* 2002). This complex steel performance requires strict control of microstructure and crystallographic orientation distribution, which are determined by parameters adopted during the manufacturing process. In this context, before the final application, the flat pearlitic steel wires can be industrially produced in the following route: hot-rolling process (HRP) \rightarrow patenting treatment (PT) \rightarrow cold forming (drawing, rolling, or drawing + rolling) \rightarrow wire coiling \rightarrow stress relief (recovery) heat treatment (DAMBRE, 1990; MALLEEN; SUGIER, 1996) \rightarrow re-winding wire into bobbins (FERNANDO *et al.*, 2017).

Concerning PT, it provides the opportunity to optimize the strength/ductility ratio and also promotes a final homogeneous pearlitic microstructure. Firstly, this thermal treatment consists in austenitizing the steel in temperatures above 900 °C (DAMBRE, 1990; MALLEEN; SUGIER, 1996). This stage corresponds to direct control of the PAGS that is dependent on the austenitizing temperature and time (SUN *et al.*, 2014). Saito et al. (2018) concluded that

austenite nucleation sites in the previous structure of carbon steels are preferentially in the following sequence: ferrite/pearlite interfaces, pearlite block boundaries, and pearlite colony boundaries. In particular, the PAGS is related to influencing the ductility and impact toughness in pearlitic steels (LEWANDOWSKI; THOMPSON, 1986; ZHOU *et al.*, 2016). Conversely, the austenitic grain boundaries are also sites for pearlite nucleation. Consequently, the PAGS has a significant impact on the volume fraction of pearlite as well as the size of colonies (PORCARO *et al.*, 2019) and blocks (BEHERA *et al.*, 2019). In contrast, the IS is not controlled by the PAGS, instead, it is strongly regulated by the austenite-to-pearlite transformation temperature. This decomposition is a diffusion-controlled reaction. Thus, by lowering this transformation temperature, the distance of carbon diffusion will decrease, resulting in a thinner IS of pearlite (ARANDA *et al.*, 2014). Following the Hall-Petch relationship, it is well-known from the literature (OHBA *et al.*, 2007) that the strength of pearlitic steels is correlated with the IS. In this way, the austenitization step is followed by a fast immersion of the steel into a molten bath (lead or salt) or fluidized bed for reducing the temperature of pearlite formation and ensuring an isothermal transformation (in the range of around 500 to 700°C). Regarding environmental pollution and cooling rate performance, a molten salt is a reasonable option as a refrigerant bath for PT (OHBA *et al.*, 2007; BHOLE; FRIEDMAN, 2014). Also, Ohba *et al.* (2007) found better mechanical properties for pearlitic steel patented in salt baths in comparison to lead baths. In addition, the mechanical property of pearlitic steels produced via PT is desired for the following cold forming process, especially for higher reductions in the cold wire drawing process (PARIS, 1996).

During cold forming, the complex structure of lamellar pearlite is usually related to undergoing inhomogeneous plastic deformation (localized strain zones). In this way, due to the lower yield strength of ferrite in comparison to cementite, the yielding in a pearlite colony may occur through plastic deformation predominantly in the ferrite matrix (TOMOTA *et al.*, 2003). Furthermore, through measurements of in situ neutron diffraction during tensile deformation of pearlitic steel, Kanie *et al.* (2004) confirmed that cementite lamellae are in an elastic state at the moment the ferrite phase is under plastic deformation. In Body-Centered Cubic (BCC) metals, the cold plastic behavior can be described in terms of the pencil glide mechanism, where dislocation slip occurs on $\{110\}$, $\{112\}$, and $\{123\}$ planes along the close-packed $\langle 111 \rangle$ direction (KESTENS; PIRGAZI, 2016). However, cementite lamellae can act as barriers against dislocation motion through the ferrite and consequently, pile-ups of dislocation may occur at the ferrite/cementite interface (ESHELBY *et al.*, 1951). Therefore, the heterogeneous strain distribution is dependent on the geometrical arrangement of cementite and the

crystallographic orientation of ferrite in a pearlite colony (YAJIMA *et al.*, 2021; GUO *et al.*, 2014). To clarify, Teshima *et al.* (2017) observed the highest local strain in pearlite colonies aligned near 45° about the applied tensile stress due to the favorable ferritic dislocations gliding in this direction. Similarly, it has been pointed out by researchers (GUO *et al.*, 2014; DURGAPRASAD *et al.*, 2018) that during cold drawing pearlite colonies non-aligned to the drawing direction experience the highest degree of plastic deformation (especially at 45°). In addition, Durgaprasad *et al.* (2018) reported that the amount of plastic deformation in pearlite colonies is also affected by their IS. More specifically, Takahashi *et al.* (1978a) described that in pearlites with refined structure, slips occur relatively homogeneously, while in coarse pearlites, slips are less uniformly distributed. Recently, Yajima *et al.* (2021) detected through the digital image correlation (DIC) method and tensile experiment that the boundaries of pearlite blocks are high-strain regions due to the anisotropic deformation among them. Furthermore, regarding the cold-rolling process, researchers (FURUHARA *et al.*, 2005; ZHANG *et al.*, 2007) noticed non-uniform distribution of pearlite colonies after a cold reduction of over 70%. In this context, the authors found three sorts of rolled pearlites (irregularly bent lamellae, coarse lamellae with shear band, and fine lamellae) which are a result of the initial deformation mode in different pearlite arrangements. Moreover, previous studies (FURUHARA *et al.*, 2005; VALIENTE *et al.*, 2005) revealed that irregular strain distribution during cold deformation of pearlitic steel can collaborate for developing shear bands that are related to crack initiation.

Then, the cold-worked pearlitic steel wrapped in coils is usually subjected to stress relief treatment that is generally performed below A_{c1} temperature, in a vast range of temperatures (400 to 710 °C) and time (from a few seconds to several hours) (MALLEN; SUGIER, 1996; FOISSEY *et al.*, 2016). In this regard, a partial restoration of mechanical properties occurs due to the rearrangement and annihilation of part of the dislocations (HUMPHREYS *et al.*, 2004). Subsequently, the wire is unwrapped from the coils, passed through pinch and casting rollers, and then, it is rewrapped onto bobbins. This operation causes an arduous plastic deformation into the material that is usually lab-simulated through bending experiments (FERNANDO *et al.*, 2017). Finally, as tensile armor in flexible pipelines, the pearlitic rectangular wires are submitted to cyclic loading conditions and are exposed to a corrosive environment, which can assist the progress of fatigue cracks (BAI; BAI, 2005). Thus, it is paramount to identify and avoid manufacturing parameters that can provide crack events. Concerning specifically the aforementioned sequential processes for tensile armor application, the microstructural and crystallographic behavior of pearlitic steel in each of those process steps

and together combined are not reported simultaneously in the literature. In this manner, this study mainly focuses on investigating the evolution of microstructure, microtexture, and crack formation in commercial pearlitic steel, regarding different manufacturing routes with variations of key parameters under laboratory scale. This lab manufacturing design was able to provide a harmful condition prone to crack formation. The microstructural and crystallographic assessments were conducted, respectively, by secondary electron (SE) image and electron backscattered diffraction (EBSD) techniques. Finally, this work can provide additional and relevant technical information for avoiding microstructural issues during the manufacturing of flat pearlitic steel wires.

2.2 Methodology

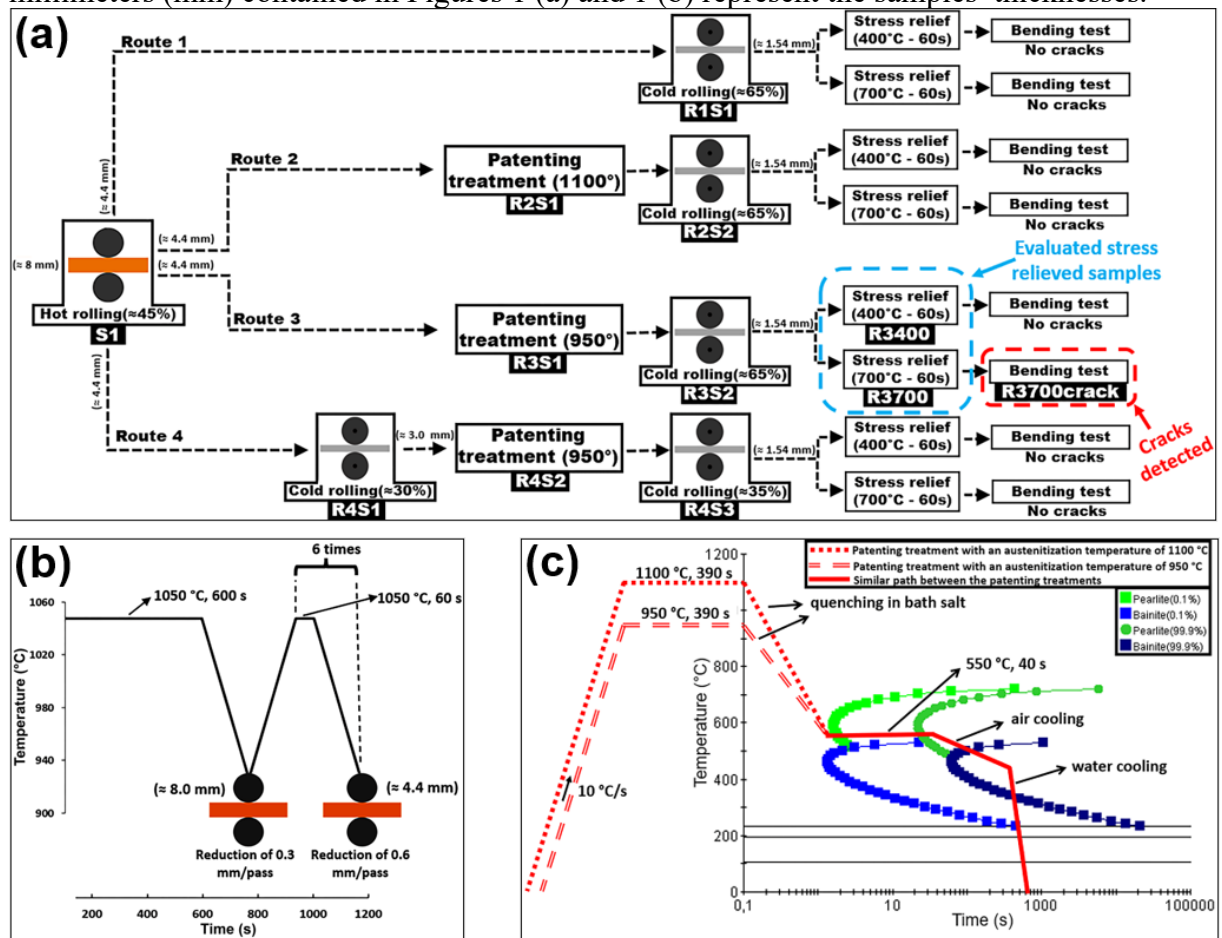
2.2.1 Samples processing

The four lab-simulated routes employed in this chapter are presented in Figure 10. The chemical composition of the as-received pearlitic steel obtained by an optical emission spectrometer (THERMOARL 4460 M) is shown in Table 1. The dimensions of the starting steel samples were 8 mm (thickness) x 40 mm (length) x 50 mm (width). A laboratory scale rolling machine with 110 mm diameter rolls and a rolling speed of 8 m/min was employed in the rolling stages. An infrared thermometer was adopted for measuring the hot-rolling (immediately before the hot passes) and salt bath temperatures. Regarding the hot-rolling process in Figure 10a and its detailed steps in Figure 10b, the starting samples were austenitized at 1050 °C for 600 seconds in a muffle furnace, and after that, they were transferred instantly to the rolling machine for a hot pass of adjustment (≈ 0.03 mm of reduction). Subsequently, the samples were put back in the furnace at the same temperature (1050 °C) for 60 seconds followed by an additional hot pass (≈ 0.6 mm of reduction/pass). The last procedure was repeated six times up to $\approx 45\%$ of thickness reduction (≈ 4.4 mm in final thickness) followed by air cooling. The average finish rolling temperature was 906 °C. This hot-rolling process was identically implemented at the beginning of the four routes. The hot-rolled specimen was named Sample 1 (S1) and it worked as an initial comparative reference of microtexture and microstructure to the following step in each route.

Additionally, in this chapter, two PTs were carried out with two different austenitization temperatures (ATs), 1100 °C (Route 2 in Figure 10a) and 950 °C (Routes 3 and 4 in Figure 10a) for 390 seconds both (as illustrated in Figure 10c). Next, the samples were direct quenched in a bath salt (60% potassium nitrate + 40% sodium nitrate) at 550 °C for 40

seconds followed by air and water cooling. The specimens from these patented conditions were entitled, accordingly to their respective route and sample order, such as Route 2 - Sample 1 (R2S1), Route 3 - Sample 1 (R3S1), and Route 4 - Sample 2 (R4S2).

Figure 10 – Scheme of the four laboratory processing routes performed in the present work. (a) Overall flowchart representation of the process routes. (b) Illustrative diagram of the individual steps performed in the hot rolling ($\approx 45\%$) process. (c) Isothermal transformation diagram with representative details of the patenting treatments carried out in this study. The numbers in millimeters (mm) contained in Figures 1 (a) and 1 (b) represent the samples' thicknesses.



Source: Elaborated by the author.

Table 1 – Chemical composition of the as-received pearlitic steel (wt%).

C	Mn	Si	S	P	Cr	Ni	V	Al	Ti	Fe
0.736	0.648	0.227	0.006	0.011	0.179	0.023	0.004	0.023	0.003	Bal.

Source: Elaborated by the author.

The cold-rolling process was performed by introducing many passes at room temperature (≈ 0.1 mm in thickness reduction/pass) until the aimed thickness (≈ 1.54 mm). In Route 1 - Sample 1 (R1S1), Route 2 – Sample 2 (R2S2), and Route 3 – Sample 2 (R3S2), the cold thickness reductions were executed from ≈ 4.4 mm up to ≈ 1.54 mm ($\approx 65\%$ of reduction). In contrast, in Route 4 the cold thickness reduction occurred in two moments; firstly, just after

the HRP, in Route 4 - Sample 1 (R4S1) from ≈ 4.4 mm of thickness to ≈ 3 mm ($\approx 30\%$), and secondly, after PT, in Route 4 – Sample 3 (R4S3) from ≈ 3 mm of thickness to ≈ 1.54 mm ($\approx 35\%$), also resulting in $\approx 65\%$ of cold reduction.

As shown in Figure 10a, the 65% cold-reduced samples from the four different routes underwent stress relief heat treatments at 400 and 700 °C for 60 seconds. Then, for simulating the process of re-winding wire into bobbins, a three-point bending experiment at room temperature was applied in all the eight stress-relieved conditions, using samples with dimensions of 1.54 x 12.5 x 60 mm³ (the larger length was aligned to the rolling direction) (FERNANDO *et al.*, 2017). The bending experiment was executed by a universal testing machine (landmark 370.10) with a maximum load of 100 kN. In addition, the rollers' diameter of the pins, the distance between support pins, the displacement rate, and the maximum displacement of the loading pin were, respectively, 10 mm, 40 mm, 2 mm/min, and 4.5 mm. This procedure was performed four times in all stress-relieved conditions alternating the superior and inferior sample's surfaces which were in contact with the pins. However, after the bending tests, cracks were only observed in the stress-relieved condition at 700 °C from Route 3, as indicated in Figure 10a. In this regard, the stress-relieved and bent conditions evaluated in this work were only, respectively, from Route 3 (R3400 and R3700) and the cracked one (R3700crack).

2.2.2 *Samples Characterization*

All the samples, except the cracked ones, were investigated in the sample's centroid region (in the middle thickness and width of the rectangular samples) and on the longitudinal section parallel to the rolling direction (RD). The samples were prepared through a regular metallographic procedure based on grinding (using sandpapers from #240 to #2000 grit) and polishing (using diamond suspensions of 6, 3, and 1 μm). Then, the specimens were etched in 4% Nital solution for microstructural SE observation through a field emission gun (FEG) THERMO SCIENTIFIC QUATTRO environmental scanning electron microscope (Quattro ESEM). An accelerating voltage of 20 kV and a beam current of 1.6 nA were adopted during the SE image acquisition. For crystallographic microtexture examinations, the samples were prepared with vibrometer polishing using 0.04 μm colloidal silica for two hours in addition to the grinding and polishing processes. The EBSD maps were acquired via the EDAX EBSD detector coupled with the Quattro ESEM. The EBSD analysis was carried out using an operating voltage of 20 kV, a step size of 50 nm, a working distance of 10 mm, and a sample

tilt angle of 70° . The EBSD file evaluations were performed by OIM software. Inverse pole figure (IPF) maps were plotted in the Z-direction (sample's normal direction), while Taylor factor maps were calculated considering the $\{110\}\langle 111\rangle$ slip system and tensile loading in the longitudinal direction (parallel to the rolling direction). Moreover, the interlamellar spacing and pearlite colony size were measured from SE micrographs via ImageJ software.

Finally, microhardness measurements were accomplished using a Leco AMH43 automatic machine setting a load of 200 gf and a holding time of 10 seconds. On each sample, the indentations were performed in a 5 by 30 matrix with a spacing of 150 microns between them.

2.3 Results and discussion

2.3.1 Samples before 65% cold-rolling reduction

There are two main reasons for applying PT in pearlitic steels: refining and homogenizing the pearlitic microstructure which results in an optimization of mechanical properties. This section focuses on investigating the fundamental effects of PT on the microtexture and microstructure of pearlitic steel. Figure 11 presents color-coded IPF maps and their respective orientation distribution function (ODF), of the samples under different setups of PT (R2S1, R3S1, R4S1, and R4S2), including the non-patenting treated one (S1). The ODF intensities are expressed in multiple random densities (mrd) and their main microtexture components are summarized in Table 2.

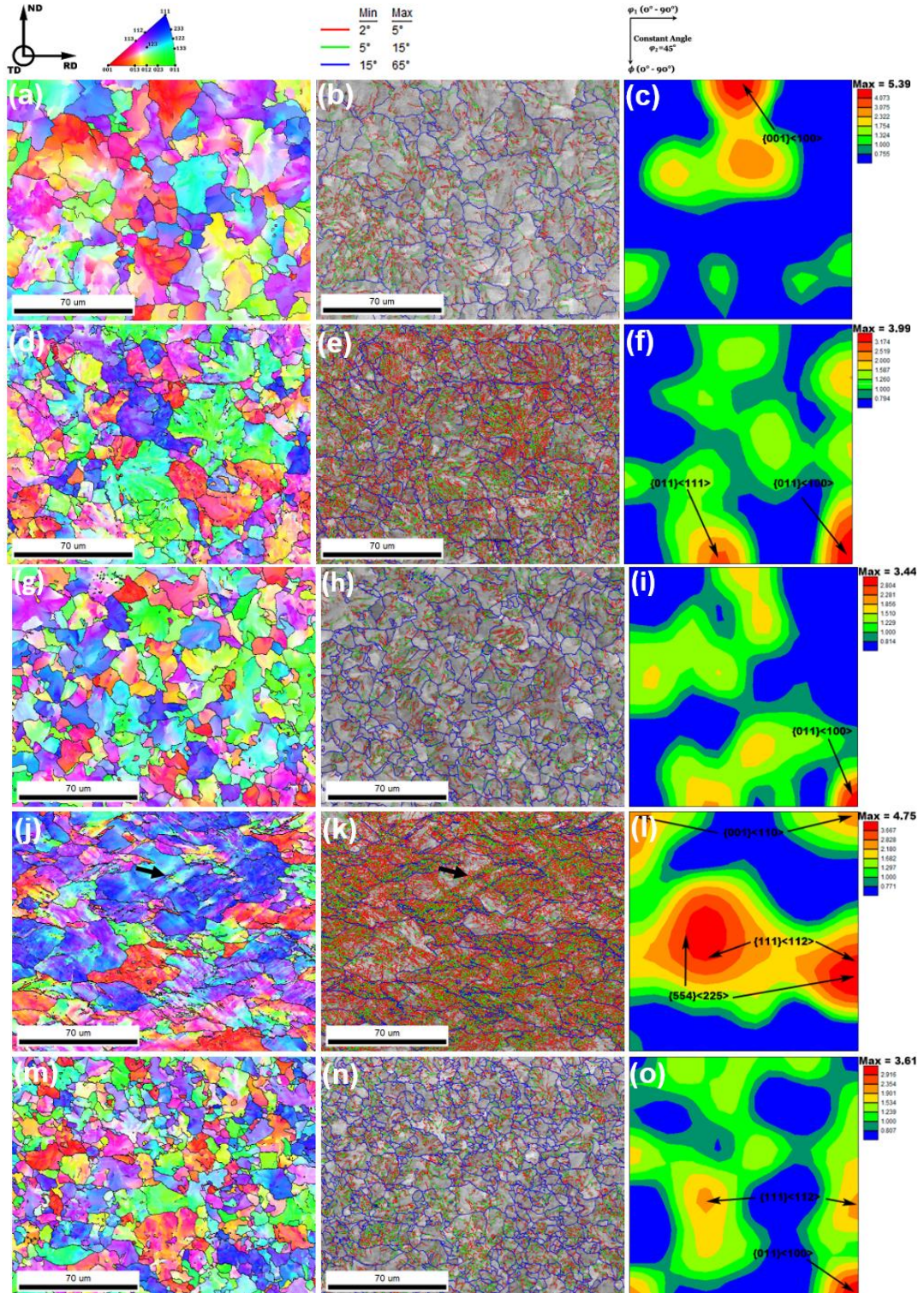
Additionally, the average pearlitic block size (PBS) measured from the IPF maps in Figure 11 of the samples just before the final 65% cold-reduction (S1, R2S1, R3S1, and R4S2) is presented in Figure 12a. While Figure 12b exhibits the total length per area of the grain boundary types found in each IPF map provided in Figure 11. Under the S1 condition (only hot-rolled), it was found the average PBS of $14.1 \mu\text{m} \pm 1.2 \mu\text{m}$, and the shaper ferritic orientation was the $\{001\}\langle 010\rangle\alpha$ (cube) component. In comparison to S1, the introduction of PT after the HRP decreased the average PBS to $9.9 \mu\text{m} \pm 0.7 \mu\text{m}$ (R2S1) and $8.7 \mu\text{m} \pm 1.1 \mu\text{m}$ (R3S1). It has been pointed out (ZHOU *et al.*, 2016; BEHERA *et al.*, 2019) that the PBS is affected by the PAGS which, in turn, depends mainly on the temperature and time of austenitization. Additionally, the subsequent cooling rate can affect the final microstructure. For instance, higher cooling rates suppress atomic diffusion leading to smaller ferritic grains and increasing the dislocation density in the material (GHOSH *et al.*, 2005; DAS *et al.*, 2003). Therefore, the PBS refinement in the R2S1 and R3S1 specimens may be a consequence of their shorter

austenitization time as well as their faster cooling rate about the S1 condition. More specifically, the average PBS in the R2S1 sample is bigger than in the R3S1 condition. This difference in PBS between these patented samples was assumed to be an effect of the different austenitization temperatures (1100 and 950°C) since they have the same austenitization time (390 seconds).

Also, the smallest average PBS, $5.9 \mu\text{m} \pm 0.4 \mu\text{m}$, was observed in the sample R4S2 which underwent prior cold-rolling deformation (30% of reduction) before the PT. In Figure 11j and 11k, it is possible to observe in the R4S1 sample shear bands mainly constituted by LABs (2-5°) and MABs (5-15°), as indicated by black arrows. The local lattice distortions with misorientation $< 15^\circ$ (LABs and MABs) indicate areas with a concentration of geometrically necessary dislocations (GNDs) (WRIGHT *et al.*, 2011). In contrast to the S1 sample, the 30% cold-worked sample (R4S1) presented the highest total length of LABs ($2.0 \mu\text{m}/\mu\text{m}^2$) and MABs ($0.7 \mu\text{m}/\mu\text{m}^2$) per area. Therefore, R4S1 has a greater number of sites for austenite nucleation than S1 during PT. This circumstance leads to the earlier meeting between the R4S1's austenitic grains still in small sizes. As a consequence, the smaller austenitic grains may act as a barrier against each other, preventing them to grow excessively (HUMPHREYS *et al.*, 2004). As a result, a refined prior austenitic grain may provide smaller pearlitic blocks as previously mentioned. Moreover, the R4S2 microtexture in Figure 11l did not exhibit the cube component, instead, it reveals a weak $\{001\}\langle 110 \rangle$ orientation and a sharp component around the $\{554\}\langle 225 \rangle$ and $\{111\}\langle 112 \rangle$ orientations. This result indicates that the cube component is unstable during the cold-rolling process and initially, it may be rotated into $\{001\}\langle 110 \rangle$ (Kestens and Jacobs, 2008). Subsequently, intermediary rotations along RD// $\langle 110 \rangle$ components ($\{114\}\langle 110 \rangle$, $\{113\}\langle 110 \rangle$, $\{112\}\langle 110 \rangle$, $\{223\}\langle 110 \rangle$ or $\{445\}\langle 110 \rangle$) are also able to occur during the cold-rolling deformation, followed by rotations toward more stable components such as $\{554\}\langle 225 \rangle$ to $\{111\}\langle 112 \rangle$ to $\{111\}\langle 110 \rangle$ (TÓTH *et al.*, 1990). Furthermore, the total length of HABs of the S1, R2S1, R3S1, and R4S2 conditions in Figure 12b shows an expected inversely proportional relationship with the measured PBS in Figure 12a. However, a smooth divergence in this trend was found in the R3S1 condition in contrast to the R2S1. This exception should be due to the huge standard deviation in the R3S1's PBS.

Moreover, it is worth noting that all the three samples just after the PT (R2S1, R3S1, and R4S2) in Figure 11f, 11i, and 11o, have an identical $\{011\}\langle 100 \rangle$ (Goss) component, and their maximum microtexture intensities decreased in comparison to their prior process step (S1 or R4S1). Mandal *et al.* (2016) revealed that an increase in cooling rate from the austenitic region affects the variant selection during γ/α transformation that strengthens the ferritic Goss

Figure 11 – Color-coded inverse pole figure (IPF) map, grain boundary distribution map, and orientation distribution function (ODF) at $\phi_2 = 45^\circ$, respectively, for the samples: (a)(b)(c) S1, (d)(e)(f) R2S1, (g)(h)(i) R3S1, (j)(k)(l) R4S1 and (m)(n)(o) R4S2. The black arrows in the color-coded IPF and grain boundary distribution maps of the R4S1 sample point out a shear band.



Source: Elaborated by the author.

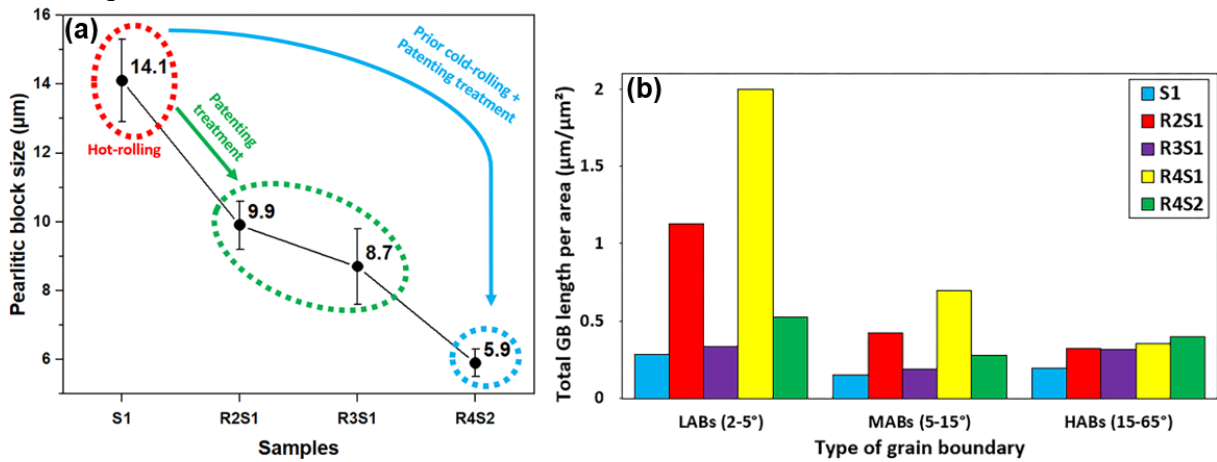
Table 2 – Summary of the main microtexture components found in the ODFs shown in Figure 2 for the five samples before 65% cold-rolling reduction.

Sample's name	Main components	Intensity (mrd)
S1	{001} <100>	5.39
R2S1	{011} <100>	3.99
	{011} <111>	2.52
R3S1	{011} <100>	3.44
R4S1	{111} <112>	4.68
	{554} <225>	4.68
R4S2	{011} <100>	3.61
	{111} <112>	2.13

Source: Elaborated by the author.

texture. Moreover, it is well known from the literature (WATERSCHOOT *et al.*, 2002) that the ferritic Goss component is strong evidence of recrystallized austenite with {001}<100> γ (cube) texture. Therefore, it is reasonable to consider that during the PT's austenitization the new austenitic grains were likely nucleated with cube orientation, and then, the faster cooling rate could have assisted the development of ferritic grains with Goss orientation. Additionally, the most stable component detected in R4S1, the {111}<112> orientation, is still seen after PT in the R4S2 condition, however, with a weaker intensity. In particular, R2S1 also exhibited a significant {011}<111> α component. Javaheri *et al.*, (2021) reported that the development of {011}<111> α is related to shear strain. It reflects that the higher undercooling (ΔT) applied in the R2S1 condition, from 1100 to 550 °C, may have resulted in some lattice shear strain. Regarding the cooling effect under the ferritic matrix, Figure 12b shows an increase in the total length of LABs and MABs in the following sequence: S1 < R3S1 < R4S2 < R2S1. It may support the assumption that the higher undercooling in R2S1 resulted in more distortion/strain in the ferritic lattice. Moreover, there is a huge difference in the total length of LABs and MABs between the R3S1 and R4S2 samples, which may be a consequence of their distinct thickness of 4.4 mm and 3 mm, respectively. It means that the quenching in bath salt from the same temperature (950 °C) should have more influence on the center of the thinner sample (R4S2) in comparison to the thicker one (R3S1). Likewise, this low quenching efficiency in the central region of the R3S1 sample may explain its larger standard deviation in the PBS which may be assumed as an indicator of a less homogeneous microstructure.

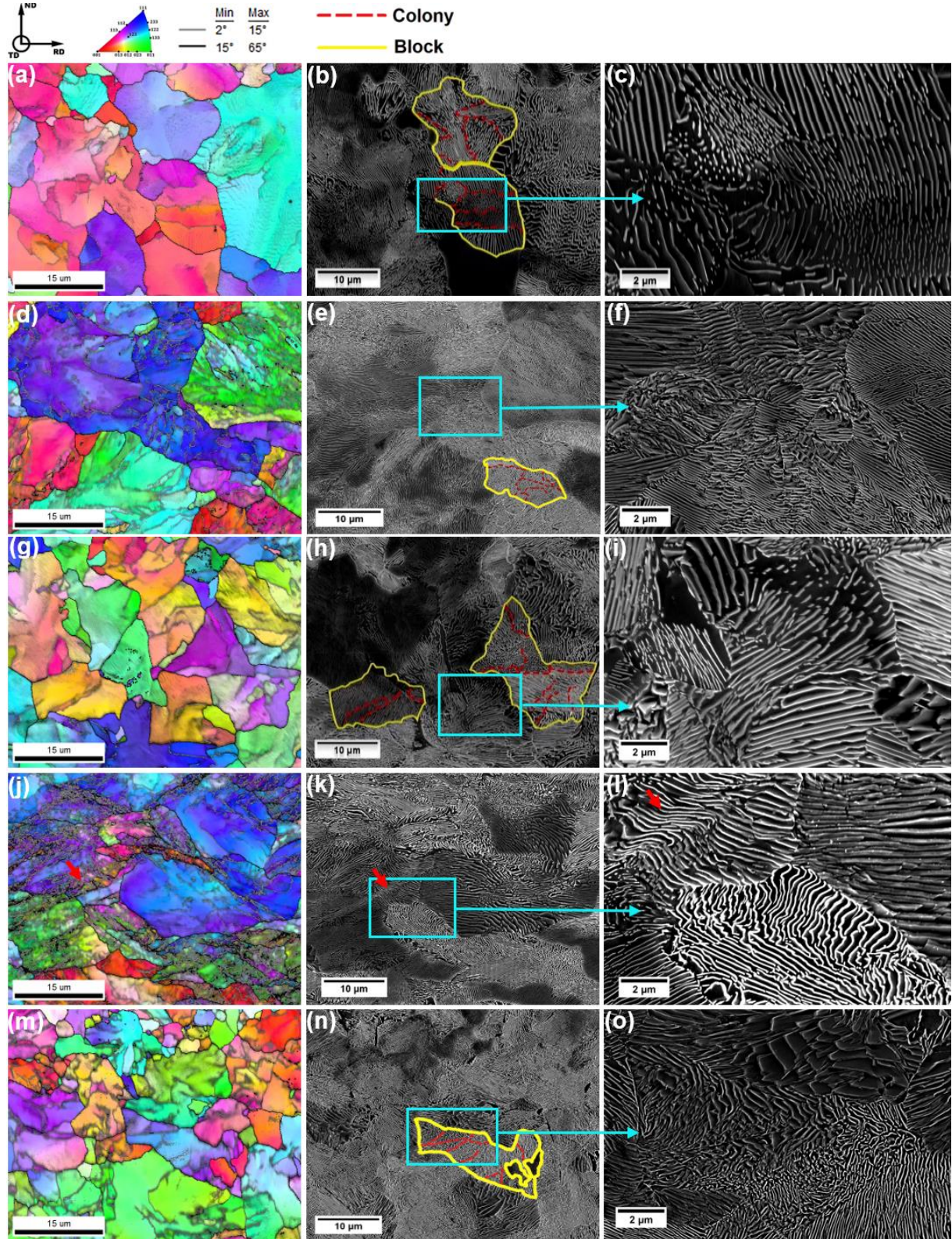
Figure 12 – (a) Pearlitic block size average of the hot-rolled (S1) and the patenting treated (R2S1, R3S1, and R4S2) samples, and (b) distribution of grain boundary type per area regarding the samples S1, R2S1, R3S1, R4S1, and R4S2.



Source: Elaborated by the author.

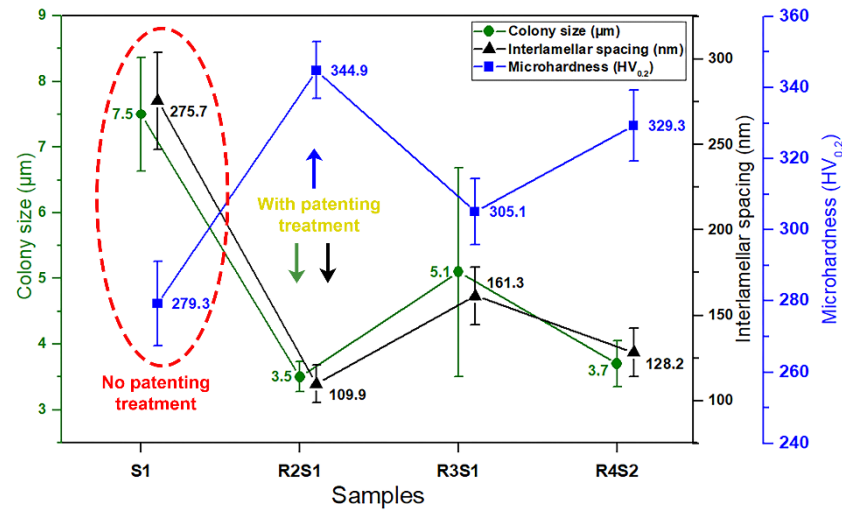
Furthermore, Figure 13 shows IPF maps and their respective SEM images from the central region of each IPF map presented in Figure 11. In Figure 13j, 13k, and 13l, it is possible to confirm shear bands in the sample as indicated by red arrows. Also, Figure 14 displays a summary of the IS, colony size, and microhardness measured in the four studied scenarios (S1, R2S1, R3S1, and R4S2) before the total 65% of cold-reduction. In general, it is possible to realize that, in comparison to the S1, the PT employment refined the IS and colony sizes as well as increased the microhardness. This increment in microhardness can be justified by the Hall-Petch relationship (OHBA *et al.*, 2007). Specifically, R2S1 presented the greatest microstructural refinement and homogenization (shorter standard deviation) likely due to the highest undercooling ($\Delta T_{R2S1} = 550 \text{ }^\circ\text{C}$) introduced in this condition. Otherwise, the IS, colony size, and standard deviation were larger in the R3S1 sample. In this context, the PT was performed under the same sample thickness (4.4 mm) and bath salt temperature (550 °C) in the R2S1 and R3S1 conditions, while the undercooling ($\Delta T_{R2S1} = 550 \text{ }^\circ\text{C}$ and $\Delta T_{R3S1} = 400 \text{ }^\circ\text{C}$) and austenitization temperature ($AT_{R2S1} = 1100 \text{ }^\circ\text{C}$ and $AT_{R3S1} = 950 \text{ }^\circ\text{C}$) were the different parameters between them. Aranda *et al.*, (2014) suggested that the ΔT may influence the diffusion distance for the solute transport, which is the main mechanism to control the interlamellar spacing. Moreover, the IS refinement as a result of an increase in the austenitization temperature was also reported by Dey *et al.* (2018). They described that carbon diffusion is more pronounced at higher austenitization temperatures, so a more homogenized distribution of carbon is expected in the austenitic matrix. Therefore, this event retards the formation of cementite plates, decreasing the IS. Otherwise, it can be seen in the R4S2 sample, that the low microstructural refinement and homogenization (reduction in the standard

Figure 13 – Color-coded inverse pole figure (IPF) map, Scanning electron microscope (SEM) Secondary electrons (SE) image of the IPF map area and SEM SE image in higher magnification, respectively, of (a)(b)(c) sample S1, (d)(e)(f) sample R2S1, (g)(h)(i) sample R3S1, (j)(k)(l) sample R4S1 (the red arrows indicate a shear band) and (m)(n)(o) sample R4S2.



Source: Elaborated by the author.

Figure 14 – Values of interlamellar spacing, microhardness, and colony size for the S1, R2S1, R3S1, and R4S2 processed conditions.



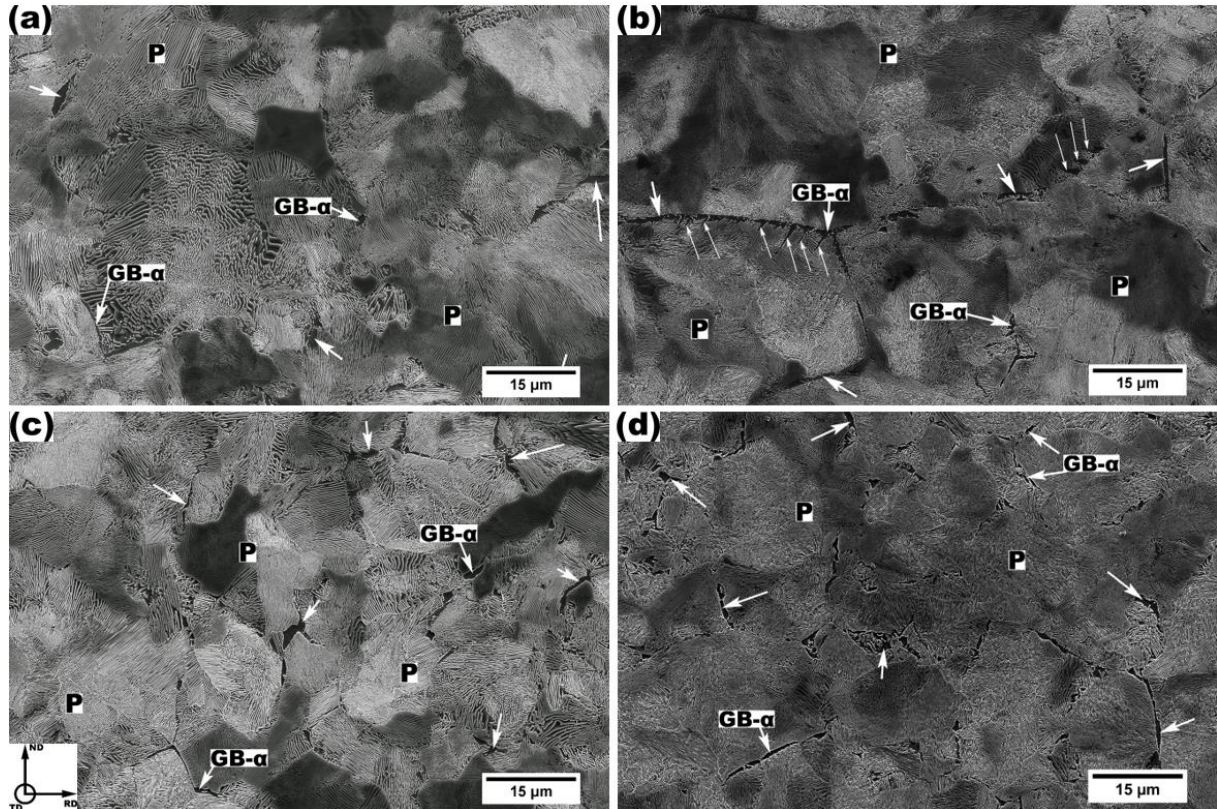
Source: Elaborated by the author.

deviation) efficiency caused by a shorter ΔT or lower austenitization temperature can be compensated by the thickness reduction.

Regarding the formation of ferritic grain boundary (GB- α) in the studied pearlitic steel, Figure 15 displays many GB- α regions pointed out by white arrows. The measured volume fraction of GB- α increased from 0.42% in the S1 condition to 1.63%, 1.76%, and 2.84%, respectively, in the patented conditions R2S1, R3S2, and R4S2. Miyamoto et al., (2016) revealed that the amount of GB- α increased with the decrease of the prior austenitic grain boundary and γ/α transformation temperature. In this context, the authors described that the prior austenitic grain boundaries are sites for GB- α nucleation and GB- α growth is faster at lower γ/α transformation temperatures due to the inhibition of manganese partitioning. Thus, the resultant amount of GB- α can be explained by the austenitization condition and the sort of cooling applied in each of the four evaluated scenarios. Therefore, as the S1 austenitization condition has in sum the longest total hold time (960 seconds), it suggests that S1 has the biggest resultant PAGS. Another point is that S1 underwent the smallest cooling rate, which means it has the highest γ/α transformation temperature in which the mechanism of manganese partitioning may be able to occur, slugging the GB- α growth. So, these phenomena should justify the smallest volume fraction of GB- α found in the S1 condition as shown in Figure 15a. Regarding the patented specimens and also their austenitization parameters, as previously mentioned, they have the trend of decreasing their PAGS in the following sequence R2S1 > R3S2 > R4S2, which may justify their different amount of GB- α . As evidence, it is possible to realize that the GB- α seems to nucleate essentially in the boundaries of a bigger PAGS in Figure

15b and smaller PAGS in Figure 15d. Furthermore, probably due to the higher ΔT , Widmanstatten ferrite was only found in the R2S1 sample, as pointed out through thin white arrows in Figure 15b.

Figure 15 – SEM SE image of GB- α (indicated by the big white arrows) and pearlite distribution in the matrix of the (a) sample S1, (b) sample R2S1 (the smaller white arrows indicate Widmanstatten ferrite), (c) sample R3S2, and (d) sample R4S2.



Source: Elaborated by the author.

2.3.2 65% cold-rolled samples

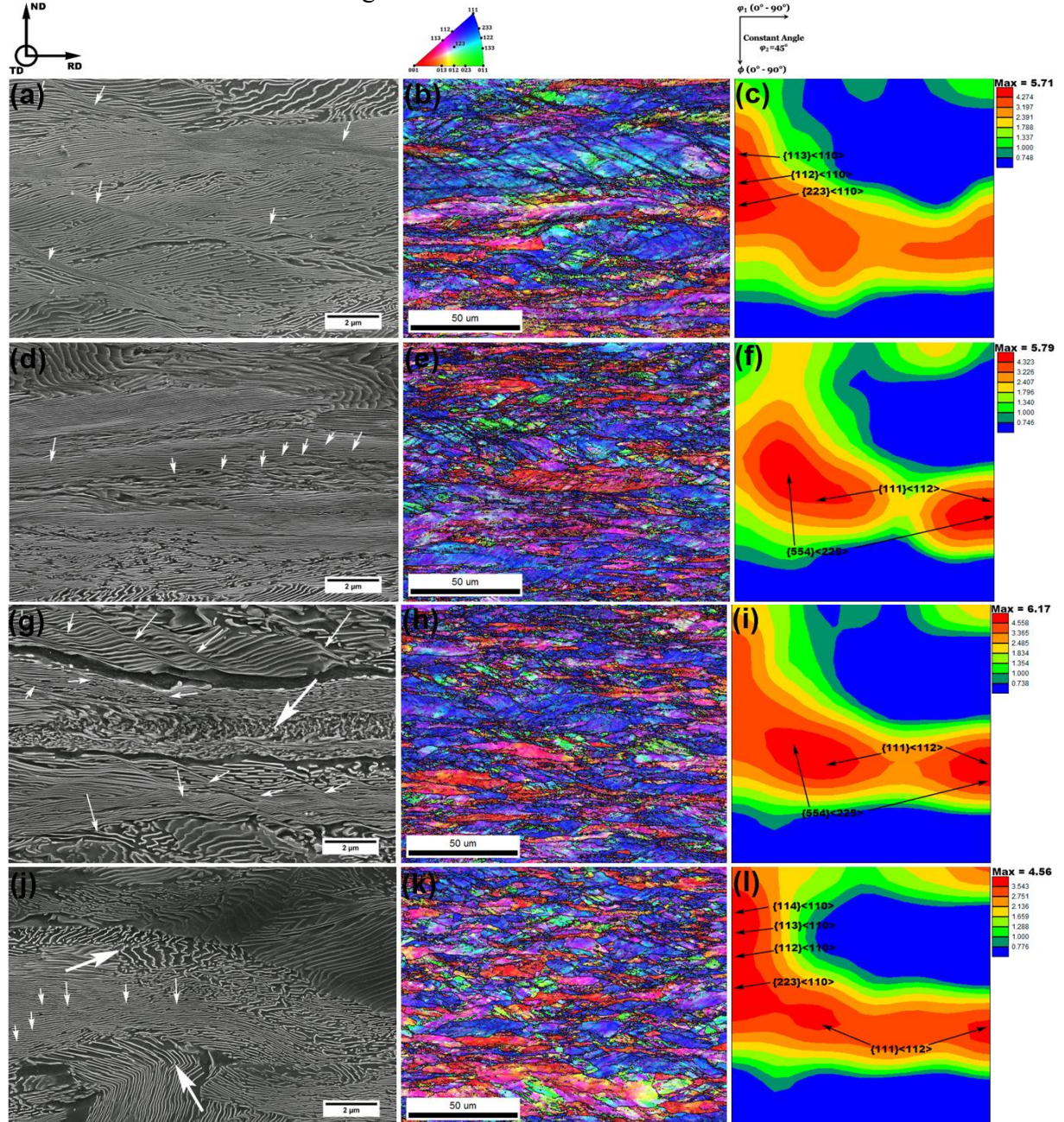
This section centers attention on the four 65% cold-rolled samples (R1S1, R2S2, R3S2, and R4S3) produced from distinct lab-simulated process routes as illustrated in Figure 10a. Figure 16 exhibits SEM images and IPF maps with their respective ODFs of the R1S1, R2S2, R3S2, and R4S3 samples. After the 65% cold-rolling deformation, it is possible to observe that the pearlitic colonies, the GB- α , and the pearlitic blocks tend to be stretched in the rolling direction, as shown in Figure 16. Specifically, it is possible to see in Figure 16a, 16d, 16e, and 16g bent and broken cementite lamellae due to shear bands (indicated by smaller white arrows) or the hard initial orientation of the cementite lamellae about the rolling direction (indicated by bigger white arrows).

In addition, it is worth realizing that the thickness and length of the stretched

pearlitic blocks are proportional to their size before the cold deformation, which means that the initial condition with the biggest undeformed pearlitic blocks resulted in the longest stretched ones after deformation (for example, see Figure 16b) and so on. In this context, the pearlitic blocks seem to have different trends of deformation. The bigger pearlitic blocks with larger stretched areas presented a greater density of shear bands, such as in the samples R1S1 (Figure 16b) and R2S2 (Figure 16e) which is consistent with a previous investigation (JAZAERI; HUMPHREYS, 2004). This phenomenon can be associated with a lower strain-rate sensitivity (m) in the conditions of pearlitic steel with big pearlitic blocks. In this regard, Figueiredo and Langdon (2022) demonstrated in their model that strain-rate sensitivity has an inversely proportional relationship with the grain size in BCC metals. Also, the authors reported that lower flow stresses are required to continue deforming plastically the coarse-grained materials with low strain-rate sensitivity. Additionally, Yan et al. (2021) described that low strain-rate sensitivities can lead to, eventually, strain localization in the material. Therefore, it may imply that the big pearlitic blocks are more susceptible to the development of shear bands in comparison to the smaller ones under the same reduction per pass, rolling speed, and total reduction during the cold rolling process. Moreover, it is also reasonable to consider that the lattice rotations during deformation occur less distributed inside the big pearlitic blocks due to the development of many local deformations (shear bands). It suggests that this mechanism may slice the block into different sections that can slightly slide over each other as deformation occurs. As consequence, a large pearlitic block may be stretched into the rolling direction by undistributed lattice rotation and predominantly local deformation (shear bands).

Another relevant indicator of lattice rotation is microtexture development. From the ODFs in Figure 16c, 16f, 16i, and 16l the main cold-rolling components found were in the α (RD//<110>) and γ (ND//<111>) fibers. However, considering just the samples R1S1, R2S2, and R3S2, it can be seen that the intensity of the ND//<111> fiber, mainly represented by $\{111\}$ <112> component or dark blue pearlitic blocks, increases as the PBS before the cold-forming decreases. This relationship is evidenced in Figure 17a. However, in Figure 17a, the R4S3 condition was indicated as a special case because its smallest PBS before cold-forming did not result in the biggest $\{111\}$ <112> intensity. It can be explained due to the application of the PT (ND//<111> fiber weakener) after the first 30% of cold reduction. However, after just an additional 35% of cold thickness reduction, the R4S3 condition possessed as one of its main components the $\{111\}$ <112> orientation, which was even bigger than in the R1S1 condition. Therefore, the special case condition (R4S3) also provides a noticeable effect of the PBS on the crystallographic lattice rotation during the cold-rolling process. So, the ODFs' microtexture in

Figure 16 – SEM SE image, color-coded IPF map and ODF at $\phi_2 = 45^\circ$, respectively for each cold-rolled samples: (a)(b)(c) R1S1, (d)(e)(f) R2S2, (g)(h)(i) R3S2 and (j)(k)(l) R4S3. In the SE images, small white arrows indicate bent and broken cementite lamellae caused by shear bands, while big white arrows point out bent and broken cementite lamellae due to their hard initial orientation with the rolling direction.



Source: Elaborated by the author.

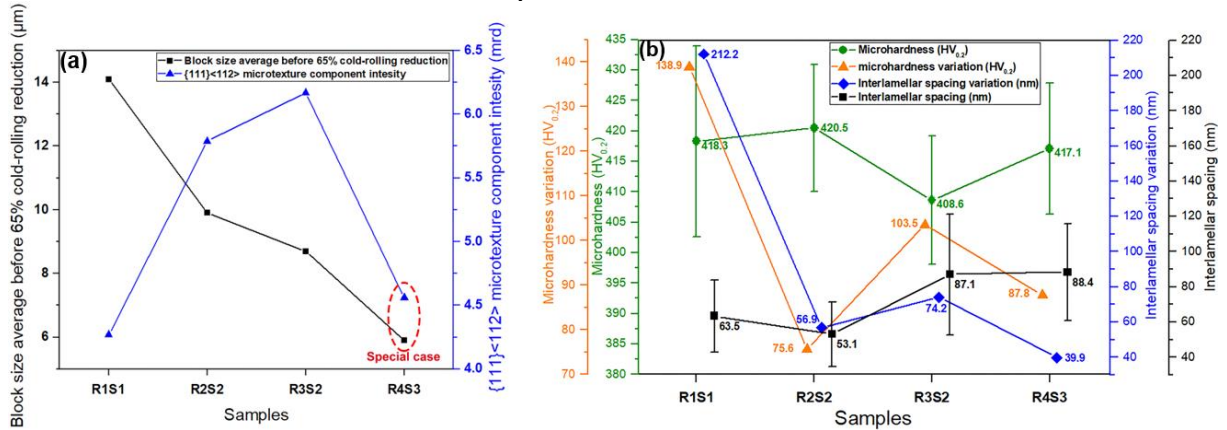
Figure 16 may confirm that the smaller pearlitic blocks which have greater restraint limits (block boundaries) have more effective lattice rotation in comparison to the bigger pearlitic blocks. Therefore, it suggests that the PT application before cold-rolling can have a straight influence on the cold-rolling microtexture by modifying the initial PBS.

Furthermore, Figure 17b summarizes the IS and microhardness obtained from the

four investigated 65% cold-rolled samples (R1S1, R2S2, R3S2, and R4S3) and their respective variation concerning the sample one position backward in their respective manufacture route sequence (S1, R2S1, R3S1, and R4S2, respectively). The IS and microhardness variation reveals that all the samples underwent an IS reduction and microhardness increase as a result of the cold-rolling deformation. In addition to this, it can be seen that the magnitude of the increase in microhardness (orange plot in Figure 17b) followed a close trend to the IS refinement (blue plot in Figure 17b). In this regard, the cementite lamellae are barriers to the dislocation slip in the ferrite phase that can generate dislocation pile-ups at the lamellae interface (ESHELBY *et al.*, 1951). So, the corresponding IS/microhardness variation can be explained via the Hall-Petch relationship (OHBA *et al.*, 2007). Moreover, dislocations formed at the cementite/ferrite interface can drag carbon atoms from the cementite into the ferrite matrix resulting in a hardening contribution through a ferrite solid solution (LI *et al.*, 2011). However, the IS and microhardness varied differently for the same degree of cold-rolling reduction (65%). In this way, the biggest IS change was noticed between S1 (hot-rolled) and R1S1 (65% cold-rolled) conditions. This high IS refinement capacity may be attributed to the higher elongation undergone by the big blocks in the R1S1 sample during the cold-forming process. Also, Li *et al.* (2011) reported that pearlites with coarse IS are the preferable source for dislocation nucleation due to their lower critical stress. It means that coarse microstructure pearlites may undergo higher strain than the thinner ones under the same degree of cold reduction. So, the initial tick IS colonies in sample S1 with lamellae soft orientated to the rolling direction may be drastically refined due to their superior capacity for stretching and undergoing strain. Moreover, between the four 65% cold-rolling reduced conditions, the thinnest IS average was achieved in the sample R2S2. In this case, it should be a result of the combined contribution of the already refined IS before plastic deformation in sample R2S1 and its second-largest PBS with relevant stretching performance. Regarding the same assumption, although the samples R3S2 and R4S3 (with the smaller PBS) presented IS reduction, they did not reach great thinning efficiency likely due to their poor lengthening ability.

In addition, the microhardness values (green plot in Figure 17b) of the four 65% cold-rolled samples (R1S1, R2S2, R3S2, and R4S3) were considered indistinguishable from each other, mainly because their standard deviation involved an extensive correspondent range of fluctuation between them. Thus, it is plausible to consider that the different IS magnitudes generated after the same degree of cold-rolling deformation in the four investigated conditions were not enough to affect individually their microhardness. Instead, as reported by several researchers (TAGASHIRA *et al.*, 2000; GUO *et al.*, 2014; ZHANG *et al.*, 2007), the variation

Figure 17 – (a) Pearlitic block size before 65% cold-rolling reduction against its $\{111\}\langle 112\rangle$ microtexture component intensity after 65% cold-rolling reduction for the R1S1, R2S2, R3S2, and R4S3 samples (the red dashed circle and the special case reference meaning a different cold-rolling process in the R4S3 condition) and (b) Values of microhardness, interlamellar spacing, and their variation concerning one condition before in the process route of the R1S1, R2S2, R3S2, and R4S3 cold-rolled samples.



Source: Elaborated by the author.

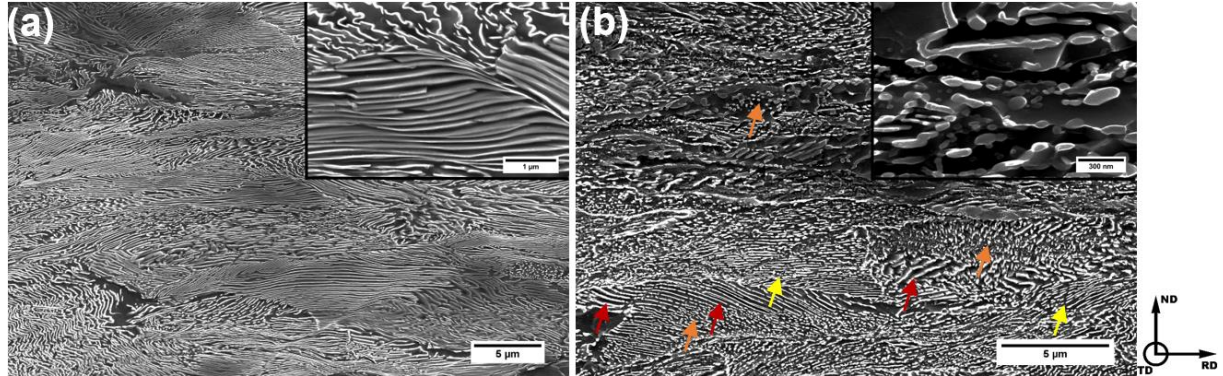
in the amount of plastic deformation may be the dominant parameter for producing significant IS variance and consequently, mechanical properties divergence after the cold-forming process. Finally, the most distinct microhardness average (408.58 HV) and the highest standard deviation (± 16.16) were observed in the R3S2 (which had the smaller microhardness) and R1S1 conditions, respectively. These discrepancies may be a consequence of inhomogeneous microstructure resulting from no PT adoption (S1 condition) or low efficiency of PT employment (R3S1 condition).

2.3.3 Stress-relieved samples after 65% cold-rolling reduction in route 3

In the current work, only the stress-relieved condition at 700°C for 60 seconds in route 3 presented cracks during the bending experiments (see Figure 10a). Regarding the route 3 pathway, this topic focuses on investigating the microstructural effects caused by the stress relief treatments applied just before the three-point bending procedure in the R3400 (400°C for 60 seconds) and R3700 (700°C for 60 seconds) samples.

Figure 18 exhibits the resultant pearlitic microstructures after stress relief treatment at 400°C (R3400) and 700°C (R3700) for 60 seconds of holding time in both. The lamellar morphology was the dominant sort of pearlite found in the R3400 condition as shown in Figure 18a, which means that this microstructure is similar to the 65% cold-rolled state (R3S2). Also, the R3400's microhardness, 409 ± 7 HV, did not reveal an appreciable difference about R3S2

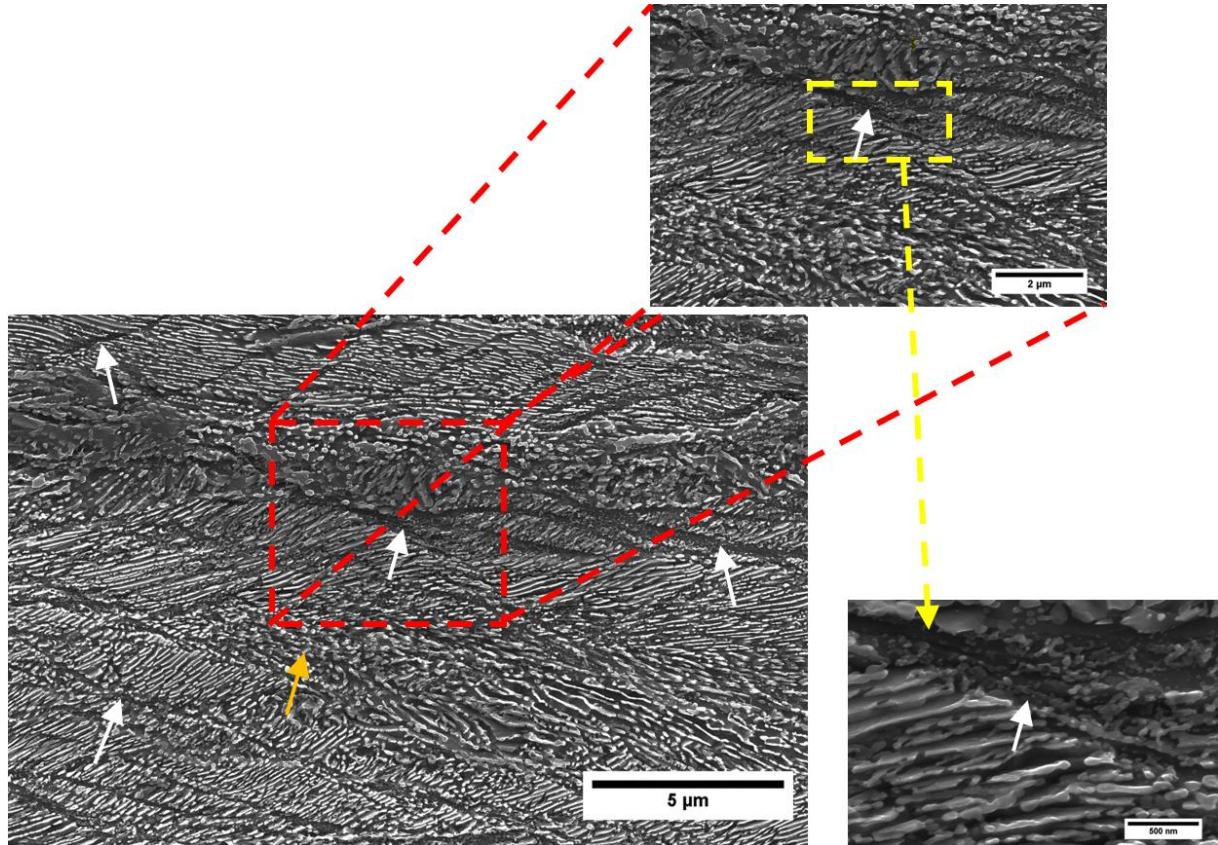
Figure 18 – SEM SE image of the 65% cold-rolled pearlitic steel (R3S2) after stress relief treatment at (a) 400 °C during 60 seconds (R3400) and (b) 700 °C during 60 seconds (R3700) (The red arrows point out disconnected and elongated cementite, the yellow arrows indicate partially spheroidized cementite, and the orange arrows indicate the completely spheroidized cementite).



Source: Elaborated by the author.

(407 ± 9 HV). Therefore, it is reasonable to suggest that the thermal treatment at 400°C for 60 seconds was not enough to strain-relief the prior cold-deformed state (R3S2). In contrast, the short holding time (60 s) at 700°C was enough to start the process of cementite spheroidization as shown in Figure 18b. As a consequence, the microhardness dropped to 358 ± 6 HV. The regular process of cementite spheroidization is reported to take many hours (Montana et al., 2022). So, the faster spheroidization event observed in the R3700 condition may be attributed to the introduction of subgrains to the ferrite and cementite phases during the prior plastic deformation process (MONTANA *et al.*, 2022; LUPTON; WARRINGTON, 1972). However, it is worth noticing that this cementite spheroidization was not homogeneous. In this regard, it is possible to identify in Figure 18b three different cementite morphology: disconnected but still elongated cementite (red arrows), partially spheroidized cementite (yellow arrows), and completely spheroidized cementite (orange arrows). This outcome may be a consequence of the heterogeneous microstructure produced from both; irregular PT application (huge variation of IS) and cold-rolling process (undistributed strains). Concerning the irregularities and discontinuities even within the same pearlite, it is pointed out from the literature (MONTANA *et al.*, 2022; ZHAO *et al.*, 2022) that lamellae cementite from thinner IS regions in pearlites are easier to dissolve into the matrix during thermal treatments, and localized strains in pearlites, such as shear bands, are regions prone to cementite spheroidization. Moreover, after a short annealing time at 700°C of 70% cold-rolled pearlitic steel, Furuvara et al. (2005) described that spheroidization cementite starts in large misorientation regions in the ferritic matrix where lamellae are heavily deformed, such as in irregular bent lamellae and shear bands. Also, the authors found non-spheroidized cementite from coarse lamellae regions. They still reported

Figure 19 – SEM SE images indicate cementite spheroidization in the shear bands (pointing out by white arrows) and in the irregular bent cementite zone (pointing out by an orange arrow) after stress relief treatment at 700 °C for 60 seconds (R3700 condition).



Source: Elaborated by the author.

disconnected cementite but still elongated from fine cementite lamellae areas with no local strain. In agreement with the aforementioned investigation, Figure 19 shows that spheroidization cementite mainly occurs in the shear bands (indicated by white arrows) followed by irregular bent lamellae zone (pointed out by an orange arrow).

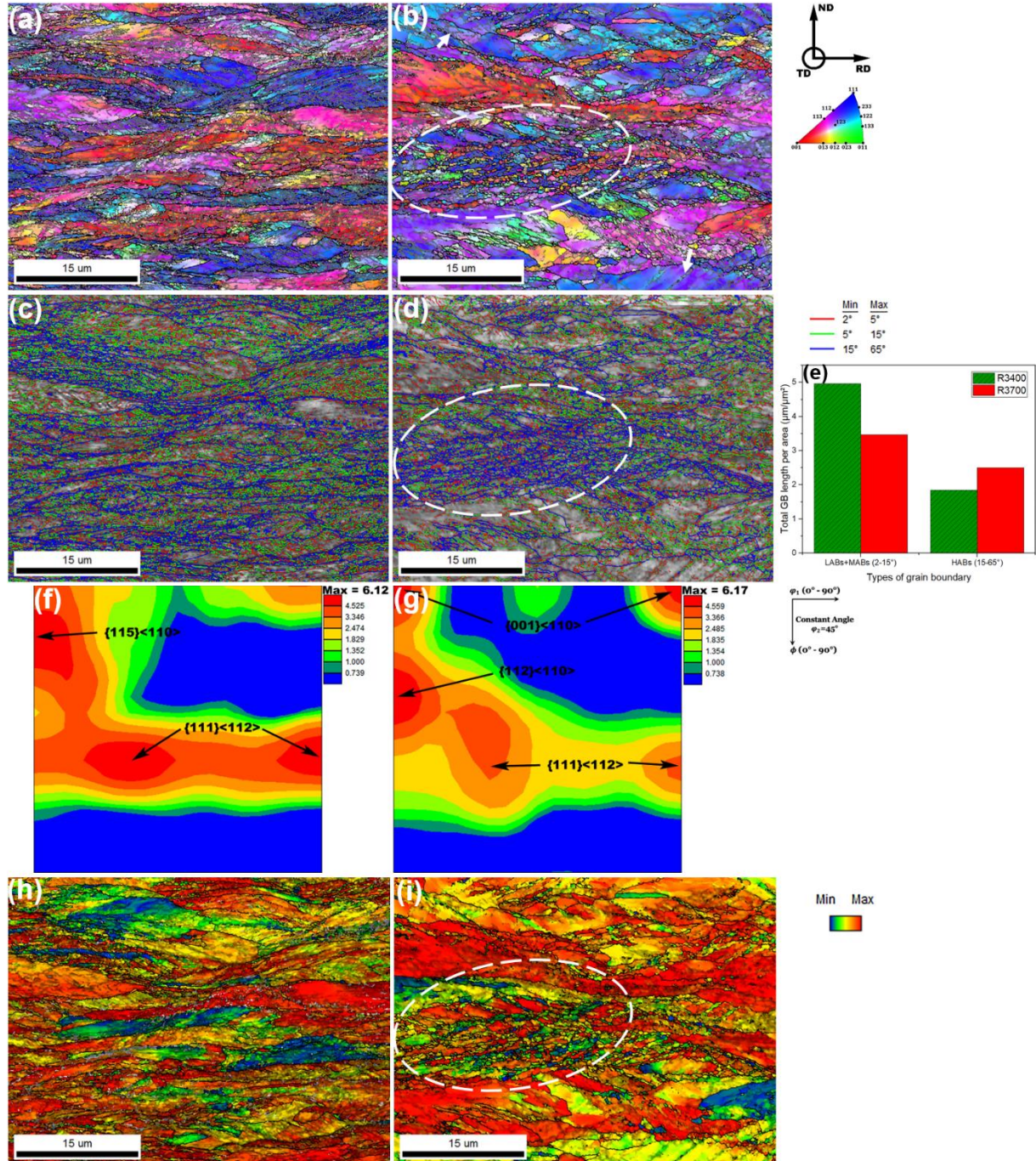
Furthermore, Figure 20 presents IPF maps for the two evaluated stress-relieved conditions (R3400 and R3700) and their respective grain boundary distributions, ODFs, and Taylor factor maps. It is interesting to note that the ferritic blocks in the IPF maps are still elongated to the rolling direction in both investigated circumstances. However, as indicated by a white dashed circle, Figure 20b presents many small randomly orientated and equiaxed ferritic grains inside a blue block, which are aligned to each other and seem to follow the same direction as the previously observed shear bands. In addition to this, in Figure 20e the stress-relieved condition at 700°C presented a lower amount of LABs summed to MABs and a greater amount of HABs in comparison to the stress-relieved state at 400°C. Regarding this, a high density of HABs is concentrated in the region where the small equiaxed ferritic grains were found, as

shown in Figure 20d. It means that these new grains are surrounded by high-angle boundaries. Conversely, the R3400 sample displayed a resultant distribution of HABs more homogeneously spread throughout the matrix. Moreover, regarding $\{111\}\langle 112\rangle$ component formed during the prior 65% cold-rolled reduction (R3S2), the ODFs presented in Figure 20f and 20g exhibited a reduction of $\{111\}\langle 112\rangle$ intensity only for the R3700 condition.

In this context, it may be considered that the small equiaxed grains found in R3700 seem to be formed via recrystallization. Besides, it is known from the literature (FURUHARA *et al.*, 2005; LEÃO *et al.*, 2022) that the $\{111\}\langle 112\rangle$ orientation originated via plastic deformation is the component that contains the highest stored energy, and the shear bands are regions with high misorientation. Based on this information, it is plausible to assume that the preferential site for new recrystallized grains should be in the shear bands inside the $\{111\}\langle 112\rangle$ orientated blocks (dark blue ones), which can explain the arrangement of how the set of the small ferritic grains are displayed in Figure 20b. As a consequence of this mechanism, the intensity of $\{111\}\langle 112\rangle$ component should smoothly decrease as shown in Figure 20g. However, it can still be seen that the fast thermal treatment did not eliminate all the $\{111\}\langle 112\rangle$ blue grains with shear strains as pointed out by white arrows in Figure 20b. Concerning that cementite spheroidization was intensively developed mainly in the shear bands (see Figure 19), the small recrystallized ferritic grains hardly grow due to the pinning effect of the distributed cementite particles in these regions (UMAR *et al.*, 2021). This can make it difficult for high-angle boundaries to migrate. Moreover, the reduction of grain boundaries with low/medium misorientation ($\leq 15^\circ$) and the increase of HABs due to the nucleation of many small grains with low capacity of motion implies that the formation of the new grains happens basically via recovery. This event is known as continuous recrystallization (HAESSNER, 1978).

Also, Figure 20h and 20i display Taylor factor maps for both evaluated stress relief conditions. Taylor factor analysis can predict the ability of grains to undergo plastic deformation based on the crystallographic orientation distribution and active slip systems concerning the external loading direction (LIU *et al.*, 2016). To clarify, slip plains' grains already aligned into the loading direction, easily slip when the resolved critical shear stress is achieved. These grains have low Taylor factor values and are represented by blue grains in the Taylor factor maps. There are also initially not aligned slip systems' grains, which can rotate to a suitable position where plastic deformation can occur. This type of grain possesses a moderate Taylor factor and is indicated in yellow or green color in the Taylor factor maps. Finally, the red and dark yellow grains with a high Taylor factor cannot rotate to provide the occurrence of plastic deformation. To summarize, the low Taylor factor means easy grain deformation, and conversely, the high

Figure 20 – Color-coded IPF map, grain boundary distribution map, distribution of grain boundary type per area, ODF at $\phi_2 = 45^\circ$ and Taylor factor map, respectively, of the (a)(c)(e)(f)(h) sample R3400 and (b)(d)(e)(g)(i) sample R3700. The dashed white circle indicates a region with recrystallized small grains.



Source: Elaborated by the author.

Taylor factor represents grains with higher resistance to deforming. In this context, the Taylor factor map from the R3700 condition in Figure 20i shows that the region with small equiaxed grains (indicated by a white dashed circle) developed many local Taylor factor heterogeneities that are not possible to be observed in the R3400 (Figure 20h). In the region surrounded by a white dashed circle in Figure 20i, there are small blue and green grains oriented for easy slip,

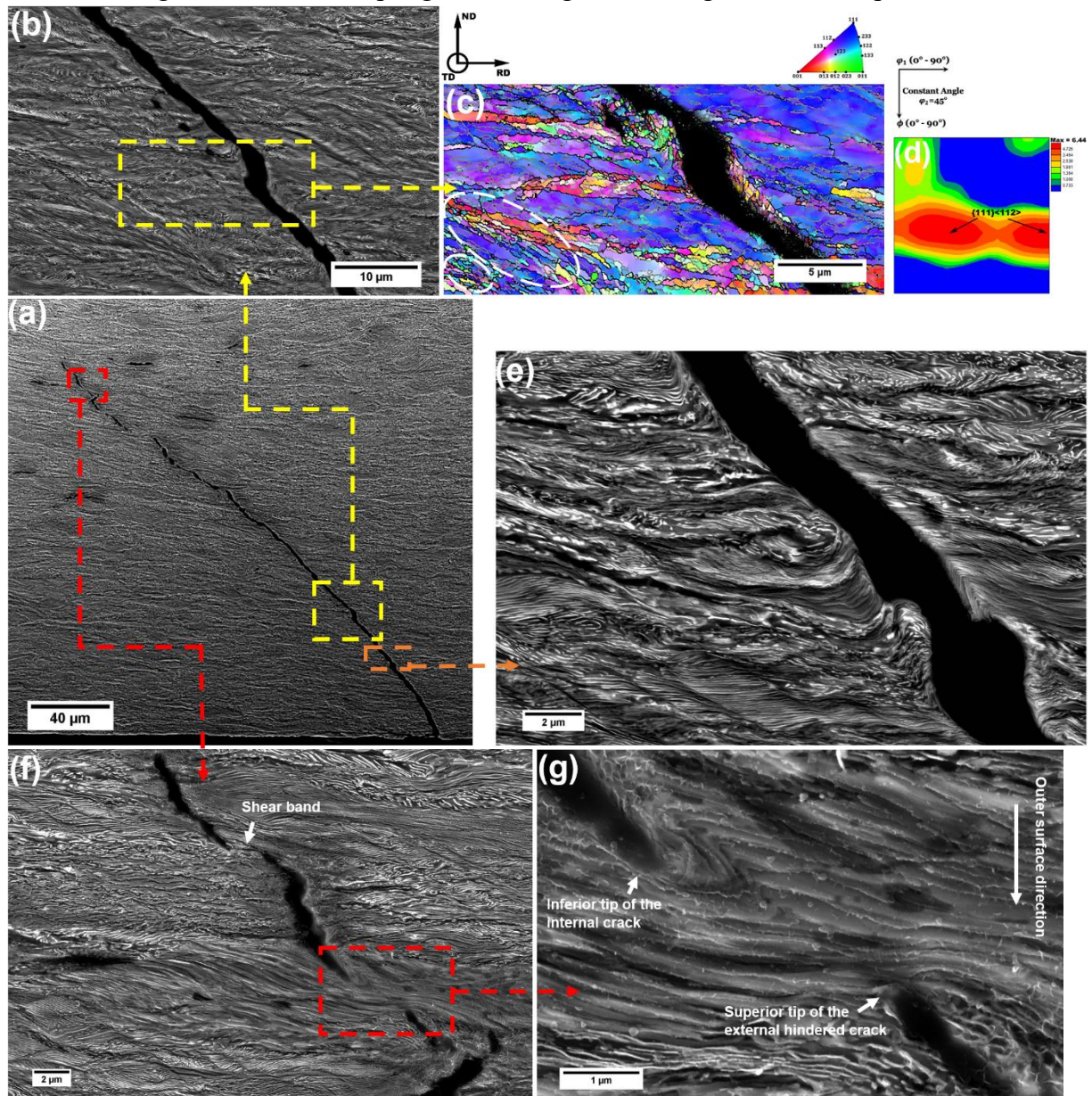
while those grains in dark yellow or red provide resistance for yielding. This mismatch of the Taylor factor between adjacent grains is prone to form intergranular cracks (SZPUNAR *et al.*, 2015b).

2.3.4 Mechanism of crack nucleation and propagation during bending test

This section aims attention to investigate cracks detected during bending experiments. These defects were found only in samples that came from the 65% cold-rolling process in route 3 followed by stress relief treatment at 700°C for 60 s (see Figure 10a). In this context, Figure 21, 22, and 23 present three cracks found in three R3700crack samples after undergoing four consecutive and alternated three-point bending tests. In general, these cracks were found in the area close to the outer surface during the fourth bending sequence. Therefore, the cracked regions were under tensile at that testing moment, but this region was already submitted under the states of compression (first bending), tensile (second bending), and then, compression again (third bending). Recent works (KAPP *et al.*, 2022; AROLA *et al.*, 2021) reported that the tensile region under bending conditions tends to form shear bands while the compressed one is kept smooth. Also, it is interesting to note that in some regions the microstructure was tilted and stretched into a specific direction that the cracks also tend to follow. This outcome was related to the round shape of the superior pin. It means that this new lengthened direction depends on which side of the superior pin the evaluated region is located. For instance, the areas shown in Figure 21 and 22 were situated just below the left side of the superior pin, while Figure 23 was below the right side. Moreover, it is not easy to observe the GB- α and the spheroidized cementite in the bent state, probably due to the severe plastic deformation associated with the repeated bending processes. For example, it is possible to recognize some stretched GB- α in Figure 22a and 23b, and some deformed regions with cementite partially spheroidized in Figure 21e, 21f, and 23d.

Figure 21a exhibits a crack with a length of 279.3 μm and an angle of $\approx 42.7^\circ$ about the rolling direction. This crack presents many deviations. One of these crack path divergences is shown in Figure 21b, where the pearlite colonies around the crack were not found much tilted, instead they presented shear bands. In this regard, the crack is aligned to those specific local strains. Moreover, in Figure 21b it is possible to notice three microcracks around the big one aligned to the inferior part of the main crack below the deviation. Additionally, it can be realized in the IPF map, in Figure 21c, that small grains are surrounding one of the microcracks and in some regions around the principal crack. Moreover, the crack is passing through a $\{111\}\langle 112\rangle$

Figure 21 – Crack from the R3700crack sample condition in the tensile region of the fourth bending experiment and below the left side of the superior pin. (a) SEM SE image of the entire crack. (b) SEM SE image of a region with crack deviation and microcracks. (c) Color-coded IPF map of the region containing the crack deviation and one microcrack. The dashed white circles indicate small grains deformed in a direction almost parallel to the main crack and shear bands. (d) ODF at $\phi_2 = 45^\circ$ calculated from the IPF map in Figure 102 (c). (e) SEM SE image of a smooth crack deviation. (f) SEM SE image of the region close to the crack tip. (g) SEM SE image from a crack's tip region showing the bending of a lamellar pearlite.



Source: Elaborated by the author.

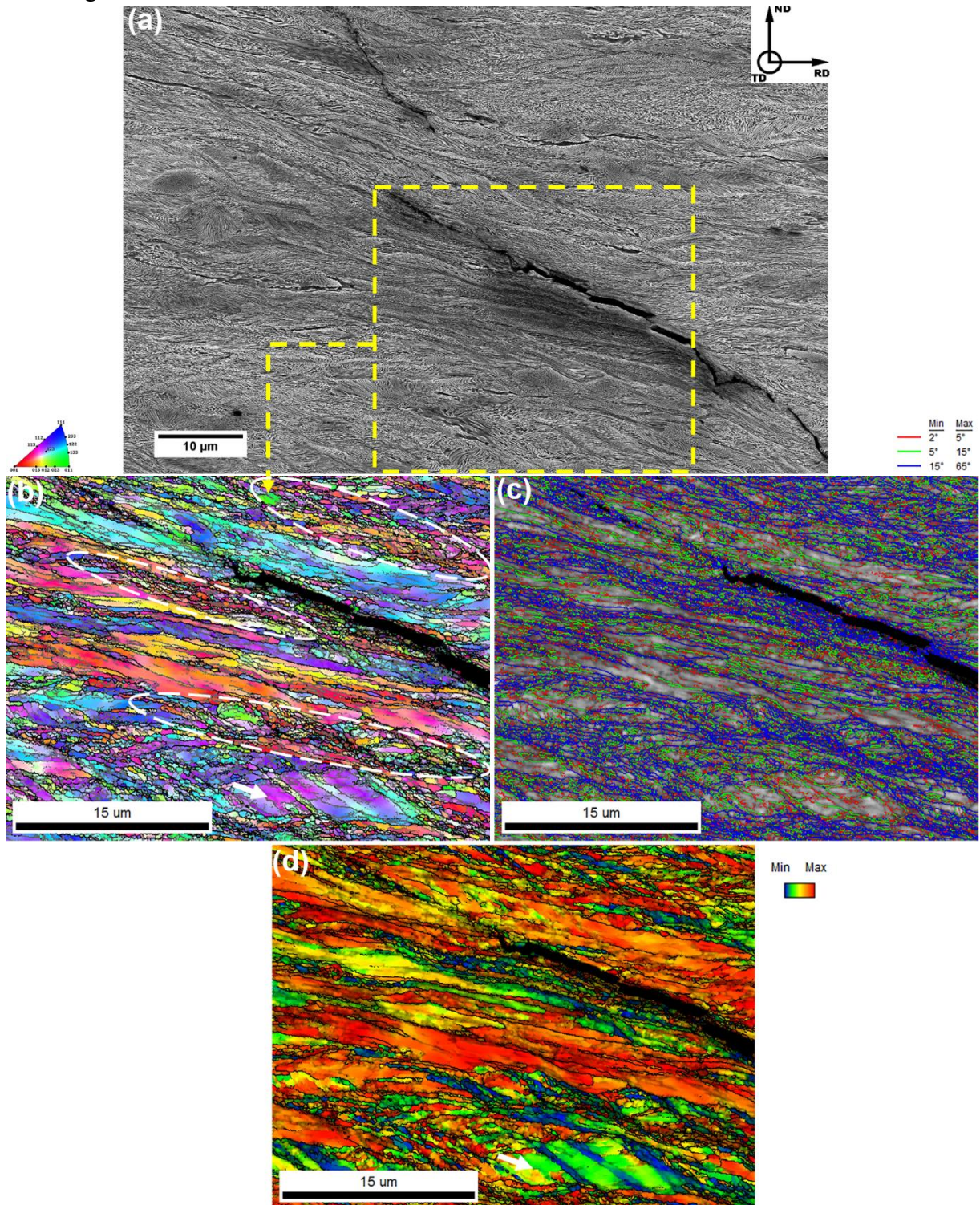
orientated grain as shown in Figure 21d. Supplementary, Figure 21e depicts another region in which the crack underwent a smooth path deviation. In this case, it is possible to detect quite bent cementite lamellae around the deviation region. The bent lamellar pearlite looked to be perpendicular to the direction of the crack propagation. Besides, the crack region just below the

bent lamellae is round and thicker which seems that its prior propagation was hindered there. Another point is that the direction in which the lamellae were bent suggests that the superior crack reached the inferior one. Moreover, Figure 21f displays an area close to the tip of the evaluated crack. In this region, there are four main crack segments and four microcracks. In this context, it can be noticed that the pearlitic lamellae around the two superior crack segments are partially spheroidized. In addition, it is possible to observe in the region between these two superior cracks they are connecting following a shear band, as indicated by a white arrow. This mechanism agreed with the model developed by Hu et al. (2010). The authors concluded that cracks initiated in distinct regions can be connected throughout shear bands during bending deformation. Otherwise, the inferior crack is deviating from a perpendicular and fully lamellar pearlite, however, the propagation of the inferior crack seems to be blocked. Then, in Figure 21g, it is visible that the crack segment located in the middle of Figure 21f is bending the pearlitic lamellae in the direction of the inferior microcrack. It seems to be the same phenomenon shown in Figure 21e. This crack propagation mechanism may be attributed to the gradient of tension during the bending experiment that should be zero in the middle thickness of the sample and increase to a maximum in the region close to the external surface (KAPP *et al.*, 2022). So, this condition leads to a higher tensile stress in the inferior tip of the internal crack which promotes easier crack growth into the outer surface direction (see Figure 21e). In contrast, in the superior tip of the hindered external crack, the tensile stress is supposed to be smaller than in the rest of the crack which becomes difficult for the crack propagates through the transversal pearlitic lamellae.

In particular, the crack presented in Figure 22a has a length of 138.4 μm . In the region surrounding this crack, there are pearlitic lamellae lengthened to $\approx 29.4^\circ$ concerning the rolling direction. Saastamoinen et al. (2017) showed microcracks nucleating inside a shear band and following its direction during a bending test. Also, it is worth pointing out that a non-rotated grain, indicated by white arrows in Figures 22b and 22d, presented three local shear strains aligned near ($\approx 33.8^\circ$ about RD) to the direction of the stretched pearlitic lamellae around the crack. Therefore, it is reasonable to accept that this local deformed microstructure may be part of a shear band caused by the bending deformation. In addition, it is possible to realize in Figures 22b, 22c, and 22d that the crack is propagating between the small high-angle boundary grains with a considerable mismatch of Taylor factors, which are also aligned close to the shear band direction. This result agrees with the microstructure described in the previous section (Figure 20b and 20i).

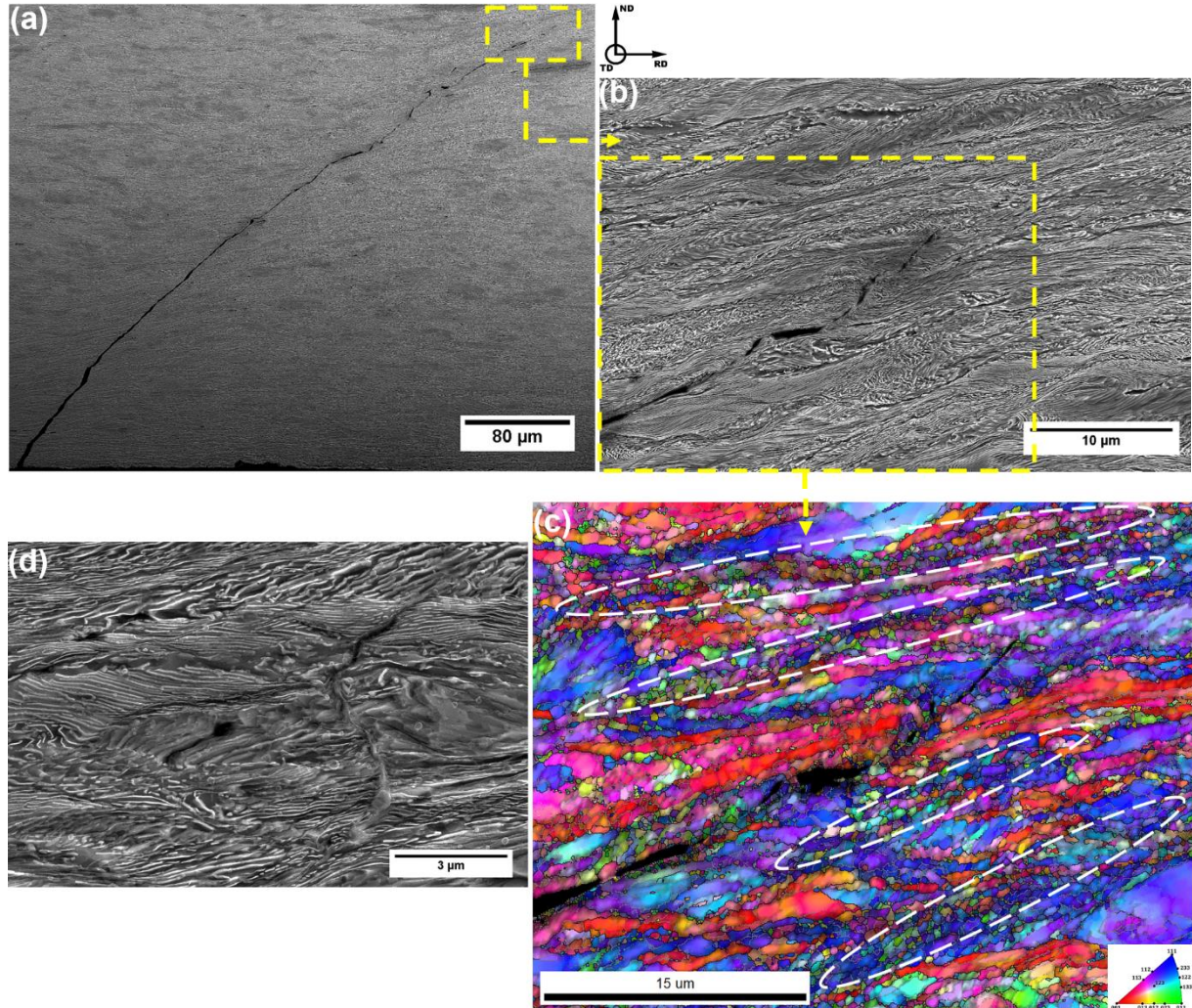
Additionally, Figure 23a exhibits another deep crack (542.4 μm) tilted $\approx 48.7^\circ$ with

Figure 22 –Tip of a crack in the R3700crack sample condition, located below the left side of the superior pin in the tensile region after four alternating bending experiments. (a) SEM SE image. (b) Color-coded IPF map. The dashed white circles indicate regions of small grains deformed in a direction close to the crack propagation and shear bands. (c) Grain boundary distribution map. (d) Taylor factor map. The white arrow indicates a non-recrystallized and non-rotated grain with local shear strains.



Source: Elaborated by the author.

Figure 23 – Crack from the R3700crack sample condition in the tensile region of the fourth bending experiment and below the right side of the superior pin. (a) SEM SE image of the entire crack. (b) SEM SE image of the crack tip. (c) Color-coded IPF map of the crack tip. The dashed white circles indicate regions of small grains deformed in a direction close to the crack propagation. (d) Microcracks from an adjacent region around the main crack.



Source: Elaborated by the author.

the rolling direction. Figure 23b shows the tip of that crack which is also surrounded by deformed pearlites in the same direction of crack propagation. Moreover, the IPF map of this crack tip is shown in Figure 23c. It is possible to observe similarities in the propagation path to the prior cracks. In this case, the crack is passing between small grains inside the $\{111\}$ oriented pearlitic block (blue) and follows the direction of the deformed blocks. It is clear to observe that the crack deviated from the $\{100\}$ blocks in red color. Furthermore, Figure 23d displays two microcracks found around the region of the main crack. One of them is propagated between the cementite/ferrite lamellar interface (decohesion) that probably originated from the round microcrack. While the second microcrack seems to be in pearlite with broken or partially spheroidized cementite. These cracks in Figure 23d are tilted and aligned in the same direction

($\approx 33.4^\circ$ with the rolling direction), which suggests that they are likely in a shear band orientation.

In summary, regarding the evidence discussed in the current section, it is reasonable to accept that shear band deformation can be induced via the three-point bending test in the sample's tensile region. However, part of the shear bands previously created during the cold-rolling process in the $\{111\}\langle 112\rangle$ blocks was replaced by many small recrystallized grains. In this way, every time this structure is submitted under a tensile condition, imposed throughout the successive bending deformation, new shear directions start to be developed in the material and the small grains inside the $\{111\}\langle 112\rangle$ blocks tend to align into the newly settled shear directions. This behavior can be seen in the regions indicated by white dashed circles in the IPFs maps presented in Figure 21c, 22b, and 23c. Moreover, it is plausible to acknowledge that the small recrystallized grains inside the $\{111\}\langle 112\rangle$ blocks are prone to microcracks nucleation due to their different deformation behavior (mismatch of Taylor factor) and higher local density of HABs resulting in a region susceptible to local strain-hardening and pill-ups of dislocations. Following the arrangement of the small grains, the microcracks can also nucleate lined up with each other as indicated in Figure 21b, 21f, and 23d. Moreover, the shear bands are regions containing mostly spheroidized cementite as presented in Figure 19, which is supposed to have less resistance to the growth of microcracks. So, the microcracks may grow and connect themselves easily through the shear bands' path as pointed out in Figure 21f. Regarding the tensile gradient imposed by the bending state, the connection between two aligned microcracks likely happened through the growth of the more external microcrack (closer to the external surface of the specimen under tensile stress) in direction of the internal one (farther from the external surface of the specimen under tensile stress). However, the external microcrack growth can be hindered by fully lamellar pearlitic colonies orientated near the perpendicular direction of the crack propagation (see Figure 21f and 21g). In this case, the most internal defect can bend the pearlitic lamellae in the opposite direction of crack growth reaching the hindered microcrack. It may also occur due to the tensile gradient of the bending condition that facilitates the internal microcrack to overcome the lamellar obstacle.

3 RESULTS: IN-SITU AND INTERRUPTED CYCLIC THREE-POINT BENDING TESTS IN SEM OF TWO PEARLITIC STEEL MICROSTRUCTURES: LAMELLAR AND PARTIALLY SPHEROIDIZED

3.1 Review

Tensile armor layers on unbonded flexible pipelines (risers) are typically made of several rectangular pearlitic steel wires, which are, together, helically twisted around the pipeline structure. The crucial role of the tensile armor is to ensure a good balance of axial rigidity and flexibility in risers. In addition to this, these pearlitic steel layers must support all the riser weight and transfer the load to the vessel infrastructure on the sea surface. In view of this, these flat wires are, in general, produced throughout a particular manufacture route for obtaining the mechanical properties required by the tensile armor application: hot-rolling → patenting treatment → cold forming (drawing, rolling, or drawing + rolling) → stress relief treatment → re-winding wire into bobbins → helical twisting process (DAMBRE, 1990; MALLÉN; SUGIER, 1996; FERNANDO *et al.*, 2017).

Concerning specifically the process of re-winding wire into the bobbins (RWWB), this procedure starts with the pearlitic steel wire in a stress-relieved condition wound in coils. In this case, the wire has an arch shape along its length due to the coil curvature. This circumstance induces an initial bending state in the component. Next, the wire is initially unwound from the coil and follows an arduous deformation path through two distinct roller machines (pinch and casting rollers) arranged in sequence. Based on this, the pearlitic wire is first stretched in the pinch rollers to eliminate the starting arch profile. Then, the straight flat wire goes to the casting rollers comprising two succeeding rolls. In this setting, the wire passes below the first roll and goes up above the second roll. In this case, the wire follows, consecutively, the opposite concavities shape of the two rolls. As a result, the wire undergoes two more similar bending deformations during its passage through the casting rollers apparatus. The RWWB operation ends up with the re-winding wire into bobbins, which establishes one more bending condition. This deformation practice guarantees the integrity of the wire in the bobbin and its defect tolerance. Therefore, after stress relief, the wire is submitted to a repeated bending condition during the RWWB process, establishing a new residual stress state in the pearlitic microstructure (FERNANDO *et al.*, 2017). Based on this, the initial stress-relieved pearlitic steel wire should be mechanically suitable for overcoming that rigorous deformation process without failure.

In this regard, pearlitic steels present a great combination of high strength and good ductility, which makes them broadly employed in wire-related applications as tensile armor layers. This mechanical balance is manageable by controlling the set of variables related to the pearlitic microstructure, including its morphology. In most cases, the refined lamellar morphology (alternated nanometric layers of soft ferrite and hard cementite) is adopted in practices that require high strength (ultimate tensile strength or yield strength) with a satisfactory ductility performance (ALLAIN *et al.*, 2019). This fact is attributed to the Hall-Petch relationship that is followed by the pearlitic interlamellar spacing (FIGUEIREDO; LANGDON, 2021). In this way, fine lamellar morphology is usually obtained through the patent treatment that enables a fast and isothermal eutectic transformation from austenitic temperatures (ARANDA *et al.*, 2014). Likewise, regarding flat pearlitic steel products, the lamellar morphology is still preserved after cold-rolling and some fast thermal treatments (annealing and stress relief treatments) (ALLAIN *et al.*, 2008; LEÃO *et al.*, 2023a).

Otherwise, an increase in ductility accompanied by a reduction in strength can be designed through the partial or total spheroidization of the cementite from its starting lamellar structure. In the past, this morphological modification was obtained via many hours of heat treatment at temperatures below A1. However, nowadays, there are many faster ways to produce spheroidized cementite particles. For instance, Stodolny *et al.* (2019) accomplished the spheroidization process at 700 °C for an hour by reducing the initial interlamellar spacing. In this regard, aluminum (strong ferrite stabilizer) content in high-carbon steels can lead to a faster process of cementite spheroidization by refining the prior pearlitic interlamellar spacing during the eutectoid transformation (YI *et al.*, 2012). Moreover, it is possible to produce spheroidal cementite by the divorced eutectoid transformation (DET) (VERHOEVEN; GIBSON, 1998). The DET thermal treatment consists of two subsequent steps: an austenitization and an isothermal transformation, both in temperatures close to A1. In this context, the presence of chromium optimizes the process of cementite spheroidization during the DET (SUN *et al.*, 2014). Moreover, the introduction of a prior warm rolling deformation minimizes the hold time of the succeeding spheroidization treatment (SUN *et al.*, 2014; PRASAD *et al.*, 2018). Additionally, some researchers (LEÃO *et al.*, 2023a; FURUHARA *et al.*, 2005) observed that introducing a prior cold-rolling deformation in pearlitic steels resulted in partial or total spheroidization of cementite after a few seconds at 700 °C.

Concerning pearlite deformation, the ferritic matrix has lower yield strength than the cementite phase (TOMOKA *et al.*, 2003). In that manner, the ferrite is prone to achieve an earlier plastic state than cementite during the progress of deformation (KANIE *et al.*, 2004). In

this scenario, dislocations can be nucleated at the cementite(θ)/ferrite(α) interface and glide throughout the ferritic matrix. However, further dislocation slippage can be hindered for other cementite structures spread in the matrix. In this way, piles-up of dislocation can occur. This restriction in dislocation movement increases the required stress to keep the material deforming (strain-hardening) (MOURITZ, 2012). Therefore, the cementite morphology plays a crucial role in strain-hardening behavior in pearlitic steels. Taking this into account, it is pointed out from the literature (RASTEGARI *et al.*, 2012; YASUDA *et al.*, 2017; LI *et al.*, 2012) that the strain-hardening rate depends on the loading direction, the thickness and crystallographic orientation of the ferrite layers in pearlitic steels with lamellar microstructure. It implies that in the lamellar microstructure, the high strain-hardening rates are achieved when the activated systems in ferrite have small Schmid factors and short mean-free paths.

Otherwise, in the spheroidized condition, the strain-hardening rate is proportional to the square root of the division between the volume fraction and the average size of the cementite particles (RASTEGARI *et al.*, 2015). Moreover, Zheng *et al.* (2021) have observed that the strain-hardening increases from a fully spheroidized to a completely lamellar pearlitic microstructure due to the effective barrier provided by the lamellar shape against the dislocation movement. Furthermore, these authors noticed the highest strain-hardening for a pearlitic microstructure with a mix of lamellar and spheroidized cementite. They explained that this morphological merger raises the amount of θ/α interfaces, enhancing dislocation nucleation during plastic deformation. In addition to this, the study of Zhou *et al.* (2019) describes that amorphous cementite can absorb dislocations while crystalline ones do not. However, Tagashira *et al.* (2000) proposed that crystalline cementite can activate multiple slip systems during plastic deformation to maintain the compatibility between ferrite and cementite phases. They also reported that this mechanism of cementite deformation depends on other features, such as the θ/α orientation relationship (OR). Moreover, the initial dislocation density also affects the strain-hardening rate of carbon steels (RASTEGARI *et al.*, 2015; KRAUSS *et al.*, 1995).

Additionally, the behavior of the pearlitic wires under the RWWB deformation can be lab-simulated by implementing several bending cycle proceedings (HANONGE *et al.*, 2022). Within this scope, bending experiments develop a stress gradient throughout the specimen's thickness (KAPP *et al.*, 2022). In particular, the longitudinal thickness fibers near the top surface (in touch with the punch) and the bottom surface (in contact with the support pins) undergo compression and tensile stresses, respectively. Conversely, the middle thickness region remains in a neutral stress state. Also, recent works (LEÃO *et al.*, 2023a; KAPP *et al.*, 2022; SAASTAMOINEN *et al.*, 2017; AROLA *et al.*, 2021) reported that the outer tensile fiber is

prone to produce local deformations (shear bands) that lead to the beginning of catastrophic failure during the bending experiments. In particular, Kapp et al. (2022) demonstrated that the lamellar architecture of the pearlitic morphology retards the development of shear bands and their propagation, which delays the damage initiation. However, the introduction of cyclic bending arrangements imposes recurrent compression-tensile stresses in both aforementioned outer fibers of the specimen. In this regard, pearlitic steels can experience hardening and softening (Bauschinger effect) mechanisms. The Bauschinger effect is usually related to the rearrangement and annihilation of dislocations due to their reservable motion (WANG *et al.*, 2016). Finally, Leão et al. (2023a) lab-produced flat pearlitic steel under different process routes based on the actual manufacture of tensile armor wires. The authors noticed a harmful pearlitic microstructure that quickly failed under cyclic bending deformation. This microstructure with small ferritic recrystallized grains and partial spheroidized cementite was obtained by applying a stress relief treatment at 700 °C for 60 seconds in a deformed lamellar pearlitic microstructure with a $\{111\} \langle 112 \rangle$ predominantly ferritic crystallographic orientation. On the other hand, the lamellar structure was maintained under stress relief at 400°C for 60 s. Therefore, to deeply investigate this issue, the present chapter focused on evaluating the performance of these microstructural pearlitic conditions under cyclic three-point bending (TPB) circumstances. In-situ secondary electron imaging was employed during the TPB operation inside a scanning electron microscope. In addition to this, high-resolution techniques (transmission electron backscattered diffraction and scanning transmission electron microscopy) and EBSD interrupt analyses were employed in this investigation to supply rich details about the starting specimens and their behavior under cyclic bending deformations.

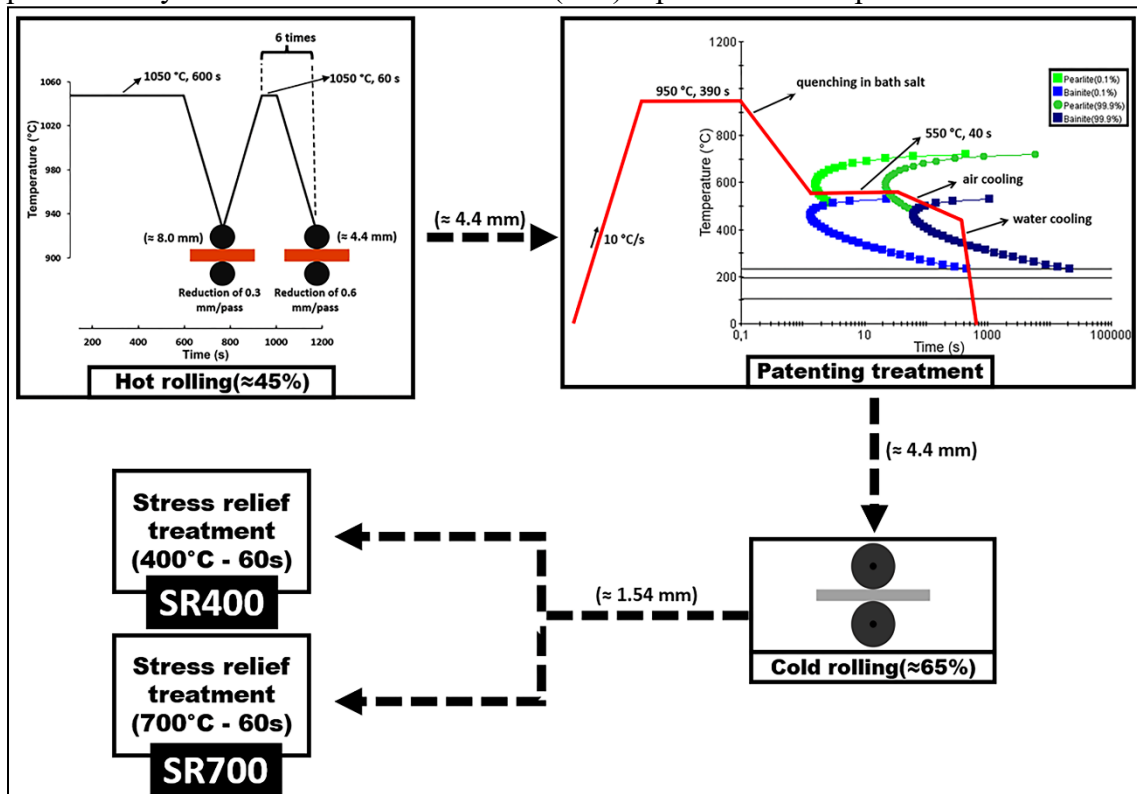
3.2 Methodology

3.2.1 Specimens processing

In this work, a lab-simulated process route, illustrated in Figure 24, was performed in a commercial SAE 1075 pearlitic steel. This lab operation was planned based on actual manufacturing processes of rectangular wires employed on flexible pipelines as tensile armor (DAMBRE, 1990; MALLÉN; SUGIER, 1996; FERNANDO *et al.*, 2017). The chemical composition of the as-received pearlitic steel is provided in Table 1 available in the section 2.2.1. Within the lab-simulated route scope, the rolling processes (hot and cold) were carried out by using a rolling machine with a roll diameter of 110 mm and a rolling speed of 8 m/min. The temperatures of the specimen and the bath salt (60% potassium nitrate + 40% sodium nitrate),

respectively, in the hot rolling process (HRP) and the patent treatment (PT) were measured via an infrared thermometer. A muffle furnace was employed in the HRP, PT, and stress relief (SR) treatments. Concerning the HRP, a start rectangular specimen (thickness ≈ 8 mm x length ≈ 40 mm x width ≈ 50 mm) underwent an initial rolling pass of adjustment (≈ 0.3 mm thickness of reduction) immediately after its austenitization at 1050 °C for 600 seconds. Subsequently, the specimen was quickly put back in the furnace at 1050 °C and kept in there for 60 more seconds, followed by an additional regular hot pass (≈ 0.6 mm of reduction). The last procedure was repeated six times, succeeded by a final air cooling. The final sample's thickness was ≈ 4.4 millimeters ($\approx 45\%$ of hot reduction), and the average finish rolling temperature was 906 °C. After the HRP, the PT treatment was applied in the 45% hot reduced specimen. This PT consisted of an initial sample's austenitization (at 950 °C for 360 seconds) and its direct quenching in a bath salt (at 550 °C for 40 seconds) followed by a final air cooling step. Then,

Figure 24 – Flowchart sketch of the lab-simulated processing route performed in the present study. The numbers in millimeters (mm) represent the sample's thickness.



Source: Elaborated by the author.

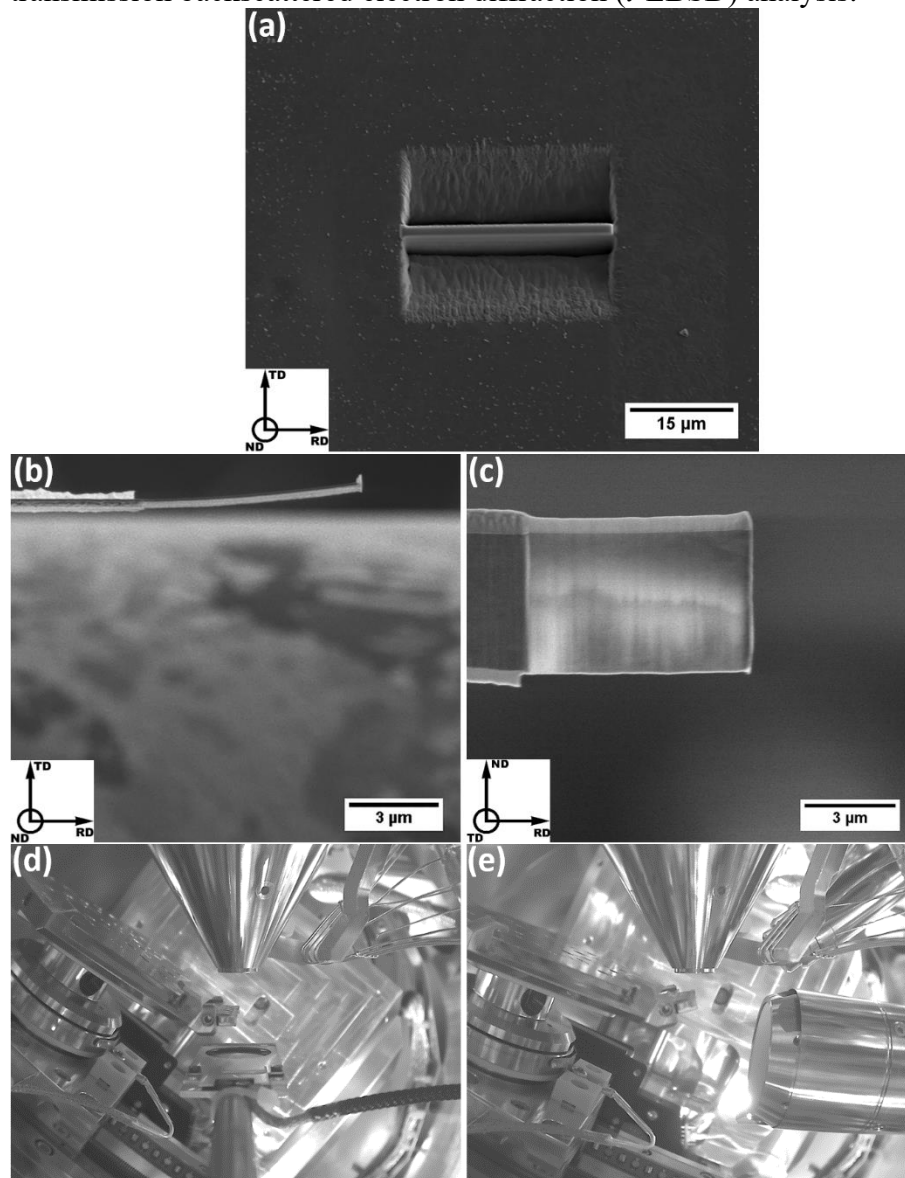
the patented specimen was 65% cold rolled (at a rate of ≈ 0.1 mm/pass), achieving a final thickness of ≈ 1.54 mm. After that, the 65% cold rolled specimen was cut into a smaller rectangular dimension of ≈ 26 (length//rolling direction) x ≈ 10 (width) x ≈ 1.54 (thickness) mm³.

Then, the resized samples in the cold rolled condition received two different SR treatments at 400 and 700 °C using the same holding time of 60 seconds. As a result, the two final lab-processed conditions of SAE 1075 pearlitic steel used in this study were named SR400 and SR700, as shown in Figure 24. In addition to this, in the actual production route, the following process step that succeeds the SR treatment is the re-winding wire process (FERNANDO *et al.*, 2017). The re-winding wire operation is usually lab-simulated via alternated successive bending tests (HANONGE *et al.*, 2022) that are the focus of a further section.

3.2.2 Tensile test, scanning transmission electron microscopy (STEM) image, and transmission electron backscatter diffraction (t-EBSD) analysis

Tensile tests were performed for the two stress-relieved pearlitic steel states (SR400 and SR700) by using a universal testing machine (landmark 370.10 with a maximum load of 100 kN). The tensile samples were machined according to the ASTM E8/E8M standard concerning the tensile direction parallel to the rolling direction. Additionally, a THERMO SCIENTIFIC APREO field emission gun (FEG) scanning electron microscope (SEM) coupled with an EDAX EBSD detector was adopted to carry out the scanning transmission electron microscopy (STEM) image and transmission electron backscatter diffraction (*t*-EBSD) techniques in the SR400 and SR700 specimens. In this case, a thin rectangular foil was obtained from each investigated sample, as displayed in Figure 25. The transparent foils were shaped and prepared through a focused ion beam (FIB) microscope (Helios NanoLab 600 DualBeam Field Emission Gun). Also, in the FIB procedure, a small amount of amorphous platinum was inserted in the tip of the foil's edge to correct the background of the Kikuchi diffraction patterns during the *t*-EBSD performance. Regarding the stress-relieved specimens, the transparent foils were obtained in a position parallel to the longitudinal section from the normal surface area. It means that the analyzed areas were delimited by the normal direction (ND) and rolling direction (RD) (see Figure 25a, 25b, and 25c). Then, the transparent specimens were mounted in a proper holder, as presented in Figure 25d and 25e. For the acquisition of high-resolution images, the STEM detector was placed below the thin foil that was perpendicular to the incident electron beam. This operation was performed by employing an accelerating voltage of 30 kV, a current of 50 pA, and a working distance (WD) of 10 mm. While for the *t*-EBSD analyses were implemented, an operating voltage of 20 kV, a step size of 1.6 nm, a WD of 5 mm, and a sample tilt angle of -20°. Finally, (100), (110) and (111) pole figures were plotted for ferrite and cementite from five *t*-EBSD maps.

Figure 25 – Details of the scanning transmission electron microscopy (STEM) implemented in this work. (a) Schematic position of the thin foils extracted from the surfaces of the SR400 and SR700 samples via focused ion beam (FIB) microscopy. (b) Superior view of the transparent foil after its thickness reduction by FIB technique (c) Lateral view of the transparent foil after its thickness reduction by FIB technique (d) FIB thin foil set up for STEM imaging, and (e) for transmission backscattered electron diffraction (*t*-EBSD) analysis.

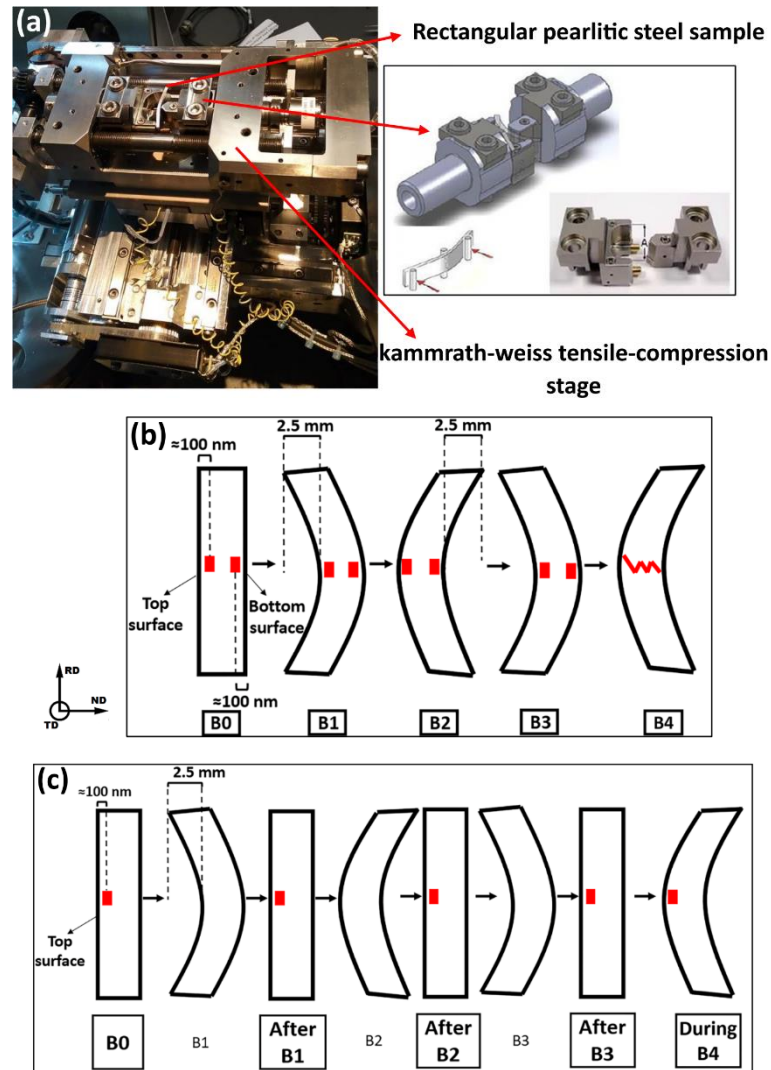


Source: Elaborated by the author.

3.2.3 *In-situ and interrupted three-point bending experiment*

To simulate the behavior of pearlitic steel under the re-winding wire operation (FERNANDO *et al.*, 2017), the two lab-manufactured pearlitic conditions (SR400 and SR700) were submitted to a three point bending (TPB) test. This experiment was conducted by using a

Figure 26 – Details of the in-situ and interrupted three-point bending (TPB) experiments carried out in this work. (a) Kammrath-Weiss tensile-compression stage coupled with an adapter MZ.V32 for the TPB tests. (b) Schematic sketch of the areas (red squares) where the high magnification secondary images were acquired during the in situ TPB performance. (c) Illustrative scheme of the region (red squares) where the electron backscattered diffraction analyses were performed during the interrupted TPB operation.



Source: Elaborated by the author.

kammrath-weiss tensile-compression stage (maximum loading of 5 kN) integrated with a special adapter MZ.V32 for the TPB procedure (see Figure 26a). In this context, the TPB experiment was run at room temperature with a maximum loading pin (central pin or punch) displacement of 2.5 mm, a length between the support pins (outer pins) of 26 mm, and a constant displacement rate of 5 $\mu\text{m/s}$. The longitudinal section (rolling direction x normal direction) of the rectangular samples was the inspected region. In addition, the bending investigation was comprised of four consecutive bending cycles by alternating the superior and inferior sample

surfaces in contact with the pins. This is illustrated in the schemes shown in Figure 26b and Figure 26c. In this way, the bending conditions were labeled according to the resultant amount of consecutive bending undergone in the sample. For instance, “B1”, “B2”, and “B3” represent the bent samples in the maximum displacement (2.5 mm) of the loading pin, respectively, after the first, second, and third subsequent alternated bending procedures. However, “B4” was bending up to the point where the specimen failed during the fourth consecutive bending step. In this case, the displacement of “B4” will depend on the material’s bending resistance. Moreover, “B0” symbolizes the unbent condition, which means the initial stress-relieved specimen state. Also, the displacement direction of “B1” was referenced as a positive bending direction. In this way, “B2” and “B4” displace in a negative direction about “B1” and “B3”. Moreover, the conditions named “After B1”, “After B2”, and “After B3” mean, respectively, that after the first, second, and third consecutive bending, the specimens were bent back up to the initial displacement position of the loading pin, which refers to the location of 0 mm in displacement. Likewise, the “During B4” condition was performed after four consecutive bending procedures. However, “During B4” was not brought back to the initial position; instead, the central pin moved until 1.17 mm during the fourth bending step, which was determined by the earlier failure of the SR700 pearlitic conditions.

Furthermore, the acquisition of the in-situ secondary electron (SE) images was carried out by setting the Kammrath-weiss stage inside the chamber of a THERMO SCIENTIFIC QUATTRO FEG SEM. These SE images were captured in a resolution of 1536 x 1024 pixels. The SEM operation was conducted by using an accelerating voltage of 5 kV, a current of 0.18 nA, and a working distance (WD) of 13.5 mm. More specifically, SE images in low magnification (macro) were obtained in real time throughout the experiment’s progress. Otherwise, SE images in high magnification (micro) were taken on two pre-selected regions that were located around 100 nm below the external surfaces (top and bottom) and aligned to the loading pin. In this regard, the two initially chosen regions were tracked and micro-photographed only at the maximum displacement periods (B0, B1, B2, and B3). Figure 26b shows a schematic sketch of these displacement instants where the red squares represent the captured micro image zones. Additionally, the fourth consecutive TPB step of the investigated conditions (SR400 and SR700) was set to run up to their failure, aiming to evaluate the samples’ resistance under the final accumulated bending state. Additionally, the fractography was obtained by using an accelerating voltage of 20 kV, a current of 3.2 nA, and a WD of 8.5 mm in the THERMO SCIENTIFIC QUATTRO SEM. Finally, the digital image correlation (DIC) technique was applied to the recorded micro SE images. In this regard, the open-source 2D-

DIC MATLAB software (Ncorr v1.2) was adopted to compute the Eulerian strain (e_{yy}). A subset size of 55 pixels and a subset space of 1 pixel were chosen for the DIC proceeding.

Moreover, to assess the lattice strain behavior after each bending procedure of the SR400 and SR700 specimens, an electron backscatter diffraction (EBSD) examination was adopted on an area located around 100 nm from the top surface and aligned to the loading pin. This EBSD investigation region was chosen because the failure started on the top side under tensile stress during the fourth bending test. In this context, the same corresponding EBSD region was evaluated in the unbent condition (B0) and after introducing successive bending steps (After B1, After B2, and After B3). On this point, the fourth bending procedure in both specimen conditions was performed up to the earlier failure of SR700 (at 1.17 mm elongation) to compare them (SR400 and SR700) under the same final bending circumstance. In this setting, Figure 26c depicts an illustrative diagram of the sequence of the EBSD analyses where the red squares are the EBSD evaluated zone position. Additionally, in this case, the interrupted TPB tests were implemented outside the SEM chamber with interruptions for the EBSD investigations. A THERMO SCIENTIFIC APREO FEG-SEM coupled with an EDAX EBSD detector was adopted to perform the EBSD procedures with an operating voltage of 20 kV, a step size of 50 nm, a WD of 8 mm, a sample tilt angle of 70° and a square grid system.

The rectangular samples were mounted in resin for metallographic preparation. For in-situ SE imaging, the longitudinal section of the specimens was grounded (using sandpapers from #240 to #2000 grit), polished (using diamond suspensions of 6, 3, and 1 μm), and etched with 4% nital solution. An indentation reference was inserted in the middle thickness of the samples to ensure that the loading pin was placed in the correct position during the bending cycle transition. Regarding the EBSD analyses, the specimens' longitudinal sections also received the regular metallographic preparation with an additional vibratory polishing (with 0.04 μm colloidal silica), and no etch was applied to them. After sample preparation, the mounting resin was removed via its dissolution in acetone. Finally, the EBSD data were evaluated through TSL OIM software, and their inverse figure pole (IPF) maps were plotted in the z-direction.

3.3 Results and discussion

3.3.1 The characteristics of the starting pearlitic steel before the in-situ bending experiment

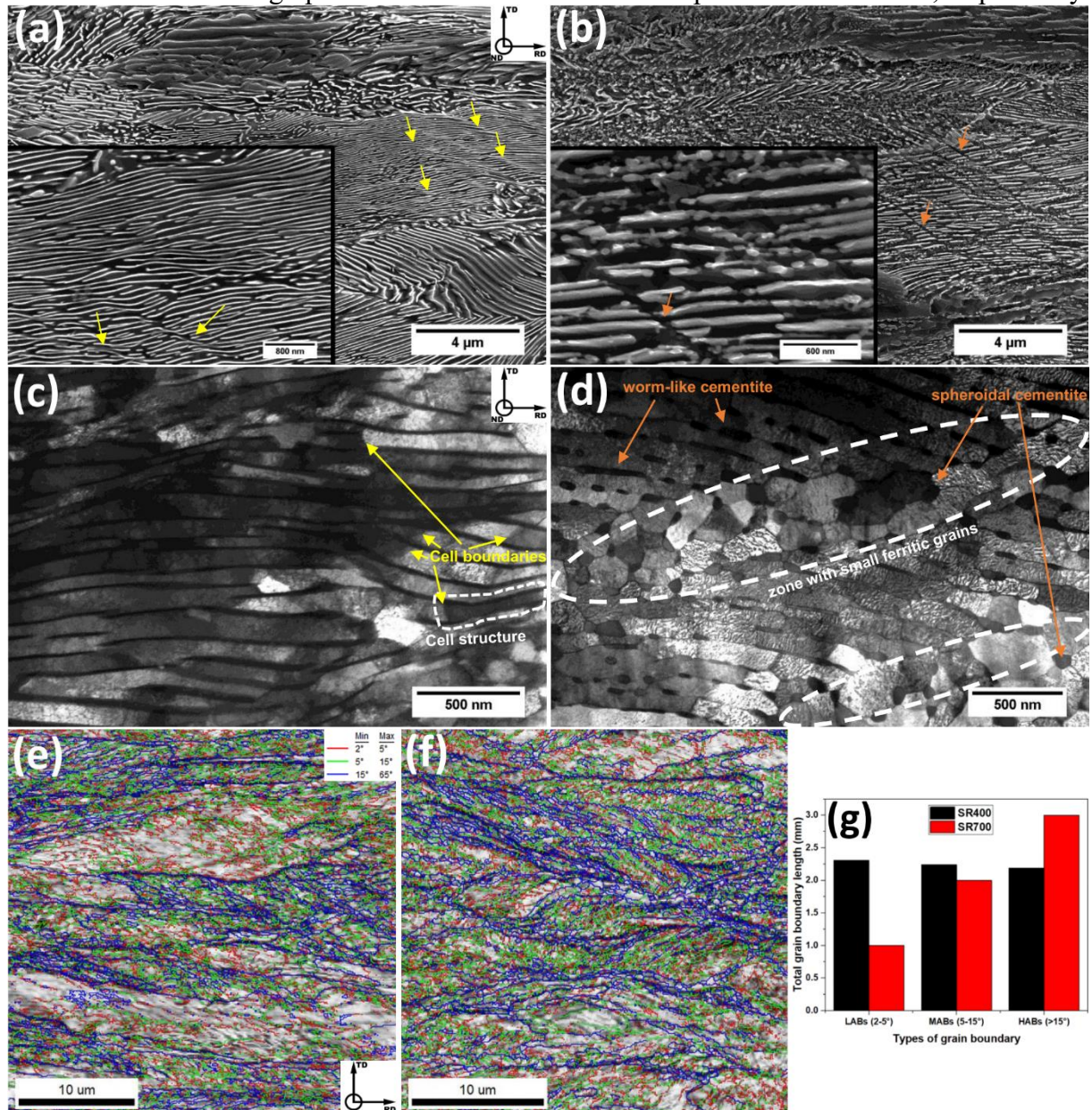
This section aims to describe the main microstructural and mechanical differences between the initial unbent steel states (SR400 and SR700) studied in this work. In addition to

this, the present topic provides some possible θ/α ORs for both starting conditions. In this way, Figure 27 exhibits the SE micrograph, the STEM bright field image, and the map of grain boundary distribution for the SR400 and SR700 specimens. In detail, Figure 27a and 27c show that the SR400's microstructure mainly consists of lamellar pearlitic morphology with its interlamellar spacing around 173.2 (± 37.6) nm. Moreover, it is possible to observe in Figure 27a some narrow tilted regions with bent cementite lamellae (identified by yellow arrows). This locally damaged cementite suggests the presence of shear bands (LEÃO *et al.*, 2023a). Also, it is pointed out (by yellow arrows) in Figure 27c many dark contrast lines connecting two following lamellar cementite. This sort of demarcation is often acknowledged as cell or subgrain boundaries (HUMPHREYS, 2004; AKSENOVA *et al.*, 2022; TUNG *et al.*, 2021). These substructures found in SR400 were likely generated during the prior 65% cold rolling process. Therefore, the resultant SR400 microstructure indicates that the combined low temperature with the short holding time introduced during the stress relief treatment was insufficient to promote significant microstructural changes from the cold deformed state (LEÃO *et al.*, 2023a).

Otherwise, it can be seen in Figure 27b and Figure 27d that the SR700's cementite is comprised of a partially spheroidized structure with worm-like and spheroidal shapes. This fast process of cementite spheroidization, which means in just 60 seconds, may be attributed to the employment of the high temperature (700 °C) in a high defect content microstructure introduced by the prior cold rolling stage (MONTANA *et al.*, 2022; LUPTON; WARRINGTON, 1972). Moreover, the orange arrows in Figure 27b indicate narrow tilted zones where the cementite is disrupted. In addition, the white dashed circle in Figure 27d delimitates an area that contains many small ferritic grains, which are surrounded by coarse spheroidal cementite particles at their grain boundaries and triple junctions. These grains follow an alignment pattern identical to the shear bands. In this context, Furuhashi *et al.* (2005) found small recrystallized ferritic grains in a 70% cold rolled pearlitic steel after a short time thermal treatment at 700 °C. They observed that the new small grains nucleated in the shear bands produced in the prior cold-rolling process. Also, the authors mentioned that the spheroidization of cementite starts earlier in high misorientation regions, such as shear bands of the ferritic matrix, where the cementite is heavily deformed. Likewise, Leão *et al.* (2023a) studied the same processing route of SR700 performed in this work. The authors revealed that small and recrystallized grains were nucleated in shear bands of $\{111\}\langle 112 \rangle$ orientated pearlitic blocks. However, they have detected these recrystallized ferritic grains via the EBSD technique. Therefore, it is reasonable to consider that the high-resolution STEM image can confirm the presence of the small ferritic

grains in the SR700 condition.

Figure 27 – Initial microstructural characteristics of the SR400 and SR700 conditions. Start secondary electron (SE) micrographs obtained via scanning electron microscopy, bright field images acquired via scanning transmission electron microscopy technique, and grain boundary distribution (GBD) maps collected via electron backscattered diffraction analysis, respectively, of (a) (c) (e) SR400 and (b) (d) (f) SR700 specimens. (g) The total length of the grain boundary types measured from the GBD maps of SR400 and SR700 conditions. The yellow and orange arrows in the SE micrographs indicate shear bands and disrupted cementite zones, respectively.



Source: Elaborated by the author.

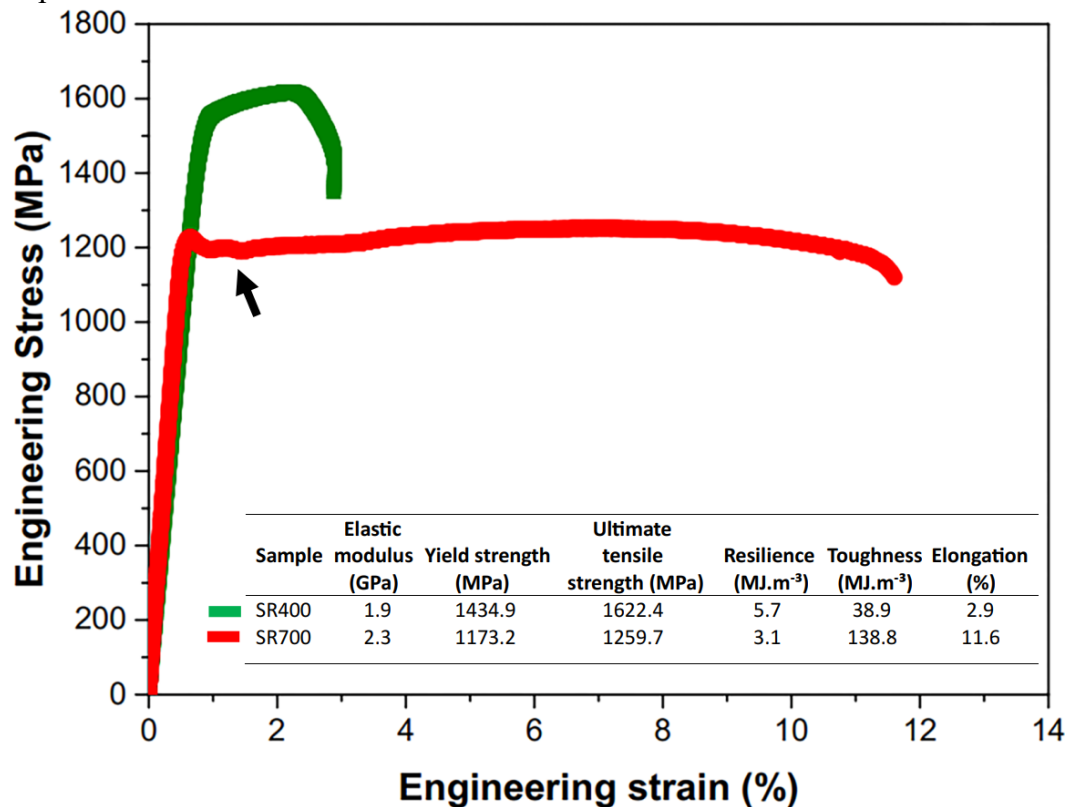
Another point is that the SR700's ferritic matrix (in Figure 27d) seems to have a stripped contrast. This phenomenon may be related to the carbon diffusion from cementite to the ferritic matrix, resulting in the *Cottrell* atmosphere (COTTRELL; BILBY, 1949). This event

becomes possible due to the higher binding energy between the carbon (C) atom and ferrite's dislocation compared to the C in cementite (TAKAHASHI *et al.*, 2012; JOHNSON, 1967). Therefore, the higher temperature (700 °C) during the stress relief treatment introduced in the 65% cold rolled pearlitic condition may have led to the segregation of some C atoms to the dislocations' cores due to the establishment of a new and more stable energetic state (VENTELON *et al.*, 2015). However, this arrangement results in dislocations pinning. Consequently, these held dislocations are barely recovered during the thermal treatment and stay in the ferritic matrix, which explains the regions in the black contrast in Figure 27d. Additionally, Figure 27e and 27f show the maps of grain boundary distribution for SR400 and SR700, while Figure 27g displays the total length of the grain boundary type content on these maps. In this context, low-angle boundaries (LABs) and medium-angle boundaries (MABs) with ranges of local lattice misorientation, respectively, of 2-5° and 5-15°, are related to the presence of geometrically necessary dislocations (GNDs) (WRIGHT *et al.*, 2011). Based on this, it is possible to realize that the high-stress relief temperature (700°) introduced in the SR700 condition resulted in a moderate total length decrease of LABs and MABs. However, there is still a considerable density of LABs and MABs spread throughout the SR700's ferritic matrix, as shown in Figure 27f. Therefore, these retained LABs and MABs may support the pinning effect of carbon on dislocations during the recovery process during the high temperature (700°C) thermal treatment.

Regarding the mechanical properties, Figure 28 depicts the tensile test curves (engineering stress against engineering strain) for the SR400 and SR700 samples. This result indicates that SR400 has superior yield strength, ultimate tensile strength, and resilience, whereas SR700 presents higher values of elongation and toughness. In this way, it is well known from the literature (MISHRA *et al.*, 2020; LI *et al.*, 2011; HOSFORD, 2011) that plastic deformation in ferritic matrix with body-centered cubic crystalline structure occurs based on dislocation's glides, and in pearlitic steels, the cementite lamellae act as barriers against the dislocation motion. Furthermore, the initial work-hardening state (dislocation density) can affect the required critical stress for starting the dislocation flow due to their own restrictive interactions (tangles and pile-ups) (MOURITZ, 2012). In this regard, the combination of the cementite in a lamellar geometry together with a significant degree of defects in the ferritic matrix can significantly make the movement of dislocations difficult. This may explain the higher resistance of SR400 to its permanent deformation and fracture. Conversely, the set of a partially spheroidized cementite shape and a slightly lower length of LABs and MABs retained in the ferritic matrix suggests a more effortless plastic flow. This justifies the more significant

elongation and toughness presented by the SR700 specimen. In addition to this, it is still possible to eliminate the effect of the block size on the mechanical properties of both evaluated pearlitic conditions because the prior hot-rolling and patent treatment were carried out identically.

Figure 28 – Engineering stress-Engineering strain curves obtained from tensile tests of SR400 and SR700 conditions. The black arrow indicates a discontinuous yielding behavior for the SR700 specimen under tensile deformation.



Source: Elaborated by the author.

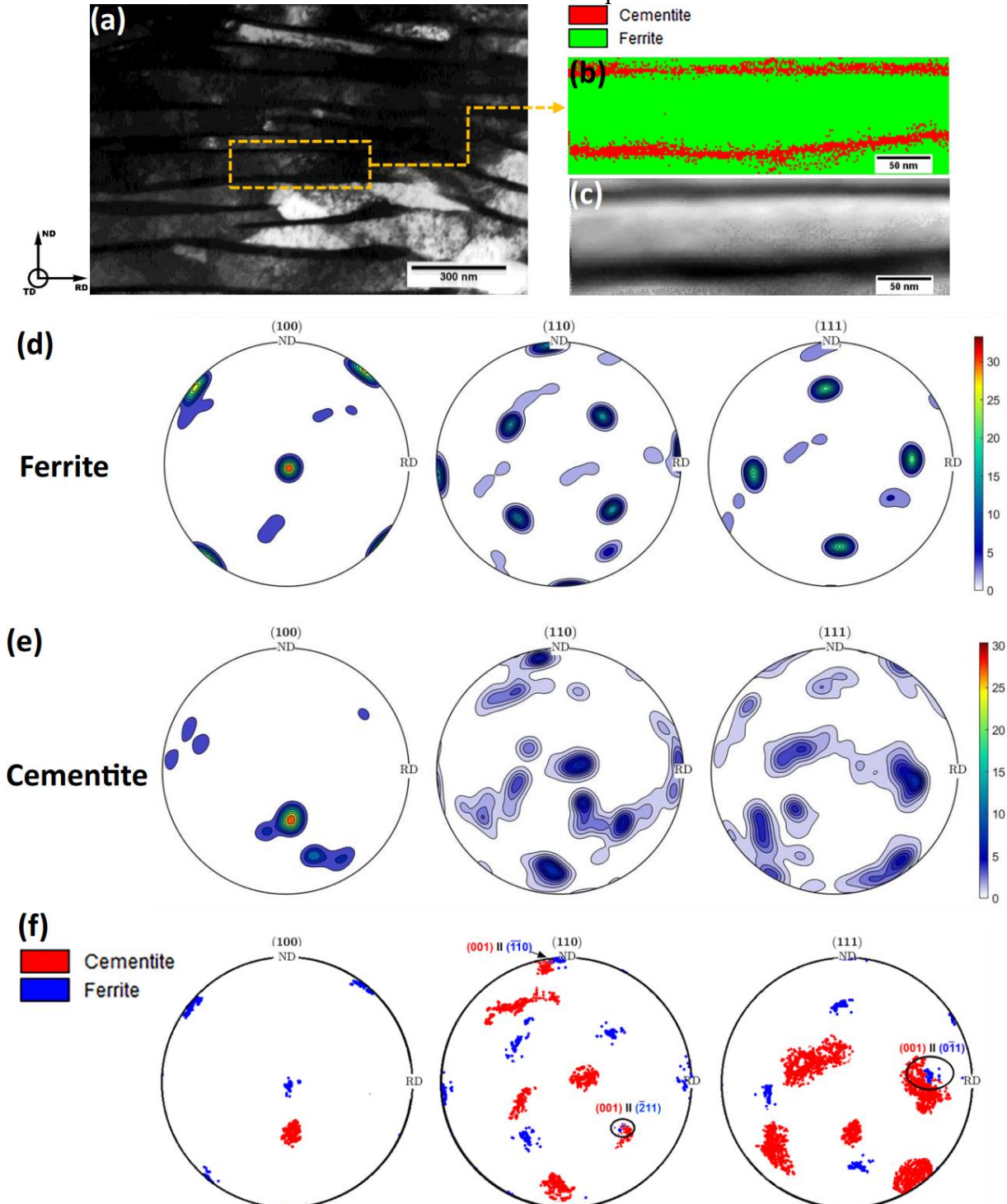
Another aspect to consider is that the elastic modulus of SR400 (1.9 GPa) and SR700 (2.3 GPa) presented a very small divergence. Under this subject, the elastic modulus of metals depends on their lattice constant. Also, dislocation density is one of the significant parameters that can degrade that elastic property (MÜNSTERMANN *et al.*, 2014; YU *et al.*, 2022). For instance, Yu (2009) demonstrated in their study that elastic modulus decreases with the increase of plastic strain. Therefore, the succinct elastic modulus discrepancy observed between SR400 and SR700 may result from their short difference in lattice defects (LABs and MABs). Additionally, a smooth behavior of discontinuous yielding was observed in the tensile-strain curve of the SR700 pearlitic specimen (as pointed out by a black arrow in Figure 28). Many authors (COTTRELL; BILBY, 1949; GENSAMER *et al.*, 2012; ZHENG *et al.*, 2014) reported that the release of locked dislocations in the *Cottrell* atmospheres causes this

phenomenon. This is another indication that the carbon diffused to the dislocation zones during the stress relief treatment of SR700. Furthermore, Figure 29 and Figure 30 reveal the potential θ/α ORs, respectively, for SR400 and SR700 pearlitic specimens acquired from the *t*-EBSD technique. In this case, it is possible to note in Figure 29f that the $(001)_\theta // (\bar{1}\bar{1}0)_\alpha$, $(001)_\theta // (\bar{2}11)_\alpha$, and $(001)_\theta // (0\bar{1}1)_\alpha$ ORs detected in SR400 correspond to the Bagaryatskii OR: $[100]_\theta // [1\bar{1}0]_\alpha$, $[010]_\theta // [111]_\alpha$, $(001)_\theta // (11\bar{2})_\alpha$ (GUZIEWSKI *et al.*, 2016). On the other hand, the $(031)_\theta // (0\bar{1}1)_\alpha$, and $(\bar{1}03)_\theta // (101)_\alpha$ ORs identified in R700 (see Figure 30f) are equivalent to the Isaichev OR: $[010]_\theta // [111]_\alpha$, $(103)_\theta // (01\bar{1})_\alpha$ (GUZIEWSKI *et al.*, 2016). In this context, some scholars (GUZIEWSKI *et al.*, 2016; ZHANG; SHIFLET, 1997) have reported that Isaichev OR was often considered an experimental error of Bagaryatskii OR. In addition to this, they have also mentioned the high difficulty of distinguishing these ORs via conventional electron diffraction techniques. This situation happens because the Bagaryatskii and Isaichev ORs present a few degrees of rotation (less than 4°) about their similar axis $[010]_\theta // [111]_\alpha$. Although this slight angular difference Zhou *et al.* (1992) confirmed that the Bagaryatskii and Isaichev ORs have different cementite habit plans that match the same atomic plan of ferrite. Also, the authors indicated that the development of one of these ORs depends on the initially established interface at the pearlite nucleation onset. In view of this, some hypotheses about the ORs formation have been formulated from the literature. For instance, Dippenaar and Honeycombe (1973) mentioned that the Bagaryatskii OR tends to be satisfied when pearlite nucleates from proeutectoid cementite in hypereutectoid steels. Conversely, the Isaichev OR is related to being settled when pearlites grow from proeutectoid ferrite, which usually happens in hypoeutectoid steels (ZHOU *et al.*, 1992). Moreover, Zhou *et al.* (1992) confirmed in their experiment the presence of Isaichev OR in a hypoeutectoid steel. However, the authors found no Bagaryatskii OR in the hypereutectoid steel.

In this regard, once the stress relief treatment performed in SR400 (at a low temperature and short time) did not provide meaningful microstructural changes, it is possible to consider that this thermal treatment may not have a significant effect on the SR400's θ/α OR. Therefore, it suggests that the Bagaryatskii OR was the θ/α OR in at least one condition before both stress relief treatments in the process route performed in the present research. So, the SR400's Bagaryatskii OR may have been developed in one or a combination of the preceding processes. However, it is quite difficult to determine where this SR400's OR was generated because the track of θ/α OR throughout the evaluated manufacturing route was not conducted in this work. Thus, this case demands additional and accurate investigations. On the other hand,

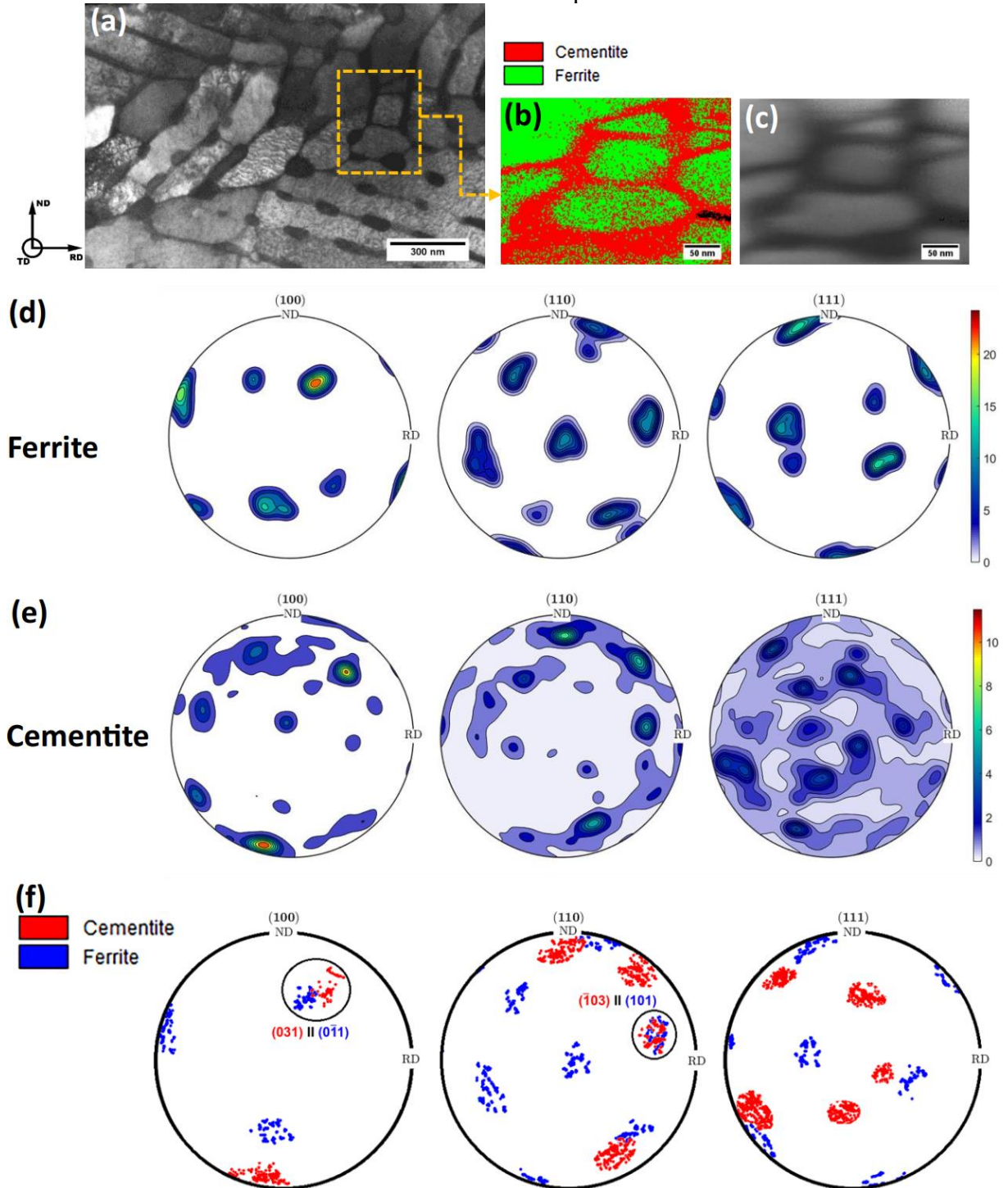
SR700 showed potential Isaichev OR together with a considerable microstructural modification,

Figure 29 – Scanning transmission electron backscattered diffraction (*t*-EBSD) of SR400. (a) Scanning transmission electron microscopy bright field image of SR400 specimen. (b) Phases map of one region where the *t*-EBSD was performed in SR400. (c) Image quality map from the same *t*-EBSD area shown in Figure 6(b). (d) (100), (110), and (111) pole figures of ferrite obtained from five *t*-EBSD maps in SR400. (e) (100), (110) and (111) pole figures of cementite obtained from five *t*-EBSD maps in SR400 (f) Overlapped (100), (110) and (111) pole figures from ferrite and cementite from the SR400's *t*-EBSD maps.



Source: Elaborated by the author.

Figure 30 – Scanning transmission electron backscattered diffraction (*t*-EBSD) of SR700. (a) Scanning transmission electron microscopy bright field image of SR700 specimen. (b) Phases map of one region where the *t*-EBSD was performed in SR700. (c) Image quality map from the same *t*-EBSD area shown in Figure 6(b). (d) (100), (110), and (111) pole figures of ferrite obtained from five *t*-EBSD maps in SR700. (e) (100), (110) and (111) pole figures of cementite obtained from five *t*-EBSD maps in SR700 (f) Overlapped (100), (110) and (111) pole figures of ferrite and cementite from the SR700's *t*-EBSD maps.



Source: Elaborated by the author.

such as the partial cementite spheroidization that was accompanied by the mechanisms of carbon diffusion, coarsening, and decomposition. Based on this information, it is plausible to recognize that a new rearrangement of the cementite atoms (Isaichev OR) at the new cementite/ferrite interfaces produced during the partial cementite spheroidization may have taken place with a slight divergence from the prior lamellar structures (Bagaryatskii OR). Additionally, the mechanisms related to cementite redistribution, or the production of new θ/α interfaces, occurred in an already stabilized ferrite structure during the partial spheroidization process that is analogous to the establishment of Isaichev OR in hypoeutectoid steels.

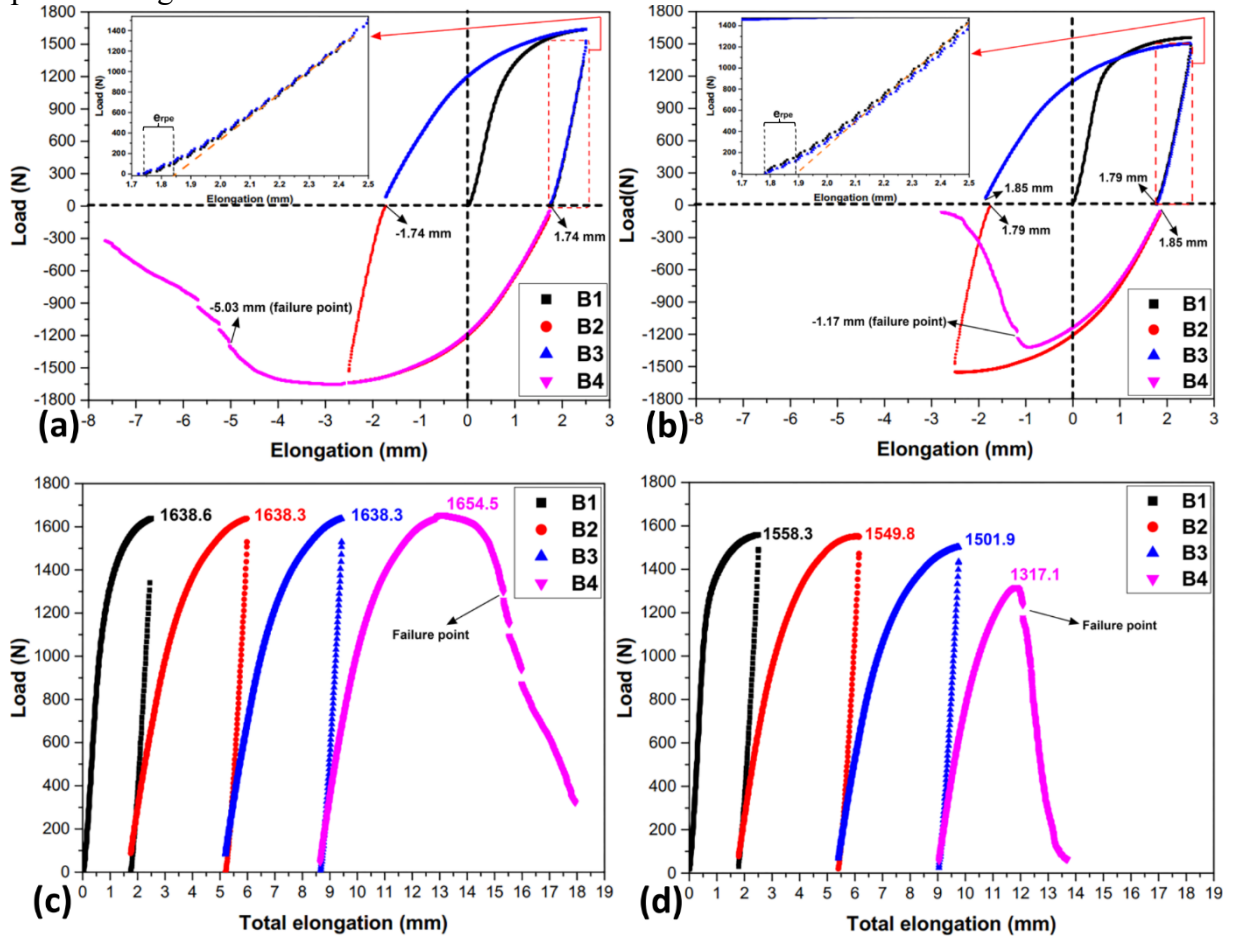
Therefore, the SR400 and SR700 pearlitic steel conditions, which are the starting point of the further in-situ TPB investigations, presented different cementite morphologies, discrepancies in the degree of defects in their ferritic matrixes, distinct mechanical properties, and a potential divergence in their cementite/ferrite ORs.

3.3.2 In-situ three-point bending (TPB) experiments and digital image correlation (DIC)

This topic focuses on designing the relationship between the mechanical performance and microstructural behavior of the SR400 and SR700 specimens during the introduction of four successive in-situ TPB experiments. In this context, Figure 31 provides the load and elongation data acquired during the TPB analyses. More specifically, Figure 31a and Figure 31b exhibit the elongation-load curves plotted in a hysteresis shape for SR400 and SR700, respectively. In this case, the loops represent the cyclic bending alternation between the loading (B1 and B3) and reverse loading (B2 and B4), while the magnitude zero marked by the intersection of the two black dashed lines refers to the initial position of the loading pin. Regarding the elastic zones of the first bending (B1) in Figure 31a and 31b (indicated by black lines), they presented an elastic stiffness of 2.04 kN/mm for SR400 and 2.33 kN/mm for SR700. This result agrees with the elastic trend previously observed in the corresponding tensile test curves (in Figure 28) of SR400 and SR700. Moreover, the episode of working hardening can be noticed in both B1 curves with the progress of the bending deformation. It means that both samples achieved the plastic region at the maximum preset elongation of 2.5 mm. Furthermore, it required a maximum load of 1638.6 N and 1558.3 N, respectively, for bending SR400 and SR700 up to 2.5 mm during B1. This outcome demonstrates again the tougher dislocation mobility in the lamellar pearlitic condition (SR400).

After that, the loading pin was displaced backward to the starting point, and the charge was released. At this moment, an elongation recovery occurred in both investigated

Figure 31 – Elongation-load hysteresis curves obtained during the cyclic in-situ three-point bending (TPB) test for (a) SR400 and (b) SR700 pearlitic steel conditions. Total elongation-load plotted from Elongation-load hysteresis data obtained during the in-situ cyclic TPB experiment for (c) SR400 and (d) SR700 specimens. In Figure 8 (a) and 8 (b), ϵ_{rpe} means reverse plastic elongation.



Source: Elaborated by the author.

pearlitic steel conditions. As a result, the samples accompanied the return of the pin by keeping physical contact between them (loading pin and sample). However, the loading drop during the discharge events described an elastic restoration followed by an inelastic recovery that can be noticed in the amplified zones of Figure 31a and 31b. These magnified areas represent the unloading regions of B1 and B3 (indicated by red dashed rectangles). In this context, the deviation from Hooke's line may be an implication of micro-plastic strain caused by dislocation movement (BENITO *et al.*, 2005). In this regard, it is pointed out from the literature (YU, 2009; CHATTI; FATHALLAH, 2012; NAOFAL *et al.*, 2019; GAU; KINZEL, 2001; YANG *et al.*, 2016; ZHUANG *et al.*, 2019) that this nonlinear return after plastic deformation is usually attributed to the rearrangement of dislocations or damage. After B1, regarding the maximum elongation of 2.5 mm, the total elongation recovered for SR700 (around 0.71 mm) was a bit less pronounced than in SR400 (about 0.76 mm), which may be a consequence of their

respective elastically recovered region that matches their corresponding initial elastic properties. On the other hand, the reverse plastic elongation (e_{rpe}) of the inelastic recovered zone was slightly higher for SR700 (around 0.13 mm) in relation to the e_{rpe} of SR400 (around 0.10 mm). In view of this, it has been reported that the reverse plastic strain has a straight relationship with the intensity of the Bauschinger effect (ZHUANG *et al.*, 2019). The Bauschinger effect is characterized by a softening response of the material under cyclic conditions due to the reverse change in the loading path.

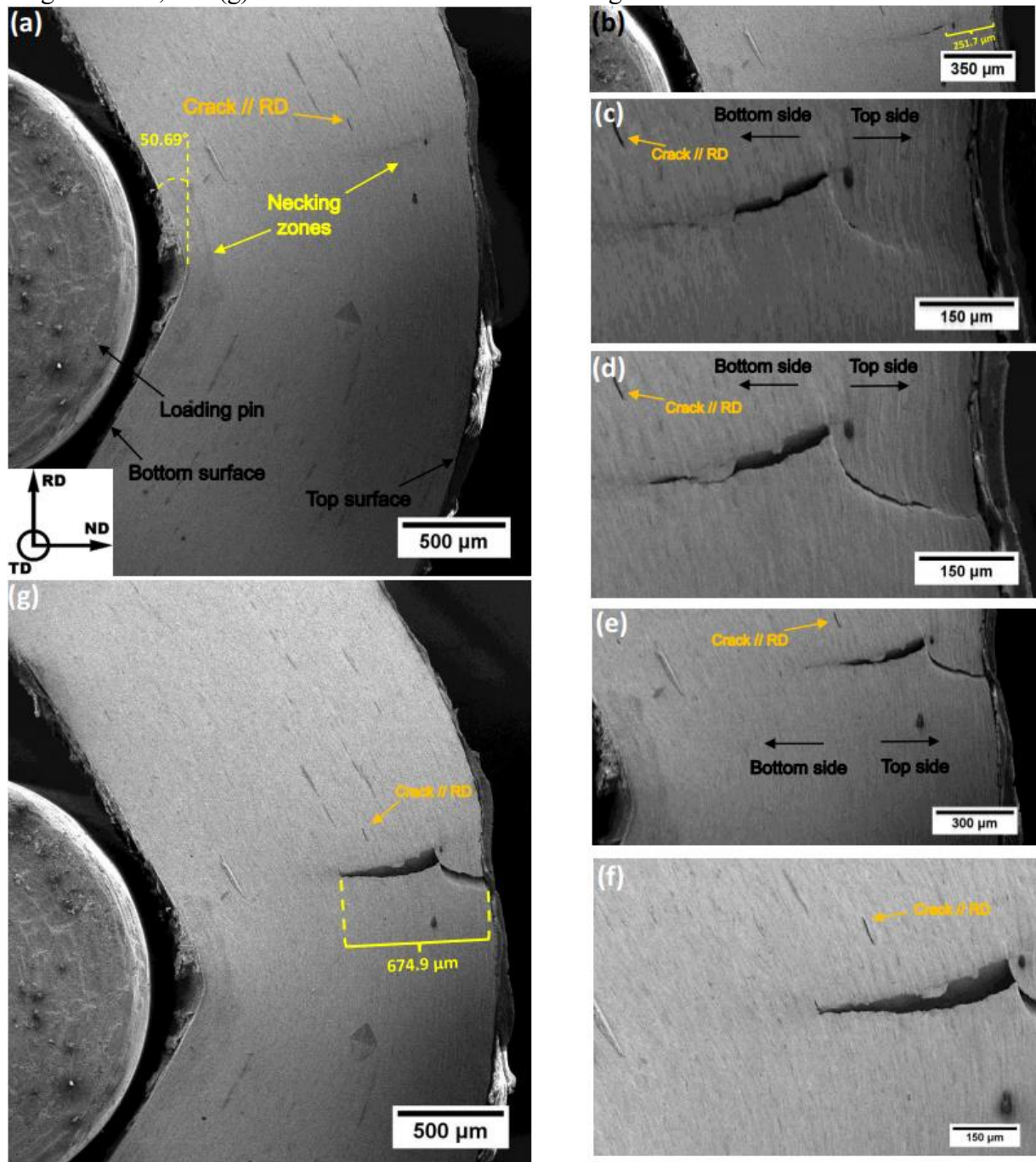
Then, after resetting the rectangular sample's position by putting the surface that was in contact with the loading pin for touching the support pins, the reverse bent (B2) was introduced in the samples just after the B1's unloading stage. In this regard, the initial position of the following bending (B2) in SR400 started around the point where the inelastic recovery effect ceased, which was about 1.74 mm. Conversely, this behavior did not occur for SR700. Instead, the start point of B2 in SR700 was greater (1.85 mm) than the final location (1.79 mm) of its B1 discharge step. This phenomenon was a consequence of the slippage of the SR700 specimen when the loading pin touched its surface. So, it may likely be due to the weaker strength of SR700. Likewise, these transition patterns detected between B1 and B2 were also observed during the further shift steps between the succeeding bending (B2/B3 and B3/B4) for both conditions (SR400 and SR700). Moreover, the resultant elongation-load curves of B2, B3, and B4 developed an almost parabolic behavior that seems to have a small elastic region and a predominant hardening zone. Furthermore, it is possible to realize that the phenomenon of restoration still happened during the other discharge stages (after B2 and B3) in both investigated conditions. In addition, it is interesting to note that SR400 provides a symmetric hysteresis pattern while SR700 does not. In view of this, the loading, in positive values, was plotted against the total elongation undergone by each sample throughout the four-succeeding bending procedures, as shown in Figure 31c for SR400 and Figure 31d for SR700. Based on this, there is a continuous trend of softening (Bauschinger effect) throughout the progress of the four-bending applied in SR700. This event suggests that the SR700 may be susceptible to the rearrangement and annihilation of dislocation, probably due to the inferior number of obstacles available in its microstructure for avoiding dislocation gliding in addition to microstructural heterogeneity (small recrystallized grains). Otherwise, SR400 showed a balanced mechanical performance during the four TPB experiments with a slight hardening in the last bending phase (B4). In this case, the almost constant mechanical behavior of SR400 evidences the high stability of the lamellar pearlitic microstructure that inhibits the plastic flow in the ferritic matrix like a reinforcement grid. These microstructural effects on the bending mechanical performance

of SR400 and SR700 also corroborate with their maximum failing elongation, which was 5.03 mm for SR400 and just 1.17 mm for SR700 during the last bending procedure (B4). In summary, this fact reinforces the higher microstructural stability of SR400 about SR700 for damage onset.

Furthermore, the first nucleated cracks at the failure point of SR400 (at 5.03 mm) and SR700 (at 1.17 mm) could not be recorded during the in situ B4 step. Unfortunately, the initial cracks were nucleated on the outer top surfaces (TD – RD) under a tensile state. This event was also reported by Arola et al. (2021) and Saastamoinen et al. (2017). These authors have observed a similar position of crack nucleation on rectangular steel samples under TPB conditions. After nucleation, the flaws propagated predominantly into the TD direction up to find the samples' lateral section (ND - RD). In this way, the cracks arrived on the ND – RD surface quickly, which means immediately after the specimens' failure. Then, the fracture grew essentially throughout the specimen's thickness (around ND direction). So, Figure 32 and Figure 33 exhibit the macro view of the exact moment the cracks achieved the lateral section (ND - RD) of SR400 and SR700, respectively. The references of the top and bottom surfaces are exhibited in Figure 32b. Regarding the SR400 condition, Figure 32a shows the ND - RD lateral surface at the failure instant (at 5.03 mm). In this regard, it can be noticed two local necking zones pointed out by two yellow arrows in Figure 32a, one in the top area (located almost below the loading pin lateral) and another near the bottom surface (just below the loading pin center). This situation suggests the SR400 condition underwent a severe local plastic deformation before its failure. In addition to this, the deflection angle of SR400 was around 50.69° at the failure point. In this case, the crack reached a location on the lateral section (ND – RD) 251.7 μm below the top surface and near the necking zone (Figure 32b). This fact may result from a structural stress relief in this edge volume as the initial crack propagated into the TD and ND directions. Next, the defect grew, at the same time, into the bottom (compressed region) and the top (area under tensile) sides (Figure 32c, 32d, and 32e).

In this regard, the failure propagation into the top side presented some deviations. In this case, it first propagated into the RD direction, then shifted into a diagonal path until it arrived on the top surface. This phenomenon may occur due to the structural stress relaxation in the edge zone. Based on this, the fracture may lose part of its driving force to grow into this region. Therefore, pearlitic blocks stretched into the RD direction with lamellae cementite may have initially held this crack propagation as a barrier. As a result, it kept the fracture progress in the RD direction until it found a region prone to crack growth, such as shear bands. Many researchers (AROLA *et al.*, 2021; SAASTAMOINEN *et al.*, 2017; BJØRN *et al.*, 2022; MUHAMMAD *et al.*, 2019a) have confirmed the formation of shear bands in regions near the

Figure 32 – Macro scanning electron microscope (SEM) images around the moment the crack achieved the lateral surface (RD - ND) of the SR400 specimen during the fourth successive in-situ three-point bending test: (a) Just before the crack arrived on the lateral surface (RD - ND), (b) At the moment the crack arrives on the lateral surface (RD - ND), (c) Just after the crack arrived on the lateral surface (RD - ND), (d)(e) Different instants of the crack propagation throughout the specimen's thickness (about the ND direction), (f) At the moment the crack stopped to propagate throughout the specimen's thickness (about the ND direction) in higher magnification, and (g) Final lateral crack in a lower magnification.



Source: Elaborated by the author.

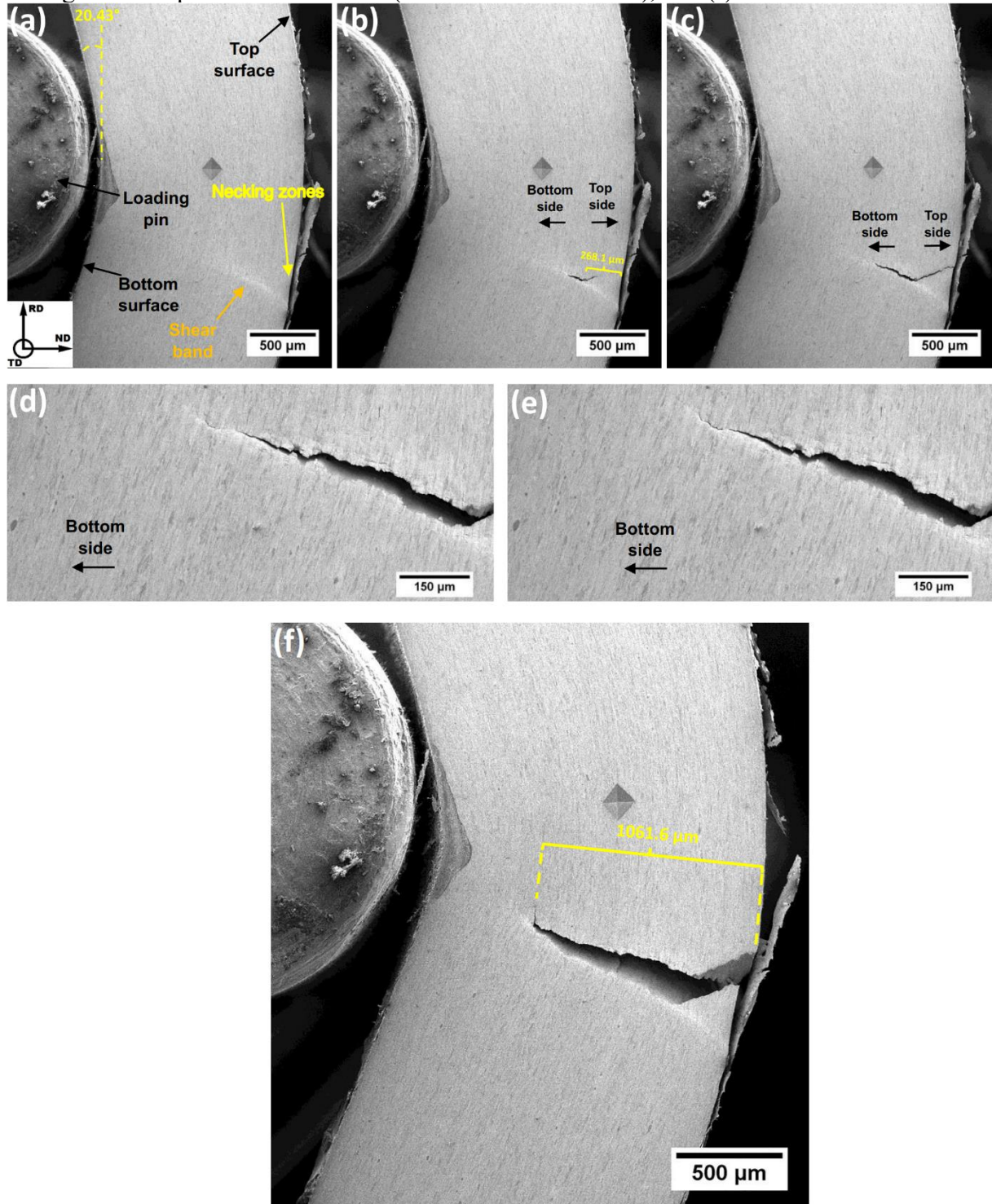
external surface of the specimen under tensile stress during TPB experiments. Then, the failure developed and reached the top surface by following a tilted shear band-like profile. On the other

hand, concerning the behavior of the break going into the bottom side, the fracture tended to be almost perpendicular to the sample's external surfaces (top or bottom). This behavior may be a consequence of the tensile stress components that are arranged around the same direction of the sample's outer surfaces. Thus, the tensile components act by opening the crack. Also, Figure 32f and 32g indicate that the fracture depth from the top surface was 674.9 μm in the SR400 condition. Moreover, it is interesting to note that the final crack tip changed to the RD direction. This fact suggests the effect of the pearlitic blocks stretched into the RD direction that may stabilize the defect propagation. In this setting, it is also possible to observe in Figure 32 (indicated by orange arrows) a stable crack parallel to the RD direction that did not change in length during the failure progress due to its parallel arrangement about the tensile component. Additionally, the neighbor pearlite colonies, with their set of lamellae in divergent directions, may help to inhibit this crack growth.

Concerning the SR700 condition, Figure 33a displays the lateral surface (ND – RD) at the SR700's failure instant. At this moment, it was observed a very small necking zone indicated by a yellow arrow in Figure 33a. Moreover, it can be seen a long shear band as the brighter line near the necking area of SR700 (pointed out by an orange arrow). This shear band was formed in the top region (under tensile stress) and situated in a zone almost below the loading pin lateral. Moreover, the deflection angle at the failure of the SR700 was only 20.47° , which is smaller than in the SR400 condition. In Figure 33b, it is possible to realize that the crack achieved the lateral surface (ND - RD) precisely in the macro shear band zone. Moreover, the break found the SR700's ND - RD lateral, 268.1 μm below the top surface. Likewise, in SR400, this event may also happen due to the structural stress relief in the edge region as the crack grew into the TD and ND directions. After arriving on the SR700's lateral surface, the fracture had the same behavior as in the SR400 condition by spreading at the same time into the bottom and the top sides (Figure 33c, 33d, and 33e). However, the SR700's defect propagated faster than in the SR400 condition. Moreover, the SR700's crack provided a similar profile to the defect found in the SR400 specimen. Otherwise, it was not observed traces of crack growth restriction in the shape of SR700's fracture. Therefore, the exact mechanisms related to the fracture propagation of SR400 may also be considered for the SR700 condition, but with lesser barriers against the crack growth due to SR700's non-lamellar pearlitic architecture. As a result, the total fracture depth in the SR700 specimen was 1061.6 μm from the top surface (Figure 33f).

Based on the bending failure behavior of SR400 and SR700, it is plausible to

Figure 33 – Macro scanning electron microscope (SEM) images at the moment the crack achieved the lateral surface (RD - ND) of the SR700 specimen during the fourth successive in-situ three-point bending test: (a) Just before the crack arrived on the lateral surface (RD - ND), (b) At the moment the crack arrives on the lateral surface (RD - ND), (c) Just after the crack arrived on the lateral surface (RD - ND), (d)(e) Different instants of the crack propagation throughout the specimen's thickness (about the ND direction), and (f) Final lateral crack.



Source: Elaborated by the author.

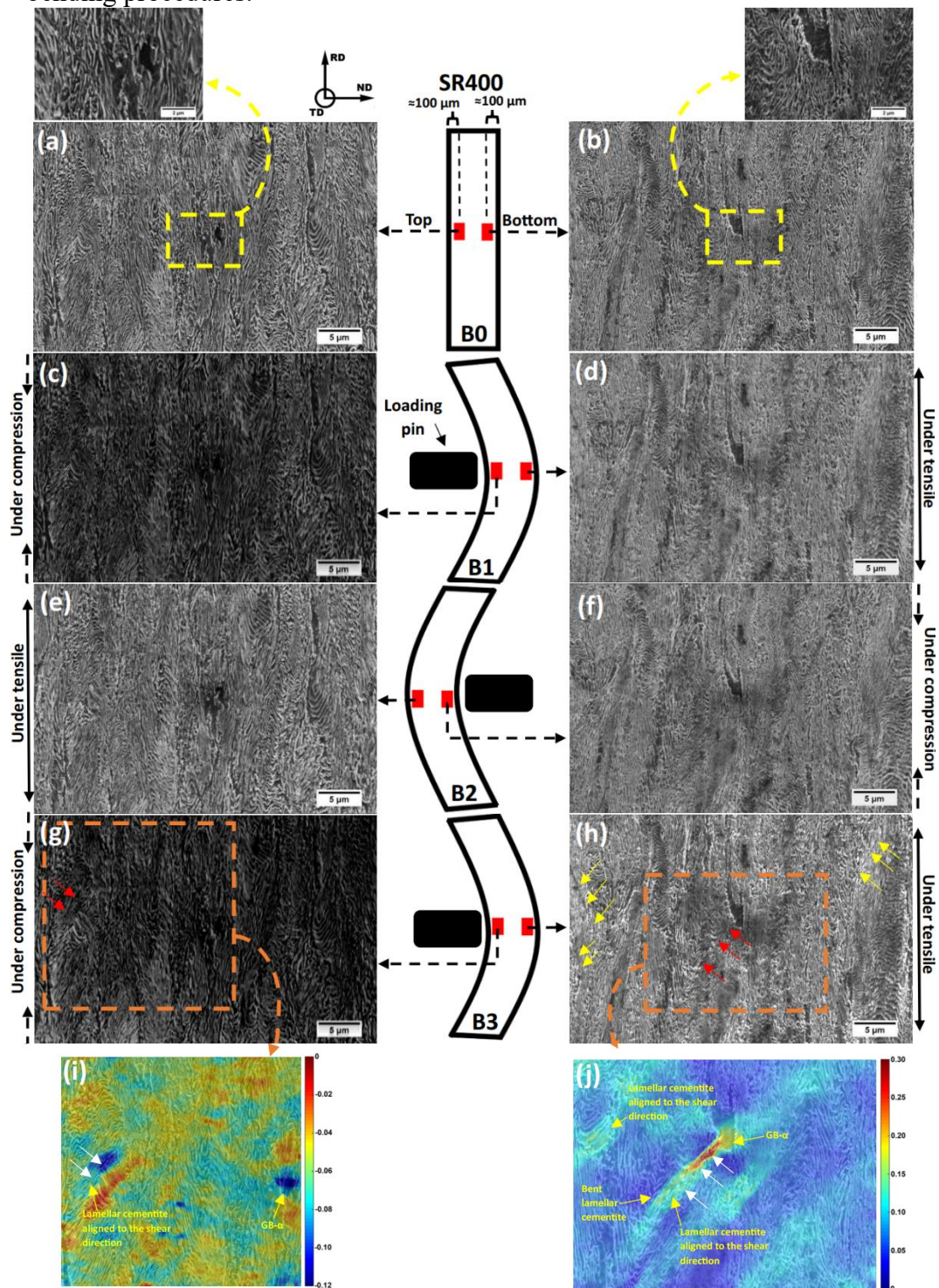
acknowledge that the region in the top zone of the samples located nearly below the lateral of

the loading pin is prone to strain concentration. In this case, it may be a consequence of the combined effect of the moment and stress gradient distributions, respectively, throughout the length and thickness of the specimens (KAPP *et al.*, 2022; SAASTAMOINEN *et al.*, 2017). Moreover, the different features of crack propagation between the SR400 and the SR700 reveal the significant influence of the cementite morphology since both evaluated conditions have the same profiled stretched pearlitic blocks. Furthermore, these observations confirm that the lamellar pearlitic architecture tends to retard the macro shear band development and damage initiation, as mentioned by Kapp *et al.* (2022).

Additionally, Figure 34 and 35 present, respectively, for SR400 and SR700, the microstructural behavior on their top and bottom regions during the first three consecutive TPB experiments. These evaluated zones were situated just below the middle point of the loading pin. In detail, the magnified central regions of Figure 34a, 34b, 35a, and 35b (marked by dashed yellow rectangles) confirm that the cementite morphology before the bending deformation on the top and bottom zones is lamellar for SR400 and partially spheroidized for SR700. Concerning the microstructural behavior between the bending steps, it is difficult to realize how the microstructure was changed in Figure 34 and Figure 35. However, the pearlitic microstructures were, in general, slightly stretched into RD and contracted into ND directions when they were located on the opposite side of the loading pin, for example, on the top regions of B2 (Figure 34e and 35 e) and bottom regions of B1 (Figure 34d and 35d) and B3 (Figure 34h and 35h). On the other hand, the microstructures were elongated in ND and compressed in RD when they were situated on the same side of the loading pin, for instance, on the bottom zones of B2 (Figure 34 (f) and Figure 35f) and top zones of B1 (Figure 34 c and 35c) and B3 (Figure 34g and 35g). Furthermore, it was realized that the microstructures underwent small rotations mainly during the B3, likely due to the deformation mechanism of shear bands. In this context, the detected local regions where a microstructural sliding was noticed (shear bands) are pointed out by yellow and red arrows in Figure 34g, 34h, 35g, and 35h. Again, these slight displacements are tough to be noticed. Based on this, it was included in Figure 34i, 34j, 35i, and 35j, the resultant Eulerian strain (e_{yy}) maps obtained via DIC from the first three subsequent bending procedures. The areas assessed by DIC are marked by dashed orange rectangles in Figure 34g, 34h, 35g, and 35h. In this way, the local strain visualization is easier to be noticed in the e_{yy} maps.

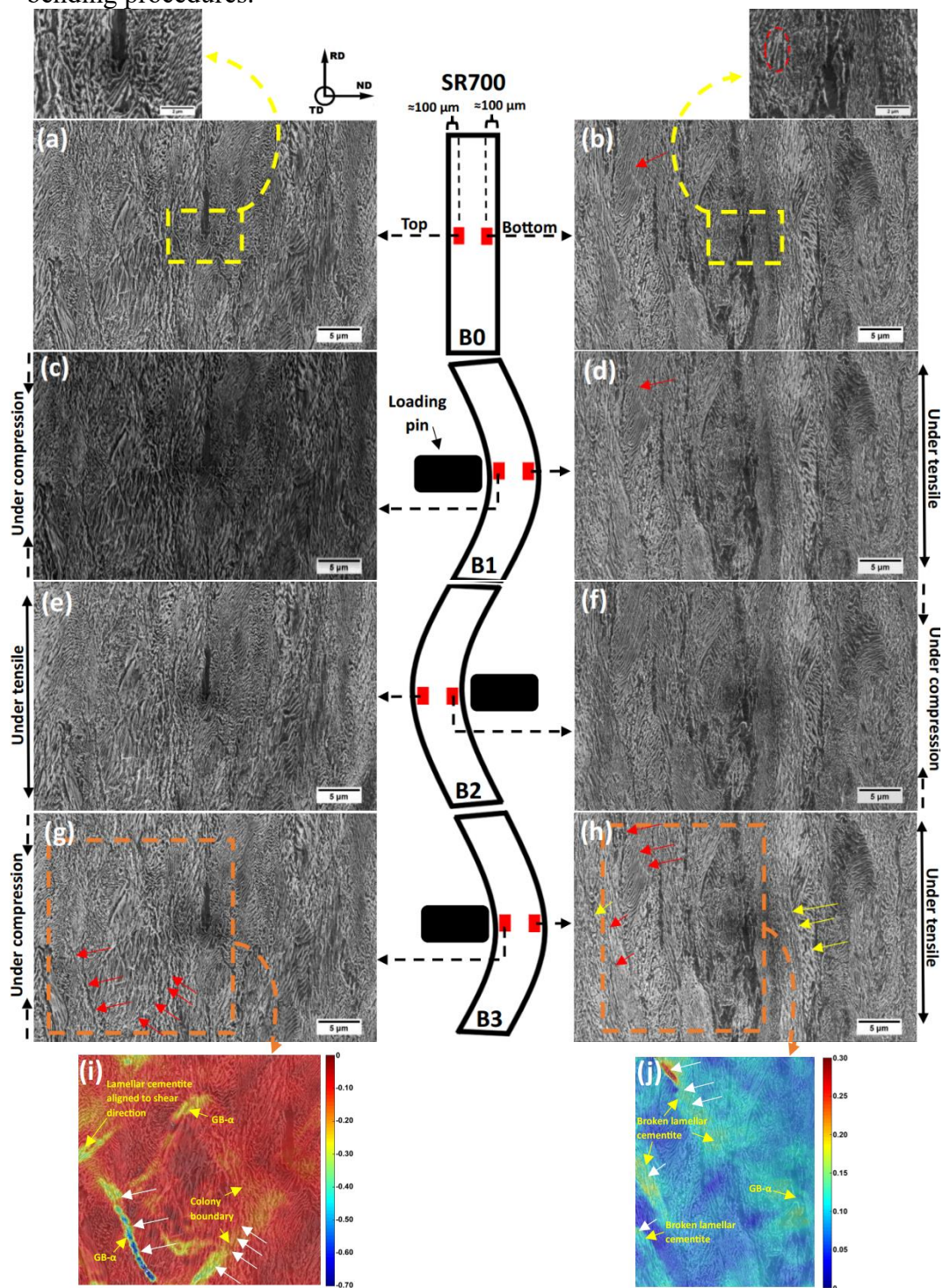
So, it can be seen in Figure 34j and 35j positive strain values due to the tensile stress component lengthening the microstructure in the y-axis. Conversely, the negative strain values in Figure 34i and 35i express the effect of the compressive stress that squeezes the

Figure 34 – High magnification SEM images of SR400 specimen during cyclic in-situ TPB experiment, in the unbent condition (B0) and at the maximum loading pin displacement (2.5 mm) during B1, B2 and B3, respectively, for the two constant evaluated specimen's regions: 10 nm below the (a)(c)(e)(g) top and 10 nm above the (b)(d)(f)(h) bottom. (i) (j) Eulerian strain maps, ϵ_{yy} , obtained via digital image correlation (DIC) from the area marked by orange dashed rectangles in Figure 34(g) and Figure 34(h) during the first three subsequent bending procedures.



Source: Elaborated by the author.

Figure 35 – High magnification SEM images of SR700 specimen during cyclic in-situ TPB experiment, in the unbent condition (B0) and at the maximum loading pin displacement (2.5 mm) during B1, B2 and B3, respectively, for the two constant evaluated specimen's regions: 10 nm below the (a)(c)(e)(g) top and 10 nm above the (b)(d)(f)(h) bottom. (i) (j) Eulerian strain maps, ϵ_{yy} , obtained via digital image correlation (DIC) from the area marked by orange dashed rectangles in Figure 35(g) and Figure 35(h) during the first three subsequent bending procedures.



Source: Elaborated by the author.

microstructure in the y-axis. Moreover, the profile of the higher local strained regions in the e_{yy} maps seems to be concentrated in lines aligned around 45° about the ND. In addition, the higher strained areas shown in the Eulerian strain maps matched the local slid zones (shear bands) found inside the orange rectangles on the SE images. In this scenario, the equivalent regions of shear bands are pointed out by red arrows in the SE images and white arrows in the e_{yy} maps. Thus, these outcomes may confirm the strain concentration inside shear bands and their formation on both border regions (top and bottom) during the third successive bending procedure. More specifically, Figure 34g, 34h, 34i, and 34j display the higher strains (e_{yy}) values in the top (around -0.12) and bottom (in the range of 0.17-0.30) areas of SR400 during B3 were located near or inside ferritic grain boundaries (GB- α), bent lamellar cementite and colonies with lamellar cementite orientation aligned to the shear direction (as indicated by yellow arrows in Figure 34i and 34j).

Regarding SR700, Figure 35h and 35j show, in the bottom zone, that the higher strain values (around 0.17 - 0.30) are mainly concentrated around the broken cementite lamellae. This result suggests that the remaining lamellae of cementite in SR700 are brittle. This phenomenon may result from a partial cementite dissolution into the ferrite matrix. Consequently, holes can be produced throughout the cementite lamellae, as indicated by a red dashed circle in the amplified zone of Figure 35b. In this case, these holes may concentrate stress when the lamellae are submitted to the external effort, and consequently, they are easily broken. In addition, the region with fractured lamellae cementite, situated higher up within Figure 35h, is presented in Figure 35b (indicated by a red arrow) before the bending deformations, which means in the stress-relieved condition at 700 °C. In this stage, some cementite lamellae were already disconnected, while others were still linked but bent. These features are similar to the previously presented shear band zones in Figure 27. Therefore, this region seems to indicate a prior shear band that was formed during the cold rolling process, which then was partially spheroidized (disconnected region) after the stress relief treatment at 700 °C. Next, Figure 35d shows that the bent lamellae are easily fractured (pointed out by a red arrow) under the tensile stress caused by the first bending (B1). This event insinuates again a lamellae cementite embrittlement after the stress relief at 700 °C. Thus, in addition to cementite lamellae fragilization, it is also reasonable to consider that after undergoing a stress relief treatment at a high temperature (700°C), the shear bands introduced during the prior cold rolling process become regions prone to strain concentration under the TPB state.

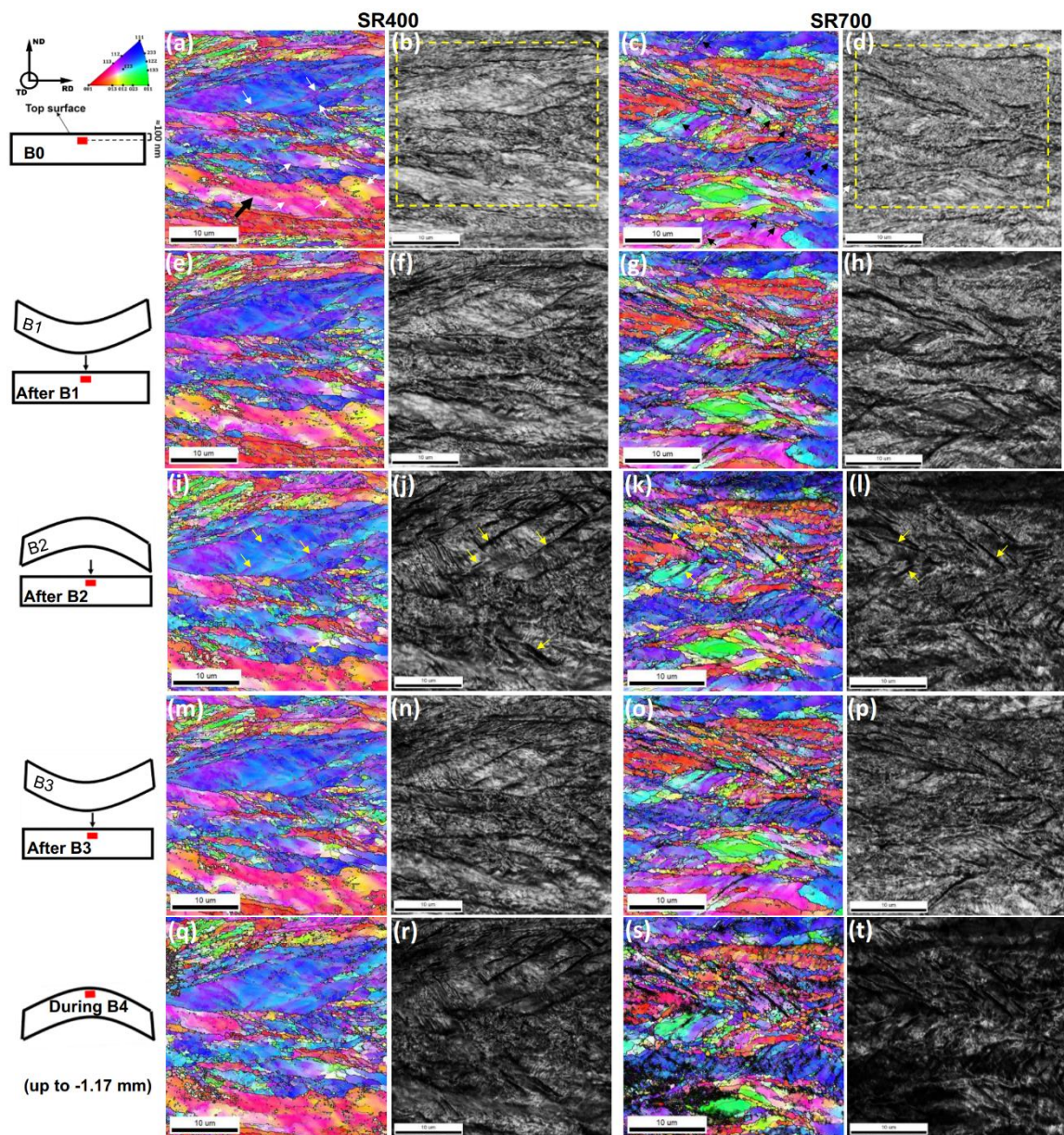
Furthermore, the overall highest value of strain (-0.70) was found in the SR700's top zone during B3 (see Figure 35i). In this case, the strain was concentrated in an elongated

GB- α area aligned about the shearing direction. In view of this, the combination of factors in this specific region together with the microstructure of the SR700 may have contributed to this highest local strain concentration: partially spheroidized and brittle cementite, lack of barriers in the GB- α against dislocation slippage, and easier alignment of the GB- α length for dislocation motion (just like in lamellae of pearlites aligned into the shear direction). Still, in this setting, the boundary of a pearlitic colony also accumulated a considerable degree of strain (around -0.25), as shown in Figure 35i. In this instance, it was seen that this specific pearlitic colony rotated more than its neighborhood area. This may indicate a possible initial phenomenon of decohesion between the pearlitic colony due to the malleable behavior of SR700's microstructure in addition to the anisotropic colonies' deformability (YAJIMA *et al.*, 2021). This event agrees with a recent work (LEÃO *et al.*, 2023b) that identified via an in-situ SEM experiment that pearlitic colony decohesion can occur in soft pearlitic microstructure under shear deformation. In addition, the researchers showed that the fracture propagation passed through the pearlitic colony boundary where decohesion occurred. Therefore, it demonstrated a potential interface for crack nucleation in SR700. Based on these results, it is reasonable to state that the rectangular SR400 specimen has a solid and balanced microstructural behavior on its near border regions during the cyclic bending deformations. Otherwise, SR700 does not.

3.3.3 Electron backscattered (EBSD) in interrupted three-point bending (TPB) experiments

The current section centers attention on providing supplemental information about the behavior of lattice strain after each of the four consecutive bending procedures applied in the two evaluated pearlitic steel conditions. Based on this, the plastic strain investigation was conducted by tracking the diffraction patterns degradation (image quality intensity) from a determined EBSD area evaluated after consecutive interruptions of the TPB cycles (After B1, After B2, After B3, and During B4). In this context, the image quality (IQ) is strongly affected by residual strains in the microstructure, and therefore, indirect interpretations of lattice defects, such as dislocations, can be drawn. In this way, the IQ data can be plotted in a gray contrast map where the higher deformed regions (high dislocation density) are darker and under low intensities of IQ (degraded pattern quality) (WRIGHT *et al.*, 2011).

Figure 36 – Color-coded inverse pole figure (IPF) map and image quality (IQ) map, respectively, in the interrupted TPB condition of: (a)(b) unbent condition (B0), (e)(f) After B1, (i)(j) After B2, (m)(n) After B3, and (q)(r) During B4 for SR400 specimen, and (c)(d) unbent condition (B0), (g)(h) After B1, (k)(l) After B2, (o)(p) After B3, and (s)(t) During B4 for SR700 specimen. The big black and the small white arrows in Figure 36(a) indicate the mostly violet big pearlitic block with many small bad indexed regions and shear bands, respectively. The small black arrows in Figure 36(g) indicate zones with many small ferritic grains. The yellow dashed rectangles in Figure 36(b) and Figure 36(d) show the reference areas for both evaluated specimens, where the image quality intensities were acquired for all TBP steps. The small yellow arrows in Figure 36(i), Figure 36(j), Figure 36(k), and Figure 36(l) indicate the matched regions between the IPF and IQ maps.



Source: Elaborated by the author.

Figure 36 displays the inverse pole figure (IPF) and their IQ maps of SR400 and SR700 conditions obtained from the interrupted bending tests. The analyzed areas were situated

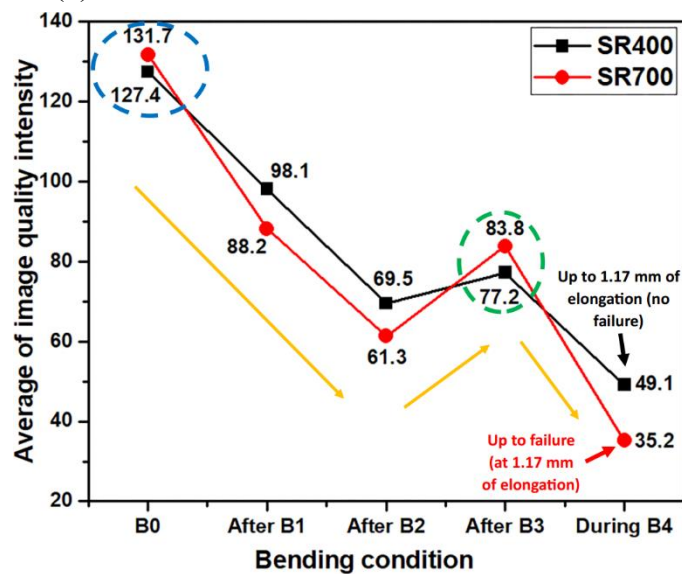
100 nm below the top surface. Moreover, the IQ intensities were extracted and tracked from the invariable areas delimited by yellow dashed rectangles in Figure 36b and 36d. These constant areas were defined because of the physical distortion of the microstructure during the bending deformations. The averages of the IQ intensities for each specimen and bending condition were plotted in Figure 37. Based on this, initially in B0 (stress-relieved condition), it is possible to observe that there is a slight difference between the IQ averages of SR400 (127.4) and SR700 (131.7). In this case, SR700 has a great value or better pattern of IQ than SR400. This IQ divergence agrees with the shorter length of LABs and MABs (lattice imperfections) previously detected in SR700 about the SR400 (see Figure 27). So, After B1 and After B2, the pattern quality tended to decrease in both samples, which means that the amount of lattice defects increased during the two first bending deformations. However, it is interesting to note that the rate of IQ reduction is higher in the SR700 than in the SR400 condition. In this context, the partial spheroidization of cementite increases the total length of the θ/α interfaces in the SR700 specimen, where are the primary sources for dislocation nucleation in pearlitic steels (ZHENG *et al.*, 2021; LI *et al.*, 2011). In addition to the total length of θ/α interfaces, the degree of atomic mismatch at the θ/α interface affects the dislocation generation during plastic deformation (GUZIEWSKI *et al.*, 2016; WANG *et al.*, 2020). However, there is just a slight angular difference between the orientation relationships found in SR400 (Bagaryatskii) and SR700 (Isaichev). Therefore, it demands additional and accurate investigations to prove distinctions between the Bagaryatskii and Isaichev ORs as a source for dislocation nucleation.

Conversely, there was a recovery of the pattern quality for both evaluated specimens (as marked by a green dashed circle in Figure 37) in the After B3 bending condition. This event may be related to the annihilation of dislocations (ZHUANG *et al.*, 2019). In this case, the image quality restoration was higher for SR700 than SR400. This potential higher dislocation annihilation in SR700 may result from its ineffective impediment for dislocation motion due to its non-entirely lamellar cementite morphology. In this case, dislocations have more freedom to move and interact with dislocations in the neighbor ferritic lamellae. Consequently, it may increase the probability of opposite signals dislocations meet and annihilate each other (LI *et al.*, 2011; ZHUANG *et al.*, 2019; LI *et al.*, 2015).

Furthermore, SR700 failed at 1.17 mm during B4. Regarding the interrupted EBSD analyses, this failed elongation (1.17 mm) was taken as a reference and set as the maximum elongation for SR400 during its B4 step. Therefore, this bending standard enables the comparison between SR400 (no failed) and SR700 (failed) under the same bending circumstances (During B4). In view of this, Figure 37 shows that the IQ intensity started to

decrease again during the fourth bending condition (During B4) for both investigated samples. In this instance, SR700 achieved the lowest IQ intensity. This indicates again a greater rate of defect formation in the partially spheroidized pearlitic specimen.

Figure 37 – Average image quality (IQ) intensity vs. bending condition during the interrupted three-point bending operation for SR400 and SR700. The IQ intensities were obtained from the image quality maps in Figure 36 on the delimited areas indicated by yellow dashed rectangles in Figure 36 (b) and Figure 36 (d).



Source: Elaborated by the author.

In general, the IQ maps presented in Figure 37 suggest that the SR700 has a higher capacity for generating and eliminating dislocations than the SR400 specimen concerning cyclic bending events. In this way, it confirms, again, the microstructural stability of SR400. In particular, it was noticed that the improvement of IQ intensity in the two studied specimens happened only in the After B3 bending step. Under this circumstance, the EBSD areas were evaluated after being submitted to a compression stress state. This situation may suggest that the compressed region under cyclic bending deformation is more susceptible to the phenomenon of dislocation annihilation. However, it did not happen in the After B1 conditions, which were also evaluated just after a compressive step. In this case, it may imply that the amount of defect distributed in the ferritic matrix was not enough to enable the occurrence of interaction between dislocations of opposite signals. Therefore, in addition to the compressive state, the different trend between the IQ data of After B1 and After B3 suggests that a minimum amount of lattice defects is required for starting the destructive interaction among opposite

signal dislocations.

Moreover, regarding the mechanical behavior of SR400 and SR700 in Figure 31, it is reasonable to consider that the lamellar pearlitic condition (SR400) is less sensitive to the divergence of lattice defects (IQ intensity). This means that the variation of crystallographic imperfection during B1, B2, and B3 was not enough to cause any strain hardening during the three first successive bending experiments in the SR400 specimen, once more demonstrating its microstructural stability. Otherwise, it is possible to recognize that the Bauschinger effect in the SR700 indicates a significant dependence of the SR700's mechanical performance on its set of lattice irregularities during the cyclic bending procedure. Based on this, SR700 had a short but considerable maximum loading reduction from B1 to B2. At the same time, the IQ average of SR700 also decreased from After B1 to After B2 (see Figure 37). In this scenario, the reverse loading path applied during B2, together with the no effective cementite obstacles in SR700, may have led to the redistribution of dislocations from pill-ups and tangles created during B1. Meanwhile, more dislocations were introduced into the SR700's ferritic matrix during B2 due to the IQ reduction in After B2 condition. As a result, the maximum charge was reduced by only 8.5 N from B1 (1558.3 N) to B2 (1549.8 N). Then, a more significant reduction in the maximum loading (47.9 N) was observed in SR700 from B2 (1549.8 N) to B3 (1501.9 N). In this case, as the IQ average increased from After B2 to After B3, the B3's softening was likely due to the annihilation of dislocations. Finally, the highest abrupt lowering in the loading (184.8 N) was observed in SR700 from B3 (1501.9 N) to B4 (1317.1 N), followed by failure (at 1.17 mm of B4), insinuating a possible microstructural damage influence.

More specifically, the IPF maps, shown in Figure 36, were acquired with a square grid geometry. This grid type usually has a lower resolution for EBSD data indexation in relation to the hexagonal one. So, this can generate some local incorrect index extrapolations (TECHNICAL, 2013). For instance, the large pearlitic block (mostly in violet color) indicated by a big black arrow in Figure 36a has many small grains that may result from the unsuitable indexation. Despite this inconvenience, it can be realized some evidence of shear bands in the SR400 that are pointed out by small white arrows in the IPF map (Figure 36a). Otherwise, the same shear band feature was not identified in the SR700 (Figure 36c). Instead, despite the mentioned problem for EBSD data indexation, many possible small grains were observed in Figure 36c, and small black arrows indicate some of them. In this case, the potential small grains are aligned in profiles similar to shear band patterns identified in Figure 27d, which supports a potential proper indexation of these small-scaled areas.

Moreover, it can be noticed that the darker regions (higher strained area) of the IQ

maps during the progress of the cyclic bending were concentrated mainly in the shear bands and small grains zones, respectively, for the SR400 and SR700 conditions. For example, Figure 36i and 36j exhibited some corresponding regions (marked by yellow arrows) of shear bands and deformed zones for SR400. Likewise, Figure 36k and 36l displayed equivalent regions of small aligned grains and strained areas (also identified by yellow arrows) in SR700. In this context, Zhao et al. (2014) presented in their work, via transmission electron microscopy micrographs, the behavior of dislocations inside a shear band in a lamellar pearlitic steel. Based on this research, the dislocations were piled up at the θ/α interfaces, and consequently, the cementite lamellae were bent due to their plasticity. Then, when the strain was large enough, the cementite lamellae broke, and the flow of dislocations continued into the neighbor ferritic lamella, which allowed the interaction between more dislocations. Finally, the softening mechanism may occur due to the annihilation of dislocations. Therefore, the deformation mechanism via shear band in lamellar pearlitic steel has a long flow path before the occurrence of some mechanical deterioration. This agrees with the solid mechanical efficiency under successive bending deformations of the studied lamellar pearlitic steel (SR400).

Conversely, the replacement of shear bands per small recrystallized grains during the stress relief treatment at 700 °C in the SR700 condition may also cause strain concentration. However, it may bring an earlier mechanical degradation. In view of this, a recent study (LEÃO *et al.*, 2023a) has reported the propagation of macro cracks between small recrystallized grains in pearlitic steel manufactured similarly to the SR700 in the present work. In this case, the authors showed that the zones comprised of small recrystallized grains were prone to microcracks nucleation. Also, the authors mentioned that this event was a consequence of the dissimilar capacity of plastic deformation between the small new grains and the local susceptibility of strain-hardening and pill-ups of dislocation because of the large local density of high-angle boundaries in the zone of small recrystallized grains. In addition to this, Li et al. (2015) have concluded that coarse spheroidized cementite particles at the ferritic grains can negatively affect the ductility of pearlitic steel. Moreover, Maeda et al. (2018) investigated the formation of voids under tensile test in spheroidized carbon steel with cementite particles located at the ferritic grain boundaries and triple junctions. In this case, the researchers observed two types of voids: one nucleated at the interfaces between ferrite and cementite particles, while the other was cracking the cementite particle itself. Therefore, it is plausible to assume that the presence of spheroidized and coarse cementite particles (hard particles) at the ferritic grain boundaries and triple junctions around softer grains with divergences of deformation and strain concentration may cause damage (voids) initiation and finally, the earlier failure of the

component under repeated bending condition. This supports the sooner failure of the SR700 specimen.

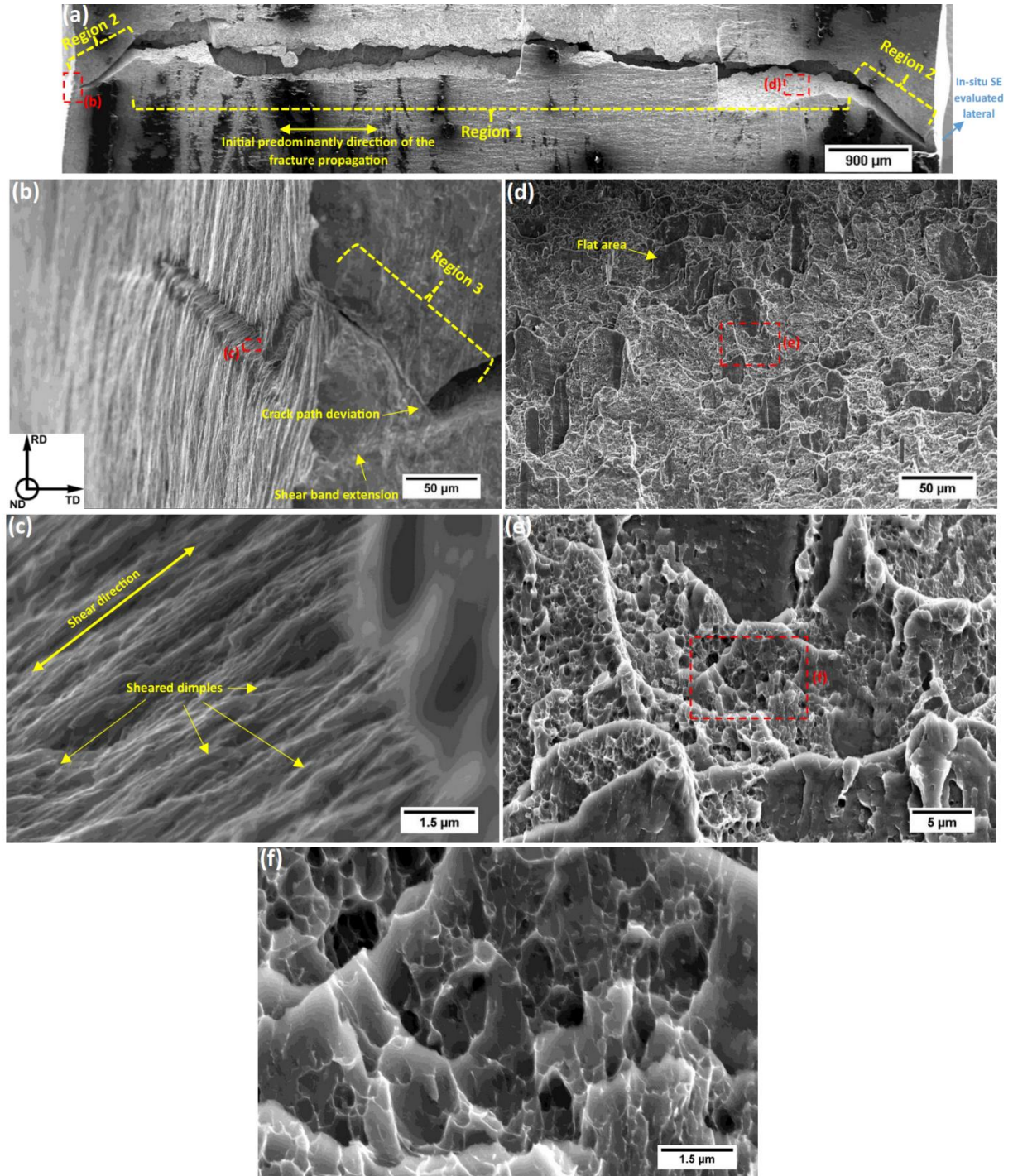
3.3.4 *Fractured surfaces after the in-situ three-point bending (TPB) experiments*

The purpose of the present topic is to explore the fracture surfaces of SR400 (Figure 38) and SR700 (Figure 39) specimens after their failure obtained from the fourth cyclic TPB (B4) experiment. In this way, Figure 38a and 39a exhibited the macro view of the cracks in the outer top surfaces (RD-TD) of SR400 and SR700, respectively. In this regard, the fractures presented an almost U-like shape on the RD-TD surface, with their concavities pointed in opposite directions due to their nucleation on the inverse side of the loading pin. Therefore, the concavities of both fracture conditions were positioned down in Figure 38a and 39a to allow a more accessible visual comparison. These U-like cracks were likely caused by the combined effect of the tensile stress parallel to the RD direction (Region 1) and the formation of shear bands near the edge zones (Region 2).

Regarding Region 1 and Region 2 in Figure 38a and 39a, the tensile stress, parallel to the RD direction, may have highly stretched the RD-TD surface, resulting in an abrupt tearing and nucleation of a large crack that follows an almost linear pattern (Region 1). At this failure instant, the quickly nucleated fracture already has a considerable depth in the TD direction. Then, the defects grow secondarily into the lateral surfaces (RD-ND), accompanying the trend of shear bands (Region 2) that are regularly formed around the edge zones during bending experiments (AROLA *et al.*, 2021; SAASTAMOINEN *et al.*, 2017; BJØRN *et al.*, 2022; MUHAMMAD *et al.*, 2019a). This secondary growth achieved the RD-ND lateral areas 251.7 and 268.1 micrometers below the top outer surface, respectively, for SR400 and SR700, as previously shown in Figure 32b and 32b. This event may relieve the structural stress in the remaining uncracked border zone. Therefore, it is possible to observe in Figure 38b and 39b that the cracks changed their pathway in the edge region (Region 3), forming a final zig-zag profile. In this case, the structural stress relief and the potential presence of X-shear bands (NIU *et al.*, 2022; MUHAMMAD *et al.*, 2019b) in the border area may have induced the crack deviation by tracking a lower energy path-way.

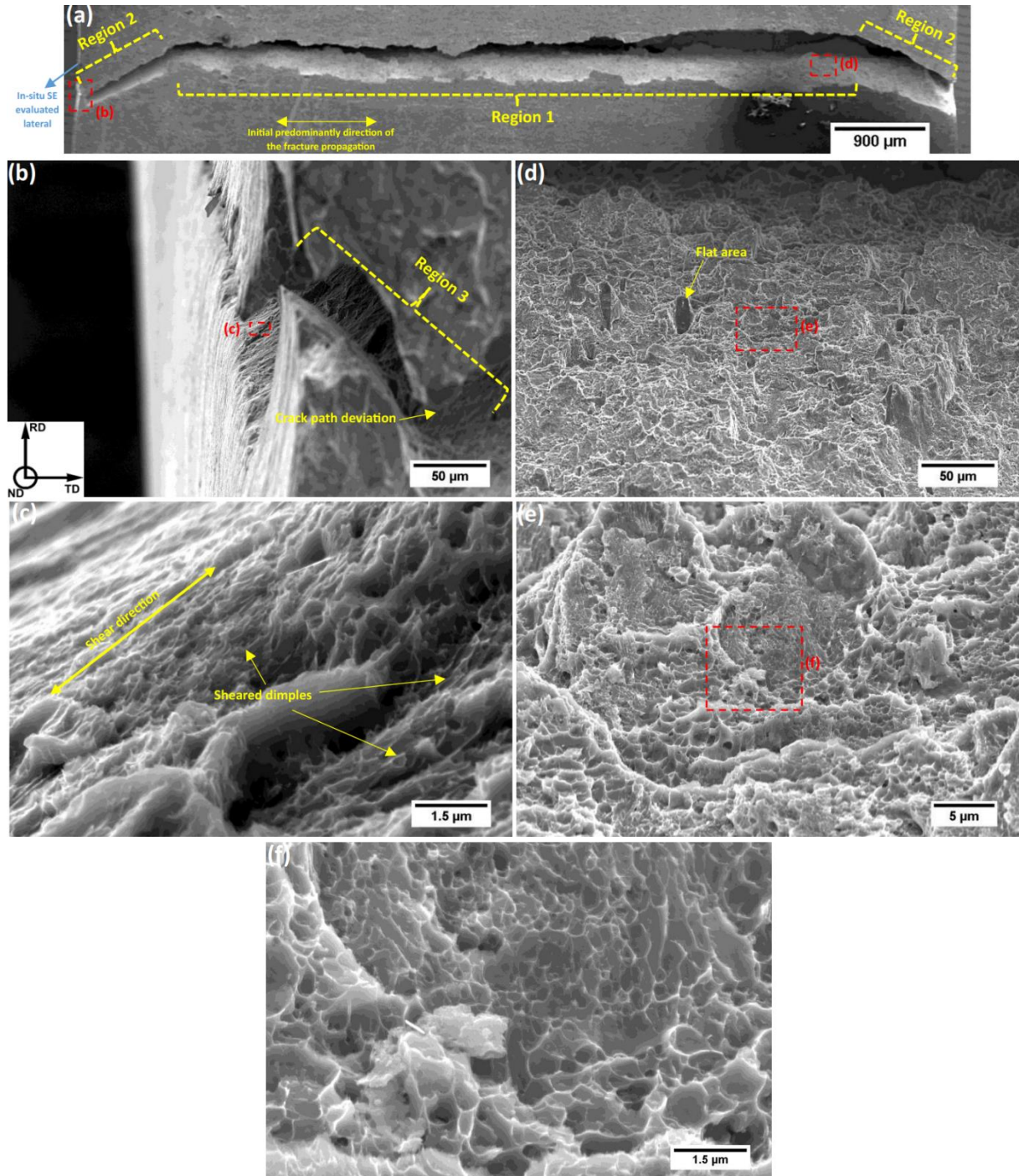
Furthermore, it can be seen that the fracture propagation into the lateral surfaces (ND-RD) was smoother for SR700 in comparison to the SR400 condition. This demonstrates an easier crack path for the SR700 that collaborates with its earlier collapse in relation to the SR400 condition. In view of this, the two evaluated fracture surfaces (Figure 38 and Figure 39)

Figure 38 – Scanning electron microscope (SEM) fractographic observation of the SR400 specimen after the cyclic in-situ three-point bending test. (a) Overview of the SR400 bending fracture on the RD-TD surface. (b) Fracture region in the edge of the SR400 specimen. (c) Fracture surface of the crack in the lateral section (RD-ND). (d)(e)(f) Fracture surface, in different magnifications, of the crack in the RD-TD area.



Source: Elaborated by the author.

Figure 39 – Scanning electron microscope (SEM) fractographic observation of the SR700 specimen after the cyclic in-situ three-point bending test. (a) Overview of the SR700 bending fracture on the RD-TD surface. (b) Fracture region in the edge of the SR700 specimen. (c) Fracture surface of the crack in the lateral section (RD-ND). (d)(e)(f) Fracture surface, in different magnifications, of the crack in the RD-TD area.



Source: Elaborated by the author.

occurred under distinct bending circumstances due to the divergent mechanical properties of the two studied pearlitic steel specimens. For this reason, the SR400's failure happened on the outer top surface under greater curvature and higher loading stress compared to the breakdown

scenario provided by SR700 (see Figure 32 and Figure 33). These particular bending divergences, at the failure instant, can affect the shear influence on the structural collapse and, consequently, the morphological aspect of the fractured surfaces.

Therefore, Figure 38c (for SR400) and Figure 39c (for SR700) exhibit the surfaces of the cracks in the DR-ND macro view, previously shown in Figure 38b and Figure 39b. In this case, the cracks have internal tilted surfaces that follow the orientation of the Region 2 cracks. This implies that from the spot where the breaks achieved the DR-ND areas, the cracks propagated toward the bottom side following the angular profile fracture of Region 2 in the zones close to the DR-ND laterals. Moreover, the dimples in Figure 38c are highly stretched and elongated in a direction almost parallel to the SR400 fracture surface. This indicates an intense plastic deformation caused by the shear process. In this case, the microstructural shearing reduces the stress concentration around the voids initially nucleated under the maximum normal tensile stress. Consequently, this mechanism activates the shear bands among the voids' links that are propagated in the direction of the maximum shear stress. In this way, the voids will be shear-linked up, and a final fractured surface with voids in a parabolic and elongated shape will be obtained (DIETER *et al.*, 1986). Likewise, the dimples on the SR700 surface of Figure 39c were found also sheared, however, to a lesser degree. Based on this, the almost straight failure position of SR700 may minimize the effect of any shear component. Also, this outcome confirms that the Region 2 fracture, near the laterals, is developed with some influence of the shear process.

Furthermore, the surface of Region 1 fracture in the SR400 failure Figure 38d, 38e, and 38f depicted the presence of many dimples together with a considerable amount of local flat zones poor in dimples. In this regard, Li et al. (2014) reported that when local shear plastic deformation is enormous, the maximum normal tensile component cannot produce the initial voids. Instead, the void nucleation is replaced by an accumulated plastic slippage that occurs by activating many shear bands. In this context, the concentrated propagation of the local high-strained bands will promote the forming of an integrated shear fracture surface deficient in dimples. On the other hand, Region 1 of the SR700 fissure provided substantially fewer flat areas (see Figure 39d, Figure 39e, and Figure 39f) than the same region of the SR400 fracture. This contrasting shear influence on the fractured surfaces of SR400 and SR700 may result from the divergent geometric failure position of both specimens. In more detail, Figure 39f and Figure 39f display dimples from Region 1, respectively, in a stretched ellipsoidal morphology into RD direction for SR400 and no elongated round shape for SR700. This indicates that the SR400 dimples underwent a more significant plastic deformation in relation to the SR700 ones.

In general, the micrographs demonstrate that both studied conditions had a ductile failure mode. However, it is plausible to acknowledge that the SR400 holds a higher severe level of plastic deformation before its collapse, while the SR700 does not.

4 RESULTS: INFLUENCE OF HELICAL TORSION ON THE DEFORMATION BEHAVIOR OF TWO PEARLITIC STEEL MICROSTRUCTURES: LAMELLAR AND PARTIALLY SPHEROIDIZED

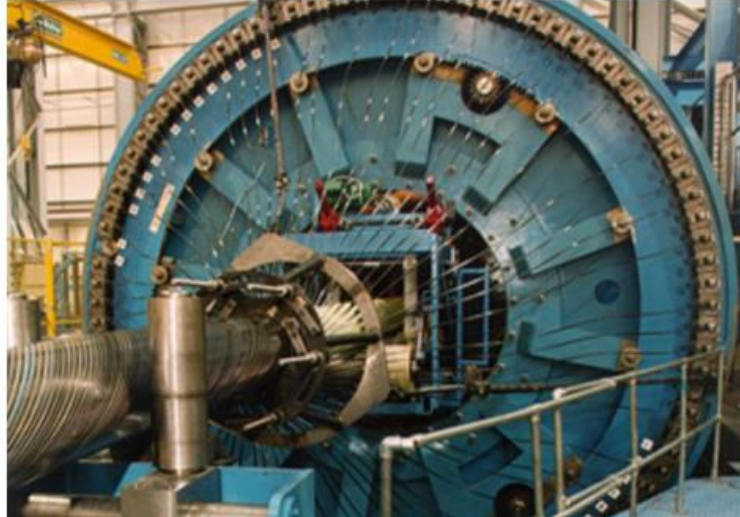
4.1 Review

In the late 1970s, flexible pipes (risers) were the product of an extraordinary development program for oil and gas production systems. These risers were a successful solution for shallow-water and deepwater flowline structures. The risers' cross-section consists of a complex arrangement of several layers: interlocked carcass, internal pressure sheath, pressure armor, tensile armor, and outer thermoplastic sheath (BAI *et al.*, 2012). In particular, the tensile armor layer (TSL) is the key element for allowing the flexible performance of the risers. In view of this, the TSL has the role of supporting all pipe structure weight, resisting axial loadings, and simultaneously providing torsional balance and bending flexibility for the dynamic motion of the pipeline system in service. This set of properties is required due to cyclic bending efforts undergone by the riser structure. This event occurs because the riser structure connects a static foundation at the seabed to a floating vessel on the ocean surface. Therefore, the random vessel movement on the ocean surface can cause riser dynamic motions (FERNANDO *et al.*, 2017).

In detail, the TSL is composed of many rectangular-shaped wires in two (for shallow-water operation) or four (for deepwater operation) cross-wound layers. This set of flat wires are helix twisted around the pipe with an angle between 20 to 60 degrees about the longitudinal pipe axis. In this context, smaller TSL wound angles are used when the riser has a pressure armor layer. Instead, when the pressure armor is not considered in the layered structure, the TSL helical torsion angle is greater and close to 60 degrees to provide a suitable torsion ability, balanced hoop, and axial load strength (RECOMMENDED, 2002). The helical torsion-shaping procedure is performed by a tensile armor machine, as shown in Figure 40. In this context, a series of wire bobbins that have passed through an arduous plastic deformation process (re-winding process) are assembled in the tensile armor machine to supply the required number of wires to completely wrap the pipe. The wires are unwound from the bobbins, and subsequently, they are helically twisted together, wrapping the pipe. This procedure causes significant wire plastic straining by twisting and bending the wire body in different planes. Figure 41 presents a sketch of the complex combination of stress components present throughout the profile of the tensile armor wire (ZHOU *et al.*, 2014; LUKASSEN, 2019). In

this case, the final wrapped wires on the pipe are not unloaded. This means that TSL's wires in risers may be considered to have residual stress (FERNANDO *et al.*, 2017).

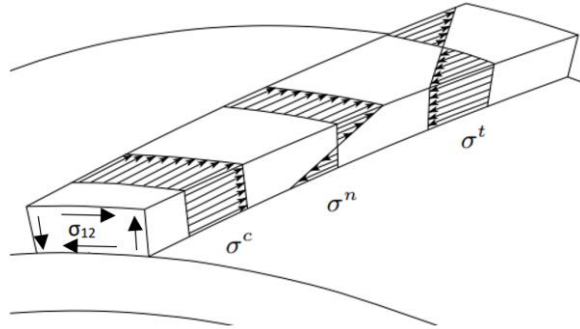
Figure 40 – A tensile armor machine during the manufacturing process of the riser.



Source: Fernando *et al.* (2017).

Furthermore, the flat rectangular wires are made of carbon steel, usually containing pearlitic microstructure. The microconstituent pearlite mostly consists of alternated lamellae (or layers) of ferrite (soft) and cementite (hard) phases. This microstructural setup makes pearlitic steels suitable for wire-related employment due to their excellent balance of strength, torsional ductility, and formability (GUO *et al.*, 2015; DURGAPRASAD *et al.*, 2018; HU *et al.*, 2013; ZHOU *et al.*, 2019). Therefore, several studies extensively reported the performance of pearlitic steels under regular torsion practices (GUO *et al.*, 2015; ZHAO *et al.*, 2014; HU *et al.*, 2013; DURGAPRASAD *et al.*, 2018; ZHOU *et al.*, 2019). However, the deformation behavior of pearlitic steel under helical torsion is scarce in the literature, and this knowledge is crucial for understanding the fatigue performance of this material in the concept of riser application. Based on this, the present chapter aims to briefly evaluate the deformation behavior of two pearlitic steel microstructures (full lamellar and partially spheroidized) under a lab-simulated helical torsion varying the wound angle (0, 20 and 60°) in relation to the longitudinal axis. In this case, with shallow insights, this thesis topic aims to provide the importance of studying helical torsion in pearlitic steels.

Figure 41 – Stress components in tensile armor. Where σ_{12} is a shear stress component, σ^n is a normal bending stress component, σ^c is a frictional stress caused between adjacent layers, and σ^t is a transverse bending stress component.



Source: Zhou (2014) and Lukassen (2019).

4.2 Methodology

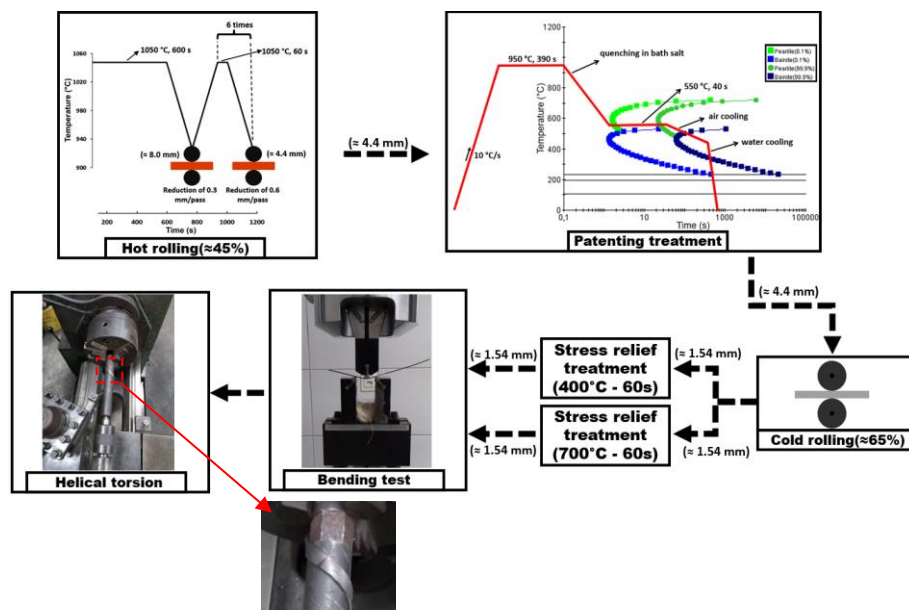
4.2.1 Samples' lab-processing

In this study, a lab-simulated process route based on the manufacture of flat wires for tensile armor application was employed in commercial SAE 1075 pearlitic steel. The chemical composition of the as-received pearlitic steel is presented in Table 1 available in the section 2.2.1. The dimensions of the starting samples were 8 (thickness) x 40 (length) x 50 (width) mm³. The lab-simulated route is schematically illustrated in Figure 42 and was constituted by the following isolated processes: hot rolling, patenting treatment, cold rolling, stress relief treatments, three-point bending, and helical torsion. In view of this, the experimental procedure of the hot rolling, the patenting treatment, and the cold rolling were identically performed, as already detailed described in the section 2.2.1 of Chapter 2. Then, the cold rolled samples were cut into long and narrow strips (rectangular wires) with $\approx 1.6 \times \approx 12.5 \times \approx 60$ (aligned to the rolling direction) mm³. After that, two stress relief treatments with different temperatures (400 °C and 700 °C per 60 seconds) were employed in the $\approx 65\%$ cold rolled and cut specimens.

Next, both stress-relieved pearlitic steel conditions were submitted under a cyclic three-point bending deformation for reproducing the process of re-winding wire into bobbins (HANONGE *et al.*, 2022). The cyclic three-point bending procedure was carried out in a universal testing machine (landmark 370.10 with a maximum load of 100 kN) by using the following parameters: rollers' diameters of 10 mm, distance between support pins of 40 mm,

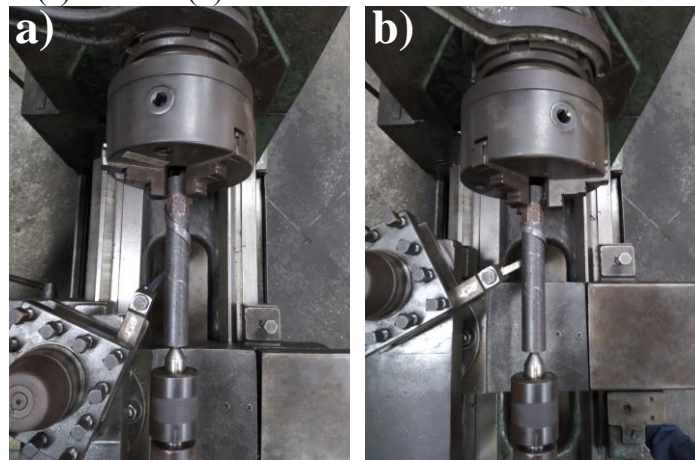
displacement rate of 2 mm/min, and maximum displacement of the loading pin of 4.5 mm. This operation was repeated four times in both stress-relieved specimen conditions by alternating the superior and inferior sample surfaces under contact with the pins. After the bending tests, a blue line mark was inserted on the samples to track where the loading pin touched the surface of these samples. Finally, the bent specimens were helically twisted using a lather machine, as shown in Figure 43. A cylindrical shaft with a diameter of 25 mm was used to guide the helical torsion of the rectangular strips. In this way, one edge of the long strips was pressed between the cylindrical shaft and one chuck’s jaw while the other edge was held by the tool post. The tool post was set up in two specific positions for making two angles, 20 and 60°, between the length of the rectangular wire and the longitudinal axis of the cylindrical shaft (see Figure 43). In this context, after the rectangular wires were settled in the lathe machine, the helical torsions were introduced through the manual rotation of the chuck and, consequently, the cylindrical shaft while the tool post was moved throughout the longitudinal axis direction of the cylindrical shaft and into the opposite orientation of the chuck. Finally, the final specimen conditions designed to be assessed in this study were summarized in Table 3 regarding the temperature of the prior applied stress relief treatment and the angle of the helical torsion.

Figure 42 – Flowchart sketch of the lab-simulated processes employed in pearlitic steel in this study. The numbers in millimeters (mm) mean the samples’ thickness.



Source: Elaborated by the author.

Figure 43 – Schematic view of the helical torsion performed in a lather machine under a wound angle of (a) 20° and (b) 60°.



Source: Elaborated by the author.

Table 3 – Summary of the samples' conditions investigated in this work with their respective abbreviated names.

Sample's name	Stress-relieved temperature (°C)	Helical twisting angle (°)
SH40	400	0
SH42	400	20
SH46	400	60
SH70	700	0
SH72	700	20
SH76	700	60

Source: Elaborated by the author.

4.2.2 Samples' characterization

The blue line marks introduced after the bending procedure were the reference region for the samples' characterization. For example, Figure 42 shows in a magnified zone a blue line mark after the helical torsion operation. Microhardness maps were made from the central location of the cross-section (parallel to the transversal direction) of the helically twisted samples. The cross-sections' surfaces were prepared via a regular metallographic procedure based on grinding (using sandpapers from #240 to #2000 grit) and polishing (using diamond suspensions of 6, 3, and 1 μm). Then, the specimens were slightly etched in 4% Nital solution. Finally, microhardness measurements were accomplished using a Leco AMH43 automatic machine setting a load of 200 gf and a holding time of 10 s. On each sample, the indentations were performed in an 8 (parallel to the sample's thickness) x 37 (parallel to the sample's width) matrix with a spacing of 180 μm between them.

On the other hand, secondary electron (SE) imaging and electron backscattered diffraction (EBSD) were performed on the longitudinal section (parallel to the rolling direction) or the lateral surface of the blue line mark. For SE imaging, the sample's surfaces were prepared via regular grinding, polishing, and etching processes above-mentioned. For crystallographic examinations, the samples were prepared with vibrometer polishing using 0.04 μm colloidal silica for two hours in addition to the grinding and polishing processes. The THERMO SCIENTIFIC APREO field emission gun (FEG) scanning electron microscope (SEM) was adopted to perform microstructural SE image acquisitions and electron backscatter diffraction (EBSD) analyses. An accelerating voltage of 20 kV and a beam current of 1.6 nA were adopted during the SE image acquisition. The EBSD maps were acquired via the EDAX EBSD detector coupled with the APREO SEM. The EBSD analysis was carried out by using an operating voltage of 20 kV, a step size of 50 nm, a working distance of 10 mm, and a sample tilt angle of 70°. The EBSD file evaluations were performed by OIM software. Inverse pole figure (IPF) maps were plotted in the Z-direction (sample's normal direction).

4.3 Results and discussion

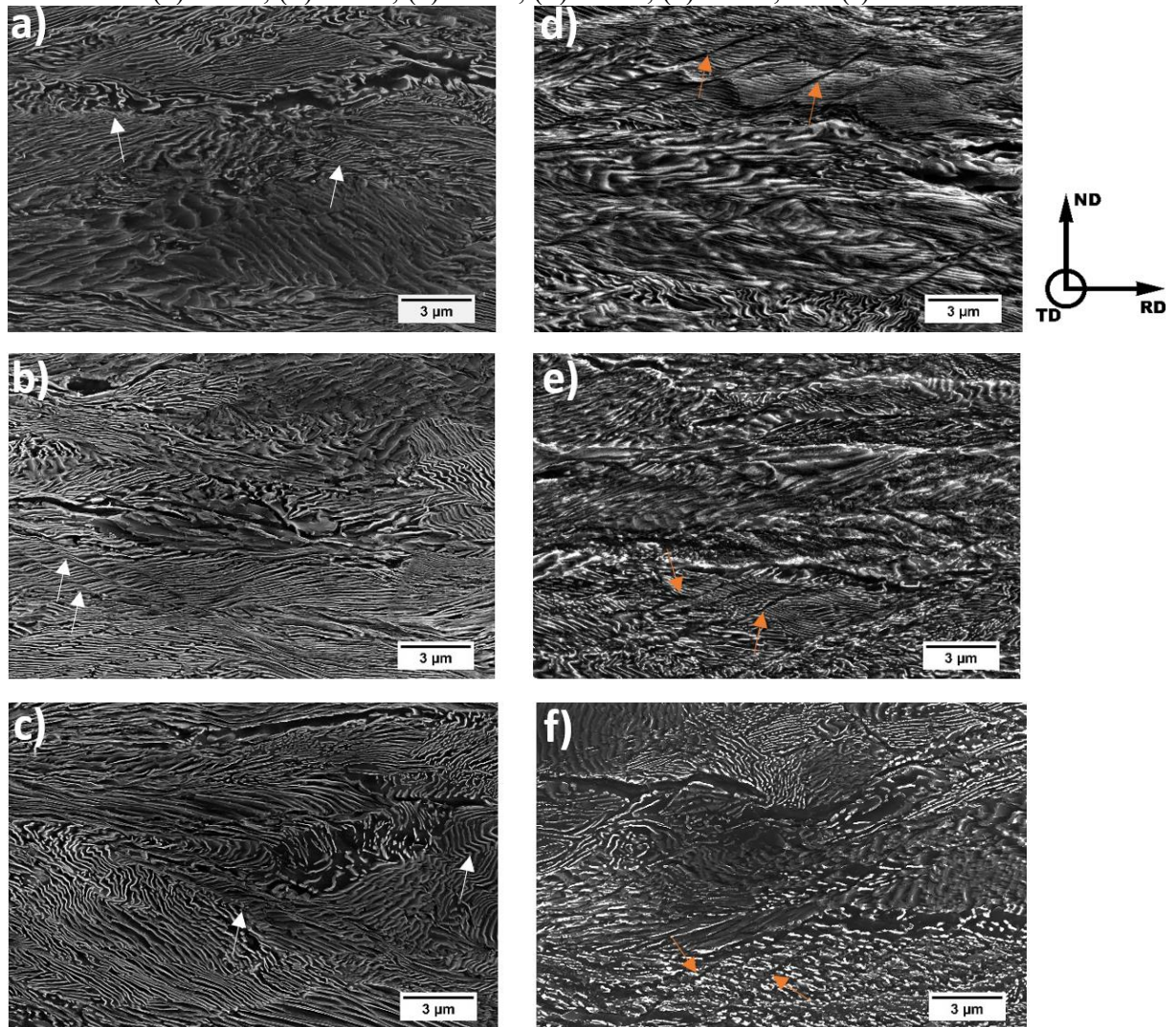
This section focuses on providing basic insights into the behavior of two stress-relieved pearlitic steels (at 400 and 700°C for 60 s) under different helical torsion angles (0, 20, and 60° about the longitudinal direction). In this regard, the 0° helical twisted states refer to the initial stress-relieved conditions, which means that these specimens' conditions were not submitted to bending or torsion loadings. On the other hand, the helically twisted specimens under 20 and 60° angles experienced different combinations of bending and torsion deformations. In particular, it is possible to realize, from Figure 41 and 43, that the smaller angle of 20° may establish a lesser normal bending component but a more pronounced shear and transverse bending components compared to the wire condition wound at 60°. In this way, Figure 44 exhibits the SE micrographs on the longitudinal section (at the middle thickness) of the stress-relieved (untwisted) pearlitic steels (SH40 and SH70) and after their helical torsions under an angle of 20° (SH42 and SH72) and 60° (SH46 and SH76) about the longitudinal direction. In general, microstructural evidence of discrepancies was not noticed among the evaluated helical torsion conditions. For instance, SH40, SH42, and SH46 presented a lamellar pearlitic morphology with bending or partially broken cementite lamellae in the shear band regions (pointed out by white arrows in Figure 44a, 44b and 44c. Whereas SH70, SH72, and SH76 displayed a partially spheroidized pearlite morphology with cementite lamellae broken

in the shear band zones (indicated by yellow arrows in Figure 44d, 44e, and 44f). In this regard, it is pointed out by the literature (LEÃO *et al.*, 2023a; FURUHARA *et al.*, 2005) that these two microstructural patterns are consequences of a combined effect of the 65% cold-rolling deformation and divergent stress relief temperatures. Another point is that the normal bending influence is neutral in the middle thickness of a bent specimen (KAPP *et al.*, 2022). In addition, the shear and the transverse bending deformations undergone by the investigated helically twisted samples may not have been enough to cause critical changes in the microstructure of the evaluated region.

Furthermore, Figure 45 depicts the inverse pole figure (IPF) maps on the longitudinal section (at the middle thickness) of the helically twisted pearlitic steel under 0, 20, and 60° about the longitudinal axis. Based on this, it can be realized that the untwisted (0° helically twisted) pearlitic steel states in Figure 45a (SH40) and Figure 45d (SH70) presented elongated pearlitic blocks due to the previous effect of the cold-rolling deformation. Moreover, the stretched pearlitic structures remained after introducing 20 or 60° helical torsion deformations, as shown in Figure 45b, 45c, 45e, and 45f. However, some pearlitic blocks were bowed for SH42 in Figure 45b and SH72 in Figure 45e. This phenomenon may result from the more significant contribution of the shear and transverse bending components caused by the helical torsion at a small angle (20°). More specifically, this curvature event is more accentuated in the pearlitic blocks of the SH42 specimen than in the SH72. This fact suggests that the lamellar cementite morphology may support a more efficient shear and transverse bending state throughout the sample during the 20° helical torsion in relation to the partially spheroidized microstructure. Moreover, the pearlitic blocks in SH46 (Figure 45c) and SH46 (Figure 45f) specimens are mostly elongated into the rolling direction without significant signs of shear or transverse bending influences. In this case, it is reasonable to assume a predominance of the normal bending component during the 60° helical torsion, as observed in Figure 43b. However, the effect of the bending stresses (tensile and compression) is minimized in the evaluated EBSD areas of SH46 and SH76 because they are located in the neutral bending region of the specimens. Therefore, the pearlitic blocks in the center of SH46 and SH46 tend to be comparable to the untwisted ones (SH40 and SH70).

Additionally, Figure 46 and Figure 47 exhibit the microhardness maps obtained from the cross-section region of stress-relieved samples at 400 and 700 °C under different helical torsion angles (SH40, SH70, SH42, SH72, SH46, and SH76). In this context, microhardness maps can provide valuable evidence about the strain distribution in metals

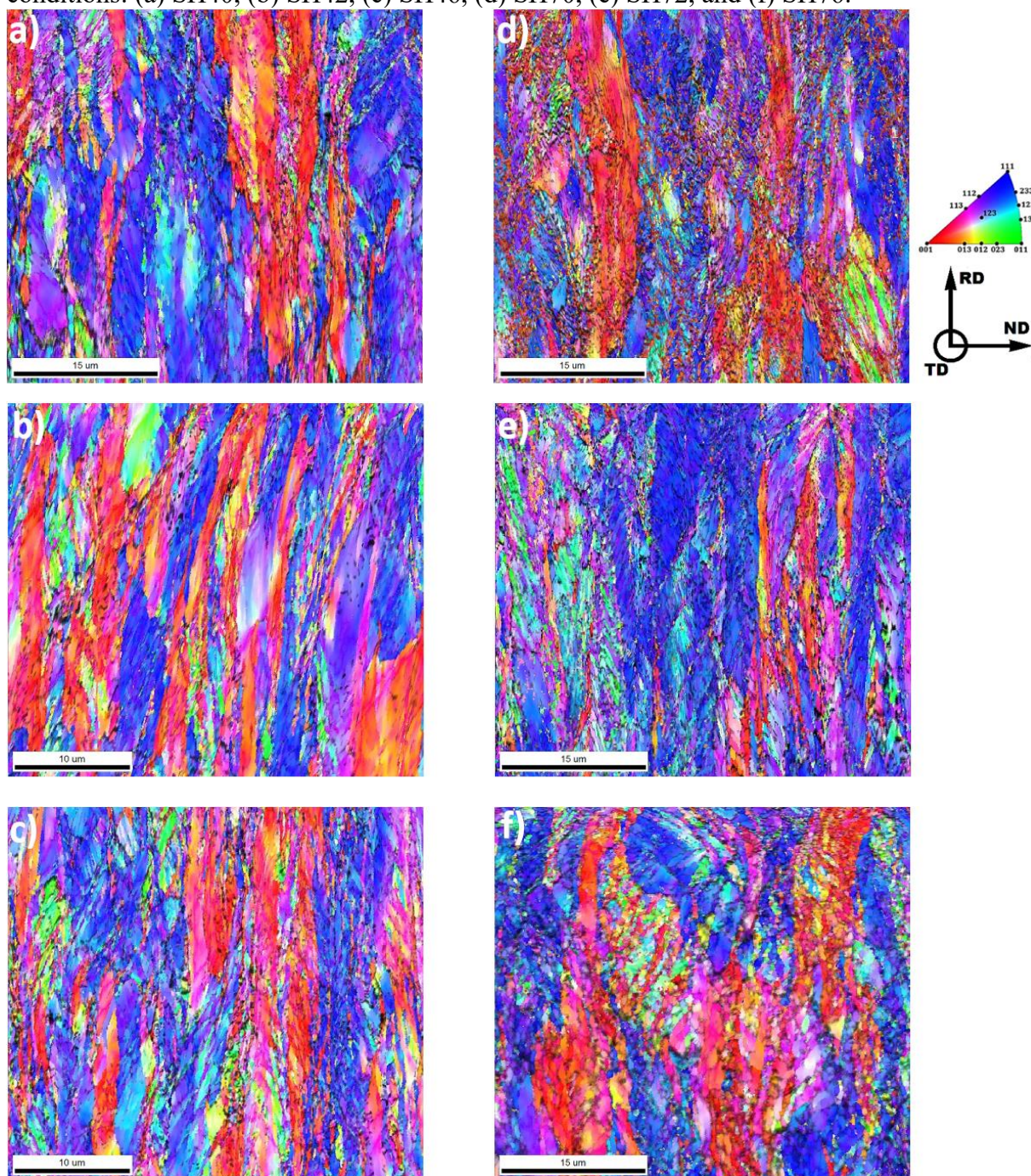
Figure 44 – Secondary electron images on the longitudinal section of the following samples' conditions: (a) SH40, (b) SH42, (c) SH46, (d) SH70, (e) SH72, and (f) SH76.



Source: Elaborated by the author.

during their deformation (ALMEIDA *et al.*, 2020). The untwisted conditions in Figure 46a (SH40) and Figure 47a (SH70) have a predominantly homogeneous microhardness distribution throughout the specimens' cross-section. This result suggests a predominantly uniform deformation gradient in the specimen conditions before employing the helical torsion. However, SH40 has a greater microhardness average (413.2 HV) than the SH70 condition (374.7 HV), as shown in Figure 48. This microhardness divergence indicates a higher resistance of SR40 to deform plastically in relation to SH70. This phenomenon is a consequence of the specimens' microstructural features. Given this, the lamellar cementite architecture in SH40 holds more efficiently the movement of dislocations in the ferritic matrix than the partially spheroidized cementite morphology in SH70 (MISHRA *et al.*, 2020).

Figure 45 – Inverse figure pole maps on the longitudinal section of the following samples' conditions: (a) SH40, (b) SH42, (c) SH46, (d) SH70, (e) SH72, and (f) SH76.

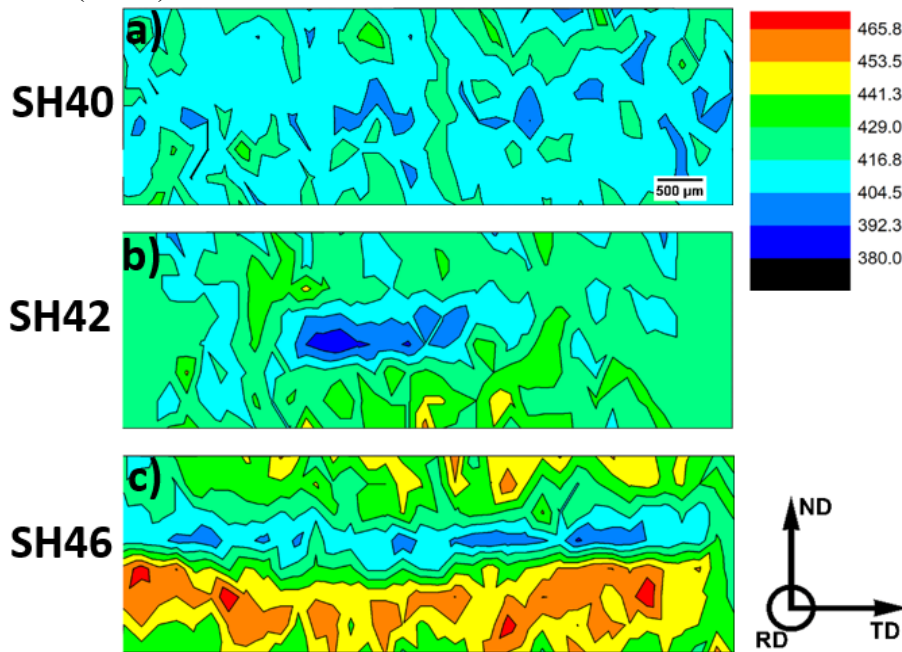


Source: Elaborated by the author.

Furthermore, it is worth noting that inhomogeneous patterns of microhardness distribution were found after applying the helical torsion procedures in SH42 (Figure 46b), SH46 (Figure 46c), SH72 (Figure 47b), and SH76 (Figure 47c). Based on this, SH42 presents in Figure 46b an almost round zone (in blue) containing a small microhardness value (in the range of 380 to 392.3 HV). This region is located in the middle thickness and displaced a little to the left side of the transversal direction. Also, the microhardness values progressively

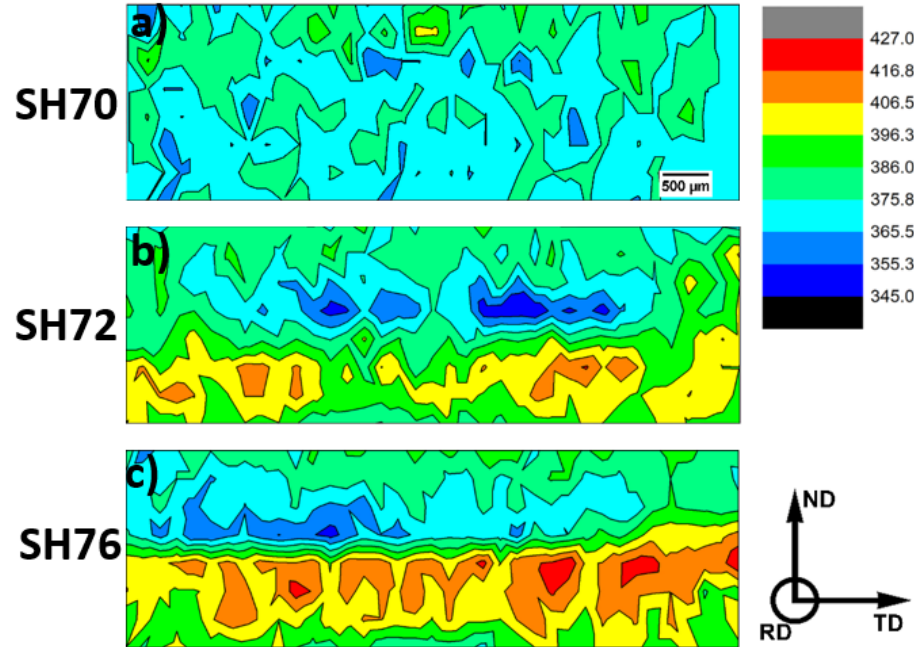
increased from that central area to the outer surfaces. Regarding regular torsion in cylindrical specimens, the shear influence rises from the specimen center to the external radial surfaces (HU *et al.*, 2013). Moreover, the slight deviation from the transverse central location toward the left side of the softer area may indicate a small effect of the transverse bending component. These behaviors suggest a predominant effect of the shear component in the SH42 sample condition and agree with the earlier assumptions about Figure 45b. Likewise, SH72 also presents a central region comprised of low microhardness values. However, in this case, the softer zone (blue) was found in a larger area spread in the transversal direction and situated around the specimen's middle thickness. Also, there is a microhardness gradient but mainly concentrated throughout the thickness of the specimen. However, some specific areas in higher microhardness (in the range of 406.5 to 416.8) were found below the softer zone, likely due to the compressive stresses from the establishment of a normal bending state. Therefore, this suggests a combined influence of normal bending and shear components in SH72.

Figure 46 – Microhardness maps on the cross-section of the stress-relieved specimens at 400°C for 60 seconds followed by helical torsion under a wound angle of (a) 0° (SH40), (b) 20° (SH42), and (c) 60° (SH46).



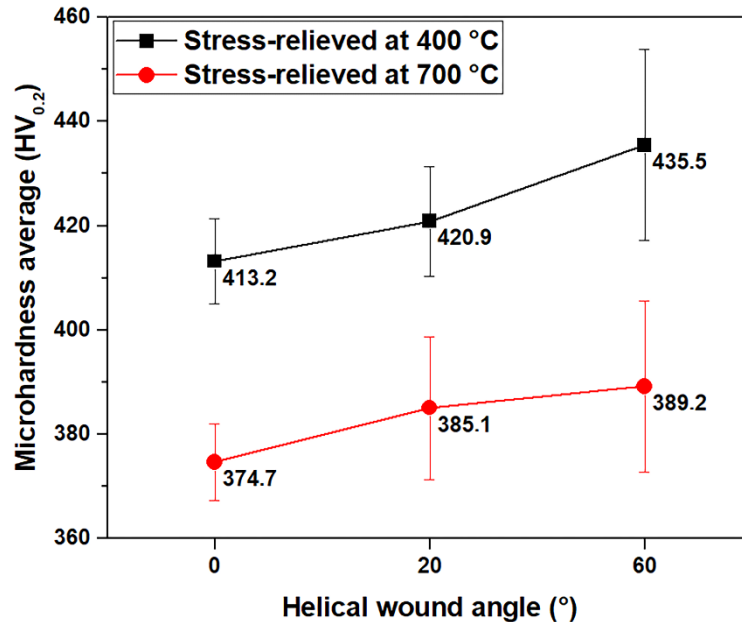
Source: Elaborated by the author.

Figure 47 – Microhardness maps on the cross-section of the stress-relieved specimens at 700°C for 60 seconds followed by helical torsion under a wound angle of (a) 0° (SH70), (b) 20° (SH72), and (c) 60° (SH76).



Source: Elaborated by the author.

Figure 48 – Microhardness average from the microhardness maps in Figure 46 and Figure 47.



Source: Elaborated by the author.

Additionally, it is worth mentioning that a minimal elastic recovery was observed in the stress-relieved specimens at 700 °C (SH72 and SH76) after the unloading of the helical torsion operation. Instead, the SH42 and SH46 exhibited a more pronounced springback. It

means that when the load was released after the helical torsion operation, the SH72 and SH76 samples kept tightened around the shape of the cylindrical shaft guide. Instead, SH42 and SH46 did not. In this regard, the stress-relieved pearlitic steel at 700 °C (SH70, SH72, and SH76) with partially spheroidized cementite morphology showed to have a lower yielding strength in comparison to the stress-relieved pearlitic steel at 400 °C (SH40, SH42, and SH46) with lamellar pearlite arrangement (see Figure 28 in Chapter 3). In this way, the pearlitic steel conditions with partially spheroidized cementite may quickly achieve the plastic state than the lamellar ones. Therefore, the lamellar pearlitic arrangement of SH42 may have worked as a grid holding the specimen mostly under small-scale shear deformation and avoiding the plastic normal bending effect. On the other hand, the less resistant initial microstructure of SH72 was susceptible to both shear and normal bending plastic deformations.

Moreover, it can be seen in Figure 46c and 47c that SH46 and SH76 have a significant microhardness gradient throughout the specimens' thickness, which is confirmed by their larger standard deviation in Figure 48. Based on this, the microhardness values are higher in the area below the samples' middle thickness, moderate in the region above the samples' middle thickness, and smaller in the zone around the samples' middle thickness. This microhardness profile may be caused by the compressive, neutral, and tensile components of the normal bending deformation in the bottom, central, and top areas, respectively. So, the SH46 and SH76 conditions underwent a more significant influence of normal bending strain due to the geometric circumstance of wire wound in the 60° helical torsion, as already indicated in Figure 43b.

Finally, it is possible to observe that the microhardness average rises as the helical wound angle increases (see Figure 48). This suggests that the normal bending event has the predominant influence on hardening lamellar or partially spheroidized pearlitic steels during helical torsion.

5 RESULTS: IN-SITU TENSILE-SHEAR TEST IN SEM AND DIC ANALYSIS OF TWO PEARLITIC STEEL MICROSTRUCTURES: UNDERFORMED-COARSE AND DEFORMED-REFINED

5.1 Review

Pearlitic steel wires are used in a wide range of engineering applications, such as tire cords, springs, suspension bridge cables, etc. The excellent balance of strength, torsional ductility, and formability make pearlitic steel suitable for wire-related employment (GUO *et al.*, 2015; DURGAPRASAD *et al.*, 2018a; HU *et al.*, 2013; ZHOU *et al.*, 2019). In this way, the pearlitic microstructure can be classified by subsets known as blocks (or nodules) and colonies. Categorically, the prior austenitic grain integrates many blocks, and an individual block comprises a few pearlitic colonies. Specifically, a block is a zone determined by an identical ferritic crystallographic orientation. While a lamellar colony, constituted of succeeding lamellae of cementite and ferrite, is defined as a region comprised of cementite lamellae orientated in the same direction (TESHIMA *et al.*, 2017; KOGA *et al.*, 2012). In general, the mechanical properties of pearlitic steel are regulated by its microstructural parameters that include prior austenitic grain size, interlamellar spacing (IS), spatial arrangement of cementite lamellae, cementite structure, block size, etc. Moreover, boundaries of block and colony are regularly mentioned as significant structures during the evaluation of strain distribution in pearlitic microstructures (GUO *et al.*, 2015; DURGAPRASAD *et al.*, 2018a; HU *et al.*, 2013; ZHOU *et al.*, 2019; TESHIMA *et al.*, 2017; KOGA *et al.*, 2012).

In this context, the literature has pointed out (ZHOU *et al.*, 2016; LEWANDOWSKI *et al.*, 1986) that the prior austenitic grain size significantly influences ductility and toughness in pearlitic steels. Additionally, Zhou *et al.* (2016) concluded that the dominant substructure that affects the toughness of pearlitic steels is the pearlitic block size due to its control of the cleavage facet size. These authors also reported that there is a proportional relationship between the sizes of the prior austenitic grains and pearlitic blocks. Moreover, the IS has straight dominance in the strength of pearlitic steels due to the restriction of the dislocation mean free path (MISHRA *et al.*, 2020). However, Hyzak *et al.* (1976) demonstrated that pearlite colony size has a minor effect on cleavage crack propagation. On the other hand, different geometrical setups of pearlite cementite lamellae about the tensile axis can result in inhomogeneous strain throughout the pearlitic microstructure related to crack initiation. More specifically, heterogeneous strain is commonly associated with divergences in the ferritic slip plans'

direction and cementite lamellae's spatial orientation. In this regard, the softer ferrite lamellae undergo earlier yielding compared to the hard cementite plates. This heterogeneous deformation behavior can develop pile-ups of dislocations and stress concentration at the ferrite/cementite (DURGAPRASAD *et al.*, 2018a; TESHIMA *et al.*, 2017). For example, Teshima *et al.* (2017) found a greater local strain in ferrites from colonies with cementite lamellae aligned at 45° about the tensile axis due to its free dislocation motion. In contrast, they noticed cracks initiating in colonies arranged at 90° about the tensile axis. Furthermore, a similar result was found by Durgaprasad *et al.* (2018a). They observed a maximum shear strain in lamellar ferrites of colonies with their cementite lamellae fitted at 45° about the drawing axis. From a macro viewpoint, the lamellar alignment of the colonies can also impact the total shear strain to the failure of a steel wire under torsion. For instance, Durgaprasad *et al.* (2018b) reported that the increase in the number of colonies with lamellae aligned in the range of 60 - 90° about the wire axis reduces the total shear strain to failure. In this regard, shear bands are prone to be developed due to the non-homogeneous strain distribution in pearlitic colonies (GUO *et al.*, 2014; TAGASHIRA *et al.*, 2000). In addition to this, block size and alignment of the colony lamellae can determine the failure mode of the component (TESHIMA *et al.*, 2017; TAKAHASHI *et al.*, 1978b; LI *et al.*, 2019).

Likewise, the cementite lamellae have also their own specific role during the deformation of pearlitic microstructures. Tagashira *et al.* (2000) suggested that the slip mechanism during pearlite deformation can start in ferrite and continue into the cementite lamellae. They also indicated that multiple slip systems might operate in cementite to preserve the compatibility between ferrite/cementite structures. However, it has been pointed out by some investigations (TAGASHIRA *et al.*, 2000; TESHIMA *et al.*, 2017) that the cementite lamellae fracture takes place, once the preferential slip plans of both, cementite and ferrite, are not in cooperation. In view of this, the main slip plan's families available in the ferrite (α) and cementite (θ) phases are $\{110\}_\alpha$, $\{112\}_\alpha$, $\{123\}_\alpha$, $\{100\}_\theta$, $\{010\}_\theta$, $\{001\}_\theta$, $\{110\}_\theta$, and $\{210\}_\theta$ (NINE, 1972; INOUE *et al.*, 1976). In addition, Zhou *et al.* (2019) noted that cold-deformed cementite lamellae are dominantly composed of an amorphous phase lattice structure. The authors also indicate a possible absorption of dislocations by the amorphous cementite lamellae which can reduce strain and stress concentrations at the ferrite/cementite interface. Otherwise, the author reported that cementite lamellae consist mainly of nanocrystalline grains after some thermal treatments acted like barriers against dislocation movement, which can promote stress accumulation. Regarding the aforementioned microstructural heterogeneity behaviors, SEM images together with the digital image correlation (DIC) technique are powerful tools widely

used to detect inhomogeneous strains throughout microstructures under deformation (VERMEIJ; HOEFNAGELS, 2022; ISAVAND; ASSEMPOUR, 2021; YAJIMA *et al.*, 2021).

In addition to tensile efforts, pearlitic steel wires must maintain a suitable level of shear resistance during their wire-related applications (CORDIER-ROBERT *et al.*, 2008). Therefore, torsion tests are extensively used to measure the shear strength and strain of pearlitic wires (ZHOU *et al.*, 2019; CORDIER-ROBERT *et al.*, 2008; FANG *et al.*, 2015). However, it is pretty difficult to assess the behavior of pearlite colonies during the progress of torsion tests due to the gradient of shear components along the circumferential direction of the wire (HU *et al.*, 2013). For instance, Guo *et al.* (2015) proved the establishment of a non-uniform shear strain gradient in the radial wire section as a result of the specimen geometry during the torsion test. In detail, they observed a heterogenous behavior of microtexture near the external wire surface and of macro texture throughout the entire radial length. With this particular context, the failure mechanisms related to the pearlitic microstructure are usually theoretically estimated after the torsion test due to the difficulties associated with the regular aforementioned test. To overcome these obstacles, the present research brings a novelty manner to evaluating the behavior of pearlite under shear deformation via a tensile-shear (TS) test. The TS test can provide a more stable shear state and easier access to the pearlite surface under shear. This experiment was conducted via in-situ observations in scanning electron microscopy (SEM) in cooperation to the DIC technique to verify the strain heterogeneities in two types of pearlitic steel microstructure: undeformed-coarse and deformed-refined.

5.2 Methodology

5.2.1 Samples processing

Commercial SAE 1075 pearlitic steel was used in this study. The chemical composition of the as-received steel is available in Table 1 (available in the section 2.21) and it was lab-processed targeting two conditions of pearlitic microstructure: undeformed-coarse (UC) and deformed-refined (DR). In this regard, the UC microstructure was achieved by applying in the starting sample (thickness 8 mm x length 40 mm x width 50 mm) a thermal treatment performed at 850 °C for 300 s followed by a slow cooling rate of 1 °C/min up to room temperature in an Argon gas-controlled atmosphere tube furnace. A representative diagram of UC's thermal treatment is exhibited in Figure 49a. On the other hand, the DR condition was obtained through five lab-simulated processes based on the manufacture of rectangular wires for tensile armor application in flexible pipelines (LEÃO *et al.*, 2023a). This lab-process route

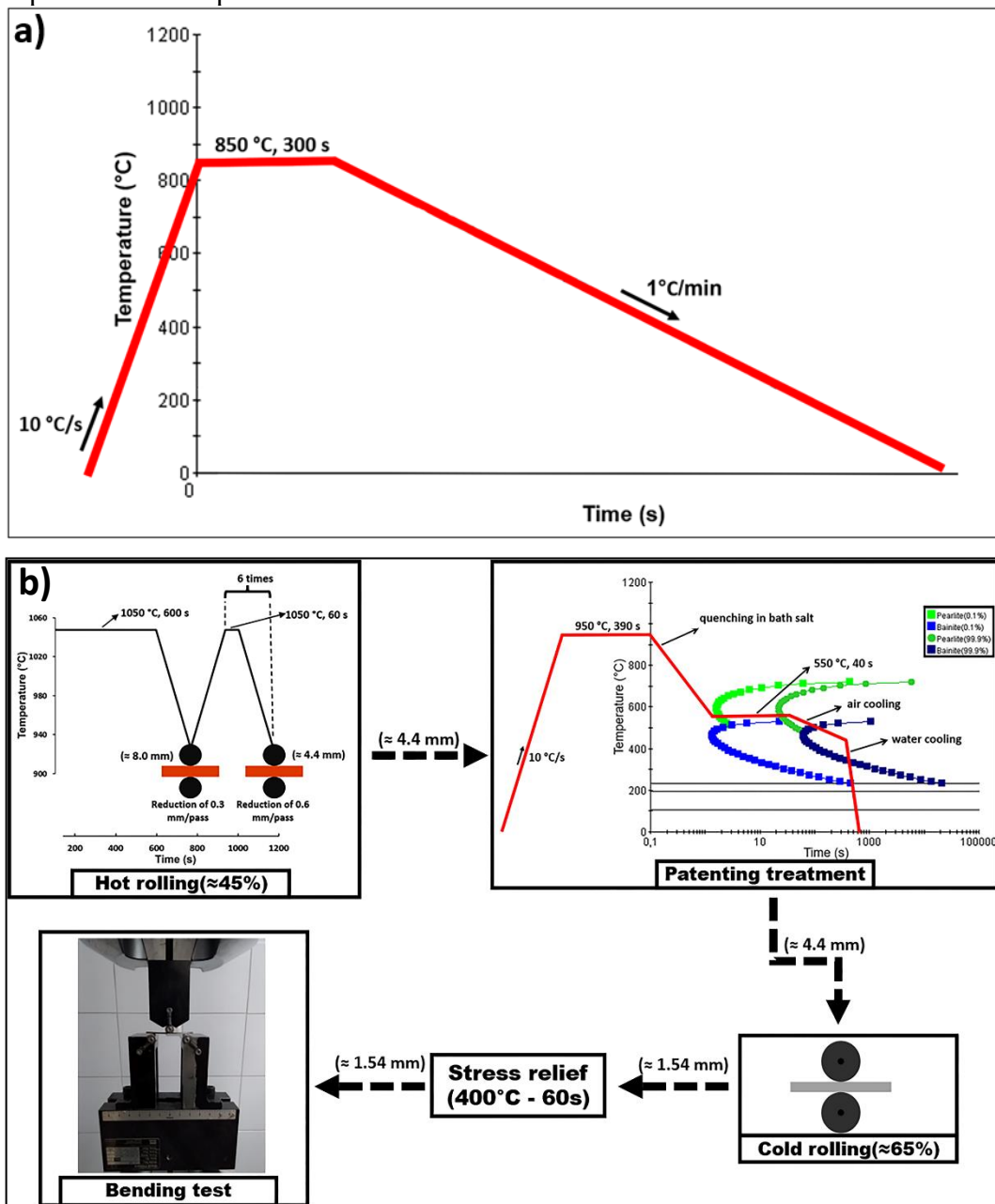
is illustrated in Figure 49b. In this context, the starting sample underwent 45% hot-rolled reduction in multiple passes (≈ 0.6 mm of reduction/pass and finish rolling temperature of ≈ 906 °C). After hot rolling, the steel was austenitized at 950 °C for 390 s, and then, quenched into a bath salt at 550 °C for 40 s (patenting treatment). Subsequently, 65% cold-rolling reduction (≈ 0.1 mm in thickness reduction/pass) was introduced in the patented specimen, followed by a short time (60 s) stress-relief treatment at 400 °C. Both rolling processes were executed by using a laboratory scale rolling machine with diameter rolls of 110 mm and a rolling speed of 8m/min. Next, the stress-relieved sample was cut in a rectangular dimension of 1.54 mm (thickness) x 12.5 mm (width) x 60 mm (length). In this case, the rolling and length directions are parallels. Finally, the DR condition was obtained after the application of four consecutive three-point bending steps alternating the superior and inferior surfaces of the stress-relieved sample. This procedure simulates the operation of re-winding wire into coils (FERNANDO *et al.*, 2017). A universal testing machine (landmark 370.10) with a maximum load of 100kN was used to carry out the bending experiments. Pins with a roller's diameter of 10 mm, a distance of 40 mm between the support pins, a displacement rate of 2 mm/min, and 4.5 mm as the maximum displacement of the loading pin were the parameters adopted during the three-point bending test. After that, the UC and DR tensile-shear (TS) specimens were obtained using an electro-discharge machine. The geometry and dimensions of the TS specimen are provided in Figure 50a, 50b, and 50c.

5.2.2 *In-situ tensile-shear (TS) experiment and digital image correlation (DIC)*

For in-situ observations, the specimens were grounded (using sandpapers from #240 to #2000 grit), polished (using diamond suspensions of 6, 3, and 1 μm), and etched with 4% nital solution. The in-situ procedure was performed using a kammrath-weiss tensile stage with a maximum loading of 5kN, as shown in Figure 50d. During the in-situ experiment, a constant displacement of 0.1 $\mu\text{m/s}$ was established and secondary electron (SE) image acquisition was carried out in real-time in a resolution of 1536 x 1024 pixels using a THERMO SCIENTIFIC QUATTRO field emission gun (FEG) scanning electron microscope (SEM). The SE images were captured employing an accelerating voltage of 5 kV, a current of 0.18 nA, and a working distance (WD) of 20 mm. The high WD was implemented in this experiment because of safety measures due to the complex dimensional setup of the tensile stage inside the SEM (see Figure 50e). After the specimen's failure, QUATTRO FEG-SEM was also employed for obtaining fractographic SE images using an accelerating voltage of 20 kV, a current of 3.2 nA,

and a WD of 8.5 mm. Additionally, the open source 2D-DIC MATLAB software (Ncorr v1.2) was adopted to compute the u -displacement component into the x-axis and the Eulerian shear strain (ϵ_{xy}) among the images collected during the in-situ TS experiment. A subset size of 55 pixels and a subset space of 1 pixel were chosen for the DIC proceeding.

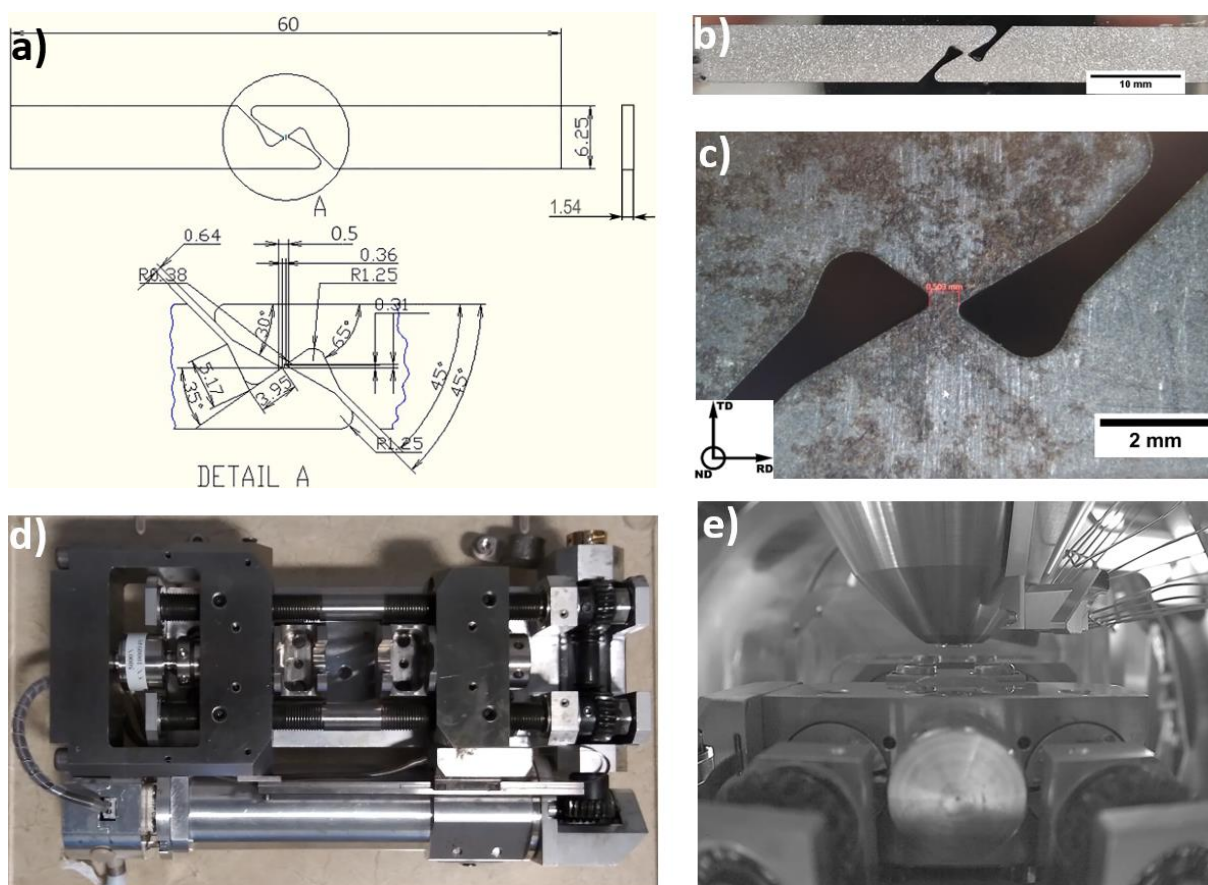
Figure 49 – Schematic proceedings employed in this work to produce the start investigated pearlitic steel conditions (UC and DR). (a) Diagram with representative details of the thermal treatment with slow cooling performed in the UC specimen (b) Illustrative flowchart of the laboratory processing route undergone by the DR specimen. The numbers in millimeters (mm) contained in Figure 49 (b) represent the samples' thickness.



Source: Elaborated by the author.

Figure 50 – Details of the In-situ shear experiment implemented in this work. (a) Sketch of the

tensile-shear specimen geometry with its dimensions in millimeters. (b) Machined tensile-shear specimen. (c) Central region of the tensile-shear specimen. (d) Kammrath-Weiss tensile stage. (e) The tensile stage set up in the SEM chamber.



Source: Elaborated by the author.

5.2.3 Interrupted tensile-shear (TS) experiment in the RD specimen

A THERMO SCIENTIFIC APREO FEG-SEM was adopted to perform electron backscatter diffraction (EBSD) analyses, SE image, and backscattered electrons (BSE) image acquisitions just before and after the interrupted TS test using the same aforementioned tensile stage apparatus. In this case, the TS procedure was performed outside the SEM chamber and it was terminated immediately after the moment when an abrupt load drop started to occur after 200 μm of elongation (based on the RD's in-situ elongation-load curve as reference). The APREO FEG-SEM was coupled with an EDAX EBSD detector and BSE detectors placed inside the microscope column. The EBSD analyses were conducted with an operating voltage of 20 kV, a step size of 50 nm, a WD of 8 mm, and a sample tilt angle of 70° . In this operation, the SE images and the BSE images were implemented using, respectively, an accelerating voltage of 20 kV and 5 kV, a current of 6.4 nA and 1.6 nA, and a WD of 8 mm and 1.5 mm. For

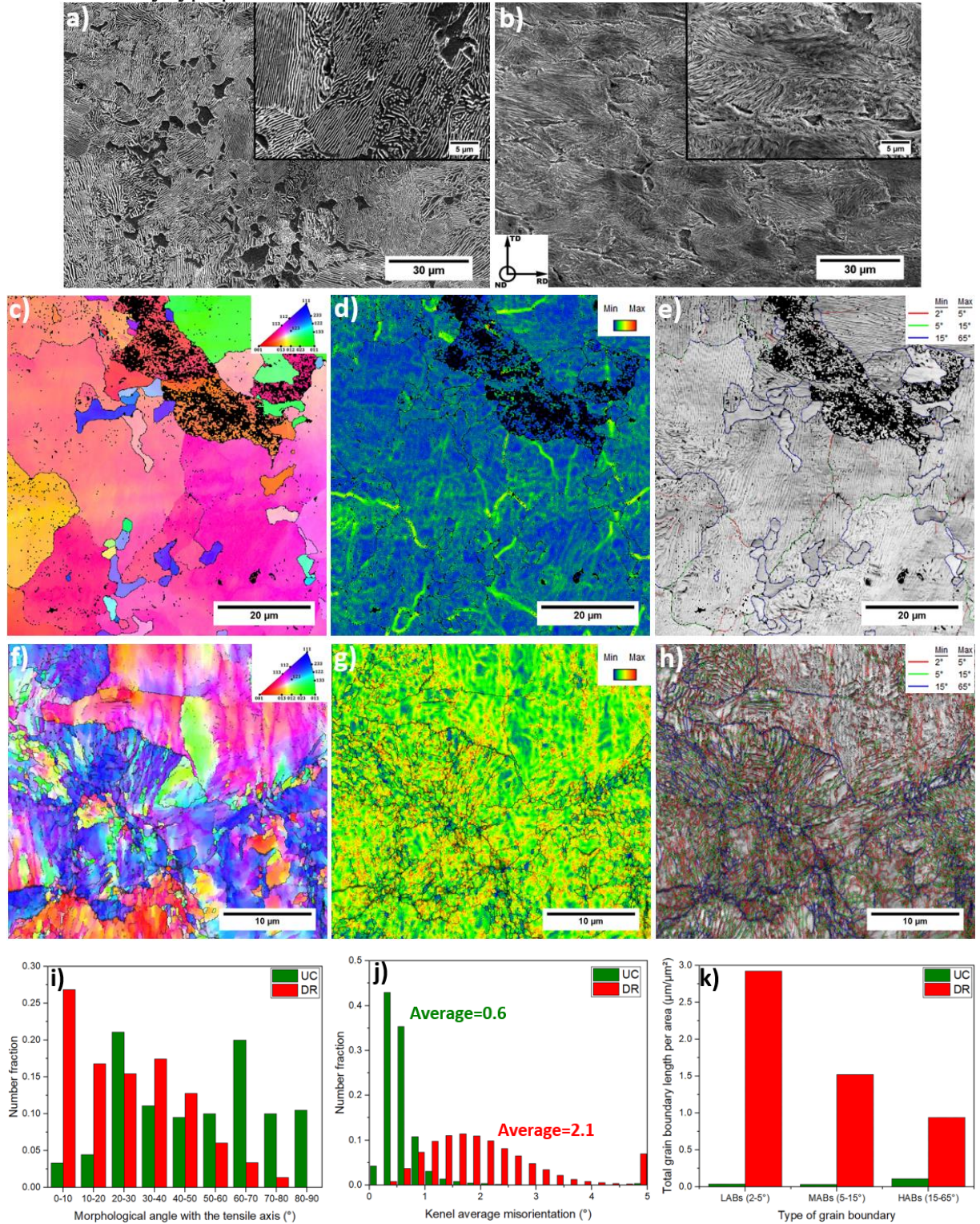
EBSD, SE, and BSE image acquisition during the interrupted investigation, prior to starting this experiment, the specimens also received the regular metallographic preparation, however, no etch and an additional vibratory polishing (with 0.04 μm colloidal silica) were applied. Finally, the EBSD data were evaluated through OIM and MTEX software and their inverse figure pole (IPF) maps were plotted in the z-direction.

5.3 Results and discussion

5.3.1 *Initial microstructural characteristics of pearlitic steel before the tensile-shear (TS) experiment*

This topic aims to detail the microstructural differences between the initial condition of UC and DR specimens. The start microstructures are presented in Figure 51a (UC) and 51b (DR). In this regard, UC reveals the coarsest pearlitic interlamellar space (IS) (402.6 ± 64.4 nm) and colony size (16.0 ± 3.9 μm) in comparison to the DR's pearlitic condition (IS = 173.2 ± 37.6 nm and colony size = 9.9 ± 1.6 μm). Based on this, the IS is controlled by the temperature of the austenite-to-pearlite transformation which is a diffusion-controlled reaction (ARANDA *et al.*, 2014). Otherwise, the size of pearlitic colonies and blocks depends on the prior austenitic grain size because the austenitic grain boundaries are sites for pearlite nucleation (ARANDA *et al.*, 2014). In this way, the slow cooling thermal treatment (Figure 49a) used to produce the UC microstructure increases this sample's holding time under austenitization temperatures. As a consequence, the UC's prior austenitic grain can significantly grow letting UC prone to produce coarse pearlitic colonies and blocks. Also, this slower cooling rate allows the austenite-to-pearlite transformation to occur in UC at a high temperature developing pearlites with thicker IS. Conversely, the faster cooling applied in DR via the patenting treatment (Figure 49b) can result in the opposite microstructural effect. After patenting treatment, DR additionally underwent 65% cold-rolling reduction that can also enhance the IS refinement (LEÃO *et al.*, 2023a). Another point is that the volume fraction of grain boundaries ferrite (GBs- α) found in UC (5.6%) and RD (4.3%) were not identical. In this context, it is expected that RD has the highest volume fraction of GB- α due to its likely inferior prior austenitic grain size and higher cooling rate after austenitization (inhibits manganese partitioning) (MIYAMOTO *et al.*, 2016). However, this contradiction was assumed to be a consequence of the distinct states and morphologies of the GBs- α in both studied conditions that can intervene in the phase quantification process. For instance, GBs- α in the UC specimen exhibit an almost polygonal shape and they are not deformed, while they are in a pancake-like

Figure 51 –Initial metallurgical characteristics of both pearlitic steel conditions (UC and DR) used in the in-situ tensile-shear experiment. Start SEM microstructures of the (a) UC and (b) DR samples. Color-coded inverse pole figure (IPF) map, kernel average misorientation (KAM) map, and grain boundary distribution map, respectively, for the (c)(d)(e) UC and (f)(g)(h) DR conditions. (i) Distribution of the pearlitic morphological angles about the tensile axis, (j) distribution of KAM values, and (k) distribution of grain boundary type per area for UC and RD.



Source: Elaborated by the author.

shape and stretched around the rolling direction in the DR condition. Also, Figure 51i displays the morphological angle distribution of cementite lamellae in pearlites about the tensile axis for both studied specimens. In view of this, the greater number fraction of the morphological angle in the DR condition is mainly concentrated in the range from 0° to 10° and it tends to decrease as the angle increases. It means that most of the pearlite colonies in DR are closely aligned to the tensile axis due to the prior cold rolling deformation (TAGASHIRA *et al.*, 2000). Otherwise, the UC's pearlite colonies seem to be randomly orientated about the tensile axis.

Moreover, Figure 51c (UC) and 51f (DR) present the inverse figure pole (IPF) maps of the two evaluated specimens in their initial states. In addition, the accumulation of local plastic strain in the steel matrix can be investigated through kernel average misorientation (KAM) and distribution of low-angle grain boundaries (LABs) as well as medium-angle grain boundaries (MABs) (ZHANG *et al.*, 2022). Specifically, KAM is the relative average misorientation between a given point and its nearest neighbors inside the same grain (ZHANG *et al.*, 2022). Figure 51d (UC) and 51g (DR) depict the KAM distribution maps obtained from both IPF maps and their kernel values are summarized in Figure 51j. It is possible to note that the UC's KAM map is mainly constituted of blue regions in low kernel values. Also, there are some intermediary KAM intensities in UC, in green lines, that seem to be around the pearlitic colony boundaries. Otherwise, the KAM distribution map for DR condition displays essentially areas with intermediary values of KAM (in green color) including some red color regions meaning higher KAM intensities ($\approx 5^\circ$). In this context, the overall average of KAM was $0.6^\circ \pm 0.4$ for UC and $2.1^\circ \pm 1.1$ for DR. Furthermore, regarding grain boundary distribution, Figure 51e (UC) and 51h (DR) show maps with the distribution of the grain boundary types, and Figure 51k reports their density normalized in length per area. The LABs and MABs (misorientation $< 15^\circ$) indicate areas with a concentration of geometrically necessary dislocations (GNDs) (WRIGHT *et al.*, 2011). In this way, the densities of LABs ($2^\circ \sim 5^\circ$) and MABs ($5^\circ \sim 15^\circ$) in UC were respectively $0.03 \mu\text{m}/\mu\text{m}^2$ and $0.02 \mu\text{m}/\mu\text{m}^2$, which are almost null values. Unlike, DR has a higher density of LABs ($2.92 \mu\text{m}/\mu\text{m}^2$) and MABs ($1.51 \mu\text{m}/\mu\text{m}^2$) in its ferritic matrix. Therefore, the evaluation of KAM and grain boundary distributions confirm that DR is initially plastic-deformed while UC is not. Additionally, a great divergence of HABs' density was found between UC ($0.10 \mu\text{m}/\mu\text{m}^2$) and DR ($0.93 \mu\text{m}/\mu\text{m}^2$). The HABs are usually related to the pearlitic block boundaries in pearlitic steels (ZHOU *et al.*, 2016; ARANDA *et al.*, 2014). In this context, although it was not possible to measure the pearlitic block size due to the small EBSD areas, it can be said qualitatively that the pearlitic block size should be larger in UC than in DR. This outcome is also expected based on the aforementioned effect of the different cooling rates

on both specimens' microstructures. All the microstructural features obtained from both initial states are summarized in **Table 4**.

Table 4 – Summary of the initial microstructure characteristics of the UC and DR pearlitic steel conditions.

Sample's name	Average of interlamellar spacing (nm)	Average of Colony size (μm)	Volume fraction of GB- α (%)	Number fraction concentration of the morphological angle ($^{\circ}$)	Overall average of KAM ($^{\circ}$)	Density of LABs ($\mu\text{m}/\mu\text{m}^2$)	Density of MABs ($\mu\text{m}/\mu\text{m}^2$)	Density of HABs ($\mu\text{m}/\mu\text{m}^2$)
UC	402.6 ± 64.4	16.0 ± 3.9	5.6	20-30 / 60-70	0.6 ± 0.4	0.03	0.02	0.10
DR	173.2 ± 37.6	9.9 ± 1.6	4.3	0-10	2.1 ± 1.1	2.92	1.51	0.93

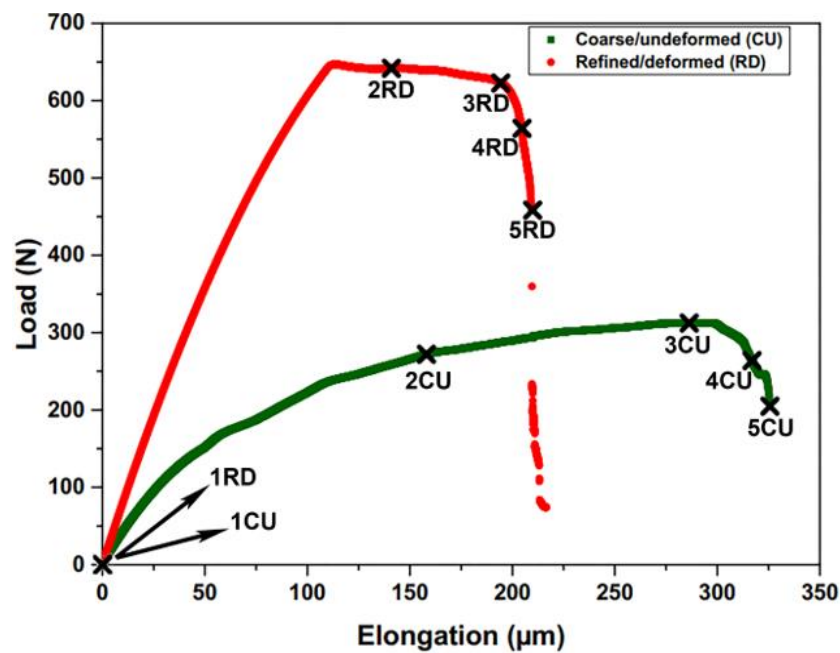
Source: Elaborated by the author.

5.3.2 *In-situ tensile-shear (TS) experiments and digital image correlation (DIC)*

This section centers attention on describing the mechanical and microstructural behavior of pearlitic steel during the in-situ TS experiment. In this regard, Figure 52 provides the elongation-load curves obtained from the TS tests performed in the UC and DR pearlitic steel states. The structural properties extracted from each elongation-load curve and the microhardness average of UC and DR are available in Table 5. Based on this, it is worth noting that DR has shorter ultimate elongation and higher values of elastic stiffness, ultimate load, and absorbed energy in comparison to UC. These structural properties indicate that DR holds higher resistance to elongate. This mechanical behavior can be attributed to the DR's microstructural features, such as its thinner IS, cementite lamellae closely aligned to the tensile axis, plastic-deformed ferritic matrix, and smaller pearlitic blocks. More specifically, the refined IS can restrain more effectively the movement of dislocations because they have shorter free paths and more cementite lamellae acting as barriers (MISHRA *et al.*, 2020; LI *et al.*, 2011). Moreover, Teshima *et al.* (2017) reported that plastic deformation can be efficiently restricted when the lamellae are aligned parallel or perpendicular to the tensile axis due to pile-ups of dislocation at the ferrite/cementite interface. Conversely, some authors (TESHIMA *et al.*, 2017; DURGAPRASAD *et al.*, 2018a) have reported that dislocation can move freely in pearlite with cementite lamellae aligned around 45° about the tensile axis. In this context, there are significant pearlitic colonies arranged in a hard set for plastic deformation in DR condition which may also contribute to its higher strength to elongate. Furthermore, the introduction of prior plastic deformation in DR develops a work-hardened state where some slip plans and ferrite/cementite interfaces can be initially saturated with dislocations that hinders the further

dislocations' motion. In this case, slips can occur again when a superior critical load is achieved, which explains why the load-elongation curve of RD has a significant elastic region and no-strain hardening behavior. Unlike, UC exhibits a small elastic region and a considerable strain hardening zone followed by a brief necking, just before the rupture. Furthermore, that divergence in the ability to resist deformation can also explain the difference in microhardness found in the DR (409 ± 7.9 HV) and UC (223.1 ± 11.2 HV) specimens. Finally, it is pointed out by the literature (ZHOU *et al.*, 2016; BEHERA *et al.*, 2019) that pearlitic block size has a significant influence on the toughness of pearlitic steels. Therefore, the highest amount of absorbed energy during the DR's TS test can be a result of its assumed smaller pearlitic block size.

Figure 52 – Elongation-load curves obtained during the in-situ tensile-shear test for UC and DR pearlitic steel conditions. The points marked with x represent the stages where the captured SEM images were selected for demonstrating the progress of the tensile-shear experiment.



Source: Elaborated by the author.

Table 5 – Structural properties and microhardness average of the UC and DR conditions.

Sample name	Elastic stiffness (N/μm)	Ultimate load (N)	Ultimate elongation (μm)	Absorbed energy (KJ)	Microhardness average (HV _{0.2})
UC	2.8	312.5	325.6	77.7	223.1 ± 11.2
DR	7.0	646.8	209.8	102.6	409.4 ± 7.9

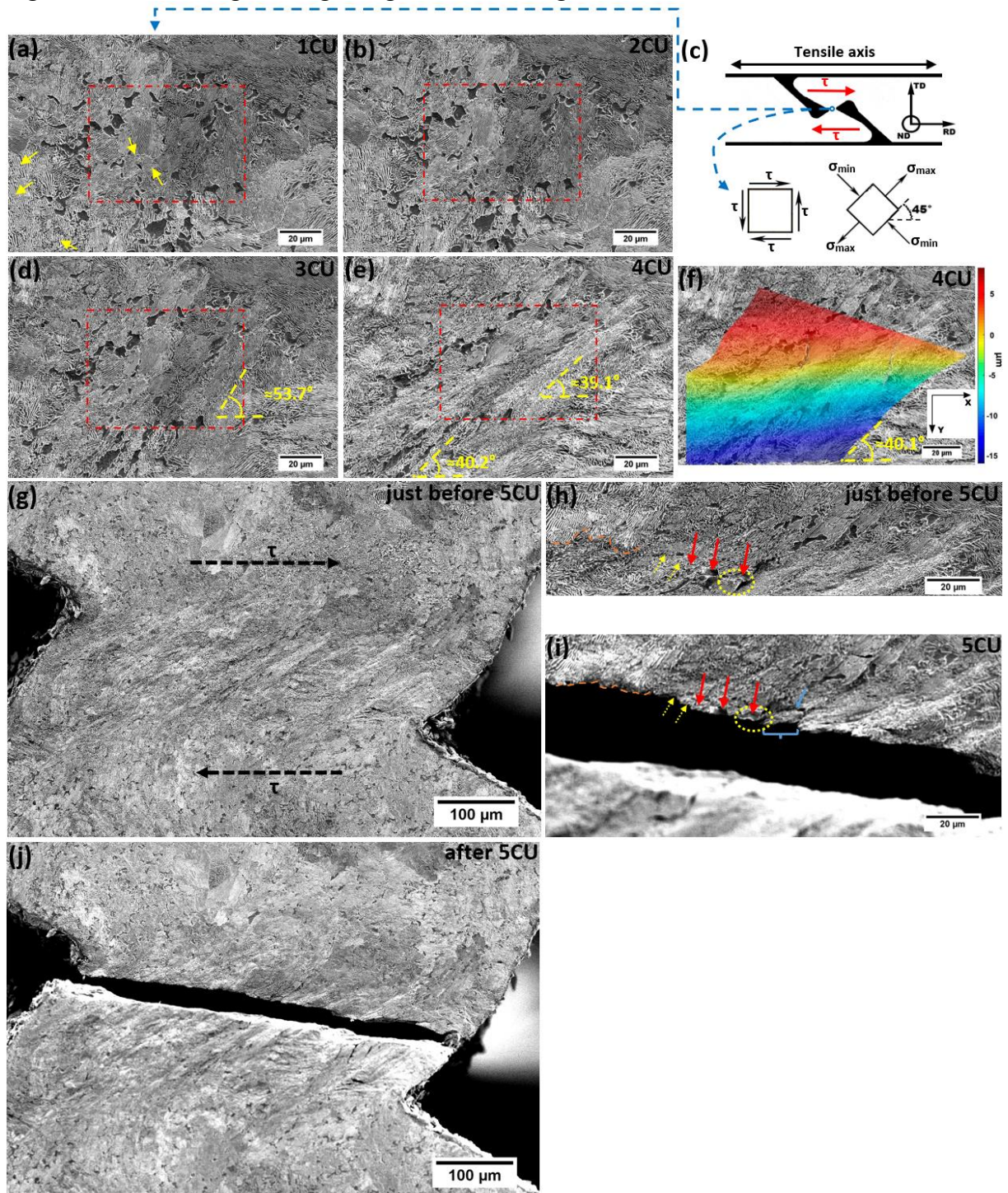
Source: Elaborated by the author.

In addition, the x-marks in Figure 52 indicate where the in-situ SEM observations

were selected for demonstrating the progress of microstructural modifications under TS deformation. In this case, each of the two elongation-load curves has its own x-mark distribution due to their distinct mechanical behavior. The chosen regions were: original state (1UC and 1DR), strain hardening (2UC and 3UC), necking (4UC, 2DR, 3DR, and 4DR), and failure (5UC and 5DR). Regarding the elastic zones, the original microstructures did not undergo any significant modifications in both studied cases. Figure 53 and 54 show the macro view of plastic deformation evolution for, respectively, UC and RD following their x-mark positions in Figure 52. In general, it is possible to observe a left-hand rotation as an effect of the shear proceeding. Also, this event was confirmed by the measurement of the u -displacement component, which was obtained via the DIC technique (see Figure 53f and 54f) from both original states (1UC and 1DR) up to the necking stages (4UC and 4DR). In view of this, the top regions slide into the right sides, while the bottom areas move into the left laterals, and between them, there are also zero u -displacement zones meaning that the in-situ investigations were performed in the geometrical middle between the shear components. However, the u -displacement values are incomparable between UC and DR because the images from each condition in Figure 53 and 54 have different magnifications that interfere with the total displacement on each of those specific evaluated regions. Moreover, the central regions of Figure 53a, 53b, 53d, 53e, 54a, 54b, 54d, and 54e marked with a red dashed rectangle are presented in higher magnification, respectively, in Figure 55 and 56 including their Eulerian shear strain (e_{xy}) maps. In this regard, the maximum shear strain value in each map is negative and represented by dark blue color because the 2D DIC code implemented in this work considers the positive reference of the Y axis going down below zero, while its negative reference is set up in the opposite direction that means above zero, as illustrated in Figure 53f and 54f.

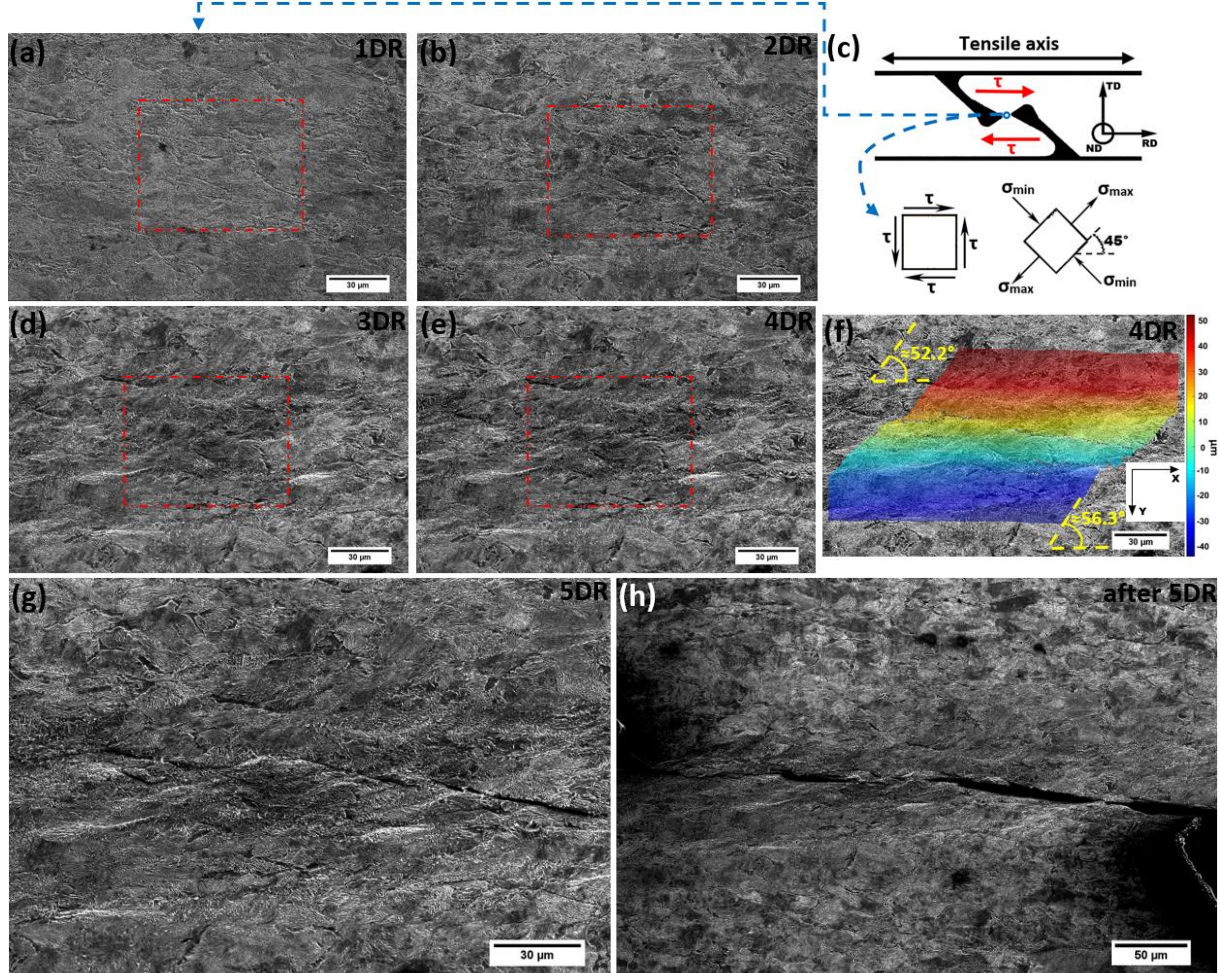
Concerning UC, it is pointed out by yellow arrows in Figure 53a, 55a, and 55b (original state) some areas with lamellae of cementite broken. It demonstrates how brittle is the thick cementite even under no loading application. Then in the hardening strain zone, it can be seen that the microstructure in 2UC (Figure 53b, 55d, and 55e) underwent a slight rotation, and a small heterogeneous strain (maximum e_{xy} of -0.08) started to be concentrated at the pearlitic colony boundary as displayed in the dark blue area of Figure 55f. Subsequently, in 3UC (Figure 53d, 55g, and 55h), the rotation increased together with a microstructural stretching into $\approx 53.7^\circ$ about the shear direction. At the same time, many lamellae of cementite started to break as indicated by yellow arrows in Figure 55h, while the maximum shear strained region reached a value of -0.7 and expanded from the pearlitic colony boundary throughout a low resistance area within a colony constituted of non-continuous cementite (see Figure 55i). Also, intermediary

Figure 53 – Macro SEM images of the UC specimen's deformation during the in-situ tensile-shear test following, as a reference, the x-marks in its elongation-load curve (see Figure 52): (a) 1CU, (b) 2CU, (d) 3CU, (e) 4CU, (g) just before 5CU in a lower magnification, (h) just before 5CU in the regular magnification, (i) 5CU, (j) after 5CU in a lower magnification. (c) Illustrative diagram reference of the stress components and geometrical analysis position during the in-situ tensile-shear test. (f) Eulerian u -displacement map obtained via digital image correlation (DIC) from the 1CU up to the 4CU stage. The red dashed rectangles represent the region where the images in high magnification of Figure 55 were taken.



Source: Elaborated by the author.

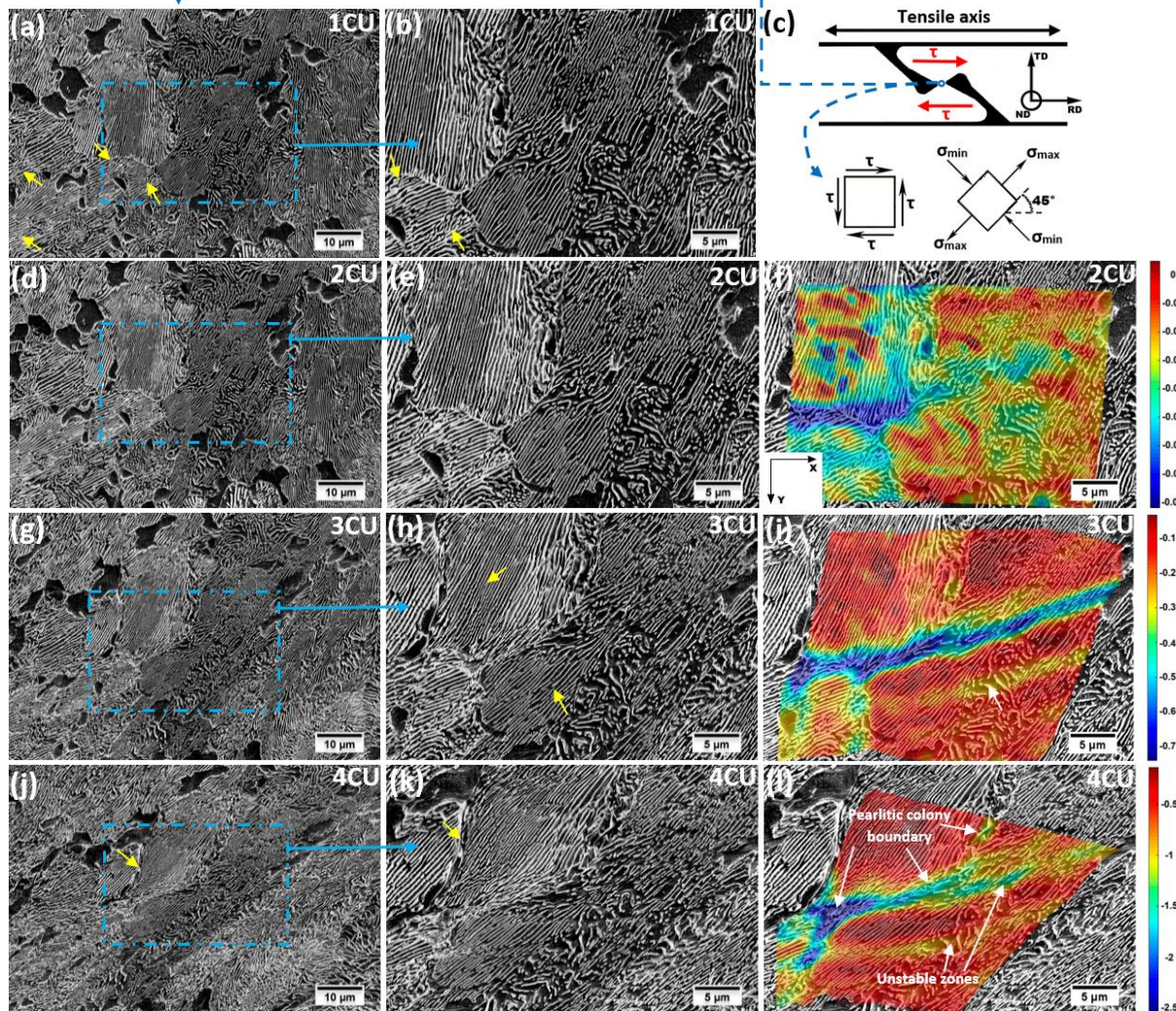
Figure 54 – Macro SEM images of the DR specimen’s deformation during the in-situ tensile-shear test following, as a reference, the x-marks in its elongation-load curve (see Figure 52): (a) 1DR, (b) 2DR, (d) 3DR, (e) 4DR, (g) 5DR, and (h) after 5DR. (c) Illustrative diagram reference of the stress components and geometrical analysis position during the in-situ tensile-shear test. (f) Eulerian u -displacement map obtained via digital image correlation (DIC) from the 1DR up to the 4DR stage. The red dashed rectangles represent the region where the images in high magnification of Figure 56 were taken.



Source: Elaborated by the author.

strained regions in yellow color (≈ -0.3) considered unstable regions (comprised of pearlitic colony boundary, coarse cementite, or broken cementite lamellae) were found in Figure 55i. It is worth mentioning that the coarse pearlitic region indicated by the white arrow in Figure 55i seems to cooperate with the instability and fracture of the nearby cementite lamellae. Next, the necking stage (4UC), in Figure 53e, 55j, and 55k, reveals that the rotation and microstructural stretch became sharper resulting in pearlitic colonies and GBs- α elongated into $\approx 40^\circ$ about the shear direction. This event can be a consequence of the combined effect of the principal stress components caused by the process of shear, as illustrated in Figure 53c (DIETER, 1986). Additionally, decohesion between pearlitic colonies was identified in 4UC as indicated by yellow arrows in Figure 55j and 55k. Moreover, it can be realized in Figure 55l that the high-

Figure 55 – High magnification SEM images of the UC specimen's deformation during the in-situ tensile-shear test following, as a reference, the x-marks in its elongation-load curve (see Figure 52): (a) (b) 1UC, (d) (e) 2UC, (g) (h) 3UC, and (j) (k) 4UC. (c) Illustrative diagram reference of the stress components and geometrical analysis position during the in-situ tensile-shear test. (f) (i) (l) Eulerian shear strain maps, e_{xy} , obtained via digital image correlation (DIC), in the respective stages 2CU, 3CU, and 4CU of the UC's elongation-load curve in Figure 52.



Source: Elaborated by the author.

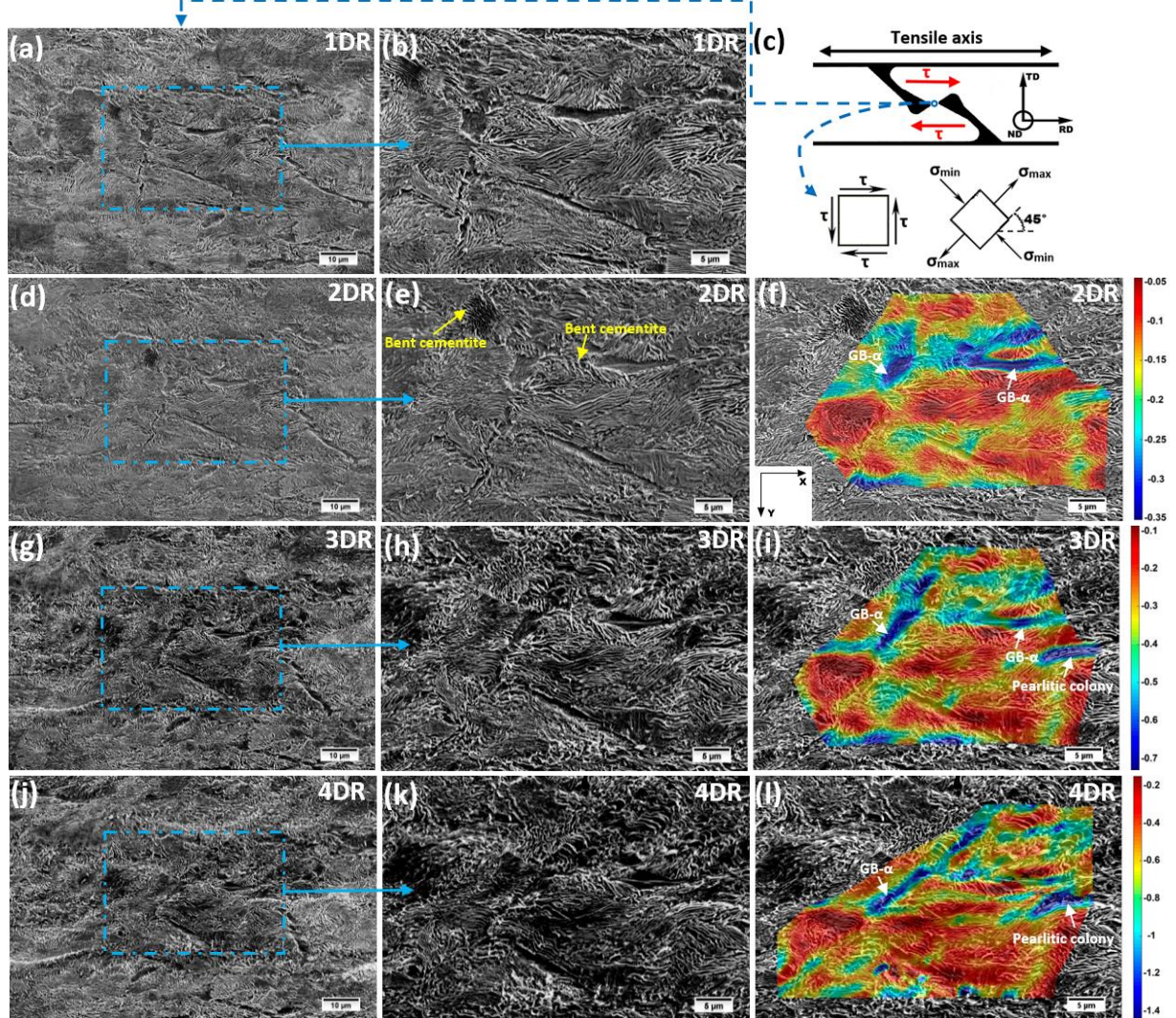
strained regions were still at the pearlitic colony boundaries followed by the unstable zones within the colonies. In this case, the maximum e_{xy} intensified to -2.5. In addition, a huge deformed region was observed just before the sample fails (see Figure 53g). Finally, the rupture in the UC specimen (5UC) occurred abruptly with a fracture almost perpendicular to the stretching direction as shown in Figure 53i and 53j. This instantaneous break caused a fuzzy image in Figure 53i due to the fast motion of the specimen. The quick UC's fracture can be likely related to its assumed big pearlitic block size (ZHOU *et al.*, 2016). Also, it is worth realizing that the crack path followed the boundaries of the pearlitic colony that underwent the episode of decohesion as indicated by dashed yellow circles in Figure 53h and 53i. In addition

to this, another event of decohesion was identified during the UC's rupture in Figure 53i, which resulted in an almost detached colony (denoted by a blue brace) where its remaining decohesion region is pointed out by a blue arrow. In this situation, the crack also seemed to cross some GBs- α (pointed out by red arrows) and other boundaries of pearlitic colonies as indicated by the dashed yellow arrows and underlined by the dashed orange line in Figure 53h and 53i.

Based on the evidence provided during the UC's in-situ TS experiment, it is reasonable to consider that in the pearlitic microstructure of UC, the rotation mechanism caused by the shear progress resulted in a massively stretched pearlitic microstructure near the maximum principal stress direction. Conversely, the UC's big pearlitic colonies seemed to be compressed and smashed against each other in a direction close to the minimum principal stress component. In this context, it is plausible to assume that the colony boundaries were highly strained due to their discontinuous lamellar arrangement. In contrast, the regions inside the colonies underwent a more homogenous deformation because there are more uniform distributed areas of cementite lamellae. Therefore, the colonies tend to slide against each other through the deformation of their colony's boundaries under shear which can result in colony decohesion. However, dissimilar morphology of cementite within the colony can develop strain concentration. As consequence, this instability is able to cause breakages of the neighbor cementite lamellae. In view of this, the phenomenon of decohesion between colonies can lead to crack initiation or an easier path of crack propagation such as at GBs- α . Moreover, the big pearlitic blocks of UC may allow a fast crack propagation conducting a quick detachment during its failure.

Now regarding the behavior of the DR specimen under TS deformation, no broken cementite was found in 1RD (Figure 54a, 56a, and 56b). Then, concerning the RD's necking stage, a small rotation can be realized through the tracking of the GBs- α movement in 2DR (Figure 54b, 56d, and 56e). At the same time, some cementite lamellae were bent as pointed out in Figure 56e. In this context, the shear strain (-0.35) started to be concentrated mainly in some GBs- α regions as indicated by white arrows in Figure 56f. After that, the microstructural rotation gradually increased in addition to a no longer smooth specimen surface due to plastic deformation in 3DR (Figure 54d, 56g, and 56h) and 4DR (Figure 54e, 56j, and 56k) images. Also, many buckled cementite lamellae were found in RD condition (see Figure 56h, and 56k) instead of breaking as in the UC sample. This behavior supports that thin cementite lamellae

Figure 56 – High magnification SEM images of the DR specimen’s deformation during the in-situ tensile-shear test following, as a reference, the x-marks in its elongation-load curve (see Figure 52): (a) (b) 1DR, (d) (e) 2DR, (g) (h) 3DR, and (j) (k) 4DR. (c) Illustrative diagram reference of the stress components and geometrical analysis position during the in-situ tensile-shear test. (f) (i) (l) Eulerian shear strain maps, e_{xy} , obtained via digital image correlation (DIC), in the respective stages 2DR, 3DR, and 4DR of the DR’s elongation-load curve in Figure 52.



Source: Elaborated by the author.

present greater plastic deformability than coarse ones (UMEMOTO *et al.*, 2003). Under this circumstance, the RD’s pearlitic colonies seemed to be very rigid and no severe readjustment into the diagonal direction was realized during the TS experiment such as it was in UC. This fact is confirmed by the DIC analysis in Figure 54f which revealed distortion angles in 4DR over 50° about the shear direction. Moreover, the highest strained regions found in 3DR and 4DR were still in the GBs- α in addition to one pearlitic colony. This sharply strained pearlitic colony has lamellae parallel to the shear components and seems to undergo interlamellar decohesion. Furthermore, in contrast to UC, the fracture detachment happened slowly and gradually in the DR specimen, as shown in Figure 54g and 54h, which may indicate an influence

of its smaller pearlitic block (ZHOU *et al.*, 2016). Finally, the orientation of the rupture in DR was similar to the UC which demonstrates again the effect of the principal stresses imposed by the shear condition.

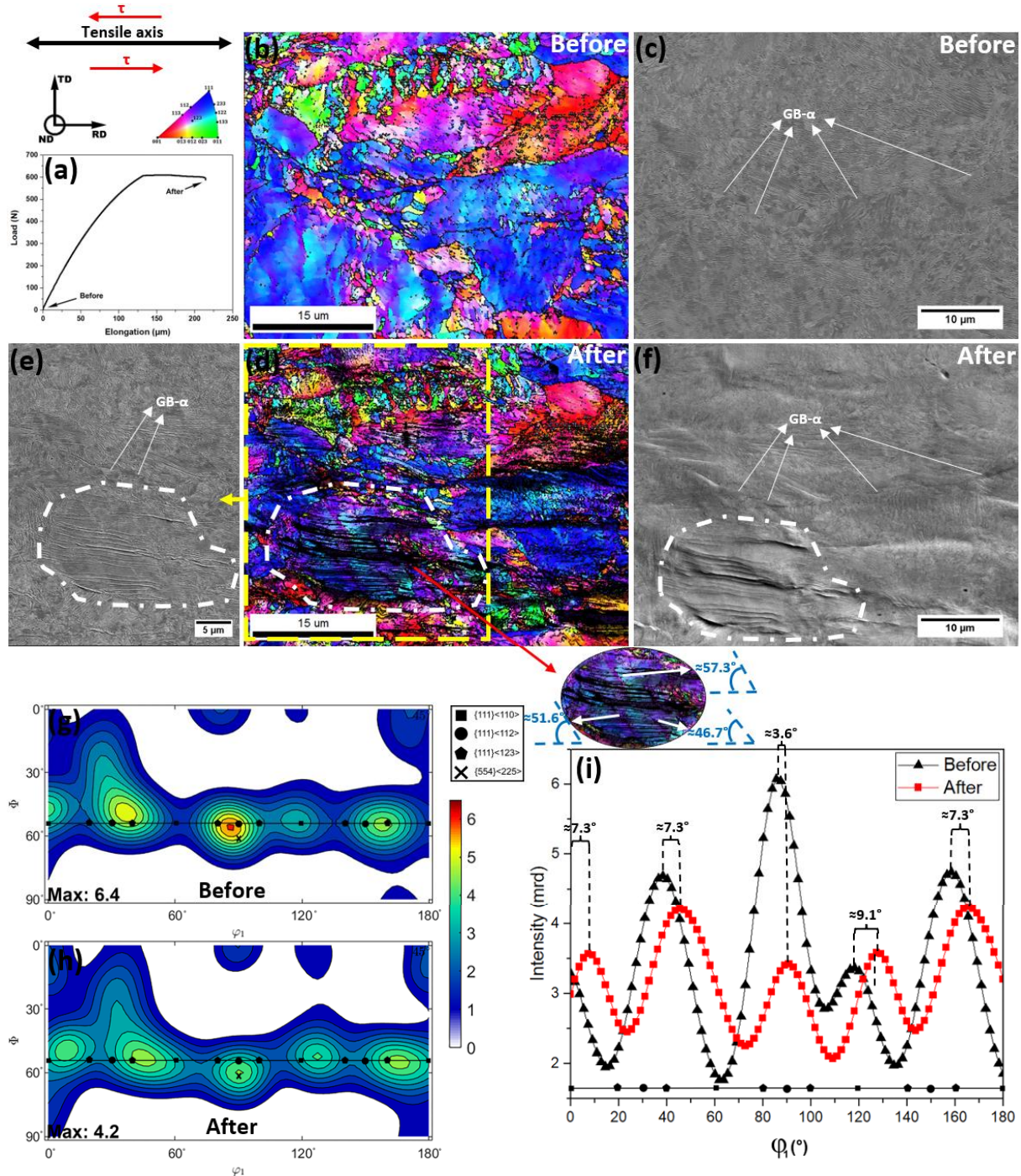
Finally, even though all aforementioned finds about the DR specimen, it was not clearly detected sites where cracks can start to nucleate or signs of the main paths for cracks propagate throughout the DR's microstructure, probably, due to its refined condition. Thus, the DR specimen was additionally and subsequently investigated by the interrupted TS experiment technique.

5.3.3 Interrupted shear-tensile (TS) experiment of DR specimen

Concerning the aforementioned issue related to the DR's refined microstructure during the SEM in-situ observation, this section specifically focuses on designing a possible mechanism for DR's mode failure through EBSD, SE, and BSE interrupted analyses. These investigations were performed before (start condition) and after (at the failure instant) the TS experiment preserving the same area. The elongation-load curve obtained from the interrupted TS experiment is displayed in Figure 57a evidencing both evaluated circumstances: Before and After. From the viewpoint of accuracy, it is relevant to highlight that DR provided a similar elongation-load curve behavior in both TS proceedings implemented in this work (see Figure 52 and 57a).

In view of this, Figure 57b and 57c show, respectively, the IPF map and its BSE image of the DR specimen before the TS test. This setup provides information about the crystallographic orientation of the ferritic matrix and the geometric lamellar orientation of the pearlites in the investigated region. Also, GBs- α were detected in the BSE image as indicated by the white arrows in Figure 57c. Likewise, Figure 57d exhibits the IPF map of the DR condition after the TS experiment preserving the initial area displayed in Figure 57b. In this case, there are many dark (not indexed) regions in the IPF map after TS deformation that seem to be potential zones of initial cracks. However, to confirm the presence of these defects, BSE and SE images available, respectively, in Figure 57e and 57f were also acquired from the same IPF map area at the failure instant. In this regard, the initial cracks in the BSE image were not validated because they had a smooth superficial relief and the potential cracks looked like scratches as seen in Figure 57e. Conversely, the SE image, in Figure 57f, supplied suitable relief information that could confirm the cracked region surrounded by a white dashed irregular circle.

Figure 57 – (a) Elongation-load curve of, (b) color-coded IPF map before, (c) backscattered electron (BSE) image on the same area of the color-coded IPF map before, (d) color-coded IPF map after, (e) BSE image on the area indicated by a yellow dashed rectangle in the IPF map after, (f) SE image on the same area of the IPF map after, (g) orientation distribution function (ODF) at $\phi_2 = 45^\circ$ calculated with monoclinic symmetry from the IPF map before, and (h) ODF at $\phi_2 = 45^\circ$ calculated with monoclinic symmetry from the IPF map after the interrupted DR's tensile-shear experiment. (i) Intensity of the γ (ND//<111>) fiber in the ODFs shown in Figure 57 (g) and (h).



Source: Elaborated by the author.

This zone rich in cracks involves mainly a pearlitic colony comprised of an initially ND//<111>

oriented ferritic matrix (blue orientation) and lamellae of cementite geometrically orientated nearly parallel to the shear stress components. Therefore, those cracks, following the same spatial orientation of the pearlitic lamellae, seem to be originated through the phenomenon of decohesion at the ferrite/cementite interface (interlamellar) since the yielding in pearlite colonies occurs predominately via plastic deformation in the ferritic lamellae (TOMOTA *et al.*, 2003). Moreover, it is worth noting the development of three violet sections (new orientation) in the ferrite lamellae of the cracked and detached region in Figure 57d. These linear segments, aligned around 46.7° , 51.6° , and 57.3° about the tensile direction, are evidence of favorable local lattice rotation or local deformation (shear band) in the initially $\{111\}$ orientated ferritic matrix during the shear progress.

Additionally, work hardening in pearlitic steel is attributed to phase stresses caused by the misfit strains (dislocation pile-ups) at the ferrite/cementite interface (WANG *et al.*, 2016). Also, plastic deformation can modify the lattice structure of cementite plates strengthening them against breakage (ZHOU *et al.*, 2019). Again, it is well known that pearlitic colonies with their lamellae aligned parallelly to the tensile direction hold dislocation slippage (GUO *et al.*, 2015; TESHIMA *et al.*, 2017). Moreover, according to Kestens and Pirgazi, (2016) the $\langle 111 \rangle$ crystallographic orientation in BCC metals provides favorable dislocation motion due to its closest-packed direction. Therefore, it is reasonable to suggest that the ND// $\langle 111 \rangle$ ferritic lamellae in the pearlitic colony enclosed by the dashed nonuniform circle in Figure 57d, 57e, and 57f had preferential activation of their primary slip plans during the shear procedure. As a result, it will promote easier plastic deformation (dislocation motion) and produce new dislocations in those ferritic lamellae. However, the hard geometrical orientation of the lamellar cementite acts as a barrier to that ferritic dislocation movement which may increase the misfit strain initiated by the work hardening mechanism. Moreover, although the cementite plates with higher yield strength do not break, they cannot accompany the same dimensional distortion experienced by the ferritic lamellae. As a consequence, local stress tends to increase at the ferrite/cementite interface leading to the event of decohesion that will work as a crack nucleation source during shear deformation.

Furthermore, considering microtexture modification during the DR's interrupted TS experiment, Figure 57g and 57h present the ODFs measured from the DR's IPF maps in the conditions Before and After, respectively. Based on this, the condition Before shows microtexture components around the γ (ND// $\langle 111 \rangle$) fiber which was likely produced during the prior $\approx 65\%$ cold-rolling process (LEÃO *et al.*, 2023a). However, this initial microtexture exhibited asymmetry of components and their intensities with a maximum of 6.4 mrd around

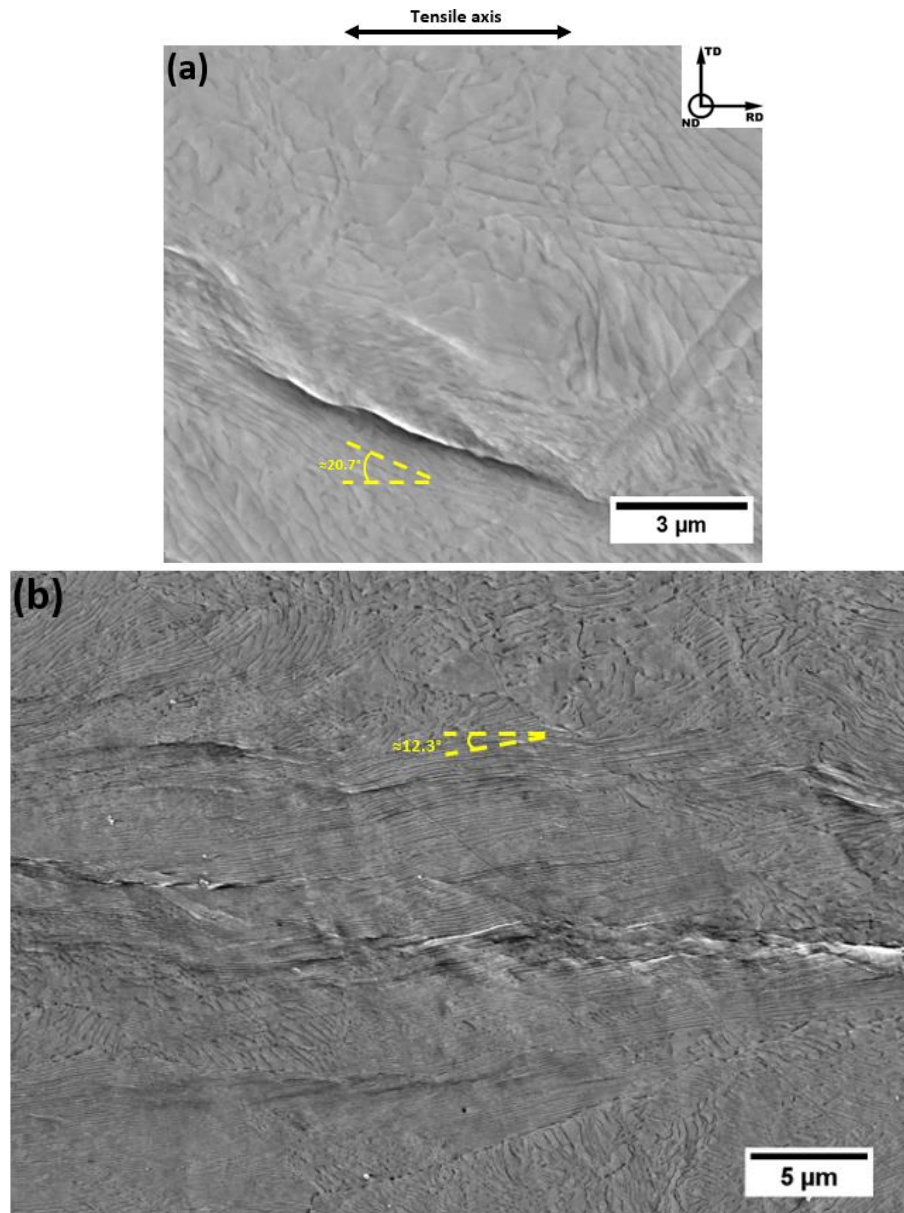
the $\{111\}\langle 123 \rangle$ and $\{111\}\langle 112 \rangle$ orientations. This design of orientation distribution can be an influence of the repeated tension and compression stresses introduced in the surface of DR's specimen by the previous four consecutive bending procedures (WANG *et al.*, 2016; KESTENS; PIRGAZI *et al.*, 2016). Moreover, the γ fiber was considered as a reference for evaluating the crystallographic rotation in the DR specimen between the Before and After TS conditions. This fiber is indicated by a continuous line in both ODFs, and their intensities were plotted in Figure 57i. In this context, it is possible to observe that TS's deformation resulted in a reduction of the initial microtexture intensity with a new maximum of 4.2 mrd. This agreed with the study of Guo *et al.* (2015). These authors demonstrated that the development of shear deformation in pearlitic steel tended to shift the microtexture into a random state (weaker microtexture). Additionally, Figure 57h reveals a smooth improvement in the symmetry of the component distribution that may be a consequence of lattice rotations during the TS procedure. In this way, a small crystallographic rotation (with a maximum of 9.1°) was identified between the two characterized conditions along the γ fiber. It is consistent with the rigid microstructural behavior of DR conferred during its in-situ investigation. In addition to this, cracks were not detected around the GBs- α .

Regarding the prior outcomes of the DR's in-situ inspection and the support of the present topic with the interrupted TS test evaluation, it can be implied that the development of shear in the DR's microstructure occurs mainly through the deformation of GBs- α , while most of the pearlite colonies are kept rigid up to the decohesion of some colonies aligned parallel to the shear components, specifically, those who has easily activation of ferritic slip plans which are able to provide a higher gradient of distortion between the hardly deformable cementite plates and softer ferrite lamellae. Likewise, other lamellar pearlitic colonies aligned almost parallel to the shear components were also found with similar crack behavior as shown in Figure 58.

5.3.4 *Fracture surfaces*

The purpose of the current topic is to explore the fracture surface of UC (Figure 59) and DR (Figure 60) specimens after their rupture during the in-situ TS experiments. The fractography indicates a ductile shear failure mode in both investigated conditions. In this way, two categories of shear fractures were identified: with dimples (Region I) and with flat surfaces (Region II) as indicated in Figure 59a and 60a. In detail, UC exhibited a shear fracture predominantly with a flat surface that corresponds to 97.7% of the fractured area. The

Figure 58 – SE image of decohesion in the cementite/ferrite interface after the interrupted tensile-shear test in pearlites with their lamellar morphological angles of (a) $\approx 20.7^\circ$ (b) $\approx 12.3^\circ$ about the tensile axis.

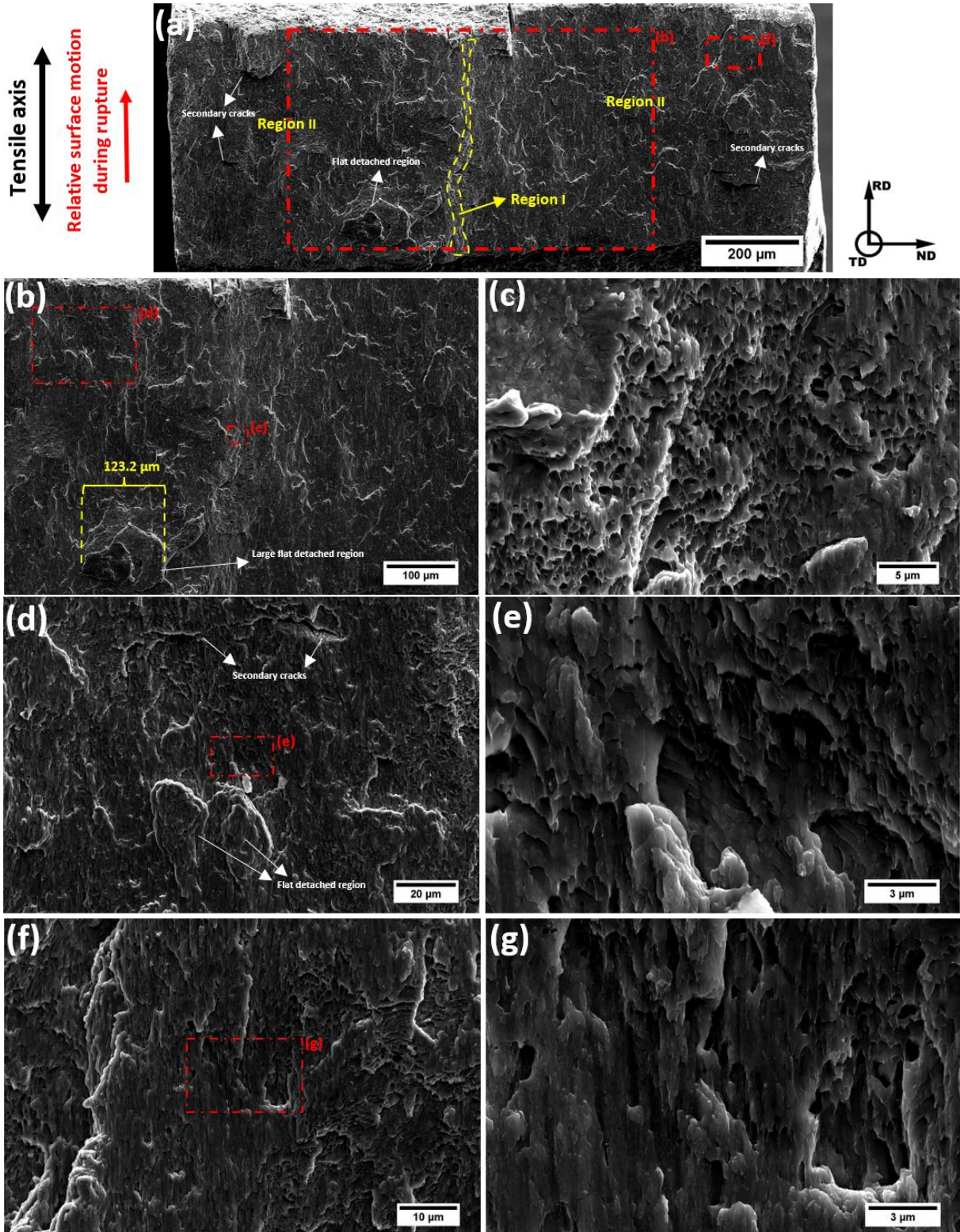


Source: Elaborated by the author.

other remaining 2.3% of the UC's area is abundant in dimples (Region I) and located close to the center of its fractured surface as shown in Figure 59a, 59b, and 59c. In contrast, DR presented mostly of its shear fractured area containing dimples (84.4%), while Figure 60a and 60b display the laterals of DR's fracture surface that are comprised of flat surfaces that represent 15.6% of DR's total fractured area.

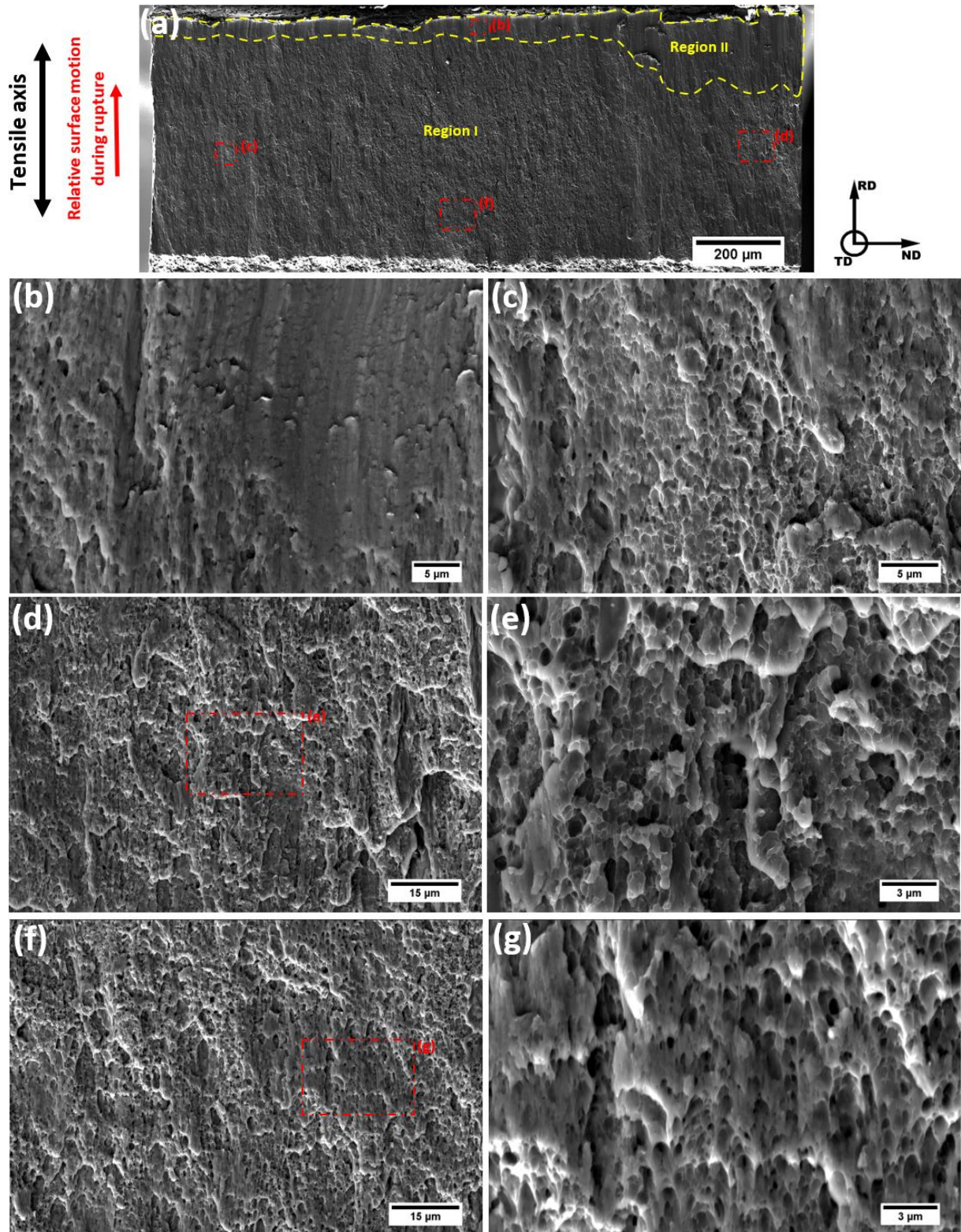
In all Region I (in Figure 59c, 60c, 60d, 60e, 60f, and 60g), there are many small, shallow, and ellipsoid-shaped dimples that are elongated about the shear direction. These morphological aspects can be attributed to the large plastic deformation caused by the shear

Figure 59 – SEM fractographic observation of the UC specimen after the in-situ tensile-shear test. (a) Overview of UC's shear fracture surface. (b) The central region of the UC's rupture surface. (c) Shear fracture with dimples (region I). (d)(e)(f)(g) Shear fracture with a flat surface (Region II).



Source: Elaborated by the author.

Figure 60 – SEM fractographic observation of the RD specimen after the in-situ tensile-shear test. (a) Overview of RD's shear fracture surface. (b) Shear fracture with a flat surface (Region II). (c) (d)(e)(f)(g) Shear fracture with dimples (region I).



Source: Elaborated by the author.

process that relaxes the stress concentration around the voids initially nucleated under the maximum normal tensile stress. As a result, the voids are not able to grow and coalesce into the

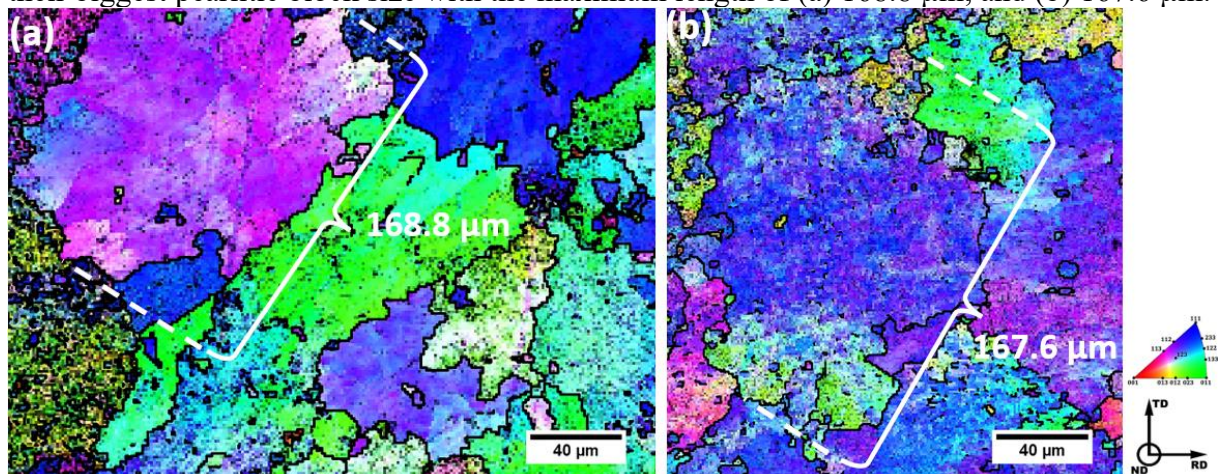
normal stress direction. However, local shear bands among void ligaments will be activated and propagated in the direction of the maximum shear stress. This mechanism will promote the growth of the voids into a parabolic shape and then, they will be shear-linked up resulting in the final fracture surface (DIETER, 1986). On the other hand, all Region II (in Figure 59d, 59e, 59f, 59g, and 60b) are composed of smooth zones that apparently are deficient in dimples. In this case, it is pointed out by the literature (LI *et al.*, 2014) that the shear plastic deformation is too large that voids will not be produced by the maximum normal tensile stress, unlikely a significant plastic slip will be the main mechanism providing many shear bands. As a consequence, the intensive propagation of these local strained bands will develop an integrated shear fracture surface poor in dimples.

Furthermore, it can be seen in Figure 59e and 59g that the smooth fractured surface on UC is also constituted by dimples. These dimples are considerably more oriented to the shear direction than those on the DR fracture. It suggests dimples formation by shear stress. In addition to this, UC underwent a great macroscopic plastic deformation before failure, as previously depicted in Figure 53g. These facts suggest that UC may have established a significant alignment of its shear bands into the maximum shear stress direction. Additionally, an increase in grain size contributes to microstructural instability during the plastic deformation, which makes the grains prone to develop shear bands (JAZAERI; HUMPHREYS, 2004; BEHERA *et al.*, 2019; LI *et al.*, 2019). In this regard, it is known from the literature (LI *et al.*, 2019) that microstructural coarsening tends to change the fracture mechanism from shear fracture with voids to shear fracture with a flat surface. Therefore, the bigger pearlitic blocks of UC may have led to its shear rupture with a flat surface by boosting plastic deformation closely to the shear stress direction, which may result in a weak influence of the normal stress. Additionally, the UC failure surface presents some secondary cracks and large flat detached regions with high topographic relief, as indicated in Figure 59a, 59b, and 59d. Concerning the very soft microstructure of UC, these features can be a consequence of microstructural heterogeneity and hard second-phase particles such as inclusions (LI *et al.*, 2019; BARSOUM; FALESKOG, 2007). In this regard, those enormous flat detached structures seemed to be slip plans of pearlitic blocks that underwent transgranular fracture achieving sizes around 123 μm . In this context, Figure 61 confirms that the pearlitic blocks in UC have a comparable dimensional magnitude (around 168 μm) to the flat areas with high topography in the UC's surface fracture. This evidence may suggest the presence of large slip plans due to the UC's coarse pearlitic blocks.

Moreover, many researchers (CHEN *et al.*, 2021; KARTHIKEYAN *et al.*, 2021;

HAN *et al.*, 2019) reveal that shear fracture with a flat surface presents lesser shear strength and occurs faster in contrast to shear fracture with dimples. This phenomenon agreed with the aforementioned ruptures behavior during the in-situ TS experiments in which UC abruptly failed and DR does not. From this perspective, the smooth fracture surface of DR is mainly concentrated on the edge of the rupture plane. It may indicate that the DR's fracture started slowly in the areas rich in dimples and ended up fast in the zone comprised of a flat surface such as shear lips (KIRAN *et al.*, 2014). Finally, the rupture in UC should also occur following the same steps just described for DR, however, the fractured region in UC that is rich in dimples is too small that its effect on the entire failure is irrelevant, resulting in a dominance of the fast failure behavior.

Figure 61 – Color-coded IPF maps on large areas of the non-deformed UC specimen containing their biggest pearlitic block size with the maximum length of (a) 168.8 μm , and (b) 167.6 μm .



Source: Elaborated by the author.

6 CONCLUSIONS AND RECOMMENDATIONS FOR FURTHER WORKS

6.1 Conclusions

This thesis aimed to research the metallurgical behavior and performance of SAE1075 pearlitic steel throughout lab-simulated processes, which were based on the actual manufacturing route for producing tensile armor wires. The most significant findings of this research are organized by their respective thesis's chapter and summarized below:

6.1.1 Microstructure, microtexture, and crack susceptibility in pearlitic steel during lab-simulated processes aiming tensile armor application in flexible pipelines

Regarding the four lab-simulated process routes performed in this work which were based on the manufacture of pearlitic steel for tensile armor application, the present study evaluated the influence of key process parameters on the microstructure, microtexture, and crack susceptibility in pearlitic steel. In this context, the following conclusions can be drawn:

- 1) The employment of patenting treatment in pearlitic steel tended to refine the pearlitic microstructure developing a weak ferritic Goss microtexture component, increasing the volume fraction of the ferritic grain boundary, and raising the microhardness
- 2) The refinement and homogenization efficiency of the pearlitic microstructure during the patenting treatment was mainly dependent on the arrangement of austenitization temperature and specimen thickness, regarding a constant austenitization holding time and bath salt temperature. Additionally, the adoption of cold deformation before the patenting treatment achieved the great refinement of pearlitic blocks.
- 3) The patenting treatment affected the development of the $\{111\}\langle 112 \rangle$ microtexture component during the cold-rolling process by controlling the initial pearlitic block size before the cold deformation.
- 4) Stress relief treatment at 700 °C for 60 s applied in cold rolled pearlitic steel with the strongest $\{111\}\langle 112 \rangle$ microtexture component resulted in small recrystallized grains nucleating in the shear bands of the $\{111\}\langle 112 \rangle$ deformed pearlitic blocks and partial cementite spheroidization. Otherwise, no significant microstructural modifications were noticed when the stress relief was performed at 400 °C for 60 s.
- 5) Cracks and microcracks detected after the three-point bending experiment were found to nucleate between small recrystallized ferritic grains with divergence in Taylor factor

inside the $\{111\}\langle 112 \rangle$ pearlitic blocks. Also, the microcracks seemed to be connected mainly via the shear bands' path. Finally, fully lamellar pearlite perpendicular orientated to the crack propagation was the only obstacle detected to hinder the microcrack growth.

6.1.2 In-situ and interrupted cyclic three-point bending tests in SEM of two pearlitic steel microstructures: lamellar and partially spheroidized

In this study, secondary electron imaging and electron backscattered diffraction (EBSD) techniques were performed, respectively, during in-situ and interrupted cyclic three-point bending tests in pearlitic steel. Two conditions of pearlitic steel were designed for the TPB experiments: stress-relieved at 400 (SR400) and 700 °C (SR700) for 60 seconds after introducing 65% cold rolled reduction. The conclusions are summarized below:

- 1) Regarding the starting specimens, the employment of low temperature (400°C) and short time (60 seconds) during the stress relief treatment (SR400) of a 65% cold rolled pearlitic steel was insufficient to promote significant changes in the cold deformed microstructure. On the other hand, raising the stress relief temperature to 700°C (SR700) and keeping the same hold time (60 seconds) was meaningful for partially spheroidizing the cementite lamellae, nucleating new small grains in shear bands zones, reducing the amount of lattice defect and slightly modifying the orientation relationship between cementite/ferrite.
- 2) SR400 condition, with lamellar cementite morphology, exhibited a mechanical and microstructural stable performance under the repeated TPBs. In contrast, SR700 with partially spheroidized cementite was prone to softening, and its ferritic lattice strain highly varied during cyclic TPB deformation.
- 3) The remaining lamellae cementite in SR700 were brittle under repeated bending deformation.
- 4) The replacement of the lamellar pearlitic design with shear bands by the partially spheroidized pearlitic architecture with recrystallized small grain zones made the pearlitic steel susceptible to earlier macro shear band development, damage initiation, and crack propagation during the fourth successive TPB step.
- 5) The interrupted EBSD assessment revealed strain heterogeneity in both evaluated pearlitic steel conditions during the successive TPB experiments. For SR400, shear bands were the main strain concentration regions. Regarding the SR700 microstructure, the strain was located in small ferritic recrystallized grain zones with coarse

spheroidized cementite at their grain boundaries and triple junctions. These zones, full of fine recrystallized grains with coarse and hard second-phase particles, were considered the potential cause of the earlier damage and failure of the SR700 pearlitic steel condition.

- 6) The lamellar and partially spheroidized pearlitic steel conditions presented a mix of dimples and sheared areas (flat) on their fractured surface produced under cyclic TPB experiments. The regions with flat aspects were greater on the fractured surface of the SR400 condition, and its dimples were elongated. While the fracture surface of the SR700 was abundant in no stretched round dimples.

6.1.3 Influence of helical torsion on the deformation behavior of two pearlitic steel microstructures: Lamellar and partially spheroidized

Considering the laboratory-simulated helical torsion of rectangular wires under different wound angles (0, 20, and 60° about the cylindrical shaft guide) performed in this work, the deformation behavior of two types of pearlitic microstructures, lamellar and partially spheroidized, were briefly investigated via electron backscattered, secondary electron imaging and microhardness maps.

Based on this, the employment of helical torsion in rectangular pearlitic steel wires resulted in a heterogeneous distribution of local hardness throughout the wires' cross-section due to the combined effect of bending (mainly normal) and shear components. Under the low angle of helical torsion, the lamellar pearlitic microstructure was more resistant against normal bending strain than the partially spheroidized pearlitic condition, which promoted a more minor divergence in hardness distribution. The pearlitic blocks were mostly bowed in the helically twisted lamellar pearlitic wire under a low wound angle, demonstrating the predominant effect of shear deformation. Increasing the wound angle of helical torsion made it possible to realize a significant influence on the normal bending deformation and, consequently, a rise in the microhardness average in both evaluated conditions, which suggests that the normal bending component is the dominant hardener factor during helical torsion operation. The longitudinal pearlitic microstructures in the middle thickness were found to be similar among the different evaluated helical torsion conditions.

6.1.4 In-situ tensile-shear test in SEM and DIC analysis of two pearlitic steel microstructures: undeformed coarse and deformed-refined

In-situ tensile-shear (TS) tests in scanning electron microscopy (SEM) and digital image correlation (DIC) technique were performed for two types of pearlitic steel microstructure: undeformed-coarse (UC) and deformed-refined (DR). In this context, the following conclusions can be drawn.

- 1) The geometry of the TS specimen adopted in the in-situ SEM experiments proved to be suitable for providing easier access to the pearlitic microstructure surface under shear deformation.
- 2) The DR pearlitic microstructure exhibited higher shear strength than the UC pearlitic condition during shear deformation. However, DR elongated less than UC.
- 3) The DIC identified strain heterogeneity in both pearlitic steel conditions under shear deformation. In the softer microstructure of the UC condition, the strain was concentrated mainly at the pearlitic colony boundary. Regarding the rigid microstructure of the DR specimen, the strain was located in grain boundary ferrite and in particular pearlites with lamellae aligned parallel to the tensile axis.
- 4) The phenomenon of decohesion was the main mechanism observed to be a potential source of crack initiation in both studied pearlitic steel microstructures. Specifically, decohesion happened at the colony boundary in the UC microstructure and at the ferrite/cementite interface (interlamellar) in the DR pearlitic condition.
- 5) Cementite showed to break easily in the UC condition as the tensile-shear test progressed and it tended to buckle in the DR pearlitic state.
- 6) The UC and DR pearlitic microstructures led to different shear failure modes. The UC pearlitic steel underwent an instantaneous rupture and its sheared fracture surface presented a flat aspect. In contrast, the failure of the DR specimen occurred slowly and its fractured surface was abundant in dimples.

6.2 Recommendation for future works

The following recommendations were made based on the research that has been conducted in this thesis:

- 1) Use a round bar as the start geometry of the as-received SAE1075 pearlitic steel in the lab-simulated processes performed in Chapter 2. Regarding the actual manufacture of tensile armor wires, the round bar will ensure a more realistic deformation profile in the studied specimens during the rolling processes. However, a sophisticated rolling machine

is required for conducting this operation.

- 2) Study the possible formation of martensite islands combined with lamellar or spheroidized pearlite during the thermal treatments studied in Chapter 2 (patenting or stress relief) as an opportunity to improve the final mechanical properties of the rectangular pearlitic wires as in dual-phase steels employed in the automotive field.
- 3) Study the orientation relationship between the shear band zones produced during the cold rolling process and the small recrystallized grains formed during the stress relief treatment (shown more clearly in Chapter 2) via in-situ heating and EBSD techniques. This knowledge is paramount for understanding the formation of those detrimental small recrystallized grains, which can bring up an opportunity to avoid them.
- 4) Identify the mode failure of the partially spheroidized pearlitic condition via in-situ secondary electron tensile shear experiment and compare it to the failure findings in Chapter 4 for the lamellar pearlitic microstructure.
- 5) Evaluate the mechanical performance of a no-stress relief and 65% cold-rolled pearlitic steel specimen under a three-point bending test (in Chapter 3) and its deformation behavior during the helical torsion operation (in Chapter 5), both compared to the stress-relieved specimens at 400 and 700 °C for 60 seconds.
- 6) Study the effect of the pearlitic block size, which was shown in Chapter 2 to be influenced by the condition of the applied patenting treatment, on the mechanical performance of pearlitic steel under the three-point bending test and its deformation behavior during the helical torsion procedure.
- 7) Identify the orientation relationship between cementite/ferrite (via transmission Kikuchi diffraction or transmission electron microscopy techniques) in the pearlites where the decohesion phenomenon occurs during the tensile shear deformation presented in Chapter 4. It can likely provide evidence of a weak bond related to the orientation relationship between cementite/ferrite in those pearlites.
- 8) Study the effect of the wound angle of the helical torsion on the crystallographic behavior throughout the cross-section of the rectangular pearlitic steel wires.
- 9) Investigate the stress corrosion cracking susceptibility of helically twisted specimens under different wound angles with lamellar and partially spheroidized pearlitic microstructures in a relevant environment (CO₂ atmosphere) by using the slow strain-rate technique.

REFERENCES

- ABREU, H. F. G., **Influência da Textura Cristalográfica na Anisotropia Magnética das Ligas Fe-Mo-NiC**, Thesis, Universidade Federal do Rio de Janeiro, 1998.
- AGENCIA NACIONAL DE PETRÓLEO, **GÁS NATURAL E BIOCOMBUSTÍVEIS – ANP**, “Anuário Estatístico Brasileiro do Petróleo, Gás Natural e Biocombustíveis” 2019.
- AKSENOVA, K., et al. Structural Phase Transformation of Rail Steel in Compression. **Metals**. v. 12, p. 1-11, 2022.
- ALLAIN, S. Y. P., et al. Microstructure-based behavior law for globular pearlitic steels. **J Mater Res Technol**. v. 8, p. 3373–3376, 2019.
- ALLAIN, S.; BOUAZIZ, O. Microstructure based modeling for the mechanical behavior of ferrite–pearlite steels suitable to capture isotropic and kinematic hardening. **Mater Sci Eng A**, v. 496, p. 329–336, 2008.
- ALMEIDA, N. G. S. et al. Hardness, Microstructure and Strain Distributions in Commercial Purity Aluminum Processed by Multi Directional Forging (MDF). **Materials Research**. v. 23, n. 4, 20200262, 2020.
- AMERICAN PETROLEUM INSTITUTE. *API RP 17B – Recommended Practice for Flexible Pipe*. Washington: **American Petroleum Institute**; 2007.
- ARAFIN, M. A., SZPUNAR, J. A. A new understanding of intergranular stress corrosion cracking resistance of pipeline steel through grain boundary character and crystallographic texture studies, **Corros. Sci.** n. 51, p. 119–128, 2009.
- ARANDA, M. M., et al. Effect of Prior Austenite Grain Size on Pearlite Transformation in a Hypoeutectoid Fe-C-Mn Steel. **Metall. Mater. Trans. A**. v. 45, p. 1778–1786, 2014.
- AROLA, A.-M., et al. The effect of mechanical behavior on bendability of ultrahigh-strength steel. **Mater. Today Commun**. v. 26, 101943, 2021.
- ATIA, A., MOHAMMEDI, K. Carbon Dioxide Chemistry, Capture and Oil Recovery Chapter 12: A Review on the Application of Enhanced Oil/Gas Recovery through CO₂ Sequestration. August 2018.
- BAI, Y. et al. **Integrity Management of Flexible Pipes**. In: Bai Y, Bai Q. *Subsea Pipeline Integrity and Risk Management*. Waltham: Gulf Professional Publishing; 2014. p. 101-124.
- BAI, Y. et al. **Subsea Production Risers**. In: Bai Y, Bai Q. *Subsea Engineering Handbook*. Boston: Gulf Professional Publishing; 2012. p. 853-890.
- BAI, Y., BAI, Q. 2005. **Subsea pipelines and risers**, first ed. Elsevier, Oxford.
- BARIK, R. K., et al. Bridging microstructure and crystallography with the micromechanics of cleavage fracture in a lamellar pearlitic steel. **Acta Mater**. v. 214, 116988, 2021.

BARSOUM, I.; FALESKOG, J. Rupture mechanisms in combined tension and shear experiments. **Int J Solids Struct.** v. 44, n. 6, p. 1768-1786, 2007.

BEHERA, S., et al. Recipe for improving the impact toughness of high-strength pearlitic steel by controlling the cleavage cracking mechanisms. **Mater. Sci. Eng. A.** v. 764, 138256. 2019.

BENITO, J. A., et al. Change of Young's modulus of cold deformed pure iron in a tensile test. **Metall Mater Trans A** v. 36, p. 3317–3324, 2005.

BHOLE, S. D., FRIEDMAN, J. A. Steel wire patenting: thermal and metallurgical comparison between quenching in lead and quenching in a fluidised bed. **IHTSE.** v. 4, p. 152-155, 2014.

BJØRN, H. F., et al. Influence of Local Microstructural Variations on the Bendability of Aluminum Extrusions: Experiments and Crystal Plasticity Analyses. **J Appl Mech.** v. 90, 04006, 2022.

CHATTI, S., FATHALLAH, R. A study of the variations in elastic modulus and its effect on springback prediction. **Inter J Mater Form. Int J Mater Form** v. 7, p. 19–29, 2012.

CHEN, C-H. et al. Effect of post-weld heat treatment on the solid-state diffusion bonding of 6061 aluminum alloy. **Appl Sci.** v. 11, n. 20, 9660, 2021.

CLARKE, T. et al. Monitoring the structural integrity of a flexible riser during a full-scale fatigue test. **Engineering Structures.** v. 33, n. 4, p. 1181-1186, 2011.

COM o pré sal, nossa capacidade produtiva continua crescendo exponencialmente. Available at: < <https://petrobras.com.br/pre-sal#3500m/4>> Accessed on: 08 nov. 2023

CORDIER-ROBERT, C. et al. Influence of torsion deformation on microstructure of cold drawn pearlitic steel wire. **J Mater Sci.** v. 43, p. 1241-1248, 2008.

COTTRELL, A. H., BILBY, B. Dislocation theory of yielding and strain ageing of iron. **Proc Phys Soc London Sect A.** v. 62, p. 49-62, 1949.

DAMBRE, P. **Process for manufacturing pearlitic steel wire.** N.V. Bekaert S. A. EP 0 232 558 B1, 1990.

DAS, S., et al. The effect of cooling rate on structure and properties of a HSLA forging. **Scr. Mater.** 48, 51-57. 2003.

DE SOUSA, J. R. M. et al. Structural response of a flexible pipe with damaged tensile armor wires under pure tension. **Marine Structures.** v. 39, n. 1, p. 1-38, 2014.

DENNIS, D. **Wet collapse behavior of Flexible UDW Risers:** Literature study into the factors influencing the critical wet collapse pressure and mode shape. Delf university of technology. 2018.

DEY, I., et al. Effect of Nb micro-alloying on microstructure and properties of

thermomechanically processed high carbon pearlitic steel. **Mat. Character.** v. 140, p. 45-54, 2018.

DIETER, G. E. **Mechanical Metallurgy**. 3rd ed. United States: McGraw-Hill book company; 1986.

DIPPENAAR, R. J., HONEYCOMBE, R. W. K. The crystallography and nucleation of pearlite. **Proc Math Phys Eng Sci P ROY SOC A-MATH PHY**. v. 333, p. 455-467, 1973.

DURGAPRASAD, A. et al. Microstructural engineering in eutectoid steel: a technological possibility? **Metall Mater Trans A**. v. 49, p. 1520-1535, 2018b.

DURGAPRASAD, A., et al. Delamination of pearlitic steel wires: the defining role of prior-drawing microstructure. **Metall. Mater. Trans. A**. v. 49, p. 2037-2047, 2018a.

ENGLER, O., RANGLE, V. **Introduction to Texture analysis: Macrotexture, Microtexture, and Orientation Mapping**, 2^a edição, CRC Press, 2009.

ESHELBY, J. D., et al. 1951. XLI. The equilibrium of linear arrays of dislocations. **Philos. Mag.** 42, 351-364.

FANG, F. et al. Microstructure and mechanical properties of cold-drawn pearlitic wires affect by inherited texture. **Mater Des**. v. 79, p. 60-67, 2015.

FERNANDO, U. S. et al. Evolution of Residual Stress in Tensile Armour Wires of Flexible Pipe During Pipe Manufacture. **Proceedings of the ASME 2017 36th International Conference on Ocean, Offshore and Arctic Engineering**, 2017, Norway.

FIGUEIREDO, R. B., LANGDON, T. G. 2022. Effect of grain size on strength and strain rate sensitivity in metals. **J. Mater. Sci.** 57, 5210-5229.

FIGUEIREDO, R. B., LANGDON, T. G. Deformation mechanisms in ultrafine-grained metals with an emphasis on the Hall-Petch relationship and strain rate sensitivity. **Journal of Materials Research and Technology**. v. 14, p.137-59. 2021.

FOISSEY, S.; et al. **Profiled steel wire with high mechanical characteristics resistant to hydrogen embrittlement**. ThyssenKrupp Steel Europe AG, ArcelorMittal Wire France SA. US 9.249.486 B2, 2016.

FURUHARA, T., et al. Ultra-fine ($\alpha+\theta$) Duplex Structure Formed by Cold Rolling and Annealing of Pearlite. **ISIJ Int**. v. 45, p. 392-398, 2005.

GAU, J-T., KINZEL, G. L. An experimental investigation of the influence of the Bauschinger effect on springback predictions. **J Mater Process Technol**. v.108, p. 369–375, 2001.

GENSAMER, M., et al. The tensile properties of pearlite, bainite, and spheroidite. **Metallogr Microstruct Anal**. v. 1, p. 171-189, 2012.

GHOSH, A., et al. Microstructure, properties, and age hardening behavior of a

thermomechanically processed ultralow-carbon cu-bearing high-strength steel. **Metall. Mater. Trans. A.** v. 36, p. 703-713, 2005.

GUO, N. et al. Influence of Torsion Deformation on Textures of Cold Drawing Pearlitic Steel. **Acta Metall. Sin.** v. 28, n. 6, p. 707-714, 2015.

GUO, N., et al. Deformation bands in fully pearlitic steel during wire drawing. **Sci. China Technol. Sci.** v. 57, p. 796-803, 2014.

GUZIEWSKI, M., et al. Atomistic investigation into the atomic structure and energetics of the ferrite-cementite interface: The Bagaryatskii orientation. **Acta Mater.** v. 119, p. 184–192, 2016.

HAESSNER, F. **Recrystallization of Metallic Materials**, second ed. Verlag GmbH, Stuttgart, p. 159. 1978.

HAN, B. et al. Shear strength, fracture mechanism and plastic performance of Cu/Sn5SbexCuNiAg/ Cu solder joints during thermal aging. **J Mater Sci Mater Electron.** n. 30, p. 18342-18349, 2019.

HANONGE, D. et al. **CO₂-Stress Corrosion Cracking Risk Mitigation for Flexible Pipe Design**. In: Subsea Pipeline Technology Congress; 2022 Mar 29; London, United Kingdom.

HILL, T., et al. “The future for flexible pipe riser technology in deepwater: Case study”, in 2006 **Offshore Technology Conference**, 17768, 2006.

HOSFORD, W. F. **Mechanical Behavior of Materials**. Cambridge: Cambridge University press; 2005

HU, X. et al. Origin and mechanism of torsion fracture in cold-drawn pearlitic steel wires. **Journal of Materials Science.** v. 48, p. 5528-5535, 2013.

HU, X. et al. Origin and mechanism of torsion fracture in cold-drawn pearlitic steel wires. **J Mater Sci.** v. 48, p. 5528-5535, 2013.

HU, X. H., et al. A macro-micro-multi-level modeling scheme to study the effect of particle distribution on wrap-bendability of AA5754 sheet alloys. **J. of Mater. Process. Technol.** v. 210, p. 1232-1242, 2010.

HUMPHREYS, F. J., HATHERLY, M., **Recrystallization and Related Annealing Phenomena**, 2^a edição, Elsevier, 2004

HYZAK, J. M.; BERNSTEIN, I. M. The role of microstructure on the strength and toughness of fully pearlitic steels. **Metall Trans A.** v. 7, p. 1217-1224, 1976.

INOUE, A. et al. Deformation and fracture behaviours of cementite. **Trans Jpn Inst Met.** v. 17, n. 10, p.663-672, 1976.

ISAVAND, S. ASSEMPOUR, A. Strain localization and deformation behavior in ferrite-pearlite steel unraveled by high resolution in-situ testing integrated with crystal plasticity simulations. **Int J Mech Sci.** v. 200, 106441, 2021.

- JAVAHERI, V., et al. Effect of post-rolling cooling on the hot-rolled microstructure and texture of a new medium-carbon steel. In: IOP Conf. Ser.: **Mater. Sci. Eng.** v. 1121, 012037, 2021.
- JAZAERI, H., HUMPHREYS, F. J. The effect of initial grain size on the microstructures developed during cold rolling of a single-phase aluminium alloy. **MSF.** v. 467-470, p. 63-68. 2004.
- JOHNSON, R. A. Clustering of carbon atoms in α -iron. **Acta Metall.** v. 15, p. 513–517, 1967.
- KANIE, A., et al. Elastic strains of cementite in a pearlite, steel during tensile deformation measured by neutron diffraction. **ISIJ Int.** v. 44, p. 1952–1956, 2004.
- KAPP, M. W., et al. The importance of lamellar architecture to obtain ductility in heavily cold-worked pearlitic steels revealed by microbending experiments. **Acta Mater.** v. 232, 117935, 2022.
- KARTHIKEYAN, K. M. B. et al. Tensile test fractography of subzero treated EN24 alloy steel. **Mater Today.** v. 46, p. 3205-3211, 2021.
- KESTENS, L. A. I., PIRGAZI, H. Texture formation in metal alloys with cubic crystal structures. **Mater. Sci. Technol.** 32, p. 1303-1315, 2016.
- KESTENS, L., JACOBS, S. Texture Control During the Manufacturing of Nonoriented Electrical Steels. **Texture, Stress and Microstructure.** 173083. 2008.
- KIRAN, R. et al. Experimental studies and models for ductile fracture in ASTM A992 steels at high triaxiality. **J Struct Eng.** v. 140, n. 2, 2014.
- KOENIG, M. J. GRI pipeline simulation facility stress corrosion cracking defect set. Topical report, June 1992-January 1993. **N NDT & E International.** v. 31 n. 5, p. 377, 1998.
- KOGA, N. et al. Distribution of elastic strain in a pearlitic structure. **Scr Mater.** v. 67, n. 4, p. 400-403, 2012.
- KRAUSS, G.; MATLOCK, D. K. Effects of strain hardening and fine structure on strength and toughness of tempered martensite in carbon steels. **J Phys IV.** v. 5, p. 51–59, 1995.
- LAST, S. et al.: “Comparison of models to predict the annulus conditions of flexible pipe”, OTC 14065, **Offshore Technology Conference**, 2002, Houston.
- LEÃO, P. B. P., et al. Microstructure, microtexture, and crack susceptibility in pearlitic steel during lab-simulated processes aiming tensile armor application in flexible pipelines. **J Mater Process Technol.** v. 316, 117950, 2023a
- LEÃO, P. B. P., et al. In-situ tensile-shear test in SEM and DIC analysis of two pearlitic steel microstructures: undeformed-coarse and deformed-refined. **J Mater Res Technol.** v. 24, p. 9441–9461, 2023b.

LEÃO, P. B. P., et al. Recrystallization kinetics and yield-strength adjustment after annealing of cold-rolled microalloyed steel. **Mater. Sci. Technol.** v. 38, p. 363-376, 2022.

LEFFLER, W. L.; et al. **Deepwater Petroleum Exploration and Production**; PennWell Books: Tulsa (2003).

LEWANDOWSKI, J. J., THOMPSON, A. W. Effects of the Prior Austenite Grain Size on the Ductility of Fully Pearlitic Eutectoid Steel. **Metall. Mater. Trans. A.** v. 17, p. 461- 472, 1986.

LI, Y. J. et al. Atomic-scale mechanisms of deformation-induced cementite decomposition in pearlite. **Acta Mater** v. 59, n. 10, p. 3965-3977, 2011.

LI, Y. J. et al. Mechanism of subgrain coarsening and its effect on the mechanical properties of carbon-supersaturated nanocrystalline hypereutectoid steel. **Acta Materialia.** v. 84, p.110-123, 2015.

LI, Y. J., et al. Atomic-scale mechanisms of deformation-induced cementite decomposition in pearlite. **Acta Mater.** v. 59, p. 3965-3977, 2011.

LI, Y. J., et al. Evolution of strength and microstructure during annealing of heavily cold-drawn 6.3 GPa hypereutectoid pearlitic steel wire. **Acta Mater.** v. 60, p. 4005-4016, 2012.

LI, Z. et al. Investigation on fracture mechanisms of metals under various stress states. **Acta Mech.** v. 225, p. 1867-1881, 2014.

LI, Z. et al. A fracture criterion for prediction of fracture initiation of metal materials at various stress states for nuclear waste storage. **Sci Technol Nucl.** v. 2019, 3591925, 2019

LIU, M., et al. Effect of microstructure and crystallography on sulfide stress cracking in API-5CT-C110 casing steel. **Mater. Sci. Eng. A.** v. 671, p. 244-253, 2016.

LU, B. T. et al. Relationship between Yield Strength and NearNeutral pH Stress Corrosion Cracking Resistance of Pipeline Steels-An Effect of Microstructure. **Corrosion.** v. 62, n. 2, p. 129-140, 2006.

LUKASSEN, T. V. **Constitutive Behavior of Tensile Armor Wires in Unbonded Flexible Pipes.** PhD thesis, Technical University of Denmark, 2019.

LUPTON, D. F., WARRINGTON, D. H. The Influence of Deformation on the Spheroidization and Coarsening of Pearlite. **Met. Sci. J.** v. 6, p. 200-204, 1972.

MAEDA, M., et al. Effect of Cementite Dispersion on Void Formation Process in Spheroidize-Annealed Steels. **ISIJ Int** v. 58, p. 1490–1499, 2018.

MALLEN, H. J.; SUGIER, A. **Procede d'elaboration de fils d'acier destines a la fabrication de conduites flexibles, fils d'acier obtenus par ce procede et conduites flexibles renforcees par de tels fils.** IFP Energies Nouvelles IFPEN. EP 0 478 771 B1, 1996.

MANDAL, S., et al. Thermo-mechanically controlled processed ultrahigh strength steel:

Microstructure, Texture and mechanical properties. **Mater. Sci. Eng. A.** v. 663, p. 126-140, 2016.

MARINHO, M. G. et al. Integrity assessment and repair techniques of flexible risers. In: **Proceedings of the 25th ASTM international conference on offshore mechanics and arctic engineering**, v. 4, n. 92467, p. 253–260, 2006.

MEHRABI, H. et al. Effects of tension-compression asymmetry on bending of steels. **Appl Sci.** v. 10, n. 9, 3339, 2020.

MISHRA, K. et al. Change of deformation mechanism through nano-structuring of pearlite: an in-situ study. **Mater Charact.** v. 167, 110487, 2020.

MIYAMOTO, G., et al. T. Formation of grain boundary ferrite in eutectoid and hypereutectoid pearlitic steels. **Acta Mater.** v. 103, p. 370-381. 2016.

MONTANA, Y., et al. Pearlite Spheroidisation and Microstructure Refinement Through Heavy Warm Deformation of Hot Rolled 55VNb Microalloyed Steel. **Metall. Mater. Trans. A.** v. 53, p. 2586-2599, 2022.

MOURITZ, A. P. **Introduction to Aerospace Material.** Cambridge: Woodhead Publishing Limited; 2012.

MUHAMMAD, W., et al. Bendability enhancement of an age-hardenable aluminum alloy: Part I — relationship between microstructure, plastic deformation, and fracture. **Mater Sci Eng A** v. 753, 179–191, 2019a.

MUHAMMAD, W., et al. Bendability enhancement of an age-hardenable aluminum alloy: Part II — multiscale numerical modeling of shear banding and fracture. **Mater Sci Eng A** v. 754, p. 161–177, 2019b.

MÜNSTERMANN, S., et al. Influencing parameters on elastic modulus of steels. **Can Metall Q** v. 53, p. 264–273, 2014.

NAOFAL, J., et al. Effects of Hardening Model and Variation of Elastic Modulus on Springback Prediction in Roll Forming. **Metals** v. 9, 1005, 2019.

NINE, H. D. Slip planes and asymmetric slip in fatigue of iron single crystals. **Phil Mag.** v. 26 n. 6, p. 1409-1418, 1972.

NING, G. et al. Deformation bands in fully pearlitic steel during wire drawing. **Science China Technological Sciences.** v. 57, p. 796- 803, 2014.

NIU, F., et al. Effect of Bending Process on Microstructure, Mechanical Properties and Crack Formation of 5% Ni Steel. **Metals** v. 12, 1188, 2022.

OHBA, H., et al. **Nippon Steel Technical Report: High-performance Wire Rods Produced with DLP.** p. 96. 2007.

PARIS, H. **Metallurgy, Processing and Applications of Metal Wires - A Review.** TMS,

Warrendale, p. 3–15, 1996.

PETROBRAS. Available at: <<https://petrobras.com.br/pt/nossasatividades/areas-de-atuacao/exploracao-e-producao-de-petroleo-e-gas/presal/>> Accessed on: 20 fev. 2021

PORCARO, R. R., et al. Microstructure and mechanical Properties of a flash butt welded pearlitic rail. **J. of Mater. Process. Technol.** v. 270, p. 20-27, 2019.

PRASAD, C., et al. Microstructure engineering by dispersing nano-spheroid cementite in ultrafine-grained ferrite and its implications on strength-ductility relationship in high carbon steel. **Mater Des.** v. 139, p. 324–335, 2018.

RASTEGARI, H., et al. Effect of initial microstructure on the work hardening behavior of plain eutectoid steel. **Mater Sci Eng A.** v. 632, p.103–109, 2015.

RECOMMENDED Practice for Flexible Pipe: API RECOMMENDED PRACTICE 17B, American Petroleum Institute Publishing Services, Third edition, N.W., Washington, D.C. March 2002.

SAASTAMOINEN, A., et al. The effect of thermomechanical treatment and tempering on the subsurface microstructure and bendability of direct-quenched low-carbon strip steel. **Mat. Character.** v. 134, p. 172-181. 2017.

SAITO, R., et al. Effects of Initial Structure and Reversion Temperature on Austenite Nucleation Site in Pearlite and Ferrite-Pearlite. **Metall. Mater. Trans. A.** v. 49, p. 6001-6009, 2018.

SIMONSEN, A. **Inspection and monitoring techniques for un-bonded flexible risers and pipelines.** University of Stavanger. Faculty of Science and Technology. Master's thesis. 2014.

STODOLNY, J., et al. Fragmentation Rate of Cementite Lamellas in Nanoppearlite. **JOM.** v. 71, p. 3298–3304, 2019.

STOJAKOVIC, D., **Microstructure Evolution in Deformed and Recrystallized Electrical Steel,** Thesis, Drexel University, 2008.

SUN, J. -J., et al. Microstructure of warm rolling and pearlitic transformation of ultrafine-grained GCr15 steel. **Mater. Character.** v. 95, p. 291-298, 2014.

SUWAS, S., RAY, R. K., **Crystallographic Texture of Materials,** Springer, 2014.

SZPUNAR, J. A., et al. The Mechanism of Failure by Hydrogen Induced Cracking in an Acidic Environment for API, 5L X70 Pipeline Steel. **Hydrogen Energy.** v. 40, p. 1096–1107, 2015a.

SZPUNAR, J. A. et al. Texture, local misorientation, grain boundary and recrystallization fraction in pipeline steels related to hydrogen induced cracking, **Mater. Sci. Eng. A.** v. 620, p. 97, 2015b.

SZPUNAR, J. A. et al. The changes of grain boundary character distribution during the secondary recrystallization of electrical steel, **Acta Mater.** v. 46, 1063, 1998.

TAGASHIRA, S., et al. Deformation microstructure and tensile strength of cold rolled pearlitic steel sheets. **ISIJ Int.** v. 40 n. 11, p. 1149-1156, 2000.

TAGLIARI, M. dos R. et al. Tensile Armor Wires Submitted to Slow Strain Rate Tests in a Corrosive Environment and Cathodic Protection: a Comparison Between Two Different Microstructures. **Material Research.** v. 22, n. 3, 2019.

TAKAHASHI, J., et al. Change in carbon state by low-temperature aging in heavily drawn pearlitic steel wires. **Acta Mater.** n. 60, p. 387-395, 2012.

TAKAHASHI, T. et al. Crystallographic features and formation processes of pearlite block. **Journal of the Japan Institute of Metals.** v. 42, p. 716–723, 1978a.

TAKAHASHI, T. et al. Microstructures dominating the ductility of eutectoid pearlitic steels. **J Jpn Inst Metals.** v. 42, n. 7, p. 708-715, 1978b.

TALEFF, E. M., et al. Microstructure-Property Relationships in Pearlitic Eutectoid and Hypereutectoid Carbon Steels. **JOM.** v. 54, p. 25-30, 2002.

TANAKA, M. et al. Nature of delamination cracks in pearlitic steels. **Scripta Materialia.** v. 112, p. 32-36, 2016.

TECHNICAL Note - EBSD – Hexagonal Data Sampling. EDAX smart Insight 2013 [homepage on the internet]. Available at: < https://www.edax.com/-/media/ametekedax/files/ebsd/technical_notes/hexagonal-data-sampling.pdf?dmc=1&la=en > accessed on: 6 Oct. 2023.

TESHIMA, T. et al. Local cementite cracking induced by heterogeneous plastic deformation in lamellar pearlite. **Mater Sci Eng A.** v. 679, p. 223-229, 2017.

THUNDER said energy. Available at: < <https://thundersaidenergy.com/2019/08/07/presalt-riser-designs/> > Accessed on: 10 nov. 2023

TOMOTA, Y., et al. Effect of carbon concentration on tensile behavior of pearlitic steels. **Mater. Sci. Technol.** v. 19, p. 1715–1720, 2003.

TÓTH, L. S., et al. Development of ferrite rolling textures in low- and extra low-carbon steels. **Metall. Trans.** v. 21, p. 2985–3000, 1990.

TUNG, P-Y., et al. Under-stoichiometric cementite in decomposing binary Fe-C pearlite exposed to rolling contact fatigue. **Acta Mater.** v. 216, 117144, 2021.

UMAR, M., et al. Investigating the effect of cementite particles size and distribution on local stress and strain evolution in spheroidized medium carbon steel using crystal plasticity-based numerical simulations. **Steel Res. Int.** v. 92, 2000407, 2021.

UMEMOTO, M. et al. Mechanical properties of cementite and fabrication of artificial pearlite. **Mater Sci Forum**. v. 426, p. 859-864, 2003.

VALIENTE, A., et al. A probabilistic model for the pearlite-induced cleavage of a plain carbon structural steel. **Eng. Fract. Mech.** v. 72, p. 709–728, 2005.

VENTELON, L., et al. Dislocation core reconstruction induced by carbon segregation in bcc iron. **Phys Rev B**. p. 91, 220102, 2015.

VERHOEVEN, J. D.; GIBSON, E. D. The Divorced Eutectoid Transformation in Steel. **Metall Mater Trans A**. v. 29, p. 1181-1189, 1998.

VERMEIJ, T. HOEFNAGELS, J. P. N. Plasticity, localization, and damage in ferritic-pearlitic steel studied by nanoscale digital image correlation. **Scr Mater**. v. 208, 114327, 2022.

WANG, C. J., et al. Effects of solutes on dislocation nucleation and interface sliding of bimetal semi-coherent interface. **Int J Plast**. v. 131, 102725, 2020.

WANG, Y., et al. In-situ neutron diffraction during tension-compression cyclic deformation of a pearlite steel. **Mater Sci Eng A**. v. 676, p. 522–530, 2016.

WATERSCHOOT, T., et al. Hot rolling texture development in CMnCrSi dual-phase steels. **Metall. Mater. Trans. A**. v. 33, p. 1091-1102. 2002.

WRIGHT, S. I., et al. A Review of Strain Analysis Using Electron Backscatter Diffraction. **Microsc. Microanal**. v. 17, p. 316-329, 2011.

YAJIMA, Y. et al. Influential factors on the deformability of colonies in pearlitic steel. **Mater Charact**. v. 177, 111197, 2021.

YAJIMA, Y., et al. Influential factors on the deformability of colonies in pearlitic steel. **Mater Charact** v. 177, 111197, 2021.

YAN, N., et al. Shear localization in metallic materials at high strain rates. **Prog. Mater. Sci.** v. 119, 100755, 2021.

YANG, X., et al. Prediction of springback in air-bending of Advanced High Strength steel (DP780) considering Young's modulus variation and with a piecewise hardening function. **Int J Mech Sci** v. 105, p. 266–272, 2016.

YASUDA, Y., et al. Strain-hardening characteristics of ferrite layers in pearlite microstructure. **Mater Sci Technol**. v. 34, p. 772-779, 2017.

YI, H. L., et al. Acceleration of spheroidization in eutectoid steels by the addition of aluminum. **Scr Mater**. v. 67, p. 645–648, 2012.

YOKOYAMA, H. et al. Development of High Strength Pearlitic Steel Rail (SP Rail) with Excellent Wear and Damage Resistance. **NKK TECHNICAL REVIEW**. 86. 2002.

YU, H. Y. Variation of elastic modulus during plastic deformation and its influence on

springback. **Mater Des.** v. 30, p. 846–850, 2009.

YU, H., et al. **Effect of loading-path on the elastic modulus degradation of high strength steels.** IOP Conf Ser.: Mater Sci Eng. v. 1270, 012042, 2022.

ZHANG, M-X., KELLY, P. M. Accurate orientation relationships between ferrite and cementite in pearlite. **Scr Mater** v. 37, p. 2009–2015, 1997

ZHANG, S. et al. EBSD-analysis of strain distribution and evolution in ferritic Pearlitic steel under cyclic deformation at intermediate temperature. **Mater Charact** v. 193, 112293, 2022.

ZHANG, X., et al. Microstructure Evolution and Mechanical Hardening of Hypereutectoid Pearlitic Steel During Cold Rolling. **Acta. Metall. Sin-Engl.** v. 20, p. 287-292, 2007.

ZHAO T.-Z., et al. Hardening and softening mechanisms of pearlitic steel wire under torsion. **Materials and Design** v. 59, p. 397–405, 2014.

ZHAO, X.-Y., et al. Effect of Prior Microstructures on Cementite Dissolution Behavior During Subcritical Annealing of High Carbon Steels. **Met. Mater. Int.** v. 28, p. 1315-1327, 2022.

ZHENG, C., et al. Microstructure evolution and mechanical properties of eutectoid steel with ultrafine or fine (ferrite + cementite) structure. **Mater Sci Eng A.** v. 599, p. 16-24, 2014.

ZHENG, H., et al. Microstructural evolution and mechanical property of ultrafine-grained pearlitic steel by cold rolling: The influence of cementite morphology. **Mater Sci Eng A.** v. 824, 141860, 2021.

ZHOU, C. **Transversal tensile amour buckling of flexible pipes.** Master thesis, Norwegian University of Science and Technology, 2014.

ZHOU, D. S., SHIFLET, G. J. A new orientation relationship between austenite and cementite in an Fe-C-Mn steel. **Scr Metall Mater** v. 27, p. 1215–1218, 1992.

ZHOU, D. S., SHIFLET, G. J. Ferrite: Cementite crystallography in pearlite. **Metall Trans A.** v. 23, p. 1259–1269, 1992.

ZHOU, L. et al. Torsion delamination and recrystallized cementite of heavy drawing pearlite wires after low temperature annealing. **Material Science and Engineering A.** v. 713, p. 52-60, 2018.

ZHOU, L. et al. Torsion performance of pearlitic steel wires: Effects of morphology and crystallinity of cementite. **Material Science and Engineering A.** v. 743, p. 425-435, 2019.

ZHOU, S. et al. Microstructural analysis on cleavage fracture in pearlitic steels. **Mater Charact** v. 119, p. 110-113, 2016.

ZHOU, S., et al. Microstructural analysis on cleavage fracture in pearlitic steels. **Mat. Character.** v. 119, p. 110-113, 2016.

ZHUANG, Z., et al. **Dislocation Mechanism-Based Crystal Plasticity: Theory and Computation at the micron and submicron scale.** London: Academic Press; 2019.